Faculty of Medicine and Health Sciences
Department of Human Anatomy, Embryology, Histology and Medical Physics

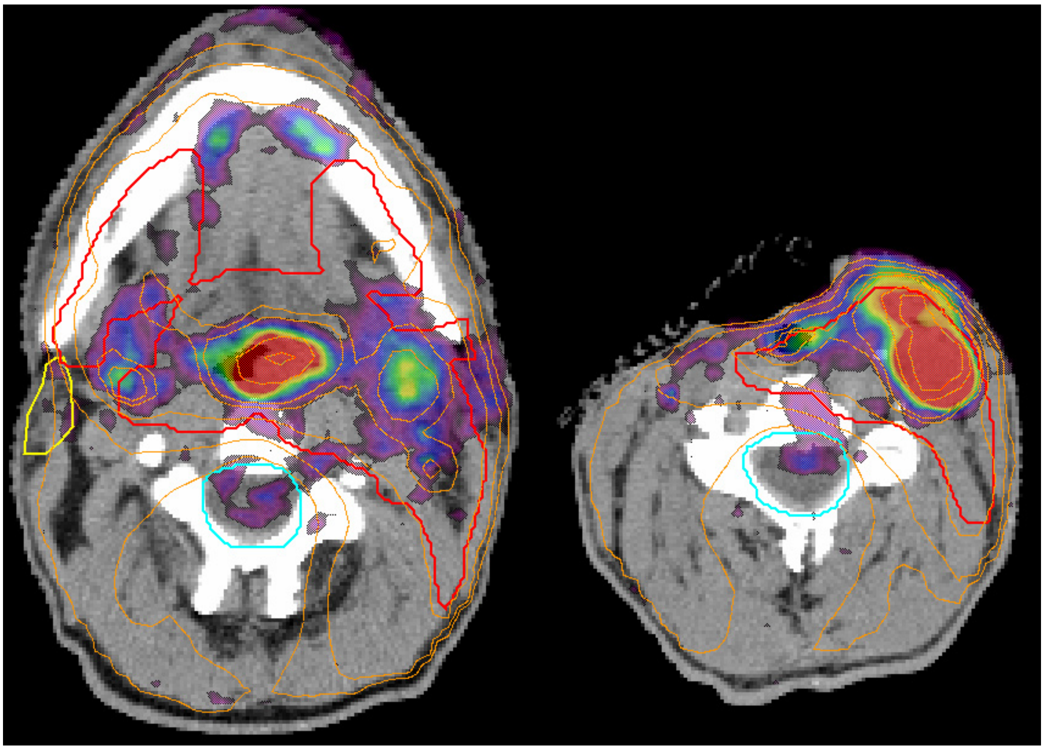

Biologically conformal radiation therapy and Monte Carlo dose calculations in the clinic

Barbara Vanderstraeten

2007

Promoter: prof. dr. H. Thierens
Co-promoter: prof. dr. W. De Neve

UNIVERSITEIT
GENT

Faculty of Medicine and Health Sciences
Department of Human Anatomy, Embryology, Histology and Medical Physics

Biologically conformal radiation therapy and Monte Carlo dose calculations in the clinic

Biologisch conforme radiotherapie en Monte Carlo dosisberekeningen in het ziekenhuis

Barbara Vanderstraeten

Promoter: prof. dr. H. Thierens
Co-promoter: prof. dr. W. De Neve

2007

Thesis submitted in fulfillment of the requirements for the degree of
Doctor in Medical Sciences

Promoter:

Prof. dr. H. Thierens	Universiteit Gent

Co-promoter:

Prof. dr. W. De Neve	Universiteit Gent

Doctoral guidance committee:

Prof. dr. H. Thierens	Universiteit Gent
Prof. dr. W. De Neve	Universiteit Gent
Prof. dr. ir. C. De Wagter	Universiteit Gent
Dr. N. Reynaert	Universiteit Gent
Ir. W. De Gersem	Universitair Ziekenhuis Gent

President of the examination committee:

Prof. dr. ir. C. De Wagter	Universiteit Gent

Examination committee:

Prof. dr. H. Thierens	Universiteit Gent
Prof. dr. W. De Neve	Universiteit Gent
Prof. dr. ir. C. De Wagter	Universiteit Gent
Prof. dr. C. Van de Wiele	Universiteit Gent
Prof. dr. L. Vakaet	Universiteit Gent
Prof. dr. V. Grégoire	Université Catholique de Louvain
Prof. dr. B. Heijmen	Erasmus Universitair Medisch Centrum Rotterdam
Dr. M. Alber	Universitätsklinikum Tübingen

Dean of the Faculty of Medicine and Health Sciences:

Prof. dr. J.-L. Pannier

Barbara Vanderstraeten is a Research Assistant (Aspirant) of the Fund for Scientific Research-Flanders (Fonds voor Wetenschappelijk Onderzoek-Vlaanderen).

Voor tante An
Voor mama en papa
Voor Bart en Jules

Table of contents

List of abbreviations

^{18}F: fluorine-18

1D: one-dimensional

2D: two-dimensional

3D: three-dimensional

4D: four-dimensional

ABST: anatomy-based segmentation tool

ANOVA: analysis of variance

ART: adaptive radiation therapy

BBST: biology-based segmentation tool

BCRT: biologically conformal radiation therapy

BOLD-MRI: blood oxygen level dependent magnetic resonance imaging

BTV: biological target volume

cb: contour-based

CBCT: cone-beam computed tomography

CM: component module

CNI: choline to N-aceltylaspartate index

CRASH: combine, re-order and step-and-shoot

CS: convolution/superposition

CT: computed tomography

CTC: common toxicity criteria

CTV: clinical target volume

Cu-ATSM: Cu(II)-diacetyl-bis-N-(4)-methylthiosemicarbazone

D: dose

DCE-MRI: dynamic contrast-enhanced magnetic resonance imaging

DD: dose difference

DLT: dose-limiting toxicity

DPM: Dose Planning Method

DRR: digitally reconstructed radiograph

DVH: dose-volume histogram

EGS: Electron-Gamma Shower

EPID: electronic portal imaging device

EPL: equivalent path-length

FDG: [^{18}F]-fluoro-deoxy-glucose

FMISO: [^{18}F]-fluoromisonidazole

fMRI: functional magnetic resonance imaging

GTV: gross tumor volume

GUH: Ghent University Hospital

Gy/fx: Gray per fraction

HNSCC: head and neck squamous cell carcinoma

HU: Hounsfield units

ICRU: International Commission on Radiation Units and Measurements

IGRT: image-guided radiation therapy

IMAT: intensity-modulated arc therapy

IMPT: intensity-modulated proton therapy

IMRT: intensity-modulated radiation therapy

linac: linear accelerator

LNR: lymph node region

LSD: Lab for Standard Dosimetry

MC: Monte Carlo

MCDE: Monte Carlo Dose Engine

MCTP: Monte Carlo treatment planning

MLC: multi-leaf collimator

MLD: mean lung dose

MMC: Macro Monte Carlo

MR: magnetic resonance

MRI: magnetic resonance imaging

MRS: magnetic resonance spectroscopy

MRSI: magnetic resonance spectroscopic imaging

MTD: maximum tolerated dose

MU: monitor unit

NIST: National Institute of Standards and Technology

NSCLC: non-small cell lung cancer

NTCP: normal tissue complication probability

OAR: organ at risk

OF: objective function

PB: pencil beam

pCTV: primary CTV

PENELOPE: PENetration and Energy Loss of Positrons and Electrons

PET: positron emission tomography

PRESTA: parameter reduced electron stepping algorithm

PRV: planning at risk volume

PTV: planning target volume

QVH: Q-volume histogram

RBE: relative biological effectiveness

ROI: region of interest

RT: radiation therapy

RTOG: Radiation Therapy Oncology Group

SEM: standard error of the mean

SIB: simultaneous integrated boost

SOWAT: segment outline and weight adapting tool

SPECT: single photon emission computed tomography

surr: surroundings

SWOT: segment weight optimization tool

TCP: tumor control probability

TERMA: total energy released per unit mass

TPS: treatment planning system

US: ultrasound

V: volume

vib: voxel intensity-based

VMC: Voxel Monte Carlo

XVMC: X-ray Voxel Monte Carlo

Summary

The development of radiation therapy treatment planning has always relied strongly on the available imaging technologies. Anatomical imaging techniques like computed tomography (CT) can visualize spatial changes in physical properties within patients. Additionally, tumor biology plays an important role in the diagnosis, treatment decision-making and the assessment of therapeutic response. Recent advances in biological imaging techniques, mainly based on positron emission tomography (PET), offer the opportunity to further individualize radiotherapy.

Highly structured dose distributions can be delivered using intensity-modulated radiation therapy (IMRT). IMRT can thus reduce toxicity by allowing a selective reduction of the dose to organs at risk, or allow dose escalation with the aim to improve local control. In current clinical practice, IMRT optimization is based on the assumption of a uniform biology distribution within each target volume and aims at achieving geometrically conformal dose distributions. By using the spatially heterogeneous biology distribution provided by one or several biological imaging modalities to guide the IMRT dose prescription, biologically conformal radiation therapy (BCRT) can be delivered.

In this thesis, BCRT is implemented into the IMRT treatment planning process at Ghent University Hospital by developing a biology-based segmentation tool and extending the objective function. A bound-constrained linear relationship between the image signal and the desired radiation dose is put forward. Additional tools are developed to assess the obtained biological conformity of the final treatment plan.

The feasibility of [^{18}F]fluoro-deoxy-glucose (FDG)-PET guided BCRT for head and neck cancer is demonstrated in a planning study. It is shown that BCRT does not compromise the planning constraints for the organs at risk. The obtained biological conformity is the best for the lowest level of dose escalation. Compared to uniform dose escalation within a contoured FDG-PET lesion, improved target dose coverage is achieved using BCRT.

Monte Carlo (MC) can be used to calculate radiation therapy dose distributions with great accuracy. The use of MC is especially advantageous in case of small, irregular treatment fields delivering dose to regions of great tissue inhomogeneity, for example in IMRT treatment of head and neck or lung tumors. In this thesis, the added value of MC compared to pencil beam and convolution/superposition algorithms is demonstrated for IMRT lung cancer patients.

Monte Carlo Dose Engine (MCDE) was developed at Ghent University as a highly accurate MC dose engine for IMRT patient dose calculations. In this thesis, the conversion of CT numbers into material composition data for MC dose calculations is studied in detail. Stoichiometric CT scanner calibration and the creation of dosimetrically equivalent tissue subsets result in a 14 bin CT conversion scheme. MCDE is further improved by the introduction of uncertainty-based stopping criteria, enabling accurate clinical treatment plan evaluation in the shortest possible time. Finally, the feasibility of integrating MCDE into the IMRT optimization process at Ghent University Hospital is demonstrated for an ethmoid sinus cancer patient case.

Optimal use of the new tools for incorporating biological imaging information into the treatment planning process will require an improved understanding of the radiobiology of tumors. Patients may benefit from the improvements in dose calculation accuracy using full MC. While faster but less accurate MC dose engines are currently being implemented into commercial treatment planning systems, highly accurate dose engines like MCDE remain indispensable benchmarking tools.

Samenvatting

Ontwikkelingen in de radiotherapieplanning hangen doorgaans sterk af van de beschikbare beeldvormingstechnieken. Anatomische beeldvorming, bijvoorbeeld computertomografie (CT), laat toe om ruimtelijke verschillen in fysische kenmerken binnen een patiënt in beeld te brengen. Daarnaast spelen de biologische eigenschappen van een tumor een belangrijke rol bij de diagnose, de keuze van de therapie en de beoordeling van het effect van de therapie. Recente ontwikkelingen op het vlak van biologische beeldvorming, voornamelijk gebaseerd op positronemissietomografie (PET), maken radiotherapie op maat van de individuele patiënt verder mogelijk.

Met intensiteitsgemoduleerde radiotherapie (IMRT) kunnen sterk gestructureerde dosisdistributies toegediend worden. IMRT kan hierdoor de dosis in de kritische organen verminderen en zo de toxiciteit verlagen, of de lokale controle verhogen door dosisescalatie mogelijk te maken. De optimalisatie van IMRT in de huidige klinische praktijk gaat uit van een homogene verdeling van de biologische eigenschappen binnen elk doelvolume, met een geometrisch conforme dosisdistributie als doel. Door het dosisvoorschrift te baseren op de met biologische beeldvorming verkregen heterogene verdeling van de biologische eigenschappen, kan biologisch conforme radiotherapie (BCRT) toegediend worden.

In deze thesis wordt BCRT geïmplementeerd in het IMRT planningsproces van het UZ Gent. Hiervoor wordt een biologisch gestuurde segmentatiemethode ontwikkeld en wordt de objectieve functie uitgebreid. Tussen de biologische beeldintensiteit en de voorgeschreven dosis wordt een begrensd lineair verband vooropgesteld. Er worden ook methodes ontworpen om de resulterende biologische conformiteit te beoordelen.

De haalbaarheid van [^{18}F]fluoro-deoxy-glucose (FDG)-PET-gestuurde BCRT voor hoofd- en halskanker wordt bewezen in een planningsstudie. Er wordt aangetoond dat BCRT de planningsbeperkingen voor de kritische organen niet in gevaar brengt. De beste biologische conformiteit wordt bereikt voor het laagste dosisescalatieniveau. In vergelijking met

uniforme dosisescalatie binnen een afgelijnde FDG-PET lesie wordt het doelvolume beter gedekt door BCRT.

Met behulp van Monte Carlo (MC) kunnen radiotherapeutische dosisverdelingen zeer nauwkeurig berekend worden. MC biedt voornamelijk voordelen bij de bestraling van gebieden met sterke weefselinhomogeniteiten met kleine, grillige bestralingsvelden, bijvoorbeeld bij de IMRT-behandeling van hoofd- en halstumoren of longtumoren. In deze thesis wordt de toegevoegde waarde van MC ten opzichte van potloodbundel- en convolutie/superpositie-algoritmes aangetoond bij de IMRT-behandeling van longkankerpatiënten.

Aan de Universiteit Gent werd Monte Carlo Dose Engine (MCDE) ontwikkeld, een uiterst nauwkeurig MC dosisberekeningsprogramma voor de berekening van de patiëntdosis bij IMRT-behandelingen. In deze thesis wordt de omzetting van CT nummers in materiaalgegevens voor MC dosisberekeningen in detail bestudeerd. Zo leiden een stoichiometrische calibratie van de CT scanner en het invoeren van dosimetrisch gelijkwaardige weefselgroepen tot een CT conversieschema met 14 groepen. MCDE wordt verder verbeterd door het invoeren van onzekerheidsgestuurde stopvoorwaarden, die een zo snel mogelijke, nauwkeurige beoordeling van klinische behandelingsplannen toelaten. Tenslotte wordt de mogelijkheid om MCDE te integreren in het IMRT-optimalisatieproces van het UZ Gent aangetoond voor een paranasale sinustumor.

Het optimaliseren van de nieuwe methodes die ontwikkeld werden om biologische beeldvorming in het planningsproces te integreren, vereist een beter inzicht in de radiobiologische eigenschappen van tumoren. Patiënten kunnen gebaat zijn bij een meer nauwkeurige dosisberekening met MC. Terwijl snellere maar minder nauwkeurige MC dosisberekeningsprogramma's commercieel beschikbaar worden, blijven uiterst nauwkeurige programma's zoals MCDE onmisbaar als maatstaf.

Résumé

Le développement de la planification de la radiothérapie dépends fortement des techniques d'imagerie médicale disponibles. L'imagerie médicale anatomique, par example la tomodensitométrie (TDM), permet de visualiser les changements spatiaux des charactéristiques physiques à l'intérieur du corps. Par contre, les caractéristiques biologiques de la tumeur influencent le diagnostic, le choix du traitement et la réponse à la thérapie. Les développements récents dans le domaine de l'imagerie médicale biologique, principalement fondés sur la tomographie par émission de positons (TEP), facilitent la radiothérapie à la mesure de chaque patient.

Des distributions de dose fortement structurées peuvent être administrées avec une radiothérapie conforme avec modulation d'intensité (IMRT). Par conséquent, l'IMRT peut diminuer la dose administrée aux organes à risque et ainsi réduire la toxicité, et augmenter le contrôle local en permettant une escalade de dose. Dans la pratique clinique actuelle, l'optimisation de l'IMRT suppose que les caractéristiques biologiques sont distribuées uniformément dans les volumes tumoraux, et l'optimisation cherche à atteindre une distribution de dose qui est géométriquement conforme. En basant la prescription de dose sur la distribution hétérogène des caractéristiques biologiques obtenue au moyen de l'imagerie médicale biologique, une radiothérapie conforme selon la biologie (BCRT) peut être administrée.

Dans cette thèse de doctorat, la BCRT est implémentée dans le processus de planning IMRT de l'Hôpital Universitaire de Gand. A cet effet, une méthode de segmentation biologique est développée et la fonction objective est étendue. Une relation linéaire délimitée est postulée entre le signal d'image et la dose prescrite. De plus, des méthodes pour évaluer la conformité biologique résultante sont développées.

La faisabilité de la BCRT dirigée par [^{18}F]fluoro-deoxy-glucose (FDG)-PET est démontrée pour des tumeurs de la tête et du cou au moyen d'une étude de planning. Il est prouvé que la BCRT ne menace pas les restrictions de planning établies pour les organes à risque. La meilleure

conformité biologique est atteinte pour l'escalade de dose la plus basse. Comparé à une escalade de dose uniforme dans une lésion FDG-PET cernée, la BCRT couvre mieux le volume tumoral.

A l'aide de Monte Carlo (MC), les distributions de dose administrée par la radiothérapie peuvent être calculées d'une manière très précise. MC a un avantage principalement en cas d'irradiation de régions qui contiennent de grandes hétérogénéités de tissus, avec des champs d'irradiation petits et capricieux, par exemple pour le traitement IMRT de tumeurs de la tête et du cou ou de tumeurs pulmonaires. Dans cette thèse de doctorat, la valeur ajoutée de MC comparé aux algorithmes faisceau-crayon ou convolution/superposition est démontrée pour le traitement IMRT de tumeurs pulmonaires.

Monte Carlo Dose Engine (MCDE), un programme de calcul de dose avec MC, a été développée à l'Université de Gand pour calculer les distributions de dose d'une manière extrêmement précise chez les patients recevant de l'IMRT. Dans cette thèse de doctorat, la conversion de valeurs TDM en charactéristiques matérielles pour des calculs de dose avec MC est étudiée en détail. Une calibration stoechiométrique du TDM et l'introduction de groupes de tissus équivalents selon la dosimétrie mènent à un schéma de conversion CT avec 14 groupes. MCDE est amélioré davantage par l'introduction de conditions d'arrêt dirigées par des incertitudes de dose, qui permettent l'appréciation rapide et précise d'un plan de radiothérapie. Finalement, la possibilité d'implémenter MCDE dans le processus d'optimisation IMRT de l'Hôpital Universitaire de Gand est démontrée pour une tumeur des fosses paranasales.

L'optimisation des méthodes développées pour introduire l'imagerie médicale biologique dans le processus de planification demande une compréhension améliorée des caractéristiques radiobiologiques des tumeurs. Les patients peuvent bénéficier d'un calcul de dose plus précis avec MC. Tandis que des programmes plus rapides (mais moins précis) de calcul de dose avec MC sont introduits commercialement, des programmes très précis comme MCDE restent indispensable en tant que résultat de référence.

Chapter 1

Introduction

1.1 Radiation therapy

Radiation therapy (RT) is the medical use of ionizing radiation as part of cancer treatment to control malignant cells. Radiation in high doses kills cells or keeps them from growing and dividing. Because cancer cells grow and divide more rapidly than most of the surrounding normal cells, RT can successfully treat many kinds of cancer. Normal cells are also affected by radiation but, unlike cancer cells, most of them recover from the effects of radiation. The goal of RT is to kill the cancer cells while minimizing normal tissue complications. To keep the risk of normal tissue complications at an acceptable level, the total radiation dose is limited and the treatment is spread out over time. Additionally, as much normal tissue as possible is shielded while the radiation is aimed at the site of the cancer.

RT can be delivered externally or internally, depending on the location of the radiation source (outside or inside the body). This thesis is devoted to external photon beam RT, in which specialized equipment is used to produce high energy X-rays. The linear accelerator (linac) is the most common type of treatment machine. Primary electrons are accelerated within the wave guide of the linac up to energies of 4-25 MeV, after which they are forced to hit a metal target composed of material with a high atomic number and produce bremsstrahlung photons. A variety of filters and collimating devices is used to shape the final photon beam. Figure 1.1 shows the Elekta SL*i*plus linear accelerator installed at Ghent University Hospital (GUH).

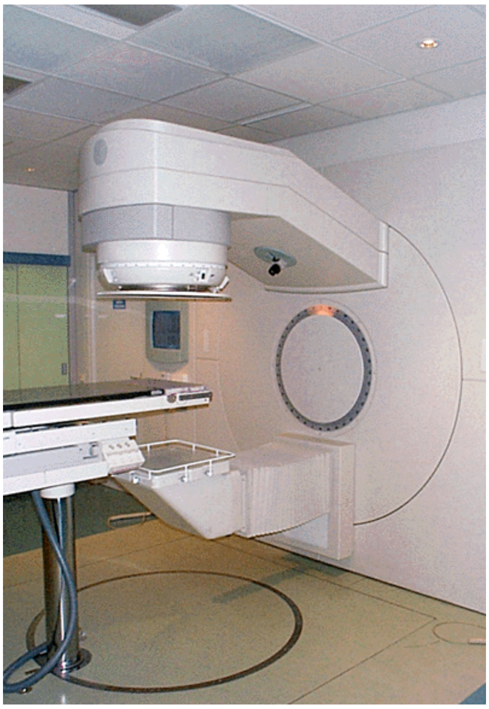

Figure 1.1: The Elekta Sl*i*plus linear accelerator at Ghent University Hospital.

Since the discovery of X-rays by Röntgen in 1896, RT has developed from an experimental application of X-rays to a highly sophisticated treatment of cancer [1]. Cross-fertilization of multiple disciplines proves to be essential as experts from many fields – mainly clinicians, physicists, engineers and biologists – have contributed to these advances. RT has particularly been revolutionized by linac and computer technology, through improvements in imaging, treatment planning and delivery.

Radiological imaging has become a cornerstone for diagnosis, staging, treatment planning and delivery, and follow-up evaluation of modern RT [2]. The ideal imaging technique is non-invasive, repeatable, safe and has a sensitivity (ability to detect disease) and specificity (ability to predict the absence of disease) of 100% [3].

1.2 Anatomical imaging

Anatomical imaging techniques provide regional spatial information. Tumors are distinguished from normal tissues based on morphological characteristics, density, size, vascularity, and fat and water content. With the introduction of computed tomography (CT) in the early 1970s [4] and magnetic resonance imaging (MRI) in the late 1970s [5], cross-sectional imaging of tumors became a reality. This strongly improved the accuracy and resolution of tumor imaging compared to plain radiography [3].

1.2.1 CT

The first CT scanner was built by Godfrey Hounsfield and his colleagues in 1972. In 1979, Hounsfield shared a Nobel Prize with Allan Cormack for their scientific contributions to the development of CT technology. X-rays transmitted transversely through the patient by an X-ray tube are detected by an array of detectors on the opposite side of the tube that rotates around the patient. The detected projection images are reconstructed into digital data and then converted to grayscale levels for display. The produced image depends (amongst others) on the physical characteristics of the imaged tissue, such as its density and atomic number. Although CT is particularly good at depicting bone detail, soft tissue contrast is suboptimal, and intravenously administered contrast agents are frequently required to enhance its tissue-discriminating ability. In general, CT has a very good spatial and temporal resolution [6].

1.2.2 MRI

In MRI, hydrogen nuclei are polarized by a magnetic field and excited from ground states to higher energy states by varying radiofrequency pulses. When these nuclei return to their ground energy state, they emit radiofrequency waves that are detected by sensitive wire coils. Differences in the time it takes for the nuclei to return to this ground state, called T1 (spin-lattice) and T2 (spin-spin) relaxation times, are the source of the distinctions between benign and malignant tissues [3]. Specialized pulse sequences and magnetic field gradients are used to label the signal as a function of space and, after appropriate post-processing, provide an anatomic image of the changes in proton density and relaxation properties. T1-weighted images are used in particular for showing anatomical detail and can be enhanced with gadolinium. T2-weighted images mainly depict the water content and are better at showing pathological conditions. Typically, tumors appear darker than surrounding normal tissue on T1-weighted images and bright white on T2-weighted images. Like CT, the spatial resolution of MRI is excellent, although geometric distortions may arise due to differences in susceptibility for the magnetic field, for example around metal implants. Such 3D deformations may hamper the accurate localisation of anatomical abnormalities. The temporal resolution of MRI is worse compared to CT and both the sensitivity and specificity of MRI in terms of tumoral properties are suboptimal [7].

1.3 Intensity-modulated radiation therapy

The development of highly accurate anatomical imaging techniques like CT and MRI has enabled the detection of complex target geometries, for instance head and neck tumors wrapped around the spinal cord or prostate tumors surrounding the rectum [8]. This has undoubtedly strengthened the call for advanced treatment techniques like intensity-modulated radiation therapy (IMRT). In 1982, Brahme *et al.* demonstrated the potential of intensity-modulated beams to create homogeneous concave dose distributions [9]. Their paper is generally considered to be the cornerstone IMRT paper.

The basic idea of IMRT is to modulate the fluence [10] of the incoming beams of radiation and to use the additional degrees of freedom (compared to conventional beams of uniform intensity) to achieve a better target dose conformity and/or better sparing of critical structures [11]. The trade-off between tumor control and normal tissue side-effects is characteristic of IMRT dose prescription and treatment planning [12]. IMRT could never become a clinical reality without inverse treatment planning [13]. In inverse planning, computer algorithms are used to calculate the beam intensity profiles that will approximate the desired dose distribution as closely as possible within the physical and technical limitations of the treatment machine. The inverse problem of IMRT was first formulated as an optimization problem by Webb [14].

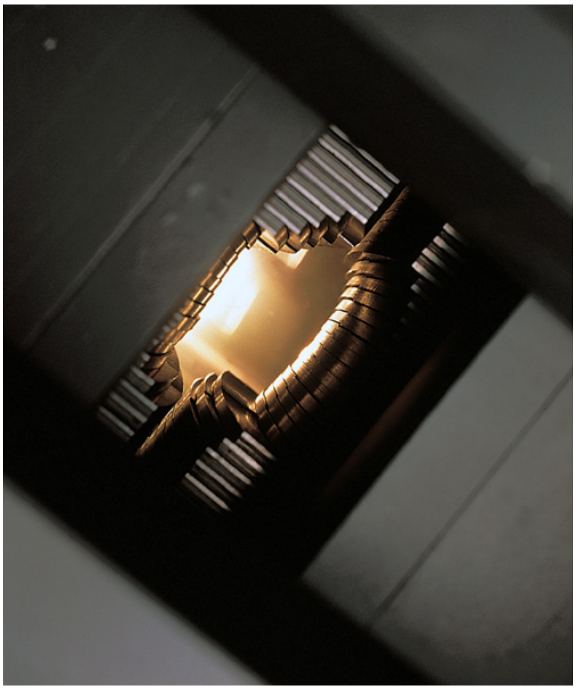

Figure 1.2. Elekta MLC, consisting of 40 leaf pairs, used to create an irregular field shape.

A variety of IMRT delivery techniques exists, including tomotherapy [15] and multi-leaf collimator (MLC)-based IMRT. An MLC is a field shaping device that consists of a large number of highly absorbing tungsten leaves (20-80 on each side of the treatment field), which can be moved indivually under computer control in order to create a large variety of field openings (figure 1.2). MLC-based IMRT can be delivered rotationally as intensity-modulated arc therapy (IMAT) [16] or using multiple static beams, either dynamically [17] or in step-and-shoot mode [18] depending on whether or not the patient is irradiated during the movement of the leaves.

Both the physical aspects and clinical implementation of IMRT have been reviewed extensively [11,19-22]. At GUH, IMRT treatment planning is based on class solutions and involves direct MLC aperture optimization [23]. Planning starts from a template beam set, characterized by each beam's isocentre, gantry, table and collimator angles, linear accelerator, radiation modality and energy. The target volumes and the organs at risk (OARs) are delineated on CT, which also provides the appropriate grid size and resolution, and voxel attenuation properties for accurate dose calculation. For every template beam, a set of initial beam segments is created by the in-house developed anatomy-based segmentation tool (ABST) developed by De Gersem *et al.* [24]. The weight and shape (MLC leaf positions) of each segment is then optimized by the in-house developed segment outline and weight adapting tool (SOWAT). The optimization uses a bio-physical objective function [25]. Several SOWAT cycles are performed until the criteria for plan acceptance are fulfilled. The final beam segments and corresponding weights are combined into a prescription that is suitable for transfer to the linear accelerator.

To allow accurate patient positioning, the patient is sent to the simulator before the start of treatment. With this X-ray device, transmission images of the patient can be generated and compared to digitally reconstructed radiographs (DRRs) created by the treatment planning software. During simulation, water-resistant positioning marks are applied onto the patient's skin. During treatment, these marks are used for accurate patient set-up at the linear accelerator.

1.4 Biological imaging

Despite their many benefits (e.g. high spatial resolution), anatomical imaging techniques are inherently deficient in visualizing tumor biology as they can only reveal spatial changes in physical properties [26]. Therefore, many research efforts have recently been invested in cellular and molecular biology, computer technology and (bio)chemistry [2]. This has resulted in advanced biological imaging techniques, mainly based on positron emission tomography (PET), single photon emission computed tomography (SPECT), functional MRI (fMRI) and magnetic resonance spectroscopic imaging (MRSI), which are capable of revealing spatial biology distributions [27,28]. These new imaging techniques have also been described as 'molecular' imaging (for the *in vivo* characterization and measurement of biological processes at the cellular and molecular level [29]) or 'functional' imaging (for example, for the measurement of cerebral blood flow change with fMRI [30]). The general term 'biological' imaging has been adopted for all techniques that provide complementary biological information to the standard anatomical imaging techniques [31].

1.4.1 PET and SPECT

PET imaging was developed by Ter-Pogossian *et al.* in the mid-1970s [32]. In PET imaging, a positron-emitting radionuclide is tagged to a molecule that is taken up selectively by certain types of tissue. Such radiolabeled molecules are called tracers. Each emitted positron will annihilate with an electron from the surroundings, resulting in the production of two 511 keV annihilation photons emitted in almost opposite directions. These coincident photons can be detected externally. After computerized reconstruction, tomographic images are obtained. The principle of PET imaging is illustrated in figure 1.3. The most frequently used radionuclides are fluorine-18 (^{18}F), carbon-11 (^{11}C) and oxygen-15 (^{15}O). In SPECT imaging, tomographic images are reconstructed based on the external detection of individual photons, emitted by tracers labelled with gamma-emitting radionuclides such as technetium-99m (^{99m}Tc), indium-11 (^{11}In) or iodine-123 (^{123}I).

For some of the isotopes suitable for PET imaging, which have short half-lives (e.g. 20.4 min for ^{11}C, 2.0 min for ^{15}O), an on-site cyclotron is required for the production of these isotopes as well as special synthesis facilities. Compared to PET, the synthesis of SPECT tracers is generally less expensive. Because collimation is required for the detection of single SPECT photons, the spatial resolution of PET is better than that of SPECT, but clearly worse than CT or MRI. The temporal resolution of both PET and SPECT is poor. Both imaging techniques offer interesting opportunities for tumor detection [2], although their sensitivity and specificity are strongly tracer- and disease site-dependent, amongst other factors [33]. As they intend to provide complementary information (biological versus anatomical), PET or SPECT images differ fundamentally from CT or MRI images with regard to their use.

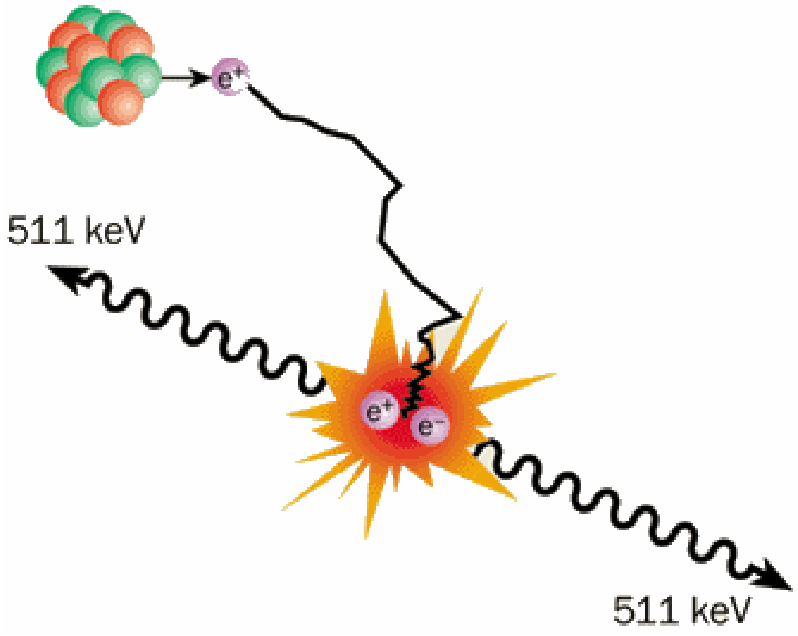

Figure 1.3. In PET imaging, a positron emitted by a radioisotope annihilates with an electron, resulting in the production of two annihilation photons, which can be detected externally (image taken from physicsworld.com).

The most widely used PET tracer is 2-[^{18}F]fluoro-2-deoxy-D-glucose (FDG) [34]. FDG is transported in a cell like glucose itself and is then transformed into FDG-6-phosphate. The presence of ^{18}F in position 2 causes the FDG-6-phosphate to remain unmetabolized [35]. Therefore, it will accumulate within the cell at a speed proportional to glucose need. FDG-PET imaging will thus highlight regions of increased glucose metabolism. Tumor cells show an increased rate of glucose consumption, due to an increase of glycolytic enzymes and the high number of glucose transporters expressed on malignant cells [27]. However, in addition to changes in tumor metabolism, FDG uptake is influenced by other factors such as tumor burden, blood flow, hypoxia and inflammation. Indeed, hypoxic tumors are known to have increased glucose metabolism, as have macrophages that invade neoplastic tissues [36]. Additionally, some tumor types are not highly metabolic, e.g. prostate tumors, or may be masked by high uptake of FDG, e.g. in the brain. To overcome these limitations of FDG, it is important to identify the entire tumor profile using additional anatomical and biological imaging information.

Because of their complementarity, multi-modality imaging techniques have been developed by combining anatomical and biological imaging modalities. Integrated SPECT/CT and PET/CT scanners were introduced clinically in 1998 and 2001, respectively [37]. Using such combined equipment, many of the limitations associated with separate CT and PET or SPECT imaging are overcome, like problems with reproducible patient positioning and immobilisation, and co-registration of the two image data sets. Multi-modality imaging provides an anatomical reference frame for the biologically detected lesions, which strongly improves the specificity compared to mono-modality biological imaging [38]. Additionally, CT data may be used for the PET or SPECT attenuation correction to increase both the imaging accuracy and speed, enabling a more efficient use of radiopharmaceuticals as well as an increased patient throughput. Figure 1.4 shows a clinical FDG-PET/CT imaging example. A Philips Gemini 16-slice PET/CT scanner came into operation at GUH in September 2004.

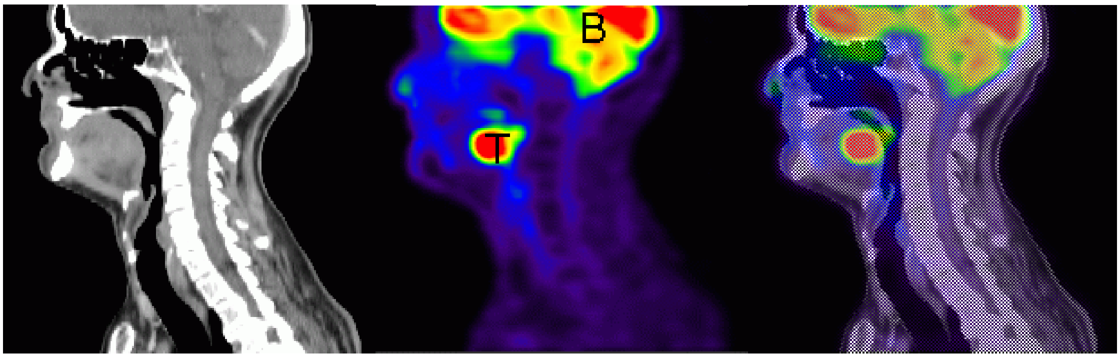

Figure 1.4. Clinical FDG-PET/CT investigation of the head and neck region: CT (left), PET (middle) and fused (right) sagittal images. B: normal FDG uptake in the brain; T: FDG uptake in the tumor in the base of tongue.

1.4.2 fMRI and MRSI

Apart from their ability to provide anatomical information, MRI techniques are capable of visualizing certain biological tumor properties. For instance, fMRI can be used to map changes in brain activity, based on the increase in blood flow to the local vasculature that accompanies neural activity in the brain [39]. One of the recent advances in fMRI is dynamic contrast-enhanced MRI (DCE-MRI), which was developed in the mid-1990s to yield information on the microenvironment of tumors and normal tissues, e.g. vascularity, blood flow and permeability [40].

MRSI allows the detection of biochemically important compounds other than water or fat molecules. The peaks in the individual MR spectra reflect the relative concentration of chemicals within each spatial location. Differences in the levels of cellular metabolites between tumors and normal tissues are thus exploited. While both the temporal and spatial resolution of MRSI are worse than that of conventional MRI, both imaging techniques show a comparable sensitivity. The specificity of MRSI is better than that of conventional MRI [6].

1.5 Biologically conformal radiation therapy

The use of biological imaging for RT can serve three different goals: 1) improvement of the diagnostic and staging accuracy, 2) guidance of target volume definition and dose prescription, and 3) evaluation of therapeutic response [26]. Within the scope of this thesis, only the potential application of biological imaging for RT treatment planning by improved target volume definition and dose prescription is considered.

1.5.1 Tumor biology and radioresistance

Using advanced biological imaging techniques, information can be obtained about tumor metabolism, proliferation, oxygenation and vascularization, and specific disease markers [31]. At first order, biological imaging may aid in visualizing tumor burden and clonogen density in order to identify the 'real' target volume consisting of malignant cells. To achieve tumor control, these cells need to be irradiated to a therapeutic dose. Moreover, hypoxic regions within tumors are associated with increased radioresistance [41]. As the development of blood supply is crucial to tumor growth, tumor vascularization or angiogenesis has been linked to radioresistance as well [42]. There has also been debate to the extent of the contribution of apoptosis to the control of human tumors by RT [43]. Additionally, rapid cell proliferation has been identified as a resistance mechanism in fractionated RT [44].

Table 1.1. Short-list of radiotracers for tumor biology characterization.

Radiotracer	Full name	Characterization
^{18}F-FDG	^{18}F-fluorodeoxyglucose	Glucose metabolism
^{18}F-FLT	^{18}F-fluorothymidine	DNA synthesis (proliferation)
^{11}C-MET	^{11}C-methionine	Protein synthesis
^{60}Cu-ATSM	Cu(II)-diacetyl-bis-*N*-(4)-methylthiosemicarbazone	Hypoxia
^{18}F-FMISO	^{18}F-fluoromisonidazole	Hypoxia
Radiolabeled Annexin V		Apoptosis
Radiolabeled $\alpha_v\beta_3$ integrin antagonists		Angiogenesis

The molecular pathways associated with the above-mentioned tumoral properties are under intense investigation. One of the main goals is to develop adequate biological imaging techniques and to continue the search for optimal tracers in order to visualize the main radiobiological properties of tumors. An overview of the most commonly studied radiotracers used for tumor characterization, including their present status (disappointing, potential or promising), is provided by Apisarnthanarax and Chao [2]. Table 1.1 presents a short-list.

1.5.2 Biological imaging for target volume definition in RT

RT aims to deliver the required therapeutic dose of ionizing radiation to tumor tissue, while minimizing the irradiation of normal tissue. Obviously, precise target volume definition is essential to this process. The nomenclature was standardized in ICRU report 62 [45], by introducing the concepts of gross tumor volume (GTV) for the known tumor, clinical target volume (CTV) for the GTV plus suspected microscopic spread, and planning target volume (PTV) for the CTV plus the marginal volumes necessary to account for setup variations and organ and patient motion.

While the GTV describes the part of the cancer that can be directly imaged or palpated, the delineation of the CTV depends heavily on *a priori* knowledge of the behaviour of a given tumor. The PTV is a construct that helps to ensure that the desired dose distribution can be anatomically achieved within the CTV [46]. Because of the high conformity, set-up errors and tumor motion during treatment may have more severe dosimetric consequences for IMRT compared to conventional RT. Therefore, IMRT makes high demands on accurate PTV definition [20].

Biological imaging may add essential information to CT and MRI with significant consequences on GTV and CTV delineation, by providing information on the tumor's microenvironment and metastasis to regional lymph nodes as well as to distant sites [2]. In this way, marginal misses and the irradiation of normal tissues can be reduced. Recently, several reviews have been dedicated to the impact of biological imaging on target volume definition for different tracers and modalities, and different disease sites. The use of FDG-PET imaging was reviewed for non-small cell lung cancer [47], for head and neck cancer [48], and for multiple disease sites including head and neck, brain, lung, esophagus, cervix and rectum tumors, and lymphomas [49,50]. Other PET tracers are included in reviews on head and neck cancer [51] and multiple disease sites [52,53].

Newbold *et al.* have reviewed the application of PET, SPECT and NMR to RT treatment planning of head and neck cancer [54].

The golden standard for target volume definition is pathologic examination. However, to date only Daisne *et al.* have compared CT, MRI and PET-based delineations of the primary tumor with pathologic specimens, for 9 pharyngolaryngeal squamous cell carcinoma patients [55]. They found the FDG-PET based GTV to be smaller than both the CT and MRI-based GTVs, and to correspond better to the macroscopic tumor specimen. Similar validation studies should be carried out to evaluate the use of other tracers, other biological imaging modalities and other disease sites for target volume definition in RT.

1.5.3 Biological imaging for dose prescription in RT: dose painting

Treatment plan optimization for external beam radiation is traditionally based on the assumption of a uniform biology distribution within the target volume and correspondingly aims at achieving a geometrically conformal dose distribution. In reality, the spatial distribution of biological properties within most tumors is far from homogeneous [56]. This distribution is visualized by biological imaging techniques, providing 3D maps of radiobiologically relevant tumor properties. It appears obvious not to limit the use of biological images to improving the accuracy of target volume definition in RT, but to use them to identify the most radioresistant subregions within tumors and target these regions with a higher radiation dose.

In 2000, Ling *et al.* introduced the term 'dose painting' (in 2D, 'dose sculpting' in 3D) for prescribing, planning and delivering an increased radiation dose to one or more radioresistant tumor subvolumes. Figure 1.5 schematically illustrates their proposed concept of treating a biological target volume (BTV) derived from biological imaging information. The BTV can be delineated either by visual interpretation of the biological images or by automatic segmentation techniques. The threshold for automatic segmentation can be a certain intensity level of the biological image signal, a percentage of the maximal intensity or a percentage of the source-to-background ratio. In 2001, Chao *et al.* demonstrated the feasibility of ^{60}Cu-ATSM-PET guided dose painting for a head and neck cancer patient [57]. The dose to the hypoxic tumor subvolume could be escalated to 80 Gy in 35 fractions without compromising normal tissue sparing of the parotid glands and the spinal cord.

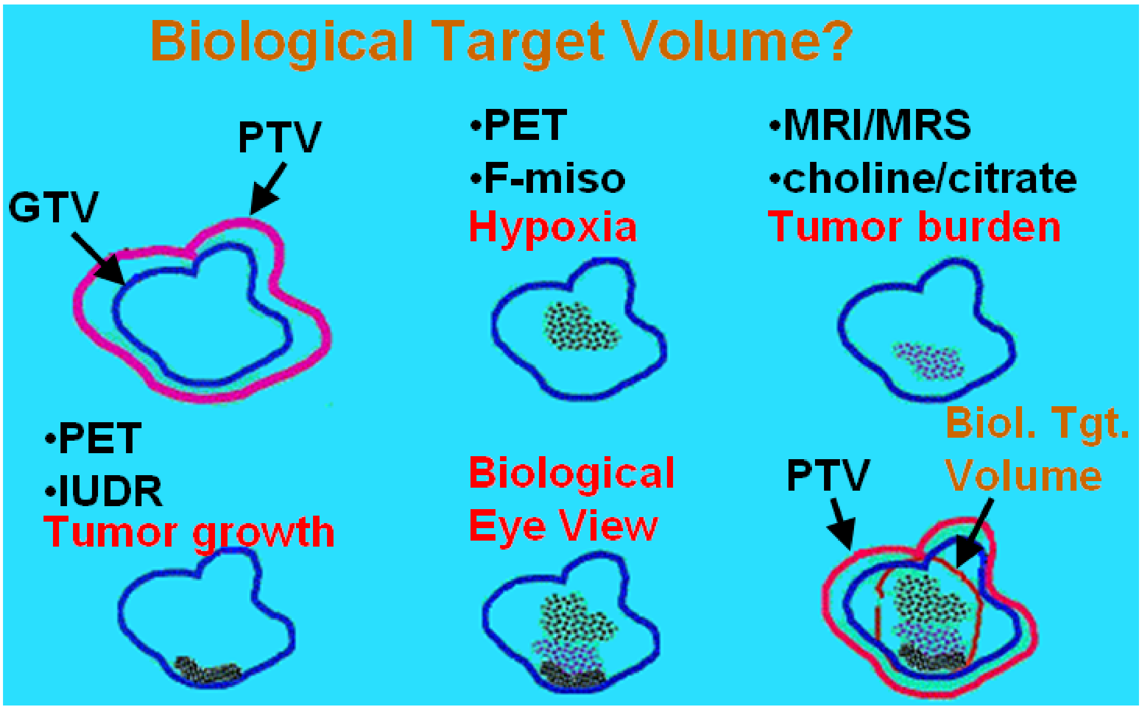

Figure 1.5. Introduction of the biological target volume (BTV) concept by Ling *et al.* [31]. The BTV is defined by combining biological imaging data, which for example identify regions of low oxygenation (from ^{18}F-misonizadole PET imaging), high tumor burden (from choline/citrate ratio NMR imaging) and high proliferation (from ^{124}I-iododeoxyuridine PET imaging). The BTV may be used to improve dose targeting to certain regions of the anatomical PTV.

At GUH, FDG-PET guided dose painting was used to treat 41 head and neck cancer patients enrolled in a phase I clinical trial between 2003 and 2005. The total treatment consisted of 32 fractions and was divided in two phases. During the escalation phase (fractions 1-10), a boost dose was planned to PTV_{PET}, which was assumed to be the most radioresistant subvolume within the PTV. Two escalation dose levels were applied: 2.5 Gy per fraction (level I; 23 patients) and 3 Gy per fraction (level II; 18 patients). The BTV was automatically segmented based on the source-to-background ratio following the method of Daisne *et al.* [58]. During fractions 11-32, standard IMRT was applied. Madani *et al.* have reported on the planning results and toxicity [59]. At dose level I, two cases of dose-limiting toxicity occurred (grade 4 dermitis and grade 4 dysphagia). A chemotherapy-related death at dose level II halted the study. Complete response was observed in 86% and 81% of the evaluated patients at dose levels I and II, respectively. Of 9 loco-regional recurrences, the site of relapse was located within the BTV for 4 patients. The maximum tolerated dose was not reached at the investigated dose levels.

The problem with discrete volumes like the BTV is that they are binary: voxels are either inside or outside the volume. In real patients, however, biological tumor characteristics present themselves at a variety of levels. It therefore seems natural to use the entire spatially heterogeneous distribution of biological information for RT treatment planning. By directly prescribing dose as a function of biological image intensities within each patient voxel, truly biologically conformal radiation therapy (BCRT) can be achieved. Bentzen has proposed to name this principle 'dose painting-by-numbers', after the 'painting-by-numbers' activities for children (figure 1.6) [60].

Figure 1.6. 'Painting-by-numbers' illustration from the collection of toy company Ravensburger®.

1.6 Dose calculation algorithms

Accurate calculation of the patient dose distribution is essential to the IMRT (and BCRT, which is hypothetically an improved version of IMRT taking into account the heterogeneity of biological properties inside the tumor) treatment planning and delivery process. The calculated dose is used to compute the objective function value steering the optimization process, and to evaluate the clinical acceptability of the final treatment plan. However, dose calculation speed is in competition with accuracy. For complex optimization problems with complex objective functions, thousands of optimization iterations are necessary. Hence, approximations are often incorporated in the dose calculation algorithm used by the optimization engine, to allow the optimization to be completed within an acceptable time frame. For the final dose computation used for treatment plan evaluation, speed issues are obviously less important, and high accuracy is essential.

For external photon beam RT, the general problem of predicting the absorbed dose delivered to an individual patient consists of two separate components. Firstly, the radiation fluence incident upon the patient geometry needs to be determined. Secondly, the absorbed dose (absorbed energy per unit of mass) needs to be determined from that incident fluence as a function of position within the patient. IMRT dose calculation algorithms have been separated into four categories by the IMRT Collaborative Working Group [20]: correction-based (1) broad beam and (2) pencil beam (PB) algorithms, and model-based (3) kernel-based and (4) Monte Carlo (MC) algorithms. The correction-based algorithms first compute dose to a homogeneous water phantom, before applying various correction strategies to account for source-to-skin distance and heterogeneities within the patient. Model-based algorithms, on the other hand, compute dose directly within the patient geometry [61].

1.6.1 Broad beam algorithms

Designed for radiation fields with a simple, smoothly varying fluence profile (open, blocked or wedged beams), broad beam algorithms are generally not recommended for use in IMRT [62]. Broad beam algorithms parametrize dose distributions in a homogeneous water phantom as a function of field size, depth, off-axis distance and source-to-surface distance based on measurements. For patient dose calculations, the specific treatment conditions are first applied in water, and then corrected for the patient anatomy. If used, heterogeneity corrections are based upon density-scaling equivalent path-length (EPL) methods.

1.6.2 Pencil beam algorithms

To reconstitute dose distributions in a homogeneous phantom, PB algorithms use energy deposition kernels in a water phantom derived from MC calculations [63] or measurements [64,65]. Figure 1.7 shows a pencil kernel, which describes the energy deposition from a monodirectional beam in a semi-infinite medium. Pencil kernels are obtained by pre-convolving point kernels over the depth dimension, which offers significant speed advantages for PB compared to kernel-based algorithms. While PB algorithms can account for beam fluence modulations and irregular field shapes, they use radiological path length scaling methods to account for heterogeneities and patient contours [66]. Because of their high calculation speed, PB algorithms are the most commonly used dose calculation algorithms for IMRT [62].

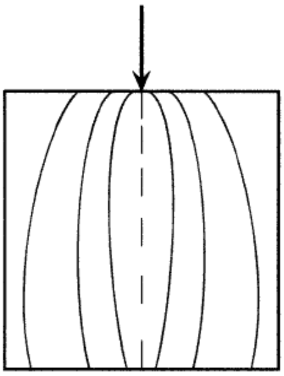

Figure 1.7. Irradiation geometry (arrow) and isodose curves (full lines) for a pencil kernel [61].

1.6.3 Kernel-based algorithms

Kernel-based algorithms, often called convolution/superposition (CS) algorithms, separate the effects of primary photons incident upon the patient from the effects of secondary radiations generated by interactions of the primary photons within the patient. Firstly, the total energy released per unit mass (TERMA) from primary photon interactions within the patient is computed. To yield the total dose distribution, pre-computed secondary energy spread kernels are then convolved with the TERMA [67-69]. Such a point kernel is illustrated in figure 1.8. While the TERMA calculations account for tissue heterogeneities, radiological path length methods are typically used to scale the secondary energy spread kernels. Compared to PB, CS algorithms are much more accurate in heterogeneous geometries but they are relatively slow [70,71]. Therefore, they are usually only applied to compute the final dose distribution at the end of optimization.

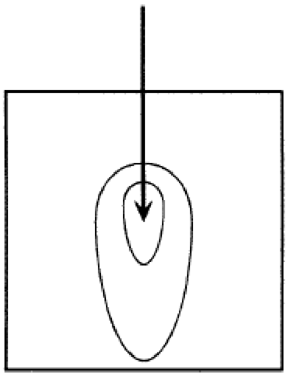

Figure 1.8. Irradiation geometry (arrow) and isodose curves (full lines) for a point kernel [61].

1.6.4 Monte Carlo algorithms

MC dose calculations simulate individual photon and electron tracks through the accelerator treatment head, the MLC and the patient. Along its track, a particle may interact with the medium through which it passes. Using a random number generator and cross section data for the different types of interactions, the program samples the distance to the next interaction for a particle at a given position and with a given speed in a given direction. After propagating the particle to the interaction location, the type of interaction that will take place is sampled. For each simulated interaction, the difference in energy between the incoming and outgoing particle(s) is calculated. By adding the contributions from all interactions taking place within a patient voxel and taking into account the voxel's mass, the total dose can be calculated.

As MC algorithms simulate stochastic processes, statistical uncertainties are inherently associated with the results. This statistical noise decreases with the square root of the calculation time, but is independent of the number of simulated beams, which is a distinct advantage for IMRT dose calculations [62]. Full Monte Carlo algorithms are considered the most accurate dose calculation algorithms as they directly account for tissue heterogeneities. Additionally, scatter and leakage effects are directly taken into account by transportation of individual particles through the MLC.

1.6.5 Dose calculation algorithms at GUH

At GUH, a broad beam algorithm is routinely applied during IMRT optimization [25]. Because the effect of a single MLC leaf movement on the value of the objective function needs to be evaluated thousands of times during the entire optimization process, a very fast algorithm is required. For lung cancer patients, a CS algorithm (Pinnacle, Philips Medical Systems, Best, The Netherlands) is used in between optimization cycles and for the final dose calculation because of the heterogeneous geometry (tumor-lung). The final dose calculation for all IMAT treatment plans is also performed using Pinnacle's CS algorithm. For research purposes, the PB and CS algorithms of Helax-TMS (Nucletron, Veenendaal, The Netherlands) are available at GUH too. At Ghent University an accurate Monte Carlo dose engine, MCDE, was developed by Reynaert *et al.* for IMRT patient dose calculations [72]. However, the present calculation times are too high for clinical use. Details on MCDE are provided in the next section.

1.7 Monte Carlo Dose Engine

1.7.1 The EGSnrc code

Four general purpose MC codes are commonly used for external photon beam RT dose calculations: EGS [73,74], MCNP [75,76], PENELOPE [77] and GEANT [78]. EGS and PENELOPE simulate the coupled transport of photons and electrons, while MCNP and GEANT can also take into account other particles such as protons or neutrons. Generally, photon transport modeling is quite similar in all four systems, although different cross section data are used. Important differences, however, are encountered in electron transport modeling, which strongly influences the speed and accuracy of the codes [79].

Much attention has been paid to the electron transport in EGS (Electron-Gamma Shower). In 2000, the EGSnrc code was released [74,80]. Compared to its precursor EGS4 [73], an improved multiple scattering theory was implemented, and the parameter reduced electron stepping algorithm (PRESTA) was replaced by PRESTA-II [81]. These adaptations improved the accuracy of angular deflection calculations for electrons, eliminated previous restrictions on the minimal and maximal electron path length, and provided an exact boundary-crossing algorithm by using single elastic collisions of electrons. The EGSnrc code has been extensively benchmarked and is widely used. Individual user codes can be created in MORTRAN, a preprocessor of Fortran77, and connected to the EGSnrc core in a pre-compilation step.

1.7.2 Linear accelerator modeling using BEAMnrc

Accurate patient dose calculations can only be performed when the treatment beams are accurately modeled. An excellent review on this subject was written by Verhaegen and Seuntjens [82]. BEAMnrc is an EGSnrc user code dedicated to the 3D simulation of RT treatment units [83]. Each linear accelerator used for external photon beam RT essentially has a modular construction. The technical specifications of the components differ from one manufacturer to another; the order of the components may differ as well. Figure 1.9 shows a schematic drawing of the treatment head of the Elekta SL*i*plus linear accelerator installed at GUH.

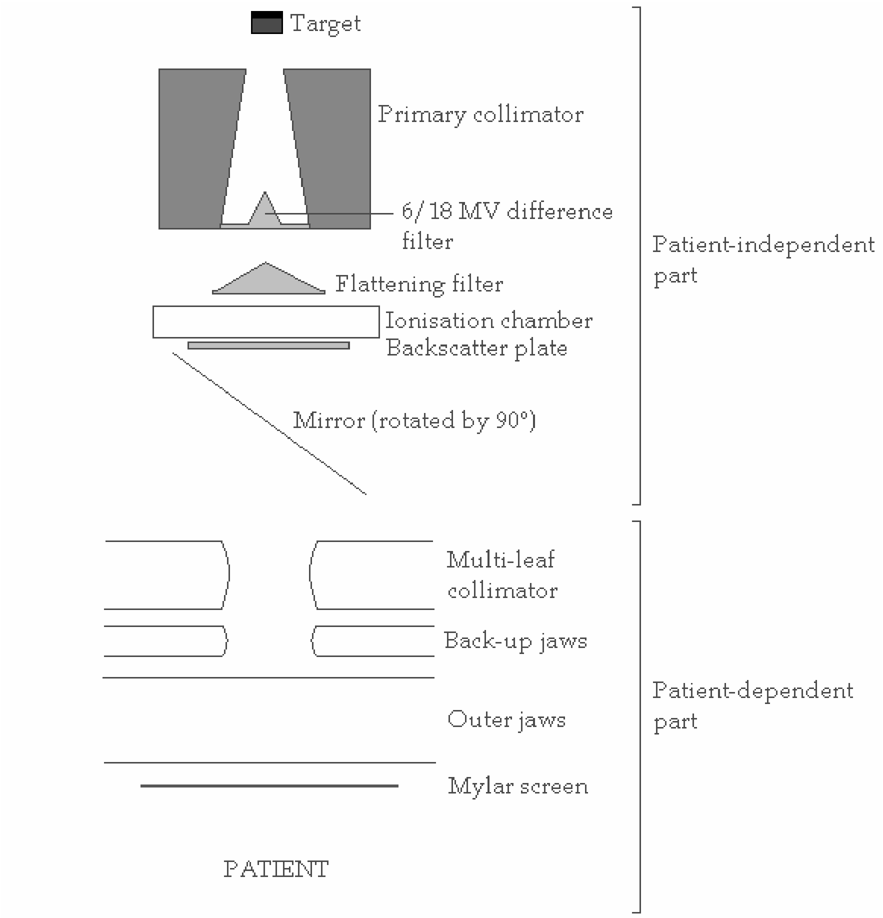

Figure 1.9. Modular construction of the treatment head of the Elekta SL*i*plus linear accelerator at GUH.

All component types are pre-programmed in BEAMnrc as component modules (CMs). Users can build their own accelerator model by selecting the required CMs. The dimensions, materials and transport parameters of each CM have to be defined in an input file but no programming efforts are required. BEAMnrc can be used to determine so-called phase-space files in a scoring plane at the end of a CM, e.g. at the exit of the linear accelerator treatment head. A phase-space file contains all necessary parameters (location, direction, energy, charge etc.) of particles that pass through the plane. Phase-space files can be used as input for further BEAMnrc simulations or for dose calculations within a patient or a phantom. BEAMnrc was used to model the treatment head of the Elekta SL*i*plus linear accelerator at GUH in detail [84,85].

1.7.3 Dose calculation using DOSXYZnrc

DOSXYZnrc is an EGSnrc user code dedicated to the calculation of dose distributions within a phantom consisting of rectangular voxels [86]. Different source types can be selected, including individual beams and full phase-space files generated by a BEAMnrc simulation. A specific material composition and mass density value can be assigned to each voxel, in which the energy deposition is scored. Voxel dimensions are independently variable in all 3 directions. DOSXYZnrc also allows the calculation of dose distributions within a phantom that is derived from a CT dataset. For this purpose, the stand-alone program CTCREATE was developed. Using CTCREATE, a CT data set can be converted into the appropriate voxel geometry for DOSXYZnrc. Material and mass density data are derived from the Hounsfield number within each voxel. Several CT data set formats are supported, including DICOM.

1.7.4 MCDE and the PHANTOM component module

In principle, the BEAMnrc/DOSXYZnrc system can be used for IMRT patient dose calculations. However, separate BEAMnrc and DOSXYZnrc calculations would be required for each IMRT treatment beam. In the end, the resulting dose maps would need to be summed taking into account the individual beam weights. This procedure is rather cumbersome, inefficient and demands a lot of user interactions. To solve these issues, MCDE was developed by Reynaert *et al.* [72]. MCDE was essentially created by reprogramming DOSXYZnrc as a CM within BEAMnrc: the PHANTOM CM. The excellent photon and electron transport algorithms and other characteristics of the EGSnrc code are thus preserved. Moreover, MCDE uses no additional variance reduction techniques or approximations that reduce the accuracy.

The components within the upper part of the treatment head (from the target up to the mirror) are independent of an individual patient's beam setup. Therefore, a BEAMnrc simulation is first performed to score a phase-space file just below the mirror. Next, MCDE is used to transport particles extracted from this phase-space file through the MLC, the jaws, the exit window and the PHANTOM. MCDE thus handles the beam modifiers and the patient in one process. All beam and patient data are included in a single BEAMnrc input file. Although still possible, it is no longer necessary to save a phase-space file for each individual beam after the exit window of the linear accelerator.

A DICOM interface allows the user to import all necessary beam and patient data from another treatment planning system (TPS): beam angles, shapes and weights; isocenter data, CT images and anatomical contours. A separate scoring grid is superimposed on the geometry grid to limit the number of scoring voxels. To minimize volume averaging effects, spherical scoring voxels were implemented. The desired voxel radius and inter-voxel distance can be defined by the user. While MCDE is able to simulate all beams in a single process, requiring only one input file, the output consists of separate 3D dose distribution files for each beam to facilitate beam weight optimization without requiring additional MC simulations.

At Ghent University, MC calculations are performed on a Linux PC cluster consisting of 1 server and 34 nodes (2.4 GHz Intel Pentium IV dual processors with 2 Gb RAM). In house-created scripts split each MCDE job into a number of sub-jobs. Each sub-job runs on a separate cluster node and uses a different part of the phase space file. As MCDE applies no variance reduction techniques, calculation times are high. A typical patient calculation, aiming at a relative uncertainty on the estimated dose below 2% within the PTV, takes 6-8 hours. MCDE is therefore not suitable for routine clinical use, e.g. as the dose calculation algorithm used at each iteration of the IMRT optimization engine. On the other hand, a very high level of accuracy can be achieved when MCDE is used to compute IMRT patient dose distributions. This makes it an excellent tool for benchmarking the performance of other dose calculation algorithms within patients, where measurements are difficult or even impossible.

1.8 Dose calculation accuracy

1.8.1 Requirements on dose calculation accuracy in RT

Because of variations in tumor and normal tissue response, it is difficult to quantify the impact of geometric and dosimetric uncertainties in a clinical setting. Figure 1.10 illustrates the sigmoidal dependence of the tumor control probability (TCP) and the normal tissue complication probability (NTCP) on the radiation dose. In the steep part of the curves, a dose error of 5% may lead to a change in TCP of 10 to 20% and to an even larger change (20 to 30%) in NTCP [87,88]. Clinical effects have been noticed for dose errors of 7% [89]. Accurate dose calculation is thus required.

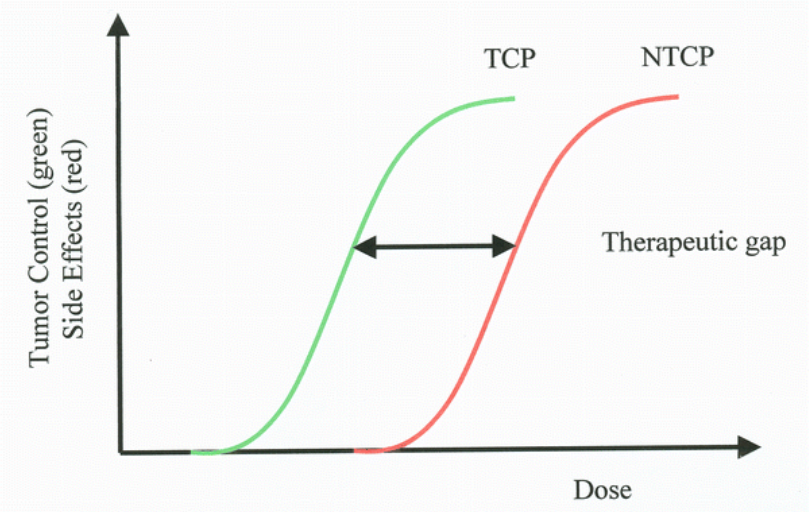

Figure 1.10. Dose dependence of tumor control probability (TCP) and normal tissue complication probability (NTCP).

A large number of steps are involved between the dose prescription and the actual dose delivery in RT. During this complex process, each step introduces a certain amount of uncertainty, accumulating in an overall uncertainty on the absolute dose delivered to the patient. An overview of estimated uncertainties accompanying different steps within the dose determination process can be found in table 1.2. Excluding the dose calculation step, an overall uncertainty (one standard deviation) of 4.3% is obtained. This overall uncertainty can possibly be reduced down to 2.5% in the near future, due to improvements in imaging and radiation technology. When 2% to 3% errors in dose computation are included in the present estimate, the total uncertainty becomes about 5%.

Table 1.2. Present and future estimates of uncertainty (one standard deviation) on the absolute patient dose for a complete RT treatment procedure using MV photons [87].

Source of uncertainty	Uncertainty at present (%)	Uncertainty in the future (%)
Dose at the calibration point in water	2.5	1.0
Additional uncertainty for other points	0.6	0.3
Beam monitor stability	1.0	0.5
Beam flatness	1.5	0.5
Patient data	1.5	1.0
Patient set-up and organ motion	2.5	2.0
Overall (excl. dose calculation)	4.3	2.5
Dose calculation algorithm (multiple levels)	1.0 / 2.0 / 3.0 / 5.0	1.0 / 2.0 / 3.0
TOTAL	4.4 / 4.7 / 5.2 / 6.6	2.7 / 3.2 / 3.9

Increasing dose calculation accuracy will reduce the overall uncertainty in the delivered dose. But due to the significant contributions of several other factors, the use of extremely accurate dose calculation methods will not automatically lead to extremely low uncertainties in clinical dose delivery. Considering future technological improvements, however, the importance of dose calculation accuracy will increase. At present, it is generally believed that dose calculation accuracy in RT should be within 2 - 3% (one standard deviation) [88].

1.8.2 Monte Carlo dose calculation accuracy

For MC calculations, the degree of accuracy that can be achieved is determined mainly by the following factors [90]: 1) how accurately the treatment beams are modeled with respect to energy and directional distribution; 2) the accuracy of the cross section data used to simulate the various interactions between ionizing radiation and matter; 3) how accurately the patient geometry and tissue properties relevant to the radiation interactions are modeled; and 4) the statistical uncertainties inherently associated with MC simulations.

The modeling of external RT photon beams has been reviewed in detail by Verhaegen and Seuntjens [82]. Rogers *et al.* have described the accuracy obtainable with EGS [91]. Additionally, Rogers and Bielajew have discussed the accuracy of the available cross section data [92]. Within the scope of this thesis, the following paragraphs address some patient-related issues in MC (heterogeneities, CT conversion and conversion to dose to water) as well as the stochastic nature of MC in more detail.

1.8.2.1 *Electron disequilibrium*

Loss of electron equilibrium occurs when there is an imbalance between the number of electrons entering and leaving a small region of dosimetric interest, i.e. between the number of absorbed and produced electrons. As the attenuation of the photon beam cannot be neglected with respect to the electron range, only transient electron equilibrium can be achieved for external MV photon beam RT [87]. Dose calculation is greatly simplified in the presence of (transient) electron equilibrium, since no detailed tracking of electron trajectories is required. Unfortunately, electron equilibrium is lost within patients at the beam edges and in the presence of tissue inhomogeneities.

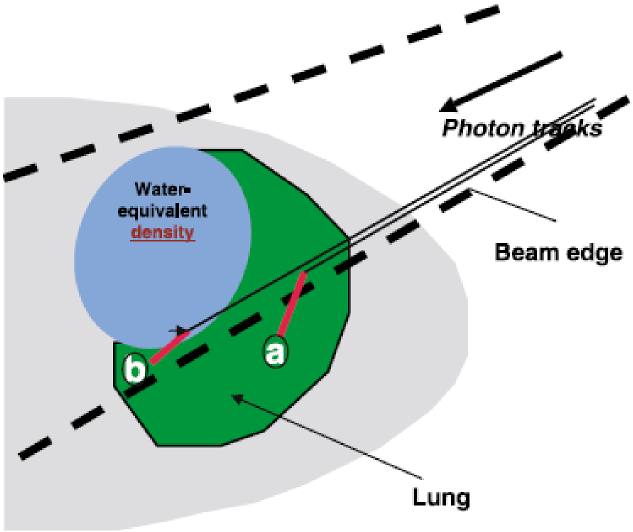

Figure 1.11. Illustration of the occurrence of electron disequilibrium at the beam edge (a) and at the interface between lower and higher density tissues (b) for a schematic lung cancer case [93].

Loss of electron equilibrium causes a dosimetric blurring of the beam edges as scattered electrons originating inside the beam deposit energy outside the beam's aperture. The effect increases as the electron range increases, i.e. as the energy of the photon beam increases or as the mass density of the tissue decreases. For extremely small or highly irregular treatment fields, commonly encountered in IMRT, even transient electron equilibrium may be completely inexistent. Moreover, at the interface between tissues with different mass density values, the number of electrons that leave the higher density tissue and deposit energy within the lower density tissue is higher than the number of electrons doing the opposite. This causes a regional overdosage within the lower density tissue close to the interface. Figure 1.11 illustrates both situations of electron disequilibrium for a schematic lung cancer case.

To perform accurate dose calculations within regions of electron disequilibrium, precise modeling of secondary electron transport is required. With regard to IMRT patient dose calculations, lung cancer and head and neck cancer cases are particularly challenging, due to the presence of tumor tissue close to or within low density tissue like the lungs or air cavities like the sinuses. Even sophisticated analytical dose calculation algorithms like CS may lead to deviations larger than 10% from measurements at lung-tissue or bone-tissue interfaces and in rebuild-up regions behind air cavities [94-97]. As secondary electron transport is modeled most accurately by MC codes like EGSnrc, they can be used for accurate patient dose calculations provided that patient geometry modeling and tissue characterization are performed adequately.

1.8.2.2 *CT conversion*

The patient geometry is usually derived from CT data. In this way, a rectangular voxel geometry with adequate spatial resolution is readily obtained. A CT number *H*, expressed in Hounsfield units (HU), is associated with each image voxel. The CT number is related to the linear attenuation coefficient μ of the material within the voxel as follows:

$$H = 1000\left(\frac{\mu}{\mu_{water}} - 1\right).$$

To model the attenuation of a primary photon beam in a medium other than water, conventional dose calculation algorithms apply tissue heterogeneity corrections. Because the correlation between the correction factors and tissue electron density is well known, CT scanners are usually calibrated in terms of electron density [98]. The effect of electron density on photon dose calculations has recently been assessed by Seco and Evans [99]. For RT beams with photon energies between 0.1 and 10 MeV, Compton scattering is the dominant interaction process within human tissues. The probability for Compton interaction is directly proportional to the electron density of the tissue. At CT imaging energies, however, the importance of the photo-electric and Rayleigh scattering strongly increases, especially within tissues with a high effective atomic number like bone. Therefore, it is advisable to use the highest available energy on the CT scanner for RT treatment planning. Although an increased tube potential slightly worsens the contrast of the resulting image, the contrast-to-noise ratio still improves thanks to a decrease in noise from the larger number of photons that is produced [100].

Unlike conventional dose calculation algorithms, MC dose engines require values for the mass density and the elemental material composition within each patient voxel. From these data, the probabilities of different interactions are derived using tabulated cross section information. Schneider *et al.* showed that human tissues cannot be uniquely resolved in terms of mass density and elemental composition by means of their CT number, especially in the range of soft tissues between 0 and 100 HU [101]. However, they did not further investigate the dosimetrical effect of this limitation. Values for the mass density can be derived from the CT number in a continuous way [102]. To correlate the CT number with the elemental composition of tissues, the CT number scale is often divided into a discrete number of subsets [103-106]. Typically, six or less different media are defined, e.g. air, lung, fat, muscle, cartilage and bone (figure 1.12). Verhaegen and Devic have shown that the misassignment of media can lead to large errors in patient dose calculations (up to 10% for MV photons) [107].

Figure 1.12. Division of the CT number scale into 6 tissue subsets initially implemented in MCDE.

Alternatively, some MC codes directly convert CT numbers into interaction probabilities, e.g. the electron code VMC [108] and its photon extension XVMC [109]. The main advantage of this approach is that there is no need to specify any boundaries separating tissue subsets. However, due to the complexity of the interaction processes some approximations have to be introduced. Moreover, the implementation into existing MC software is not straightforward.

1.8.2.3 *Conversion of dose to medium to dose to water.*

Whereas most conventional dose calculation algorithms for external photon beam RT report dose to water, MC calculates dose to medium. To compare MC results with results obtained by conventional systems, the MC dose distributions must thus be converted to dose to water. Additionally, dosimetry calibration protocols are generally based on absorbed dose to water standards. Although it would be possible to convert measurements and conventional dose results to dose to medium, the most important reason for converting dose to medium to dose to water is that TCP and NTCP data are usually given in terms of dose to water and it will take a lot of time and effort before biological data can be made available in terms of dose to medium. Liu and Keall have elaborated on this issue in a point-counterpoint discussion [110].

Siebers *et al.* have proposed a method to convert dose to medium to dose to water by applying Bragg–Gray cavity theory [111]. A single correction factor is used for each material (except for air) throughout the field for a given photon energy. Compared to an on-line (at each energy deposition event during the MC simulations) conversion of dose to medium to dose to water, their post-processing method was shown to be of equal value. The conversion factor for a certain material can be computed as the ratio of the water and medium mass stopping powers at an effective electron energy of 1 MeV. The difference between the conversion factors of soft and bone tissues easily exceeds 10%. Again, this illustrates the importance of accurate patient and tissue property modeling for accurate MC dose calculations.

1.8.2.4 *The stochastic nature of Monte Carlo*

Unlike analytical dose calculation algorithms, MC is a stochastic method providing an average dose value and a value for the statistical uncertainty (σ) on the average dose within each scoring voxel. The statistical variance (σ^2) is inversely proportional to the number of energy deposition events scored within the voxel. Therefore, an increase of the total number of simulated histories, a decrease of the voxel size or a decrease of the mass density assigned to the voxel all result in an increase of the statistical variance. For an IMRT treatment plan delivered to a certain patient geometry with a fixed voxel size, the statistical variance on the resulting dose distribution can only be reduced by increasing the MC simulation time. Severe noise is inevitably encountered within air cavities, as the mass density of air is about one thousand times smaller than that of soft tissues. In clinical practice, air may make up a significant portion of the PTV, e.g. in case of ethmoid sinus cancer (figure 1.13).

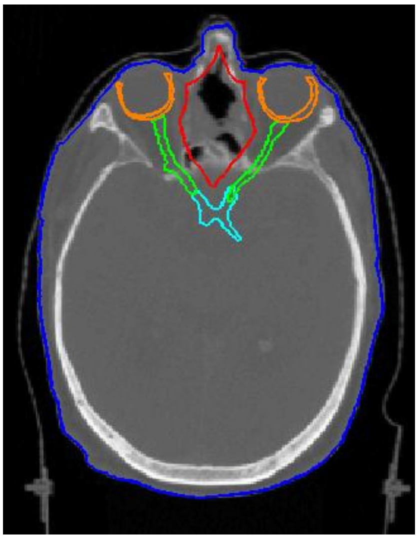

Figure 1.13. Transversal CT image of an ethmoid sinus cancer patient. The anatomical contours of the PTV (red), skin (blue), retinas (orange), optic nerves (green) and optic chiasm (cyan) are shown. The PTV contains a significant amount of air.

The statistical noise not only causes a degradation of the vizualisation of dose distributions [112], but may also mislead the optimization engine or lead to erroneous evaluation of clinical treatment plans. Several authors have studied the effect of statistical uncertainties on the evaluation of dose distributions [113,114] and radiobiological dose indices [115], as well as their impact on the inverse treatment planning process [116,117]. Moreover, denoising techniques have been developed to remove the effect of statistical uncertainties on dose-volume histograms (DVHs)

[118,119] or entire 3D dose distributions [112,120-124]. Denoising can decrease MC simulation times by a factor of ten, at the cost of accuracy [122,125].

1.9 References

1. J Bernier, EJ Hall and A Giaccia. Radiation oncology: a century of achievements. *Nat Rev Cancer* 2004;4:1-11.
2. S Apisarnthanarax and KS Clifford Chao. Current imaging paradigms in radiation oncology. *Radiat Res* 2005;163:1-25.
3. SJ Gwyther. Modern techniques in radiological imaging related to oncology. *Ann Oncol* 1994;5(Suppl.):3-7.
4. GN Hounsfield. Computerized transverse axial scanning (tomography): I. Description of system. *Br J Radiol* 1973;46:1016.
5. P Mansfield and AA Maudsley. Medical imaging by NMR. *Br J Radiol* 1977;50:188-94.
6. P Rubin and DG Bragg. Principles of oncologic imaging and tumor imaging strategies. In: P Rubin, editor. Clinical Oncology: A Multidisciplinary Approach for Physicians and Students. New York: WB Saunders. 2001;241-51.
7. RM Henkelman. New imaging technologies – prospects for target definition. *Int J Radiat Oncol Biol Phys* 1992;22:251-7.
8. C Nutting. Intensity-modulated radiotherapy (IMRT): the most important advance in radiotherapy since the linear accelerator? *Br J Radiol* 2003;76:673.
9. A Brahme, JE Roos and I Lax. Solution of an integral equation encountered in rotation therapy. *Phys Med Biol* 1982;27:1221-9.
10. S Webb and T Lomax. There is no IMRT? *Phys Med Biol* 2001;46:L7-8.
11. T Bortfeld. IMRT: a review and preview. *Phys Med Biol* 2006;51:R363-79.

12. SM Bentzen. Radiation therapy: Intensity modulated, image guided, biologically optimized and evidence based. *Radiother Oncol* 2005;77:227-30.

13. A Eklof, A Ahnesjo and A Brahme. Photon beam energy deposition kernels for inverse radiotherapy planning. *Acta Oncol* 1990;29:447-54.

14. S Webb. Optimization of conformal radiotherapy dose distributions by simulated annealing. *Phys Med Biol* 1989;34:1349-70.

15. TR Mackie, T Holmes, S Swerdloff, P Reckwerdt, JO Deasy, J Yang, B Paliwal and T Kinsella. Tomotherapy: A new concept for the delivery of dynamic conformal radiotherapy. *Med Phys* 1993;20:1709-19.

16. CX Yu. Intensity-modulated arc therapy with dynamic multileaf collimation: an alternative to tomotherapy. *Phys Med Biol* 1995;40:1435-49.

17. C Burman, CS Chui, G Kutcher, S Leibel, M Zelefsky, T LoSasso, S Spirou, QW Wu, J Yang, J Stein, R Mohan, Z Fuks and CC Ling. Planning, delivery, and quality assurance of intensity-modulated radiotherapy using dynamic multileaf collimator: A strategy for large-scale implementation for the treatment of carcinoma of the prostate. *Int J Radiat Oncol Biol Phys* 1997;39:863-73.

18. W De Neve, W De Gersem, S Derycke, G De Meerleer, M Moerman, MT Bate, B Van Duyse, L Vakaet, Y De Deene, B Mersseman, C De Wagter. Clinical delivery of intensity modulated conformal radiotherapy for relapsed or second-primary head and neck cancer using a multileaf collimator with dynamic control. *Radiother Oncol* 1999;50:301-14.

19. T Bortfeld, R Schmidt-Ullrich, W De Neve and DE Wazer, editors. Image-guided IMRT. Part III: Clinical. Berlin: Springer. 2006;287-453.

20. Intensity Modulated Radiation Therapy Collaborative Working Group. Intensity-modulated radiotherapy: Current status and issues of interest. *Int J Radiat Oncol Biol Phys* 2001;51:880-914.

21. AJ Mundt and JC Roeske, editors. Intensity modulated radiation therapy: A clinical perspective. First ed. Hamilton: BC Decker Inc. 2005.

22. S Webb. The physical basis of IMRT and inverse planning. *Br J Radiol* 2003;76:678-89.

23. DM Shepard, MA Earl, XA Li, S Naqvi and C Yu. Direct aperture optimization: a turnkey solution for step-and-shoot IMRT. *Med Phys* 2002;29:1007-18.

24. W De Gersem, F Claus, C De Wagter and W De Neve. An anatomy-based beam segmentation tool for intensity-modulated radiation therapy and its application to head-and-neck cancer. *Int J Radiat Oncol Biol Phys* 2001;51:849–59.

25. W De Gersem, F Claus, C De Wagter, B Van Duyse and W De Neve. Leaf position optimization for step-and-shoot IMRT. *Int J Radiat Oncol Biol Phys* 2001;51:1371–88.

26. L Xing, Y Yang and DM Spielman. Molecular/functional image-guided intensity-modulated radiation therapy. In: T Bortfeld, R Schmidt-Ullrich, W De Neve and DE Wazer, editors. Image-guided IMRT. Berlin: Springer. 2006;187-98.

27. C Van de Wiele. PET and SPECT in IMRT: Future prospects. In: T Bortfeld, R Schmidt-Ullrich, W De Neve and DE Wazer, editors. Image-guided IMRT. Berlin: Springer. 2006;171-6.

28. LJ Verhey, C Chuang and A Pirzkall. Magnetic resonance imaging for IMRT. In: T Bortfeld, R Schmidt-Ullrich, W De Neve and DE Wazer, editors. Image-guided IMRT. Berlin: Springer. 2006;177-86.

29. R Weissleder and U Mahmood. Molecular imaging. *Radiology* 2001;219:316-33.

30. JD Chapman, JD Bradley, JF Eary, R Haubner, SM Larson, JM Michalski, PG Okunieff, HW Strauss, YC Ung and MJ Welch. Molecular (functional) imaging for radiotherapy applications: an RTOG symposium. *Int J Radiat Oncol Biol Phys* 2003;55:294-301.

31. CC Ling, J Humm, S Larson, H Amols, Z Fuks, S Leibel and JA Koutcher. Towards multidimensional radiotherapy (MD-CRT): biological imaging and biological conformality. *Int J Radiat Oncol Biol Phys* 2000;47:551-60.

32. MM Ter-Pogossian, NA Mulani, JT Hood, CS Higgins and DC Ficke. Design considerations for a positron emission transverse tomograph (PETT V). *J Comput Assist Tomogr* 1978;2:539-44.

33. V Grégoire. Is there any future in radiotherapy planning without the use of PET: unraveling the myth… *Radiother Oncol* 2004;73:261-3.

34. T Jones. The imaging science of positron emission tomography. *Eur J Nucl Med* 1996;23:807-13.

35. D Le Bars. Fluorine-18 and medical imaging: Radiopharmaceuticals for positron emission tomography. *J Fluorine Chem* 2006;127:1488-93.

36. PM Price and T Jones. The role of PET scanning in radiotherapy. *Br J Radiol* 2005;78(Suppl. 28):2-4.

37. GK von Schulthess. Integrated modality imaging with PET-CT and SPECT-CT: CT issues. *Eur Radiol Suppl* 2005;15:D121-6.

38. GK von Schulthess, HC Steinert and TF Hany. Integrated PET/CT: Current applications and future directions. *Radiology* 2006;238:405-22.

39. J Frahm, KD Merboldt and W Hanicke. Functional MRI of human brain activation at high spatial resolution. *Magn Reson Med* 2003;29:139-44.

40. GV Shah, MJ Fischbein, D Gandhi and S Mukherji. Dynamic contrast-enhanced MR imaging. *Top Magn Reson Imaging* 2004;15:71-7.

41. AL Harris. Hypoxia: A key regulatory factor in tumour growth. *Nat Rev Cancer* 2002;2:38-47.

42. MM Eatock, A Schätzlein and SB Kaye. Tumour vasculature as a target for anticancer therapy. *Cancer Treat Rev* 2000;26:191-204.

43. TG Graeber, C Osmanian, T Jacks, DE Housman, CJ Koch, SW Loweand AJ Giaccia. Hypoxia-mediated selection of cells with dimished apoptotic potential in solid tumors. *Nature* 1996;397:88-91.

44. SM Bentzen. Repopulation in radiation oncology: perspectives of clinical research. *Int J Radiat Oncol Biol Phys* 2003;79:581-5.

45. International Commission on Radiation Units and Measurements (ICRU). Prescribing, recording and reporting photon beam therapy. Supplement to ICRU Report 50. Washington, DC: ICRU. 1999.

46. W De Neve, Y Wu and G Ezzell. Practical IMRT planning. In: T Bortfeld, R Schmidt-Ullrich, W De Neve and DE Wazer, editors. Image-guided IMRT. Berlin: Springer. 2006;48-59.

47. U Nestle, S Kremp and AL Grosu. Practical integration of [18F]-FDG-PET and PET-CT in the planning of radiotherapy for non-small cell lung cancer (NSCLC): The technical basis, ICRU-target volumes, problems, perspectives. *Radiother Oncol* 2006;81:209-25.

48. K Muylle, C Castaigne and P Flamen. 18F-fluoro-2-deoxy-D-glucose positron emission tomographic imaging : recent developments in head and neck cancer. *Curr Opin Oncol* 2005;17:249-53.

49. S Bujenovic. The role of positron emission tomography in radiation treatment planning. *Semin Nucl Med* 2004;34:293-9.

50. A van Baardwijk, BG Baumert, G Bosmans, M van Kroonenburgh, S Stroobants, V Grégoire, P Lambin and D De Ruysscher. The current status of FDG-PET in tumour volume definition in radiotherapy treatment planning. *Cancer Treat Rev* 2006;32:245-60.

51. SJ Frank, KSC Chao, DL Schwartz, RS Weber, S Apisarnthanarax and HA Macapinlac. Technology insight: PET and PET/CT in head and neck tumor staging and radiation therapy planning. *Nature Clin Pract Oncol* 2005;2:526-33.

52. AL Grosu, M Piert, WA Weber, B Jeremic, M Picchio, U Schratzenstaller, FB Zimmerman, M Schwaiger and M Molls. Positron emission tomography for radiation treatment planning. *Strahlenther Onkol* 2005;181:483-99.

53. P Zanzonico. PET-based biological imaging for radiation therapy treatment planning. *Critical Reviews in Eukaryotic Gene Expression* 2006;16:61-102.

54. K Newbold, M Partridge, G Cook, SA Sohaib, E Charles-Edwards, P Rhys-Evans, K Harrington and C Nutting. Advanced imaging applied to radiotherapy planning in head and neck cancer: a clinical review. *Br J Radiol* 2006;79:554-61.

55. JF Daisne, T Duprez, B Weynand, M Lonneux, M Hamoir, H Reychler and V Grégoire. Tumor volume in pharyngolaryngeal squamous cell carcinoma: Comparison at CT, MR imaging, and FDG PET and validation with surgical specimen. *Radiology* 2004;233:93-100.

56. J Bussink, J Kaanders and A van der Kogel. Biological basis of functional imaging. *Radiother Oncol* 2006;81:S126-7 (Abstract).

57. KSC Chao, WR Bosch, S Mutic, JS Lewis, F Dehdashti, MA Mintun, JF Dempsey, CA Perez, JA Purdy and MJ Welch. A novel approach to overcome hypoxic tumor resistance: Cu-ATSM-guided intensity-modulated radiation therapy. *Int J Radiat Oncol Biol Phys* 2001;49:1171-82.

58. JF Daisne, M Sibomana, A Bol, T Doumont, M Lonneux and V Grégoire. Tri-dimensional automatic segmentation of PET volumes based on measured source-to-background ratios: influence of reconstruction algorithms. *Radiother Oncol* 2003;69:247–50.

59. I Madani, W Duthoy, C Derie, W De Gersem, T Boterberg, M Saerens, F Jacobs, V Grégoire, M Lonneux, L Vakaet, B Vanderstraeten, W Bauters, K Bonte, H Thierens and W De Neve. Positron emission tomography-guided, focal-dose escalation using intensity-modulated radiotherapy for head and neck cancer. *Int J Radiat Oncol Biol Phys* 2007;58:126-35.

60. SM Bentzen. Theragnostic imaging for radiation oncology: dose-painting by numbers. *Lancet Oncol* 2005;6:112-7.

61. A Ahnesjö and MM Aspradakis. Dose calculations for external photon beams in radiotherapy. *Phys Med Biol* 1999;44:R99-155.

62. JV Siebers. Dose calculations for IMRT. In: T Bortfeld, R Schmidt-Ullrich, W De Neve and DE Wazer, editors. Image-guided IMRT. Berlin: Springer. 2006;61-71.

63. R Mohan and CS Chui. Use of fast Fourier transforms in calculating dose distributions for irregularly shaped fields for three-dimensional treatment planning. *Med Phys* 1987;14:70-7.

64. CP Ceberg, BE Bjarngard and TC Zhu. Experimental determination of the dose kernel in high-energy X-ray beams. *Med Phys* 1996;23:505-11.

65. P Storchi and E Woudstra. Calculation of the absorbed dose distribution due to irregularly shaped photon beams using pencil beam kernels derived from basic beam data. *Phys Med Biol* 1996;41:637-56.

66. JD Bourland and EL Chaney. A finite-sized prncil beam model for photon dose calculations in three dimensions. *Med Phys* 1992;19:1401-12.

67. TR Mackie, JW Scrimger and JJ Battista. A convolution method of calculating dose for 15-MV X-rays. *Med Phys* 1985;12:188-96.

68. A Boyer and E Mok. A photon dose distribution model employing convolution calculations. *Med Phys* 1985;12:169-77.

69. A Ahnesjö. Collapsed cone convolution of radiant energy for photon dose calculation in heterogeneous media. *Med Phys* 1989;16:577-92.

70. JV Siebers, SD Tong, M Lauterbach, QW Wu and R Mohan. Acceleration of dose calculations for intensity-modulated radiotherapy. *Med Phys* 2001;28:903-10.

71. QW Wu, D Djajaputra, M Lauterbach, Y Wu and R Mohan. A fast dose calculation method based on table lookup for IMRT optimization. *Phys Med Biol* 2003;48:N159-66.

72. N Reynaert, B De Smedt, M Coghe, L Paelinck, B Van Duyse, W De Gersem, C De Wagter, W De Neve and H Thierens. MCDE: a new Monte Carlo dose engine for IMRT. *Phys Med Biol* 2004;49:N235-41.

73. WR Nelson, H Hirayama and DWO Rogers. The EGS4 code system. SLAC Report 265. Stanford Linear Accelerator Center. 1985.

74. I Kawrakow and DWO Rogers. The EGSnrc code system: Monte Carlo simulation of electron and photon transport. NRCC Report PIRS-701. Ottawa: National Research Council of Canada. 2000.

75. JF Briesmeister. MCNPTM: A general Monte Carlo N-particle transport code, version 4C. Technical report no. LA-13709-M. Los Alamos National Laboratory. 2000.

76. LS Waters. MCNPX User's manual version 2.4.0. Report no. LA-CP-02-408. Los Alamos National Laboratory. 2002.

77. F Salvat, JM Fernández-Varea and J Sempau. Penelope – a code system for Monte Carlo simulation of electron and photon transport. Workshop Proceedings. Issey-les-Moulineaux, France, 7-10 July 2003.

78. S Agostinelli, J Allison, K Amako *et al*. GEANT4 – a simulation toolkit. *Nucl Instr Meth Phys Res A* 2003;506:250-303.

79. N Reynaert, S van der Marck, D Schaart, W van der Zee, M Tomsej, C van Vliet-Vroegindeweij, J Jansen, M Coghe, C De Wagter and B Heijmen. Monte Carlo treatment planning: an introduction. Report 16 of the Netherlands Commission on Radiation Dosimetry (NCS). Delft: NCS. 2006.

80. I Kawrakow. Accurate condensed history Monte Carlo simulation of electron transport. I. EGSnrc, the new EGS4 version. *Med Phys* 2002;27:485-98.

81. A Bielajew and I Kawrakow. High accuracy Monte Carlo calculations. *Med Biol Eng Comp* 1997;35(Suppl.2):1096.

82. F Verhaegen and J Seuntjens. Monte Carlo modelling of external radiotherapy photon beams. *Phys Med Biol* 2003;48:R107-64.

83. DWO Rogers, CM Ma, B Walters, GX Ding, D Sheikh-Bagheri and G Zang. BEAMnrc Users Manual. Ottawa: National Research Council of Canada. 2002.

84. J Van de Walle, C Martens, N Reynaert, H Palmans, M Coghe, W De Neve, C De Wagter and H Thierens. Monte Carlo model of the Elekta SLiplus accelerator: Validation of a new MLC component module in BEAM for a 6 MV beam. *Phys Med Biol* 2003;48:371-85.

85. B De Smedt, N Reynaert, F Flachet, M Coghe, MG Thompson, L Paelinck, G Pittomvils, C De Wagter, W De Neve and H Thierens. Decoupling initial electron beam parameters for Monte Carlo photon beam modelling by removing beam-modifying filters from the beam path. *Phys Med Biol* 2005;50 :5935-51.

86. B Walters and DWO Rogers. DOSXYZnrc Users manual. NRCC Report PIRS-794. Ottawa: National Research Council of Canada. 2002.

87. N Papanikolaou, J Battista, A Boyer, C Kappas, E Klein, TR Mackie, M Sharpe and J Van Dyk. Tissue Inhomogeneity Corrections for Megavoltage Photon Beams. AAPM Report No 85, Task Group No 65 of the Radiation Therapy Committee of the American Association of Physicists in Medicine. Madison: Medical Physics Publishing. 2004.

88. BA Fraass, J Smathers and J Deye. Summary and recommendations of a National Cancer Institute workshop on issues limiting the clinical use of Monte Carlo dose calculation algorithms for megavoltage external beam radiation therapy. *Med Phys* 2003;30:3206–16.

89. A Dutreix. When and how can we improve precision in radiotherapy? *Radiother Oncol* 1984;2:275-92.

90. FCP du Plessis, CA Willemse and MG Lötter. The indirect use of CT numbers to establish material properties needed for Monte Carlo calculation of dose distributions in patients. *Med Phys* 1998;25:1195–201.

91. DWO Rogers, BA Faddegon, GX Ding, CM Ma, J We and TR Mackie. BEAM: a Monte Carlo code to simulate radiotherapy treatment units. *Med Phys* 1995;22:503-24.

92. DWO Rogers and AF Bielajew. Monte Carlo techniques of electron and photon transport for radiation dosimetry. In: KR Kase, BE Bjärngard and FH Attix, editors. The dosimetry of ionizing radiation. Vol III, Chapter 5. New York: Academic. 1990.

93. W De Neve and C De Wagter. Lethal pneumonitis in a phase I study of chemotherapy and IMRT for NSCLC: the need to investigate the accuracy of dose computation. *Radiother Oncol* 2005;75:246–7.

94. BL Werner, IJ Das, FM Khan and AS Meigooni. Dose perturbations at interfaces in photon beams. *Med Phys* 1987;14:585-95.

95. BJ Mijnheer, RK Rice and LM Chin. Lead-polystyrene transition zone dosimetry in high-energy photon beams. *Radiother Oncol* 1988;11:379-86.

96. C Martens, N Reynaert, C De Wagter, P Nilsson, M Coghe, H Palmans, H Thierens and W De Neve. Underdosage of the upper-airway mucose for small fields as used in intensity-modulated radiation therapy: A comparison between radiochromic film measurements, Monte Carlo simulations, and collapsed cone convolution calculations. *Med Phys* 2002;29:1528-35.

97. P Carrasco, N Jornet, MA Duch, L Weber, M Ginjaume, T Eudaldo, D Jurado, A Ruiz and M Ribas. Comparison of dose calculation algorithms in phantoms with lung equivalent heterogeneities under conditions of lateral electronic disequilibrium. *Med Phys* 2004;31:2899-911.

98. C Constantinou, JC Harrington and LA DeWerd. An electron density calibration phantom for CT-based treatment planning computers. *Med Phys* 1992;19:325–7.

99. J Seco and PM Evans. Assessing the effect of electron density in photon dose calculations. *Med Phys* 2006;33:540–52.

100. HD Nagel, editor. Radiation exposure in computed tomography. Frankfurt: European Coordination Committee of the Radiological and Electromedical Industries. 2000.

101. W Schneider, T Bortfeld and W Schlegel. Correlation between CT numbers and tissue parameters needed for Monte Carlo simulations of clinical dose distributions. *Phys Med Biol* 2000;45:459–78.

102. CM Ma, JS Li, T Pawlicki, SB Jiang, J Deng, MC Lee, T Koumrian, M Luxton and S Brain. A Monte Carlo dose calculation tool for radiotherapy treatment planning. *Phys Med Biol* 2002;47:1671-89.

103. JJ DeMarco, TD Solberg and JB Smathers. A CT-based Monte Carlo simulation tool for dosimetry planning and analysis. *Med Phys* 1998;25:1–11.

104. CL Hartmann-Siantar, PM Bergstrom Jr., WP Chandler, L Chase, LJ Cox, TP Daly, D Garrett, SM Hornstein, RK House, EI Moses, RW Patterson, JA Rathkopf and AE Schach von Wittenau. Lawrence Livermore National Laboratory's PEREGRINE project. In: Proceedings of the XIIth Conference on the Use of Computers in Radiotherapy. Madison: Medical Physics Publishing. 1997;19-22.

105. CM Ma, E Mok, A Kapur, T Pawlicki, D Findley, S Brain, K Forster and AL Boyer. Clinical implementation of a Monte Carlo treatment planning system. *Med Phys* 1999;26:2133–43.

106. L Wang, CS Chui and M Lovelock. A patient-specific Monte Carlo dose-calculation method for photon beams. *Med Phys* 1998;25:867–78.

107. F Verhaegen and S Devic. Sensitivity study for CT image use in Monte Carlo treatment planning. *Phys Med Biol* 2005;50:937–46.

108. I Kawrakow, M Fippel and K Friedrich. 3D electron dose calculations using a voxel based Monte Carlo algorithm (VMC). *Med Phys* 1996;23:445–57.

109. M Fippel. Fast Monte Carlo dose calculations for photon beams based on the VMC electron algorithm. *Med Phys* 1999;26:1466–75.

110. HH Liu and P Keall. Dm rather than Dw should be used in Monte Carlo treatment planning. *Med Phys* 2002;29:922–4.

111. JV Siebers, PJ Keall, AE Nahum and R Mohan. Converting absorbed dose to medium to absorbed dose to water for Monte Carlo based photon beam dose calculations. *Phys Med Biol* 2000;45:983–95.

112. B Miao, R Jeraj, S Bao and TR Mackie. Adaptive anisotropic diffusion filtering of Monte Carlo dose distributions. *Phys Med Biol* 2003;48:2767-81.

113. PJ Keall, JV Siebers, R Jeraj and R Mohan. The effect of dose calculation uncertainty on the evaluation of radiotherapy plans. *Med Phys* 2000;27:478-84.

114. I Kawrakow. The effect of Monte Carlo statistical uncertainties on the evaluation of dose distributions in radiation treatment planning. *Phys Med Biol* 2004;49:1549-56.

115. FM Buffa and AE Nahum. Monte Carlo dose calculations and radiobiological modelling: analysis of the effect of the statistical noise of the dose distribution on the probability of tumour control. *Phys Med Biol* 2000;45:3009-23.

116. R Jeraj and P Keall. The effect of statistical uncertainty on inverse treatment planning based on Monte Carlo dose calculation. *Phys Med Biol* 2000;45:3601-13.

117. CM Ma, JS Li, SB Jiang, T Pawlicki, W Xiong, LH Qin and J Yang. Effect of statistical uncertainties on Monte Carlo treatment planning. *Phys Med Biol* 2005;50:891-907.

118. J Sempau and AF Bielajew. Towards the elimination of Monte Carlo statistical fluctuation from dose volume histograms for radiotherapy treatment planning. *Phys Med Biol* 2000;45:131-57.

119. SB Jiang, T Pawlicki and CM Ma. Removing the effect of statistical uncertainty on dose-volume histograms from Monte Carlo dose calculations. *Phys Med Biol* 2000;45:2151-61.

120. JO Deasy. Denoising of electron beam Monte Carlo dose distributions using digital filtering techniques. *Phys Med Biol* 2000;45:1765-79.

121. JO Deasy, VM Wickerhauser and M Picard. Accelerating Monte Carlo simulations of radiation therapy dose distributions using wavelet threshold de-noising. *Med Phys* 2002;29:2366-73.

122. I Kawrakow. On the de-noising of Monte Carlo calculated dose distributions. *Phys Med Biol* 2002;47:3087-3103.

123. M Fippel and F Nüsslin. Smoothing Monte Carlo calculated dose distributions by iterative reduction of noise. *Phys Med Biol* 2003;48:1289-1304.

124. B De Smedt, M Fippel, N Reynaert and H Thierens. Denoising of Monte Carlo dose calculations: Smoothing capabilities vs. Introduction of systematic bias. *Med Phys* 2006;33:1678-87.

125. I El Naqa, I Kawrakow, M Fippel, JV Siebers, PE Lindsay, MV Wickerhauser, M Vicic, K Zakarian, N Kauffmann and JO Deasy. A comparison of Monte Carlo dose calculation denoising techniques. *Phys Med Biol* 2005;50:909-22.

Chapter 2

Objectives and outline

2.1 Objectives and outline

Considering the recent progress in biological imaging techniques, the first objective of this thesis was ***to implement BCRT at GUH***. A constrained linear relationship was established between the biological image signal intensity and the desired dose within each patient voxel. The practical implementation involved the development of a new tool to generate initial beam segments based on biological imaging information, and an extension of the objective function. Finally, new ways for evaluating intentionally non-homogeneous dose distributions were developed to assess the obtained biological conformity. Details on the implementation can be found in Publication 1: "Implementation of biologically conformal radiation therapy (BCRT) in an algorithmic segmentation-based inverse planning approach" (p. 45).

The next objective of this thesis was ***to validate the feasibility of BCRT treatment planning and to compare the plan characteristics of dose painting and dose painting-by-numbers***. Because of the existing FDG-PET based dose painting phase I clinical trial at GUH [1], an FDG-PET based dose painting-by-numbers planning study was performed on 15 head and neck cancer patients. Since the majority of recurrences occurs within the high-dose regions, head and neck tumors are eligible for focused dose escalation [2-4]. Moreover, motion is conveniently limited within the head and neck region and is reduced by means of immobilization masks. As in the phase I clinical trial, two levels of dose escalation were investigated: 2.5 and 3 Gy per fraction. Treatment plans from BCRT and dose painting were compared through an extensive set of clinically important dose-volume parameters for both targets and organs at risk. The results of this study are reported in Publication 2: "[^{18}F]fluoro-deoxy-glucose positron emission tomography ([^{18}F]FDG-PET) voxel intensity-based intensity-modulated radiation therapy (IMRT) for head and neck cancer" (p. 59).

Experiments involving phantom measurements have already shown that MC calculations are clearly superior to conventional dose calculation algorithms near low density materials and around air cavities [5-9]. However, there is a lack of data evaluating the performance of highly developed analytical dose calculation algorithms compared to MC computations in a clinical setting. Due to the presence of electronic disequilibrium, the calculation of patient dose distributions for lung cancer makes great demands on dose calculation systems. Therefore, the third objective of this thesis was ***to evaluate the accuracy of MC, CS and PB algorithms for lung cancer patient dose calculations***. Two IMRT treatment plans (using either 6 MV or 18 MV photons) were created for each of ten lung cancer patients. MCDE, two commercial CS implementations and one commercial PB algorithm were used to recompute the final dose distribution for each treatment plan. The resulting dose distributions were compared through an extensive set of clinically important dose-volume parameters for both targets and organs at risk. The results are presented in Publication 3: "Accuracy of patient dose calculation for lung IMRT: A comparison of Monte Carlo, convolution/superposition, and pencil beam computations" (p. 79).

The comparison of MC and CS algorithms for lung cancer lead to another interesting clinical application. At GUH, 18 MV photons are generally used for IMRT treatment of lung cancer. This practice has originated from experience with the IMRT optimization software, which was able to select both 6 MV and 18 MV photons using a CS dose calculation algorithm. However, to minimize lateral electronic disequilibrium and to reduce the irradiated volume of normal lung, low-energy photons have been advised for radiotherapy of lung cancer [10]. The fourth objective of this thesis therefore was ***to evaluate whether 6 MV photon beams result in better IMRT treatment plans for lung cancer than 18 MV photon beams***. For this purpose, target dose coverage and organ at risk sparing were investigated by comparing 6 MV and 18 MV dose distributions computed by MCDE and a commercial CS algorithm for ten IMRT lung cancer patients. The results of this study are reported in Publication 4: "Comparison of 6 MV and 18 MV photons for IMRT treatment of lung cancer" (p. 101).

The conversion of CT numbers into material properties is one of the main factors that determine the accuracy of MC patient dose calculations. The fifth objective of this thesis was ***to develop a CT conversion scheme suitable for photons and electrons, and to evaluate the proposed CT conversion scheme in a European multi-center study***. Firstly, the attenuation and energy deposition properties of human tissues and their constituent elements were studied. The proposed CT conversion method is based on the stoichiometric calibration method of Schneider *et al.* [11] and makes use of dosimetrically equivalent tissue subsets. It was validated using virtual MC slab phantoms and a real CT phantom containing different inserts. Finally, the investigation was focused towards the clinical evaluation of patient treatment plans. Attention was paid to the conversion from dose to medium to dose to water in order to assess the magnitude of errors that may arise with the conversion if the wrong material composition is assigned. The CT conversion study is presented in Publication 5: "Conversion of CT numbers into tissue parameters for Monte Carlo dose calculations: a multi-centre study" (p.115).

Due to the stochastic nature of MC, statistical uncertainties are inherently associated with the resulting dose distributions. The amount of noise decreases as the simulation time increases. From a practical point of view it is thus important to determine the optimum, i.e. minimum, number of simulated histories at which a clinical treatment plan can still be evaluated adequately. Therefore, the sixth objective of this thesis was ***to develop uncertainty-based stopping criteria for MC patient dose calculations***. Upper limits on both the relative and absolute statistical uncertainties within each patient voxel were implemented into MCDE. Calculations were performed taking into account the PTV only, or the PTV and a set of critical organs. Both approaches were compared for three clinical treatment plans. The evaluation of the observed dose differences can be found in Publication 6: "Evaluation of uncertainty-based stopping criteria for Monte Carlo calculations of intensity-modulated radiotherapy and arc therapy patient dose distributions" (p. 147).

The final objective of this thesis was ***to investigate the impact of MC on IMRT optimization***. MC dose distributions were integrated into the iterative IMRT optimization process at GUH to evaluate whether treatment plans obtained using conventional dose calculation algorithms could be further improved. Two different methods were developed to incorporate the MC dose distributions. The influence of large air cavities on the outcome of the optimization process was illustrated for a paranasal sinus cancer case. The results of this study are presented in Publication 7: "The influence of air cavities within the PTV on Monte Carlo based IMRT optimization" (p. 165).

In conclusion, the overall objective of this thesis was to improve RT by incorporating biological imaging information into the IMRT treatment planning process and by using MC as a benchmark for RT dose calculations. For this purpose, suitable software applications were developed, implemented in the clinic and evaluated.

2.2 References

1. I Madani, W Duthoy, C Derie, W De Gersem, T Boterberg, M Saerens, F Jacobs, V Grégoire, M Lonneux, L Vakaet, B Vanderstraeten, W Bauters, K Bonte, H Thierens and W De Neve. Positron emission tomography-guided, focal-dose escalation using intensity-modulated radiotherapy for head and neck cancer. *Int J Radiat Oncol Biol Phys* 2007;58:126-35.

2. Dawson L, Anzai Y, Marsh L, *et al*. Patterns of loco-regional recurrence following parotid-sparing conformal and segmental intensity-modulated radiotherapy for head and neck cancer. *Int J Radiat Oncol Biol Phys* 2000;46:1117–26.

3. KSC Chao, G Ozyigit, BN Tran, M Cengiz, JF Dempsey and DA Low. Patterns of failure in patients receiving definitive and postoperative IMRT for head-and-neck cancer. *Int J Radiat Oncol Biol Phys* 2003;55:312-21.

4. A Eisbruch, LH Marsh, LA Dawson, CR Bradford, TN Teknos, DB Chepeha, FP Worden, S Urba, A Lin, MJ Schipper and GT Wolf. Recurrences near base of skull after IMRT for head-and-neck cancer: Implications for target delineation in high neck and for parotid gland sparing. *Int J Radiat Oncol Biol Phys* 2004;59:28-42.

5. MR Arnfield, CH Siantar, J Siebers, P Garmon, L Cox, RT Mohan. The impact of electron transport on the accuracy of computed dose. *Med Phys* 2000;27:1266-74.

6. C Martens, N Reynaert, C De Wagter, P Nilsson, M Coghe, H Palmans, H Thierens and W De Neve. Underdosage of the upper-airway mucosa for small fields as used in intensity-modulated radiation therapy: A comparison between radiochromic film measurements, Monte Carlo simulations, and collapsed cone convolution calculations. *Med Phys* 2002;29:1528–35.

7. G Crammer-Sargison, WA Beckman and J Popescu. Modelling an extreme water-lung interface using a single pencil beam algorithm and the Monte Carlo method. *Phys Med Biol* 2004;49:1557–67.

8. L Paelinck, N Reynaert, H Thierens, W De Neve and C De Wagter. Experimental verification of lung dose with radiochromic film: comparison with Monte Carlo simulations and commercially available treatment planning systems. *Phys Med Biol* 2005;50:2055–69.

9. T Krieger and OA Sauer. Monte Carlo-versus pencil-beam-/collapsed-cone-dose calculation in a heterogeneous multi-layer phantom. *Phys Med Biol* 2005;50:859–68.

10. KE Ekstrand and WH Barnes. Pitfalls in the use of high-energy X-rays to treat tumors in the lung. *Int J Radiat Oncol Biol Phys* 1990;18:249-52.

11. U Schneider, E Pedroni and A Lomax. The calibration of CT Hounsfield units for radiotherapy treatment planning. *Phys Med Biol* 1996;41:111-24.

Chapter 3

Publication 1:

Implementation of biologically conformal radiation therapy (BCRT) in an algorithmic segmentation-based inverse planning approach

Barbara Vanderstraeten[1,2], Werner De Gersem[2], Wim Duthoy[2], Wilfried De Neve[2], Hubert Thierens[1]

[1] *Department of Medical Physics, Ghent University, Gent, Belgium*

[2] *Department of Radiotherapy, Ghent University Hospital, Gent, Belgium*

Physics in Medicine and Biology 2006;51:N277-N286

Abstract

The development of new biological imaging technologies offers the opportunity to further individualize radiotherapy. Biologically conformal radiation therapy (BCRT) implies the use of the spatial distribution of one or more radiobiological parameters to guide the IMRT dose prescription. Our aim was to implement BCRT in an algorithmic segmentation-based planning approach. A biology-based segmentation tool was developed to generate initial beam segments that reflect the biological signal intensity pattern. The weights and shapes of the initial segments are optimized by means of an objective function that minimizes the root mean square deviation between the actual and intended dose values within the PTV. As proof of principle, [^{18}F]FDG-PET-guided BCRT plans for two different levels of dose escalation were created for an oropharyngeal cancer patient. Both plans proved to be dosimetrically feasible without violating the planning constraints for the expanded spinal cord and the contralateral parotid gland as organs at risk. The obtained biological conformity was better for the first (2.5 Gy per fraction) than for the second (3 Gy per fraction) dose escalation level.

1. Introduction

The development of radiation therapy has always relied strongly on the available imaging technologies. Anatomical imaging techniques such as computed tomography (CT), magnetic resonance imaging (MRI) and ultrasound (US) can visualize spatial changes in physical properties within patients. Additionally, tumour biology plays an important role in the diagnosis, treatment decision-making and the assessment of therapeutic response (Xing *et al* 2006). Recent advances in biological imaging techniques, mainly based on positron emission tomography (PET), single photon emission tomography (SPECT) and magnetic resonance spectroscopy (MRS), aim at revealing the spatial biology distribution within patients (Van de Wiele 2006, Verhey *et al* 2006).

Highly structured dose distributions can be delivered using intensity modulated radiation therapy (IMRT). In current clinical practice, IMRT optimization is based on the assumption of a uniform biology distribution within each target volume and aims at achieving geometrically conformal dose distributions. However, the use of biological imaging in radiotherapy treatment planning has become increasingly popular. In the first instance, biological images can aid in the delineation of target volumes, which are subsequently planned to receive a uniform dose. However, by using the entire spatially heterogeneous distribution of biological information to create the IMRT treatment plan, truly biologically conformal dose distributions can be delivered (Ling *et al* 2000). The biologically conformal radiation therapy (BCRT) treatment planning process involves several steps, from the registration of anatomical and biological images over the quantification of the biological image signal and definition of the relationship between signal intensity and prescription dose to the optimization of the treatment plan.

Several authors have described the implementation of BCRT into the inverse treatment planning process (Xing *et al* 2002, Alber *et al* 2003, Das *et al* 2004, Yang and Xing 2005). At our institution, IMRT treatment plans are created by optimizing the weights and shapes of initially generated beam segments. Our aim was to implement BCRT in this algorithmic segmentation-based inverse planning approach. This note describes the development of a new tool to generate initial beam segments based on biological imaging information and the changes that were made to the objective function. As proof of principle, an exemplary patient case of [^{18}F]fluoro-deoxy-glucose PET (FDG-PET)-guided BCRT for oropharyngeal cancer is presented.

2. Methods

2.1. A bound-constrained linear model

Although it is an essential step in the BCRT planning process, translating the available biological imaging information into the most desirable dose distribution within a tumour is not at all obvious. Radiobiological models can generate this dose distribution by maximizing the tumour control probability value, provided all necessary biological parameters are known (Xing *et al* 2006, pp 194–5). However, as our knowledge on radiobiological parameters is limited and they are hard to extract from the available biological images, a more practical approach seems to be the best option at present (Xing *et al* 2006, p 191). Several authors have suggested the use of a linear relationship between the prescribed radiation dose and the quantified biological signal (S), which is assumed to represent the level of metabolic abnormality, in every image voxel (Xing *et al* 2002, Alber *et al* 2003, Das *et al* 2004). For our study, we assume the following dose prescription within the planning target volume (PTV):

$$D_{presc} = D_{low} + \frac{S - S_{low}}{S_{high} - S_{low}} (D_{high} - D_{low}) \text{ for } S_{\mathrm{low}} \leq S \leq S_{\mathrm{high}} \quad (1)$$

Thus, the prescription dose D_{presc} is escalated linearly between D_{low} and D_{high}, respectively corresponding to S_{low} and S_{high}. The values of S_{low}, S_{high}, D_{low} and D_{high} can be chosen freely. Additionally, $D_{\mathrm{presc}} = D_{\mathrm{low}}$ for voxels within the target volume where $S \leq S_{\mathrm{low}}$, while $D_{\mathrm{presc}} = D_{\mathrm{high}}$ for voxels within the target volume where $S \geq S_{\mathrm{high}}$.

2.2. BCRT treatment planning: an algorithmic segmentation-based inverse approach

At our institution, IMRT treatment planning is based on class solutions and involves direct multi-leaf collimator (MLC) aperture optimization. Figure 1 illustrates the BCRT planning strategy. We start from a template beam set, characterized by each beam's isocentre, gantry, table and collimator angles, linear accelerator, radiation modality and energy. Delineation of target volumes and organs at risk (OARs) on anatomical images results in a set of PTV and OAR contours. Anatomical imaging also provides the appropriate grid size and resolution, and voxel attenuation properties for accurate dose calculation. For every template beam, a set of initial beam segments is created by in-house developed software. To implement BCRT, the anatomy-based segmentation tool (ABST) developed by De Gersem *et al* (2001a) was replaced by a new biology-based segmentation tool (BBST). BBST generates beam segments based on the anatomical contours, the biological imaging signal intensity values and the 4 × 4 rigid transformation matrix that characterizes the fusion of the anatomical and biological images. Once the initial set of segments is created, both segment weights and shapes (MLC leaf positions) are optimized by the in-house developed segment outline and weight adapting tool (SOWAT) (De Gersem *et al* 2001b). The optimization uses a bio-physical objective function, which was modified to implement BCRT. Several SOWAT cycles are performed until the plan acceptance criteria are fulfilled. The final beam segments and corresponding weights are then combined into a prescription that is suitable for transfer to the linear accelerator. The next paragraphs describe BBST and the modification of the objective function in detail.

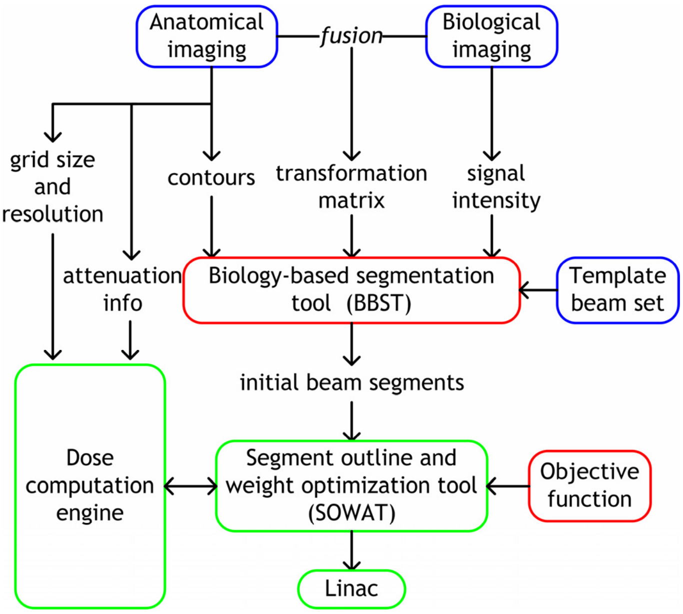

Figure 1. The BCRT planning strategy at Ghent University Hospital. Starting from a template beam set, the biology-based segmentation tool creates initial beam segments. The weights and MLC shapes of these segments are further optimized by maximizing a bio-physical objective function. The final prescription is sent to the linear accelerator.

2.3. Biology-based segmentation tool

To implement BCRT, the available biological imaging information is used to create initial beam segments. Like ABST, BBST uses one or more PTVs, OARs, the skin contours and a template beam as input. Additionally, BBST requires the biological imaging signal intensity information and the 4 × 4 transformation matrix that describes the rotations and translations needed for the rigid anatomical–biological image fusion. A detailed description of ABST has been given by De Gersem *et al* (2001a). The next paragraphs focus on the new aspects of segmentation involved in BBST; parts of the algorithm that are also performed by ABST are reproduced only in brief.

First, a two-dimensional 'segmentation grid' is created in the template beam's isocentric plane. This is the plane through the isocentre and perpendicular to the central axis. The pixel size of the grid is 1 × 1 mm^2 and all pixel values are initialized to zero. All target volumes are centrally projected from the source point onto this grid. To account for penumbra, a user-defined expansion margin is applied to each PTV projection. The segmentation grid pixel values inside each PTV projection are all set to the same positive value. By projecting the biological imaging information onto the segmentation grid, the pixel values within each PTV projection are differentiated: for every pixel inside a PTV projection, a weighted function of the signal intensity values S is integrated along each rayline emanating from the source:

$$\int_{PTV} S'\left[1+\left(S' S_{low}^{-1}-1\right)^2\right]ds \quad (2)$$

with $S' = S_{\mathrm{low}}$ if $S \leq S_{\mathrm{low}}$ and $S' = S_{\mathrm{high}}$ if $S \geq S_{\mathrm{high}}$; otherwise $S' = S$. As voxels for which the signal $S \leq S_{\mathrm{low}}$ should receive the same dose (i.e. D_{low}) as voxels for which $S = S_{\mathrm{low}}$, and as voxels for which $S \geq S_{\mathrm{high}}$ should receive the same dose (i.e. D_{high}) as voxels for which $S = S_{\mathrm{high}}$, these voxels should be taken into account equally during the segment generation, hence the introduction of S'. S' is integrated after multiplication by a dimensionless weighting function. Several weighting functions have been investigated, including linear, polynomial and exponential functions of $S'(S_{\mathrm{low}})^{-1}$. The objective function was assessed after one optimization cycle, and maximal values were found for the quadratic weighting function presented in equation (2). The integration is constrained to voxels inside the target volume; ds is the line element along the rayline. For each pixel the result is normalized by division of the integral by the total pathlength within the PTV along the rayline. Additionally, the user is allowed to enter an importance factor for a global scaling of the biological contribution to the segmentation grid. Its default value is set to 1. As the result is added to the corresponding grid value, the segmentation grid pixels reflect the biological image signal within each PTV projection.

BBST's second step involves the central projection of all OARs from the source point onto the segmentation grid. A user-defined expansion margin is applied to each OAR projection to achieve good sparing. The grid values inside each OAR projection are all set to the same, negative value. After this, all positive pixel values inside the segmentation grid are divided by $(1+D)$, where D is the distance in cm of the pixel to the nearest contour point of an expanded OAR projection. This will result in the creation of segments close to and conformally avoiding the OARs, which allows for homogeneous irradiation of a target that surrounds a critical organ with a rotational technique (Brahme *et al* 1982). To account for patient attenuation, all positive pixel values inside the segmentation grid are also divided by $(1 + d)$, where d is the distance in cm of the pixel to the entry point through the patient's surface along the rayline emanating from the source point.

Finally, beam segments can be determined from the iso-value lines of the created anatomical–biological segmentation grid. By selecting a minimal beam segment area (defined in the isocentric plane) and an area multiplication factor, the user can control the total number of beam segments created.

2.4. Optimization of segment weights and shapes: objective function

SOWAT (De Gersem *et al* 2001b) optimizes both segment weights and leaf positions. The planning goals are expressed through an objective function, which is maximized during the optimization. Its mathematical expression consists of two major parts. The biological part includes tumour control probability and normal tissue complication probability factors, while the physical part is entirely target-related and refers to target inhomogeneity and prescription dose values. The objective function has been described in detail by De Gersem *et al* (2001b).

BCRT optimization requires the minimization of the difference between the actual (D_p) and intended (D_{presc}) dose values in all dose calculation points p (n in total) that are randomly seeded within the target structure of interest. Therefore, the following term was added to the physical part of the objective function:

$$-\sum_i F_i \left(\frac{D_{dev}}{D_{mean}}\right)_i \left[\frac{1}{2}\left(\frac{D_{dev}}{D_{mean}}\right)_i + 1\right] \qquad (3)$$

The summation index i runs through all target structures involved in the BCRT optimization. F_i is a user-defined importance factor, which is used to identify the level of priority of BCRT optimization within target i over other target structures or other planning goals expressed by the objective function. $(D_{\mathrm{mean}})_{\mathrm{i}}$ and $(D_{\mathrm{dev}})_{\mathrm{i}}$ are the mean dose and the root mean square deviation between the actual and intended dose values within target volume i, respectively:

$$D_{dev} = \left[\frac{\sum_p \left(D_p - D_{presc,p} \right)^2}{n} \right]^{\frac{1}{2}} \qquad (4)$$

The optimization employs a variant of the algorithm developed by Brent (1973) to maximize the objective function. By definition of (3), the derivative of the BCRT term with respect to $D_{\mathrm{dev}}/D_{\mathrm{mean}}$ is a linearly descending function of this ratio. Thus, the larger $D_{\mathrm{dev}}/D_{\mathrm{mean}}$, the larger the force exerted by the optimization algorithm to reduce the value of this ratio will be.

2.5. Treatment plan evaluation

The new segmentation tool and the extension of the objective function can be evaluated by comparing the dose distribution of the resulting treatment plans with the prescribed BCRT dose pattern. For this purpose, a quality factor *QF* was introduced. For every point *p* within the PTV the obtained-over-intended dose ratio $Q_{\mathrm{p}} = D_{\mathrm{p}}/D_{\mathrm{presc}}$ is calculated. This information can be visualized in a *Q*-volume histogram (QVH), by display of the partial PTV volume for which *Q* is greater than or equal to each abscissa value. Ideally such a curve would drop down steeply at $Q = 1$. *QF* is defined as the average absolute deviation of *Q* to 1 within the PTV:

$$QF = \frac{1}{n} \sum_p \left| Q_p - 1 \right| . \qquad (5)$$

3. Example: [^{18}F]FDG-PET-guided BCRT for oropharyngeal cancer

As proof of principle, a patient with a squamous cell carcinoma arising from the oropharynx was considered. Planning CT images were fused with [^{18}F]FDG-PET images. Both sets of images were acquired using a thermoplastic mask to immobilize the patient. To escalate the dose within the PTV, two BCRT treatment plans were created with D_{high}-values of 2.5 and 3 Gy per fraction (Gy/fx); D_{low} was 2.16 Gy/fx. The escalation phase consisted of 10 fractions, while the total treatment consisted of 32 fractions. Thus, the total PTV prescription dose ranged from 69.12 Gy to 72.52 Gy, and from 69.12 Gy to 77.52 Gy for the 2.5 Gy/fx and 3 Gy/fx dose escalation levels, respectively. As an optimization constraint, the relative volume of the 5 mm-expanded spinal cord receiving more than 1.56 Gy/fx ($V_{>1.56\ \mathrm{Gy/fx}}$) had to be less than 5%. Additionally, sparing of the contralateral parotid gland was attempted. Therefore, the median dose D_{med} within the spared parotid had to be less than 0.84 Gy/fx.

Apart from the difference in D_{high}-value, the same segment generation and optimization settings were used to create both plans. Three optimization cycles were performed and both final treatment plans required a minimum number of 2 monitor units (MUs) per segment and per fraction. To minimize the influence of PET signal noise on S_{low} and S_{high}, the dose was escalated between 25% and 100% of the 95th percentile value of the PET signal intensity values within the PTV. BBST was performed using a minimal beam segment area of 0.8 cm^2 and an area multiplication factor of 2.5. The importance factor for BCRT optimization of the PTV was equal to 3.5. The importance factors of the PTV for the other physical terms of the objective function, which aim to achieve a homogeneous target dose, were set to 0 to avoid any conflicts during optimization. The other forces driving the optimization were the biological terms of the objective function that aimed at sparing the expanded spinal cord and the contralateral parotid gland. Their importance factors were set to 1.

Table 1. Summary of treatment planning results for the 2.5 Gy per fraction (Gy/fx) plan, the original 3 Gy/fx plan and the additionally created 3 Gy/fx plans.

	2.5 Gy/fx	3 Gy/fx original plan	3 Gy/fx more segments	3 Gy/fx changed importance	3 Gy/fx more segments and changed importance	3 Gy/fx using ABST
Initial no. of segments	86	86	121	-	-	88
Final no. of segments	55	54	58	58	55	51
QF (%)	1.8	3.4	3.4	3.1	3.0	3.4
Expanded spinal cord $V_{>1.56\mathrm{Gy/fx}}$ (%)	0.3	0.0	0.0	1.7	1.8	0.0
Spared parotid gland D_{50} (Gy/fx)	0.66	0.66	0.67	0.76	0.69	0.68
Total no. of MUs/fx	523	686	676	760	761	661
Average no. of MUs/fx per segment	9.5	12.7	11.7	13.1	13.8	13.0

Table 1 summarizes the planning results. Initially, 86 beam segments were created by BBST. The final plans consisted of 55 (2.5 Gy/fx) and 54 (3 Gy/fx) beam segments and delivered a total number of 523 (2.5

Gy/fx) and 686 (3 Gy/fx) MUs/fx, respectively. Thus, on average 9.5 (2.5 Gy/fx) and 12.7 (3 Gy/fx) MUs/fx were delivered per segment. Figures 2 and 3 illustrate the resulting dose distribution superimposed on the original PET images for D_{high} = 2.5 Gy/fx. Dose–volume histograms (DVHs) of the PTV, the expanded spinal cord and the spared parotid gland are shown in figure 4 for both escalation steps. The planning constraints were fulfilled: the $V_{>1.56\ \mathrm{Gy/fx}}$-value for the expanded spinal cord was 0.3% (2.5 Gy/fx) and 0.0% (3 Gy/fx), while the median dose within the spared parotid gland was 0.66 Gy/fx for both escalation steps. Figure 5 shows the QVHs of the PTV for both escalation steps. The *QF*-value was 1.8% for D_{high} = 2.5 Gy/fx, and 3.4% for D_{high} = 3 Gy/fx. By increasing D_{high}, the dose gradients required within the PTV become steeper, while their maximal steepness is limited by the penumbra width of the delivered beam segments. This depends on the design of the linear accelerator's treatment head and on the field shape of the individual segments.

To see whether the *QF*-value of the 3 Gy/fx plan could be improved by taking into account more initial beam segments, an additional treatment plan was generated. All parameters were the same as for the original 3 Gy/fx plan, except for the area multiplication factor which was decreased from 2.5 to 1.5. The results are summarized in table 1. Initially, 121 beam segments were generated by BBST. However, after optimization only 58 segments were retained for the final plan, which is comparable to the final number of segments (54) of the original 3 Gy/fx plan. The $V_{>1.56\ \mathrm{Gy/fx}}$-value for the expanded spinal cord was 0.0% for the plan with more segments, while the median dose within the spared parotid gland was 0.67 Gy/fx. The *QF*-value was equal to 3.4%. It is clear that the original 3 Gy/fx plan could not be improved by creating more initial beam segments.

Figure 4 shows a larger separation between the DVHs of the PTV and of the expanded spinal cord for the 3 Gy/fx plan than for the 2.5 Gy/fx plan. To investigate whether the *QF*-value of the 3 Gy/fx plan could be improved by allowing a higher dose to be delivered to the expanded spinal cord, two additional treatment plans were generated. Starting from the original 3 Gy/fx plan and from the above-mentioned 3 Gy/fx plan with more initial beam segments, an additional optimization cycle was performed with changed importance factors. While the importance factor of the expanded spinal cord in the objective function was changed from 1 to 0.1, the importance factor of the BCRT term was strongly increased from 3.5 to 35. This resulted in modified plans, consisting of 58 (changed importance) and 55 (more segments and changed importance) beam segments, respectively. The planning results are summarized in table 1. $V_{>1.56\ \mathrm{Gy/fx}}$ was raised to 1.7% (changed importance) and 1.8% (more segments and changed importance), while the median dose delivered to the contralateral parotid gland was raised to 0.76 Gy/fx (changed importance) and 0.69 Gy/fx (more segments and changed importance). However, even with these extreme settings *QF* could only be improved slightly to 3.1% (changed importance) and 3.0% (more segments and changed importance), respectively. It is clear that the 3 Gy/fx plans could not be greatly improved by allowing the dose delivered to the spinal cord to increase (within tolerance).

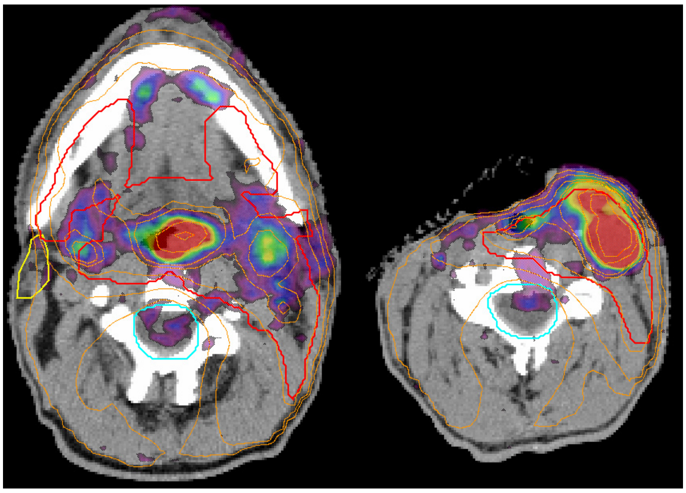

Figure 2. [^{18}F]FDG-PET-guided BCRT dose distribution superimposed on the original PET images for D_{high} = 2.5 Gy per fraction, shown for 2 transverse planes (left: 1.8 cm above the isocentre, right: 1.2 cm below the isocentre). The 1.6, 1.8, 2.1, 2.2, 2.3, 2.4 and 2.5 Gy per fraction isodose lines are indicated in orange. The contours of the PTV (red), the expanded spinal cord (cyan) and the spared parotid gland (yellow) are shown.

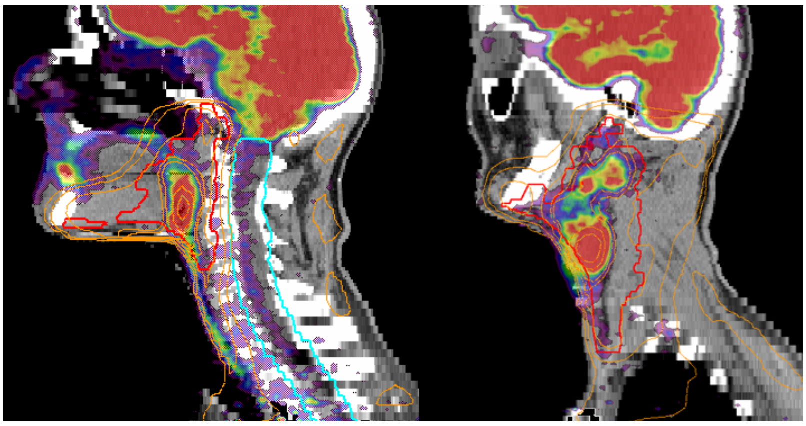

Figure 3. [^{18}F]FDG-PET-guided BCRT dose distribution superimposed on the original PET images for D_{high} = 2.5 Gy per fraction, shown for 2 sagittal planes (left: 0.3 cm to the left of the isocentre, right: 4 cm to the left of the isocentre). The 1.6, 1.8, 2.1, 2.2, 2.3, 2.4 and 2.5 Gy per fraction isodose lines are indicated in orange. The contours of the PTV (red) and the expanded spinal cord (cyan) are shown.

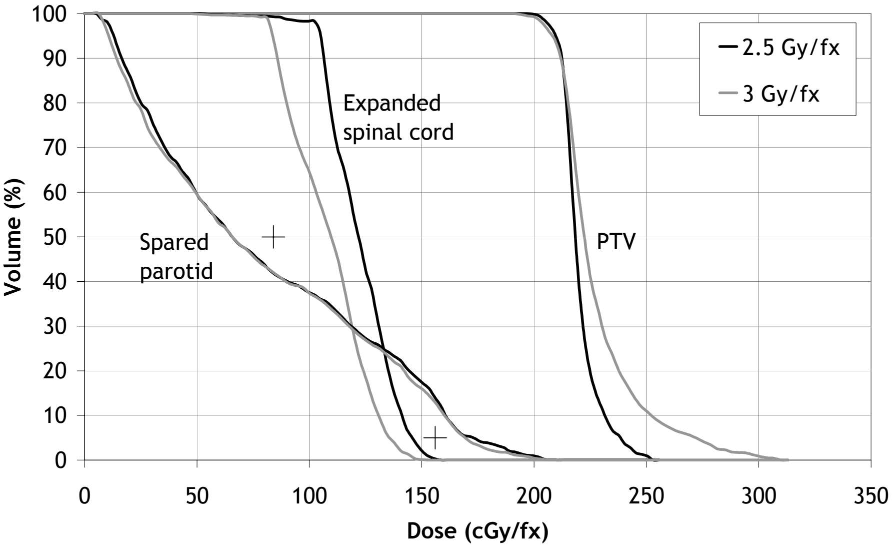

Figure 4. Dose–volume histograms of the PTV, the expanded spinal cord and the spared parotid gland for both escalation steps (2.5 and 3 Gy per fraction). The crosses represent the planning constraints.

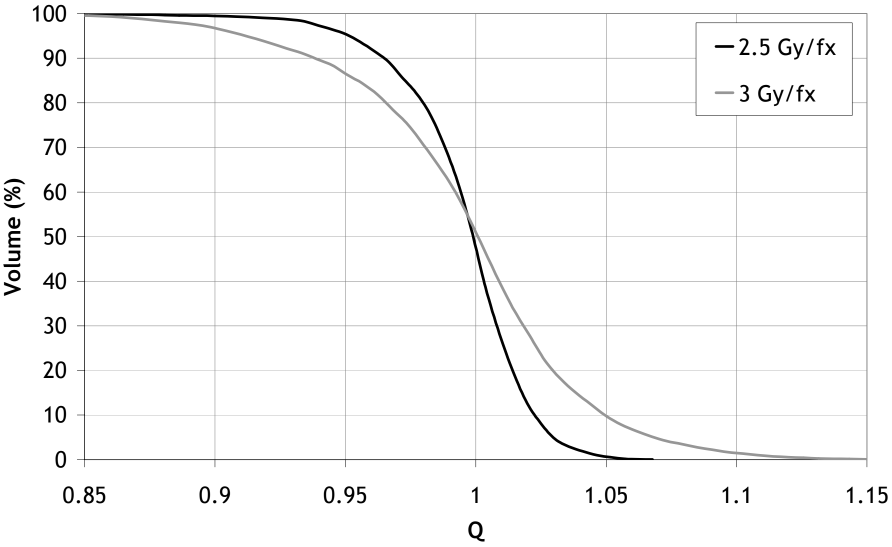

Figure 5. *Q*-volume histograms of the PTV for both escalation steps (2.5 and 3 Gy per fraction).

To investigate the influence of using BBST instead of ABST, a fourth additional treatment plan was generated. All parameters were the same as for the original 3 Gy/fx plan, except for the fact that ABST was used to create initial beam segments instead of including the biological part of the segmentation grid. This resulted in the generation of 88 initial beam segments, of which 51 segments were retained for the final plan. The results are summarized in table 1. *QF* was equal to 3.4%, while $V_{>1.56\ \mathrm{Gy/fx}}$ for the expanded spinal cord was equal to 0.0% and the median dose within the spared parotid gland was 0.68 Gy/fx. For this patient the use of ABST instead of BBST did not result in a worse BCRT treatment plan after the same number of optimization cycles, but this is unlikely to hold true for all possible patient cases. Although the use of SOWAT clearly minimizes the dependence of the final treatment plan on the initially created beam segments, we still consider BBST preferable to create initial beam segments for BCRT due to its capability of incorporating biological imaging data into the segmentation grid.

Only one patient case was presented in this note as proof of principle. In a separate planning study BCRT plans (for dose escalation levels of 2.5 and 3 Gy/fx) were compared to so-called PET contour-based plans, in which a boost dose of 2.5 Gy/fx was prescribed homogeneously to an automatically delineated PET lesion inside the PTV, for 15 patients (Vanderstraeten *et al* 2006). Thus, the PET contour-based plans did not use BBST nor the BCRT term of the objective function. According to a paired, two tailed *t*-test for those 15 patients the BCRT 3 Gy/fx plans had significantly more beam segments than the BCRT 2.5 Gy/fx plans (49 ± 6 (1σ) versus 46 ± 4), which in their turn had significantly more beam segments than the contour-based plans (41 ± 7). The total number of MUs/fx was not significantly different between the contour-based (466 ± 57) and the BCRT 2.5 Gy/fx (503 ± 26) plans, but was obviously significantly higher for the BCRT 3 Gy/fx plans (645 ± 37) than for the BCRT 2.5 Gy/fx plans. The average number of MUs/fx per segment was not significantly different between the contour-based (11.7 ± 2.0) and the BCRT 2.5 Gy/fx (11.1 ± 1.2) plans, but was significantly higher for the BCRT 3 Gy/fx plans (13.3 ± 1.2) than for the BCRT 2.5 Gy/fx plans.

In the future similar planning studies must be performed for other tumour sites to confirm the feasibility of BCRT dose escalation and to evaluate its effect on the dose delivered to the organs at risk in order to facilitate the clinical implementation of the BCRT technique proposed in this note. The quality of the final treatment plan is guarded by SOWAT.

4. Conclusions

The development of new biological imaging technologies offers the opportunity to further individualize radiotherapy. Biologically conformal radiation therapy (BCRT) implies the use of the spatial distribution of one or more radiobiological parameters to guide the IMRT dose prescription. By developing a biology-based segmentation tool and extending the objective function, BCRT could be implemented in an algorithmic segmentation-based inverse planning approach. By projecting the biological imaging information onto the isocentric plane of each template beam, BBST creates initial beam segments that reflect the biological signal intensity pattern. The weights and shapes of the initial segments are optimized using the new objective function, which minimizes the root mean square deviation between the actual and intended dose values within the PTV. BCRT plans for two different dose escalation steps were used to demonstrate the feasibility of [^{18}F]FDG-PET-guided BCRT for oropharyngeal cancer. The obtained biological conformity was better for the first (2.5 Gy per fraction) than for the second (3 Gy per fraction) dose escalation level.

Acknowledgments

The project *Conformal Radiotherapy Ghent University Hospital* is supported by the Belgische Federatie tegen Kanker (51AC8904, FBC2003/2006, ZKB2747) and by grants from the Research Foundation-Flanders (FWO-Vlaanderen) (G.0183.03), Ghent University (GOA 12050401, BOF 01112300, 011VO497, 011B3300) and the Centrum voor Studie and Behandeling van Gezwelziekten. Barbara Vanderstraeten is a Research Assistant of the Research Foundation-Flanders.

References

Alber M, Paulsen F, Eschmann S M and Machulla H J 2003 On biologically conformal boost dose optimization Phys. Med. Biol. 48 N31–5

Brahme A, Roos J E and Lax I 1982 Solution of an integral equation encountered in rotation therapy Phys. Med. Biol. 27 1221–9

Brent R P 1973 Algorithms forMinimization without Derivatives ed G Forsythe (Englewood Cliffs, NJ: Prentice- Hall)

Das S K et al 2004 Feasibility of optimizing the dose distribution in lung tumors using fluorine-18-fluorodeoxyglucose positron emission tomography and single photon emission computed tomography guided dose prescriptions Med. Phys. 31 1452–61

De Gersem W, Claus F, De Wagter C and De Neve W 2001a An anatomy-based beam segmentation tool for intensity-modulated radiation therapy and its application to head-and-neck cancer Int. J. Radiat. Oncol. Biol. Phys. 51 849–59

De Gersem W, Claus F, De Wagter C, Van Duyse B and De Neve W 2001b Leaf position optimization for step-and-shoot IMRT Int. J. Radiat. Oncol. Biol. Phys. 51 1371–88

Ling C C, Humm J, Larson S, Amols H, Fuks Z, Leibel S and Koutcher J A 2000 Towards multidimensional radiotherapy (MD-CRT): biological imaging and biological conformality Int. J. Radiat. Oncol. Biol. Phys. 47 551–60

Vanderstraeten B, Duthoy W, De Gersem W, De Neve W and Thierens H 2006 [18F]fluoro-deoxy-glucose positron emission tomography ([^{18}F]FDG-PET) voxel intensity-based intensity-modulated radiation therapy (IMRT) for head and neck cancer Radiother. Oncol. at press

Van de Wiele C 2006 PET and SPECT in IMRT: future prospects Image-guided IMRT ed T Bortfeld et al (Berlin: Springer) pp 171–6

Verhey L J, Chuang C and Pirzkall A 2006 Magnetic resonance imaging for IMRT Image-guided IMRT ed T Bortfeld et al (Berlin: Springer) pp 177–86

Xing L, Cotrutz C, Hunjan S, Boyer A L, Adalsteinsson E and Spielman D 2002 Inverse planning for functional image-guided intensity-modulated radiation therapy Phys. Med. Biol. 47 3567–78

Xing L, Yang Y and Spielman D M 2006 Molecular/functional image-guided intensity modulated radiation therapy Image-guided IMRT ed T Bortfeld et al (Berlin: Springer) pp 187–98

Yang Y and Xing L 2005 Towards biologically conformal radiation therapy (BCRT): selective IMRT dose escalation under the guidance of spatial biology distribution Med. Phys. 32 1473–84

Chapter 4

Publication 2:

[18F]fluoro-deoxy-glucose positron emission tomography ([18F]FDG-PET) voxel intensity-based intensity-modulated radiation therapy (IMRT) for head and neck cancer

Barbara Vanderstraeten[1,2], Wim Duthoy[2], Werner De Gersem[2], Wilfried De Neve[2], Hubert Thierens[1]

[1] *Department of Medical Physics, Ghent University, Gent, Belgium*

[2] *Department of Radiotherapy, Ghent University Hospital, Gent, Belgium*

Radiotherapy and Oncology 2006;79:249-258

Abstract

Background and purpose: Focused dose escalation may improve local control in head and neck cancer. Planning results of [^{18}F]fluoro-deoxy-glucose positron emission tomography ([^{18}F]FDG-PET) voxel intensity-based intensity-modulated radiation therapy (IMRT) were compared with those of PET contour-based IMRT.

Patients and methods: PET contour-based IMRT aims to deliver a homogeneous boost dose to a PET-based subvolume of the planning target volume (PTV), called PTV_{PET}. The present PET voxel intensity-based planning study aims to prescribe the boost dose directly as a function of PET voxel intensity values, while leaving the dose distribution outside the PTV unchanged. Two escalation steps (2.5 and 3 Gy/fraction) were performed for 15 patients.

Results: PTV_{PET} was irradiated with a homogeneous dose in the contour-based approach. In the voxel intensity-based approach, one or more sharp dose peaks were created inside the PTV, following the distribution of PET voxel intensity values.

Conclusions: While PET voxel intensity-based IMRT had a large effect on the dose distribution within the PTV, only small effects were observed on the dose distribution outside this PTV and on the dose delivered to the organs at risk. Therefore both methods are alternatives for boosting subvolumes inside a selected PTV.

Keywords: [^{18}F]FDG-PET; Voxel intensity; IMRT; Optimization; Head and neck cancer

Highly structured dose distributions can be delivered using intensity-modulated radiation therapy (IMRT), which serves two purposes. Firstly, IMRT can reduce toxicity by allowing a selective reduction of the dose to organs at risk (OARs). With regard to head and neck cancer, results of case series indeed suggest that conformal avoidance of radiosensitive structures like parotid or lacrimal glands, optic or auditory pathways has resulted in less morbidity [8,23,33]. Secondly, by reducing the dose to critical organs relative to the tumour prescription dose, IMRT techniques also allow dose escalation with the aim to improve local control. The target for dose escalation is mainly the gross tumour volume (GTV) [7,15]. Since [^{18}F]fluoro-deoxy-glucose positron emission tomography ([^{18}F]FDG-PET) exhibits a higher accuracy for GTV delineation than magnetic resonance imaging (MRI) or computed tomography (CT) [13], it is the preferred modality for defining the boost volume. In a phase I trial that is currently conducted at our institution, the boost dose is prescribed medianly to an automatically delineated PET-lesion [12]. The resulting dose distributions were used as a reference for the present planning study, in which the boost dose was not prescribed to a contoured volume but directly as a function of PET voxel intensity values. The rationale for testing this approach is explained in the Discussion section. The purpose of our study was to investigate the feasibility of creating PET voxel intensity-based IMRT dose distributions in head and neck tumours for different levels of dose escalation, without compromising the planning constraints set for the OARs. Therefore, we have compared the dosimetric characteristics of conventional PET contour-based dose escalation with PET voxel intensity-based planning for 15 patients and two different escalation steps (2.5 and 3 Gy/fraction).

Materials and methods

Lay-out of the study

At Ghent University Hospital (GUH), IMRT is routinely performed to treat patients with laryngopharyngeal cancer. The total treatment consists of 32 fractions (fx). Multiple dose levels are delivered in a simultaneous integrated boost (SIB) approach [46]. Planning CT and PET scans are performed for each patient. Both are acquired in treatment position using a thermoplastic mask for immobilization and are fused manually using Pinnacle (Philips Medical Systems, Best, The Netherlands) [11]. GTV_{PET} is automatically segmented based on the source-to-background ratio following the method of Daisne et al. [12].

GTV$_{CT}$ is delineated based on the planning CT, supplemented with information from physical examination and complementary diagnostic imaging data (CT and/or MRI), but not PET. Lymph node regions (LNRs) are contoured seperately based on the guidelines of Grégoire et al. [27]. A primary CTV (pCTV) containing the microscopic extension locally around GTV$_{CT}$ is delineated manually based on the idea of compartmental tumour spread [24,29]. If necessary, this pCTV is extended manually to encompass GTV$_{PET}$. All CTV subvolumes (pCTV and all separate LNRs) are grouped according to the prescription dose levels in CTV$_{69+PET}$, CTV$_{66}$, CTV$_{62}$ and CTV$_{56}$. The grouping criteria are presented in Table 1.

Table 1. Fraction (fx) dose prescription levels for the PET contour-based phase I trial during the escalation phase and for both escalation steps of the PET voxel intensity-based planning study.

	Description	SIB(cb)$_{250}$ (cGy/fx)	SIB(vib)$_{216\text{-}250}$ (cGy/fx)	SIB(vib)$_{216\text{-}300}$ (cGy/fx)
PTV$_{PET}$	PET lesion	250		
PTV$_{69+PET}$	Macroscopic tumour + margin for microscopic disease		216 - 250	216 - 300
PTV$_{69}$	PTV$_{69+PET}$ - PTV$_{PET}$	216		
PTV$_{66}$	Resected lymph node regions (LNRs) with capsular rupture	206	206	206
PTV$_{62}$	Resected LNRs containing invaded lymph nodes without capsular rupture	194	194	194
PTV$_{56}$	Elective LNRs	175	175	175

PTV names and abbreviations are defined in the Lay-out of the study section. Fraction dose intervals are denoted with a hyphen.

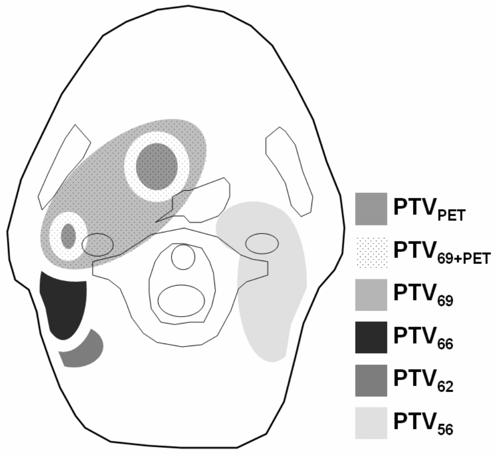

Figure 1. Illustration of a possible PTV configuration. Each PTV index refers to the total prescription dose in Gray. PTV$_{PET}$ is the PTV based on the automatically delineated PET-lesion. In this figure, it consists out of two separate subvolumes. For optimization purposes, each PTV stays away at least 6 mm from each PTV with a higher prescription dose and excludes a 6 mm-wide build-up region.

Planning target volumes (PTVs) are constructed by expanding each CTV with a 3 mm-margin to account for patient motion and set-up errors during treatment. PTV_{PET} is created by expanding GTV_{PET} with a 3 mm-margin. Moreover, each PTV is adjusted to avoid conflicts during optimization as we prioritize the highest dose prescription levels: for x>y, PTV_y is made to exclude PTV_x after expansion with a 6 mm-margin. All PTV's also exclude a 6 mm-wide build-up region. The procedures are described in detail elsewhere [20]. Fig. 1 schematically illustrates a possible PTV configuration.

The total treatment is divided in two phases of 10 and 22 fractions, respectively. During the escalation phase (fractions 1–10), the above-mentioned phase I trial prescribes a median dose of 250 cGy/fraction (cGy/fx) to PTV_{PET}, while PTV_{69} medianly receives 216 cGy/fx. During the second phase (fractions 11–32), 216 cGy/fx is delivered to the entire PTV_{69+PET} volume. This contour-based (cb) SIB technique will further be denoted as $SIB(cb)_{250}$, referring to the PTV_{PET} escalation dose. For this paper, the dose distribution obtained by $SIB(cb)_{250}$ during the escalation phase is used as the reference for a planning study in which PTV_{PET} was not used but in which the dose escalation was based directly on the PET voxel intensity values within PTV_{69+PET}. As the prescribed dose levels within PTV_{69+PET} range between 216 and 250 cGy/fx or 300 cGy/fx, these planning studies are further denoted as $SIB(vib)_{216–250}$ and $SIB(vib)_{216–300}$ (vib stands for voxel intensity-based). Table 1 summarizes the prescription dose levels. Fig. 2 illustrates the principle of PET voxel intensity-based IMRT.

Planning objectives

For PET voxel intensity-based IMRT, the relationship between the wanted dose distribution and the voxel intensities (I) within PTV_{69+PET} has to be defined. Given the lack of detailed knowledge on the radiobiological meaning of the magnitude of the PET voxel intensities, we chose to implement a proportional relationship between voxel intensity and prescribed dose. This was also proposed by Das et al. [14]. Within PTV_{69+PET}, dose values increase linearly with voxel intensity between D_{low} and D_{high}, respectively, corresponding to I_{low} and I_{high}, and the prescribed dose D_I becomes:

$$D_I = D_{low} + \frac{I - I_{low}}{I_{high} - I_{low}}(D_{high} - D_{low}) \qquad (1)$$

The prescribed dose within PTV_{69+PET} voxels where $I \leq I_{low}$ is D_{low}, while D_{high} is the prescribed dose within PTV_{69+PET} voxels where $I \geq I_{high}$. To minimize the influence of PET signal noise on I_{low} and I_{high}, the dose was escalated between 25 and 100% of the 95th percentile PET voxel intensity value within $\mathrm{PTV}_{69+\mathrm{PET}}$ ($I_{95\%}$): $I_{\mathrm{low}}=0.25\times I_{95\%}$, $I_{\mathrm{high}}=I_{95\%}$.

PET voxel intensity-based plans were made for 15 patients of the phase I trial (four hypopharynx, five oropharynx, six larynx). For PTV_{56}, PTV_{62} and PTV_{66}, the partial volume receiving less than 95% of the pre-set median dose ($V_{<95\%}$) had to be less than 5%. For every patient the following set of OARs was delineated: spinal cord, brainstem, parotid glands and mandible. The spinal cord and the brainstem were expanded with margins of 5 and 3 mm, respectively. The partial volume of the expanded spinal cord receiving more than 50 Gy ($V_{>50\mathrm{Gy}}$) should not exceed 5%. For 10 out of the 15 patients sparing of the contralateral parotid gland was attempted (four left, six right) [4,42]. The median dose D_{med} within the spared parotid had to be less than 27 Gy. A surroundings-structure (surr) was created to avoid overdosage within otherwise unspecified tissues; it contains all points more than 20 mm away from PTV_{56} and more than 30 mm away from PTV_{69} [20].

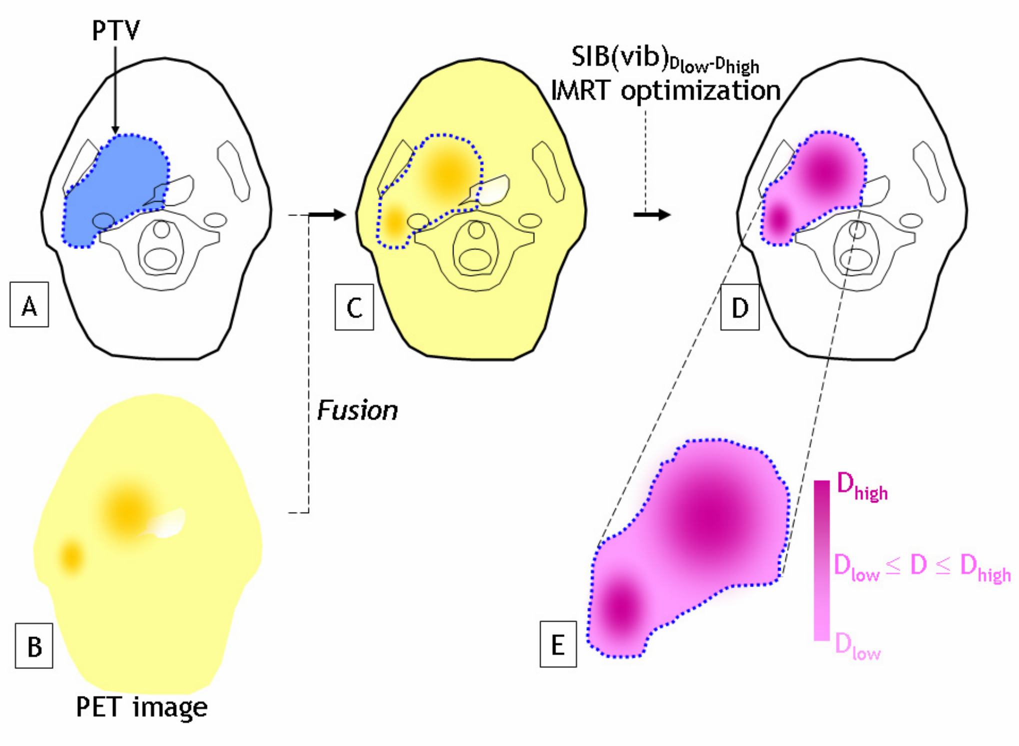

Figure 2. PET voxel intensity-based IMRT. (A) Anatomical PTV-definition is based on clinical examination, PET, CT and MRI imaging. (B) PET provides radiobiological data in the form of an intensity value within each image voxel that is proportional to a radiobiological parameter. (C) Fusing results in an image where each image voxel has a Hounsfield value (for computation of absorbed dose) and PET intensity value (for intra-tumour guidance of the dose distribution). (D) The PET voxel intensity-based IMRT optimization algorithm creates a spatial dose variation within the anatomical PTV (E), as a function of the voxel intensity values in the PET image. Abbreviations are defined in the Lay-out of the study and Planning objectives sections.

Modification to IMRT planning tools

IMRT treatment planning at GUH is based on class solutions and involves direct multi-leaf collimator (MLC) aperture optimization. In brief we start from a template beam set, which is characterized by each beam's isocenter, gantry, table and collimator angles, linear accelerator, radiation modality and energy. For every template beam initial beam segments are created by an in-house developed anatomy-based segmentation tool (ABST) based on one or more target structures, taking into account the presence of critical structures and the distance to the skin [17]. Once the initial set of segments is created, both segment weights and MLC leaf positions are optimized by the segment outline and weight adapting tool (SOWAT) [18]. The optimization uses a bio-physical objective function [18].

To implement the bound-constrained linear model of formula (1) into the IMRT planning strategy at GUH, two modifications were made to the planning tools. Firstly, ABST was adapted into a segmentation tool that also supports biological imaging information, called biology-based segmentation tool (BBST): by projecting voxel intensity data onto a combined anatomical-biological segmentation grid, the biological imaging information is already taken into account during the creation of the initial beam segments. Secondly, the bio-physical objective function of SOWAT was modified to minimize the difference between the actual (D) and intended dose distribution. The physical part of the objective function was extended by a term that minimizes the root mean square deviation between D and D_{I} in all dose calculation points within the target structure of interest (in this case $\mathrm{PTV}_{69+\mathrm{PET}}$).

Dose reporting and evaluation

For $\mathrm{PTV}_{69+\mathrm{PET}}$, the resulting dose distribution was compared to the intended voxel intensity-based dose pattern; therefore, a quality factor QF was introduced. In every point p that is randomly seeded within $\mathrm{PTV}_{69+\mathrm{PET}}$ (n points in total), the obtained-over-intended dose ratio $Q_{\mathrm{p}} = D_{\mathrm{p}}/(D_{\mathrm{I}})_{\mathrm{p}}$ is calculated. This information can be visualized in a Q-volume histogram (QVH), by displaying the partial $\mathrm{PTV}_{69+\mathrm{PET}}$ volume for which Q is greater than or equal to each abscis value. Ideally such a curve would drop down steeply at $Q = 1$. QF is defined as the mean absolute deviation of Q to 1 within $\mathrm{PTV}_{69+\mathrm{PET}}$:

$$QF = \frac{1}{n}\sum_{p}\left|Q_p - 1\right| \quad (2)$$

Dose-volume histograms (DVHs) and QVHs were computed for all individual patients. To compile the resulting curves over the whole patient group, the mean and the standard error of the mean (SEM) of the partial volume were calculated from the individual fraction dose-distributions for dose levels between 0 and 3.3 Gy in steps of 0.02 Gy for the DVHs and from the individual Q-distributions for Q-values between 0 and 1.2 in steps of 0.005 for the QVHs.

For each PTV the minimal, median and maximal dose levels (D_{min}, D_{med} and D_{max}), and $V_{<95\%}$ were evaluated. D_{min} and D_{max} are represented by the 98th and second dose percentile, respectively [46]. For the expanded spinal cord $V_{>50\mathrm{Gy}}$ and D_{max} were calculated, while for the parotid glands D_{med} and $V_{>27\mathrm{Gy}}$ are reported. For the spared parotid D_{mean} was calculated as well. $V_{>60\mathrm{Gy}}$ and D_{max} are reported for the mandible. For the expanded spinal cord and the mandible, D_{max} is also represented by the second dose percentile. Average dose-volumes values are reported as 95% confidence intervals; the half width of each interval is calculated as SEM × $t_{14,0.05}$, where $t_{14,0.05}$ represents the two-tailed t-value of the Student's t-distribution with 14 degrees of freedom for a probability of 5%. For all statistical comparisons a paired Student's t-test was used. All tests were two-tailed; P-values below 5% are considered significant.

Results

The 95% confidence intervals for the average $\mathrm{PTV}_{69+\mathrm{PET}}$ and $\mathrm{PTV}_{\mathrm{PET}}$ volumes were 194 ± 38 and 26 ± 10 cc, respectively. The volume of $\mathrm{PTV}_{\mathrm{PET}}$ was 13 ± 4% of the volume of $\mathrm{PTV}_{69+\mathrm{PET}}$. The largest $\mathrm{PTV}_{69+\mathrm{PET}}$ volume recorded was 286 cc, while the smallest volume was 66 cc. For $\mathrm{PTV}_{\mathrm{PET}}$ these volumes were 63 and 4 cc, respectively. The partial volume of $\mathrm{PTV}_{69+\mathrm{PET}}$ with PET intensity values $I \geq I_{\mathrm{low}}$ was 94 ± 33 cc or 52 ± 17% of the volume of $\mathrm{PTV}_{69+\mathrm{PET}}$. For I_{high}, this volume was 10 ± 2 cc or 5 ± 0% of the volume of $\mathrm{PTV}_{69+\mathrm{PET}}$, by definition of I_{high} as the 95th percentile intensity value within $\mathrm{PTV}_{69+\mathrm{PET}}$. Thus, the voxel intensity-based dose escalation was performed over 85 ± 32 cc or 47 ± 17% of the volume of $\mathrm{PTV}_{69+\mathrm{PET}}$.

Fig. 3 shows the compiled dose-volume histograms for the PET contour-based SIB plans ($\mathrm{SIB(cb)}_{250}$) and the PET voxel intensity-based SIB plans for both escalation steps ($\mathrm{SIB(vib)}_{216\text{–}250}$ and $\mathrm{SIB(vib)}_{216\text{–}300}$). The clinically relevant dose–volume characteristics are reported in Table 2. For all patients the OAR planning dose objectives stated in the Planning objectives section were reached. However, there was a significant difference between the $D_{\max}$-values delivered to the expanded spinal cord by SIB(cb)$_{250}$ and SIB(vib)$_{216\text{-}250}$. Both the maximal dose and $V_{>50\mathrm{Gy}}$ differed significantly between both PET voxel intensity-based plans. Additionally, the median dose within the spared parotid gland was significantly higher for SIB(vib)$_{216\text{-}300}$ than for SIB(vib)$_{216\text{-}250}$, while $V_{>27\mathrm{Gy}}$ was significantly higher for SIB(vib)$_{216\text{-}300}$ than for SIB(cb)$_{250}$. Whereas $V_{>60\mathrm{Gy}}$ within the mandible was not significantly different between both PET voxel intensity-based planning studies, its value was significantly lower for the PET contour-based SIB plans. Both $V_{>60\mathrm{Gy}}$ and $D_{\max}$ within the mandible were significantly higher for SIB(vib)$_{216\text{-}300}$ than for SIB(cb)$_{250}$.

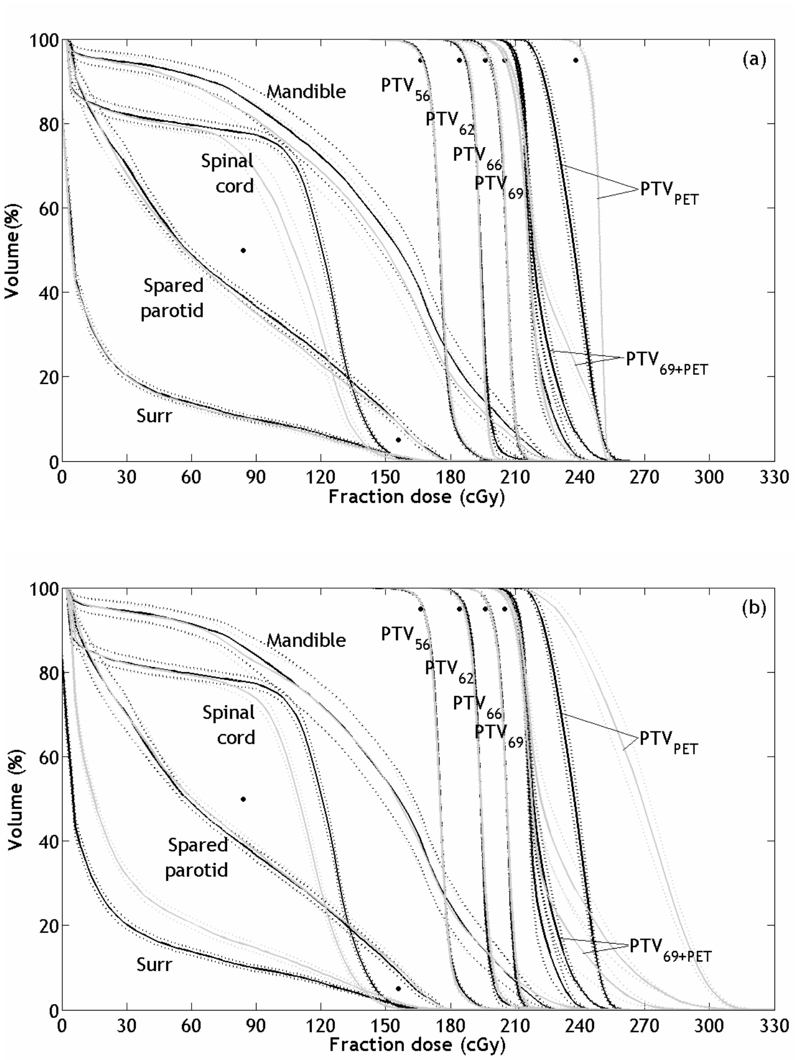

Fig. 3. Comparison of the compiled dose-volume histograms for (a): SIB(cb)$_{250}$ (grey) and SIB(vib)$_{216\text{-}250}$ (black), and (b): SIB(vib)$_{216\text{-}300}$ (grey) and SIB(vib)$_{216\text{-}250}$ (black). For each structure, the mean relative volume (solid line) ± the SEM (dotted lines) is represented. SD = 3.87 × SEM. The single dots represent the target underdosage limitations and OAR planning constraints stated in the Planning objectives section. PTV names are defined in the Lay-out of the study section and in Table 1. The DVHs for PTV$_{66}$ and PTV$_{62}$ are compiled from the six and four patients, respectively, for whom these target dose levels were prescribed. In 10 patients sparing of a parotid gland was attempted; their data are compiled into the spared parotid DVH. The spinal cord DVH is shown for the 5 mm-expanded structure.

Table 2. Clinically relevant dose-volume statistics for SIB(cb)$_{250}$, SIB(vib)$_{216–250}$, SIB(vib)$_{216–300}$.

	SIB(cb)$_{250}$ (a)	P-value (a)-(b)	SIB(vib)$_{216-250}$ (b)	P-value (b)-(c)	SIB(vib)$_{216-300}$ (c)	P-value (a)-(c)
PTV$_{PET}$						
D_{min} (Gy)	77.3 ± 0.7	**< 0.001**	71.3 ± 1.2	**< 0.001**	75.5 ± 2.9	0.177
D_{med} (Gy)	79.6 ± 0.1	**< 0.001**	75.5 ± 1.0	**< 0.001**	84.9 ± 2.3	**< 0.001**
D_{max} (Gy)	80.9 ± 0.2	0.554	80.8 ± 0.5	**< 0.001**	97.2 ± 1.1	**< 0.001**
PTV$_{69+PET}$						
D_{min} (Gy)	65.2 ± 0.4	**< 0.001**	67.0 ± 0.5	**0.001**	66.5 ± 0.7	**0.003**
D_{med} (Gy)	71.0 ± 1.2	0.402	70.3 ± 0.9	**0.010**	72.2 ± 2.2	0.421
D_{max} (Gy)	80.3 ± 0.3	**< 0.001**	78.5 ± 0.2	**< 0.001**	91.6 ± 0.6	**< 0.001**
$V_{<95}$%[a] (%)	3.2 ± 1.0	**< 0.001**	0.5 ± 0.2	**< 0.001**	1.2 ± 0.5	**0.003**
PTV$_{69}$						
D_{min} (Gy)	64.8 ± 0.5	**< 0.001**	66.7 ± 0.5	**0.001**	66.2 ± 0.7	**0.001**
D_{med} (Gy)	69.3 ± 0.3	0.228	69.9 ± 0.8	**0.024**	71.3 ± 2.1	0.068
D_{max} (Gy)	74.1 ± 1.0	0.140	72.7 ± 1.6	**0.001**	77.3 ± 4.0	0.130
$V_{<95}$%* (%)	4.7 ± 1.2	**< 0.001**	0.7 ± 0.3	**0.004**	2.0 ± 1.1	**0.003**
PTV$_{66}$						
D_{min} (Gy)	62.5 ± 2.0	0.984	62.5 ± 0.7	0.480	62.6 ± 0.7	0.898
D_{med} (Gy)	65.9 ± 0.2	0.824	65.9 ± 0.1	0.347	65.9 ± 0.1	0.581
D_{max} (Gy)	68.1 ± 0.9	0.937	68.1 ± 0.6	0.112	68.4 ± 0.8	0.574
$V_{<95}$% (%)	2.9 ± 4.0	0.718	2.2 ± 1.6	0.898	2.2 ± 1.1	0.648
PTV$_{62}$						
D_{min} (Gy)	59.4 ± 1.3	0.141	58.8 ± 0.7	0.829	58.8 ± 1.3	0.219
D_{med} (Gy)	61.9 ± 0.1	**0.039**	62.0 ± 0.0	0.529	62.1 ± 0.2	0.148
D_{max} (Gy)	63.9 ± 0.7	0.184	65.3 ± 2.4	0.416	65.8 ± 3.3	0.187
$V_{<95}$% (%)	1.5 ± 2.0	0.208	2.2 ± 1.1	0.434	2.5 ± 2.4	0.172
PTV$_{56}$						
D_{min} (Gy)	52.3 ± 0.6	0.191	52.5 ± 0.5	0.154	52.7 ± 0.3	0.063
D_{med} (Gy)	56.1 ± 0.1	0.053	56.0 ± 0.1	**0.044**	56.0 ± 0.0	**0.013**
D_{max} (Gy)	60.5 ± 0.8	0.577	60.7 ± 0.6	**0.001**	60.1 ± 0.7	0.367
$V_{<95}$% (%)	4.0 ± 1.3	0.150	3.4 ± 0.9	0.669	3.3 ± 0.7	0.106
Spinal cord						
$V_{>50Gy}$ (%)	0.3 ± 0.3	0.051	0.7 ± 0.4	**0.004**	0.2 ± 0.3	0.706
D_{max} (Gy)	44.4 ± 2.1	**0.002**	48.1 ± 0.8	**< 0.001**	46.2 ± 1.1	0.098
Spared parotid gland						
D_{med} (Gy)	18.1 ± 3.4	0.898	18.2 ± 2.5	**0.044**	19.1 ± 2.9	0.189
D_{mean} (Gy)	21.9 ± 1.9	0.212	22.5 ± 1.7	0.197	22.8 ± 1.9	0.098
$V_{>27Gy}$ (%)	37.2 ± 4.4	0.111	38.8 ± 3.2	0.183	39.8 ± 3.7	**0.013**
Unspared parotid gland(s)						
D_{med} (Gy)	54.1 ± 4.0	0.206	55.6 ± 4.6	0.479	56.1 ± 4.4	0.119
$V_{>27Gy}$ (%)	86.6 ± 8.7	0.223	88.4 ± 8.8	0.520	88.0 ± 8.7	0.351
Mandible						
$V_{>60Gy}$ (%)	15.8 ± 10.1	**0.005**	19.0 ± 11.0	0.417	18.6 ± 11.4	**0.031**
D_{max} (Gy)	64.6 ± 3.0	0.127	65.8 ± 3.3	0.076	66.8 ± 4.0	**0.030**

PTV names are defined in *Lay-out of the study* and in Table 1. All fraction dose characteristics were rescaled, i.e. multiplied by 32, because in IMRT treatments that consist of two consecutive phases, the 1st phase is planned to the total number of fractions in order to secure enough sparing of the OARs to make the planning of the 2nd phase technically possible. By rescaling, the critical absolute dose levels for the expanded spinal cord and parotid gland stated in *Planning objectives* can be maintained. D_{min} and D_{max} are represented by the 98th and 2nd dose percentile, respectively. The spinal cord data is reported for the 5 mm-expanded structure. The average dose–volume characteristics are presented as 95% confidence intervals. For all statistical comparisons, a paired Student's *t*-testwas used; *P*-values < 5% (bold) are considered significant.

[a] For SIB(vib) $V_{<0.95 \times 69Gy}$ was considered instead of $V_{<95\%}$.

The target underdosage limitation was not always respected. For SIB(vib)$_{216\text{–}250}$ the $V_{<95\%}$-values within PTV$_{56}$ were 5.6 and 5.3% for two patients; for SIB(vib)$_{216\text{–}300}$ this value was 5.0% for one patient. In all other PTVs, the underdosage constraint was met for all patients. For SIB(cb)$_{250}$, $V_{<95\%}$ was higher than 5% for one patient within PTV$_{\mathrm{PET}}$ (5.5%), for eight patients within PTV$_{69}$ (5.0, 5.5, 5.9, 5.9, 6.1, 6.1, 6.7 and 8.6%), for two patients within PTV$_{66}$ (6.1 and 9.2%) and for six patients within PTV$_{56}$ (5.5, 5.8, 5.9, 6.1, 6.4 and 8.6%). Due to the differences in escalation strategy, comparing the dose–volume characteristics of SIB(cb)$_{250}$, SIB(vib)$_{216\text{–}250}$ and SIB(vib)$_{216\text{–}300}$ showed significant differences for PTV$_{\mathrm{PET}}$, PTV$_{69+\mathrm{PET}}$ and PTV$_{69}$. Additionally, the median dose within PTV$_{62}$ was significantly different between SIB(cb)$_{250}$ and SIB(vib)$_{216\text{–}250}$, while both the median and maximal dose within PTV$_{56}$ were significantly different between SIB(vib)$_{216\text{–}250}$ and SIB(vib)$_{216\text{–}300}$. D_{med} within PTV$_{56}$ was also significantly different between SIB(vib)$_{216\text{–}300}$ and SIB(cb)$_{250}$.

For individual patients, substantial differences between the performance of each planning approach on the fields of target coverage and OAR sparing were observed. However, there was no patient for which either the voxel intensity-based or contour-based approach could provide superior results similarly on both fields: voxel intensity-based IMRT tends to perform better within the target structures, while contour-based IMRT tends to realize better OAR sparing.

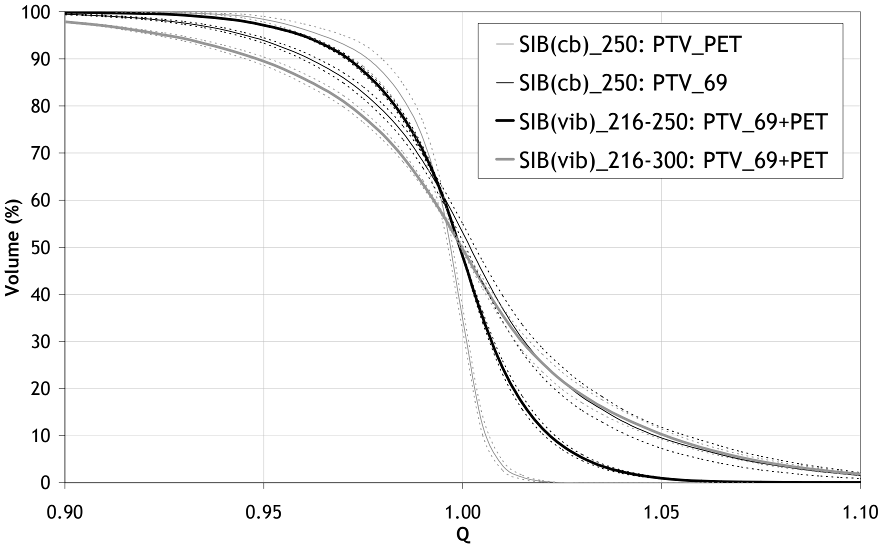

Figure 4. **Compiled Q-volume histograms for SIB(vib)$_{216\text{–}250}$ and SIB(vib)$_{216\text{–}300}$ (PTV$_{69+\mathrm{PET}}$) and for SIB(cb)$_{250}$ (PTV$_{\mathrm{PET}}$ and PTV$_{69}$). The mean relative volume (solid line) ± the SEM (dotted lines) is represented. SD = 3.87 × SEM. PTV names are defined in the Lay-out of the study section and in Table 1. Note the scale on the Q-axis (0.9–1.1).**

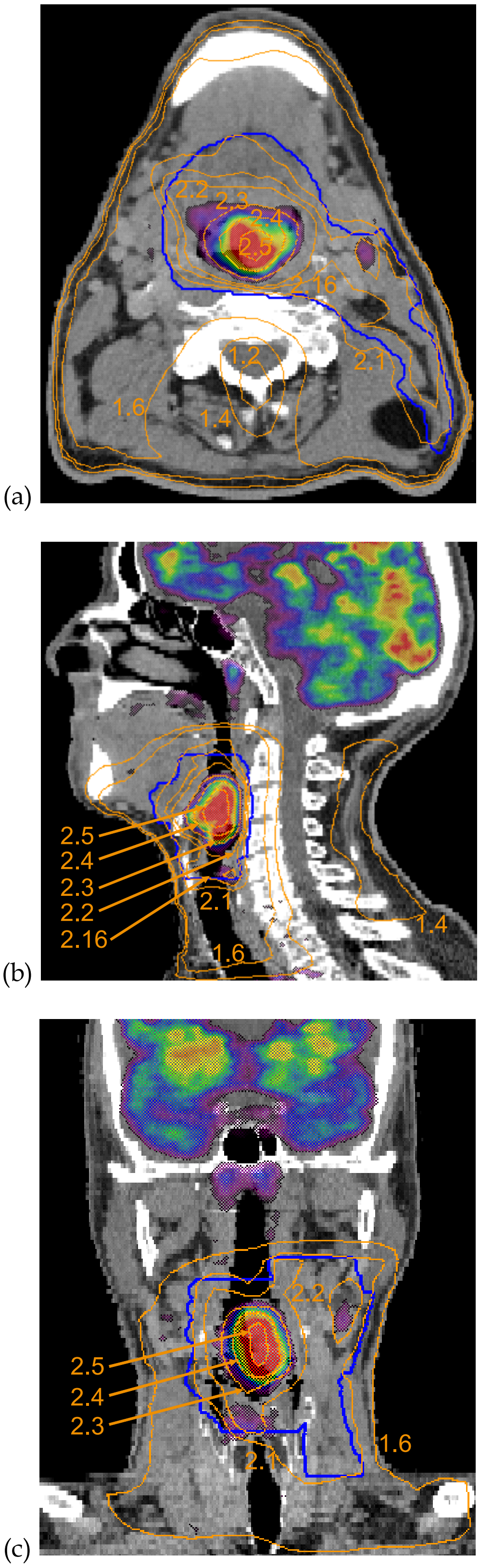

Fig. 5. Fraction dose (Gy/fx) distribution of SIB(vib)$_{216\text{-}250}$ for one patient case, superimposed on the original PET voxel intensity data. The bold blue line contours PTV$_{69\text{+PET}}$. Abbreviations are defined in the Lay-out of the study section. (a) Transverse slice. (b) Sagittal slice. (c) Coronal slice.

To evaluate the difference between the intended dose distribution and the obtained dose values within PTV_{69+PET}, Fig. 4 shows the compiled QVHs for $SIB(vib)_{216-250}$ and $SIB(vib)_{216-300}$. Fig. 5 illustrates the fraction dose distribution resulting from the PET voxel intensity-based optimization superimposed on the original PET voxel intensity data for one patient case. *Q*-values can be determined for $SIB(cb)_{250}$ as well: for each voxel within an optimization target structure *Q* can be calculated as the ratio of the obtained over the homogeneously prescribed dose; the compiled QVHs of PTV_{PET} and PTV_{69} are also shown in Fig. 4. The 95% confidence interval for the average QF-value for $SIB(vib)_{216-250}$ was 1.6 ± 0.1%; for $SIB(vib)_{216-300}$ it was 3.1 ± 0.4%. The lowest value for $SIB(vib)_{216-250}$ was 1.2%, while the highest value was 2.0%. For $SIB(vib)_{216-300}$ these values were 2.2 and 4.3%, respectively. For $SIB(cb)_{250}$ the mean QF-value within PTV_{PET} was 0.9 ± 0.3%, with values ranging between 0.3 and 1.6%. Within PTV_{69} QF was 2.6 ± 0.5%; the minimum value was 1.3%, while the maximum value was 4.6%. Apart from the comparison of the average QF-value between PTV_{69} for $SIB(cb)_{250}$ and PTV_{69CPET} for $SIB(vib)_{216-250}$ (P = 0.220), paired *t*-tests showed all mean QF-values to be significantly different ($P \leq 0.001$). However, when the QF-values for $SIB(cb)_{250}$ were averaged over PTV_{PET} and PTV_{69}, there was no significant difference with the mean QF-value of $SIB(vib)_{216-250}$ (P = 0.122).

Discussion

For head and neck cancer, IMRT can be used to lower the dose to selected organs at risk outside the PTV, thereby opening a window for dose escalation [25,36,37]. If the surrounding organs are not dose-limiting, the maximal dose escalation becomes restricted by the presence of dose-limiting structures within the PTV, such as cartilage, connective tissues, nerve tissues, bone, the swallowing apparatus or the lymphatic system [19]. We therefore hypothesize that, in this situation, a dose escalation should be focused to small subvolumes of the PTV. This hypothesis is supported by theoretical considerations, suggesting that focused dose escalation may improve local control [38]. Furthermore, the feasibility and safety of dose escalation to small volumes has been demonstrated for certain tumour sites using brachytherapy boosts [21,41], stereotactic surgery boosts [43] and IMRT SIB techniques. These techniques deliver a high dose to the GTV and a lower dose to subclinical disease with acceptable toxicity if the boost volume is kept small [46].

To improve local control by reducing the occurrence of loco-regional relapses within the high-dose regions, we may need to identify the most radioresistant regions inside the tumour [7]. It appears obvious to direct foci of dose escalation towards these regions. New biological imaging techniques, mainly based on PET, MRI and magnetic resonance spectroscopy (MRS) imaging, may be used to create three-dimensional maps of radiobiologically relevant parameters [6,35,44]. These maps can be fused with high-resolution CT and MRI images and used for treatment design and optimization with a small-volume, focused dose escalation strategy. Imaging techniques that can be used to map radiation resistant regions using specific tracers for hypoxia, proliferation or intrinsic radioresistance are still the subject of intense research. Recent publications have addressed the increased importance of PET in radiotherapy [28]. Results have been reported on the use of [^{18}F]FDG-PET for target volume definition in the treatment planning process of non-small cell lung cancer [22,30,32], thoracic lymphoma [34] and esophageal carcinoma [45], the use of ^{18}F-fluoromisonidazole PET to assess hypoxia in human soft tissue tumours [2] and the use of ^{11}C-methionine PET to delineate the tumour volume in pharyngolaryngeal squamous cell carcinoma and to address the salivary gland function after radiotherapy [5,26]. At present, [^{18}F]FDG-PET is routinely available and is—at first order—of interest for focused dose escalation. For pharyngolaryngeal squamous cell carcinoma, [^{18}F]FDG-PET defines a much smaller target volume than CT or MRI imaging, and comparison with macroscopic surgical specimens has shown PET to be the most accurate modality for GTV definition [13]. Inside a contoured PTV, the GTV is known to be the region in which local control is most difficult to achieve.

Although care should be taken as FDG-PET may not detect highly hypoxic/necrotic centers in tumours, evidence that FDG-avid regions of the tumour are of increased radioresistance is provided by in vitro and in vivo studies correlating cellular or regional FDG uptake with hypoxia. Clavo et al. [9,10] as well as Burgman et al. [3] have reported increased cellular uptake of FDG under hypoxic conditions in vitro. Positive correlation of FDG uptake and hypoxia was also observed in vivo by Dearling et al. [16], who reported increased FDG uptake in the hypoxic regions of the tumour compared to the normoxic regions. Using Dunning prostate tumours implanted in nude mice, Pugachev et al. observed that FDG uptake was highly correlated with regions of intense pimonidazole staining, the latter being a tracer of hypoxia [39]. In human patients, Rajendran et al. observed highly significant positive pixel-by-pixel correlations between PET images of FDG uptake and of the tracer of hypoxia [^{18}F]fluoromisonidazole, with the value of the correlation coefficient being highest for head and neck tumours [40]. Hypoxia-inducible factor 1-alpha (HIF-1alpha) may be involved in the mechanism of increased FDG uptake in hypoxic regions by increasing the expression levels of the glucose transporters Glut-1, Glut-3, and hexokinase-II (HK-II) that carry FDG in the cells [47].

The proportionality of the intensity-dose relationship in the PET voxel intensity-based planning studies is based on the assumption that voxels with a higher PET intensity require a higher dose. This technique hypothetically offers the possibility of improved local control by focusing dose to the most radiation resistant regions within the tumour. Of course, decisive answers can only be provided after extensive evaluation of clinical results. Individual tumour data showing that regions with the highest FDG uptake are the most radioresistant are inexistent, but indirect evidence has been given by Kitagawa et al. [31] and Allal et al. [1], who reported that head and neck cancer patients who show a high pre-radiotherapy uptake of FDG in the tumour are characterized by worse local control than the patients with a lower uptake. A linear relationship is merely the most straightforward way of expressing the demand for a monotonically increasing function, since the function relating PET-activity to tumour proliferation rate and radiosensitivity is currently unknown. The same relationship is used by Das et al. [14] for lung cancer.

When defining I_{low} and I_{high}, our main concern was to prevent the noisy background signal from affecting the escalation dose prescription, while maintaining a maximal range for dose escalation. With regard to the choice of I_{high}, the 95th percentile value of the PET voxel intensities within $\text{PTV}_{69+\text{PET}}$ was therefore considered instead of the maximal intensity value. Looking at the PET intensity maps in a number of patients, we chose $I_{\text{low}} = 0.25 \times I_{\text{high}}$ as this seemed to do well in eliminating most background noise. However, we need to emphasize the arbitrariness of this decision. An equally arbitrary choice would have been to take a separate percentile value for I_{low}, as was done for example by Das et al. [14], who took the 25th and 75th percentile PET activity values within the PTV as I_{low} and I_{high}. In this case dose is always escalated over exactly 50% of the PTV volume, while $I_{\text{low}} = 0.25 \times I_{\text{high}}$ will focus dose escalation to smaller volumes in case of more pronounced intensity peaks. Although it is clear that the volume for dose escalation depends strongly on the choice of I_{low}, it is uncertain which is the better option. Moreover, in both cases the PTV volume plays a role in determining the volume for dose escalation, while we actually want to achieve independency of the voxel intensity-based dose escalation from manually delineated target structures. For most of the patients in our study low PET intensity values represent the majority of the target volume: their PET images are characterized by one or more relatively high but narrow intensity peaks.

To evaluate the impact of voxel intensity-based IMRT, SIB(cb)$_{250}$ planning results were compared with those for SIB(vib)$_{216-250}$. From Fig. 3 the difference in dosimetric characteristics is apparent. SIB(cb) aims to achieve homogeneous dose distributions within PTV$_{\mathrm{PET}}$ and PTV$_{69}$. The dose distribution within PTV$_{69+\mathrm{PET}}$ is inevitably inhomogeneous, since the dose values vary between both intended median dose levels. In contrast, the planning dose objective in the SIB(vib) approach was to obtain a boost-dose distribution that directly reflects PET voxel intensity values within PTV$_{69+\mathrm{PET}}$, resulting in intended inhomogeneous dose distributions within both substructures PTV$_{\mathrm{PET}}$ and PTV$_{69}$. This intended inhomogeneity is fundamentally different from the inevitable inhomogeneity within PTV$_{69+\mathrm{PET}}$ for SIB(cb). The shape of the compiled PTV$_{69+\mathrm{PET}}$ DVH in Fig. 3 for SIB(vib) illustrates that the distribution of PET voxel intensities throughout PTV$_{69+\mathrm{PET}}$ is highly non-linear; otherwise, the relative PTV$_{69+\mathrm{PET}}$ volume would decrease linearly as a function of dose between D_{low} and D_{high} due to the implemented proportional voxel intensity-dose relationship. Table 2 reports a significant difference between the $V_{<95\%}$-values within PTV$_{69+\mathrm{PET}}$ and PTV$_{69}$ of SIB(cb)$_{250}$, SIB(vib)$_{216-250}$ and SIB(vib)$_{216-300}$. Indeed, the voxel intensity-based IMRT optimization algorithm inherently limits underdosage by minimizing the difference between actual and intended dose values in each voxel within PTV$_{69+\mathrm{PET}}$. The clinical importance of this difference in $V_{<95\%}$-value is unknown. In any case, the voxel intensity-based approach is more suitable to create peak-dose regions inside PTV$_{69+\mathrm{PET}}$ compared to the contour-based approach.

The comparison between SIB(vib)$_{216-250}$ and SIB(vib)$_{216-300}$ illustrates the dosimetric changes accompanying a higher dose escalation level. By increasing D_{high}, steeper dose gradients are imposed on PTV$_{69+\mathrm{PET}}$. This more complex prescribed dose pattern results in significantly more underdosage within PTV$_{69+\mathrm{PET}}$ and PTV$_{69}$. Moreover, Fig. 4 clearly shows that the agreement between the prescribed dose pattern and the obtained dose distribution becomes significantly worse if D_{high} is raised. The maximal steepness of deliverable dose gradients is limited by the penumbra width of the beam segments. This depends on the design of the linear accelerator's treatment head and on the field shape of the individual MLC segments.

Voxel intensity-based IMRT optimization results in a dose distribution that is modulated within $\mathrm{PTV}_{69+\mathrm{PET}}$. Therefore patient motion may seriously affect the tumour dose. However, motion is usually limited in head and neck tumours. Moreover, for the treatment of head and neck cancer patients at GUH all images needed for the planning are acquired in treatment position, while a thermoplastic mask is used to immobilize the patient. The purpose of the current treatment planning study was to evaluate the dosimetric characteristics of voxel intensity-based IMRT plans. Therefore, motion issues are not addressed in-depth in this paper. However, it remains important to notice not only possible treatment problems due to patient motion, but also due to shrinkage of the tumour volume during treatment. Solutions for the last problem can only be provided by non-rigid coregistration of pre- and during-treatment images, which enables us to track the location of the image voxels. This may result in tumour regression models, which can be taken into account by the optimization engine as well.

In conclusion, PET voxel intensity-based IMRT may aid to improve local control in head and neck cancer by focusing dose escalation to the most radioresistant subvolumes within the tumour. The hypothesis that tumour regions with the highest FDG uptake are the most radioresistant can only be confirmed by clinical results; this paper provides the necessary planning technology and a comprehensive set of patient data as an important and necessary step in the process of clinical implementation. The dosimetric characteristics of the contour-based and voxel intensity-based simultaneous integrated boost plans differ fundamentally. While the voxel intensity-based strategy has a large effect on the dose distribution inside $\mathrm{PTV}_{69+\mathrm{PET}}$, only small effects were observed on the dose distribution outside $\mathrm{PTV}_{69+\mathrm{PET}}$ and on the dose delivered to the organs at risk. For all patients both the contour-based and voxel intensity-based plans comply with the planning constraints set for the organs at risk, and are therefore considered clinically acceptable. Thus, both methods are alternatives for boosting subvolumes inside a selected PTV.

Acknowledgements

Wim Duthoy and Barbara Vanderstraeten are Research Assistants of the Research Foundation—Flanders (FWO—Vlaanderen). The project 'Conformal Radiotherapy Ghent University Hospital' is supported by the Belgische Federatie tegen Kanker (grants 51AC8904, FBC2003/2006 and ZKB2747) and by grants from the Research Foundation—Flanders (G.0183.03), Ghent University (GOA 12050401, BOF 01112300, 011VO497, 011B3300), and the Centrum voor Studie en Behandeling van Gezwelziekten.

References

[1] Allal AS, Slosman DO, Kebdani T, Allaoua M, Lehmann W, Dulguerov P. Prediction of outcome in head-and-neck cancer patients using the standardized uptake value of 2-[^{18}F]Fluoro-2-Deoxy-D-Glucose. Int J Radiat Oncol Biol Phys 2004;59:1295–300.

[2] Bentzen L, Keiding S, Nordsmark M, et al. Tumour oxygenation assessed by ^{18}F-fluoromisonidazole PET and polarographic needle electrodes in human soft tissue tumours. Radiother Oncol 2003;67:339–44.

[3] Burgman P, O'Donoghue JA, Humm JL, Ling CC. Hypoxia-induced increase in FDG uptake in MCF7 cells. J Nucl Med 2001;42:170–5.

[4] Bussels B, Maes A, Hermans R, Nuyts S, Weltens C, Van den Bogaert W. Recurrences after conformal parotid-sparing radiotherapy for head and neck cancer. Radiother Oncol 2004;72:119–27.

[5] Buus S, Grau C, Munk OL, Bender D, Jensen K, Keiding S. ^{11}C-methionine PET, a novel method for measuring regional salivary gland function after radiotherapy of head and neck cancer. Radiother Oncol 2004;73:289–96.

[6] Chao KS, Bosch WR, Mutic S, et al. A novel approach to overcome hypoxic tumour resistance: Cu-ATSM-guided intensity-modulated radiation therapy. Int J Radiat Oncol Biol Phys 2001;49:1171–82.

[7] Chao KS, Ozyigit G, Tran BN, Cengiz M, Dempsey JF, Low DA. Patterns of failure in patients receiving definitive and postoperative IMRT for head-and-neck cancer. Int J Radiat Oncol Biol Phys 2003;55:312–21.

[8] Claus F, De Gersem W, De Wagter C, et al. An implementation strategy for IMRT of ethmoid sinus cancer with bilateral sparing of the optic pathways. Int J Radiat Oncol Biol Phys 2001;51:318–31.

[9] Clavo AC, Brown RS, Wahl RL. Fluorodeoxyglucose uptake in human cancer cell lines is increased by hypoxia. J Nucl Med 1995;36:1625–32.

[10] Clavo AC, Wahl RL. Effects of hypoxia on the uptake of tritiated thymidine, L-leucine, L-methionine, and FDG in cultured cancer cells. J Nucl Med 1996;37:502–6.

[11] Daisne JF, Sibomana M, Bol A, Cosnard G, Lonneux M, Grégoire V. Evaluation of a multimodality image (CT, MRI and PET) coregistration procedure on phantom and head and neck cancer patients: accuracy, reproducibility and consistency. Radiother Oncol 2003;69:237–45.

[12] Daisne JF, Sibomana M, Bol A, Doumont T, Lonneux M, Grégoire V. Tri-dimensional automatic segmentation of PET volumes based on measured source-to-background ratios: influence of reconstruction algorithms. Radiother Oncol 2003;69:247–50.

[13] Daisne JF, Duprez T, Weynand B, et al. Tumour volume in pharyngolaryngeal squamous cell carcinoma: comparison at CT, MR Imaging, and FDG PET and validation with surgical specimen. Radiology 2004;233:93–100.

[14] Das SK, Miften MM, Zhou S, et al. Feasibility of optimizing the dose distribution in lung tumours using fluorine-18-fluorodeoxyglucose positron emission tomography and single photon emission computed tomography guided dose prescriptions. Med Phys 2004;31:1452–61.

[15] Dawson L, Anzai Y, Marsh L, et al. Patterns of loco-regional recurrence following parotid-sparing conformal and segmental intensity-modulated radiotherapy for head and neck cancer. Int J Radiat Oncol Biol Phys 2000;46:1117–26.

[16] Dearling JL, Flynn AA, Sutcliffe-Goulden J, et al. Analysis of the regional uptake of radiolabeled deoxyglucose analogs in human tumor xenografts. J Nucl Med 2004;45:101–7.

[17] De Gersem W, Claus F, De Wagter C, De Neve W. An anatomy-based beam segmentation tool for intensity-modulated radiation therapy and its application to head-and-neck cancer. Int J Radiat Oncol Biol Phys 2001;51:849–59.

[18] De Gersem W, Claus F, De Wagter C, Van Duyse B, De Neve W. Leaf position optimization for step-and-shoot IMRT. Int J Radiat Oncol Biol Phys 2001;51:1371–88.

[19] De Neve W, Duthoy W. Intensity-modulated radiation therapy for head and neck cancer. Expert Rev Anticancer Ther 2004;4:425–34.

[20] De Neve W, Wu Y, Ezzell G. Practical IMRT planning. In: Bortfeld T, Schmidt-Ullrich R, De Neve W, Wazer DE, editors. Image-Guided IMRT. Berlin: Springer; 2006. p. 49–54.

[21] DeNittis AS, Liu L, Rosenthal DI, Machtay M. Nasopharyngeal carcinoma treated with external radiotherapy, brachytherapy and concurrent/adjuvant chemotherapy. Am J Clin Oncol 2002;25:93–5.

[22] De Ruysscher D, Wanders S, Minken A, et al. Effects of radiotherapy planning with a dedicated combinded PET-CT-simulator of patients with non-small cell lung cancer on dose limiting normal tissues and radiation dose-escalation: a planning study. Radiother Oncol 2005;77:5–10.

[23] Eisbruch A, Ten Haken RK, Kim HM, Marsh LH, Ship JA. Dose, volume and function relationships in parotid salivary glands following conformal and intensity-modulated irradiation of head and neck cancer. Int J Radiat Oncol Biol Phys 1999;45:577–87.

[24] Eisbruch A, Foote R, O'Sullivan B, Beitler JJ, Vikram B. Intensity-modulated radiation therapy for head and neck cancer: emphasis on the selection and delineation of the targets. Semin Radiat Oncol 2002;12:238–49.

[25] Feng M, Jabbari S, Lin A, et al. Predictive factors of locoregional recurrences following parotid sparing intensity modulated or 3D conformal radiotherapy for head and neck cancer. Radiother Oncol 2005;77:32–8.

[26] Geets X, Daisne JF, Grégoire V, Hamoir M, Lonneux M. Role of 11-C-methionine positron emission tomography for the delineation of the tumor volume in pharyngo-laryngeal squamous cell carcinoma: comparison with FDG-PET and CT. Radiother Oncol 2004;71:267–73.

[27] Grégoire V, Coche E, Cosnard G, Hamoir M, Reychler H. Selection and delineation of lymph node target volumes in head and neck conformal radiotherapy. Proposal for standardizing terminology and procedure based on the surgical experience. Radiother Oncol 2000;56:135–50.

[28] Grégoire V. Is there any future in radiotherapy planning without the use of PET: unraveling the myth. Radiother Oncol 2004;73:261–3.

[29] Harnsberger HR, Willey RC. Handbook of head and neck imaging. 2nd ed. St Louis, MO: Mosby; 1995.

[30] Holloway CL, Robinson D, Murray B, et al. Results of a phase I study to dose escalate using intensity modulated radiotherapy guided by combined PET/CT imaging with induction chemotherapy for patients with non-small cell lung cancer. Radiother Oncol 2004;73:285–7.

[31] Kitagawa Y, Sano K, Nishizawa S, et al. FDG-PET for prediction of tumour aggressiveness and response to intra-arterial chemotherapy and radiotherapy in head and neck cancer. Eur J Nucl Med 2003;30:63–71.

[32] Lavrenkov K, Partridge M, Cook G, Brada M. Positron emission tomography for target volume definition in the treatment of non-small cell lung cancer. Radiother Oncol 2005;77:1–4.

[33] Lee N, Xia P, Quivey JM, et al. Intensity-modulated radiotherapy in the treatment of nasopharyngeal carcinoma: an update of the UCSF experience. Int J Radiat Oncol Biol Phys 2002;53:12–22.

[34] Lee YK, Cook G, Flower MA, et al. Addition of ^{18}F-FDG-PET scans to radiotherapy planning of thoracic lymphoma. Radiother Oncol 2004;73:277–83.

[35] Ling C, Humm J, Larson S, et al. Towards multidimensional radiotherapy (MD-CRT): biological imaging and biological conformality. Int J Radiat Oncol Biol Phys 2000;47:551–60.

[36] Longobardi B, De Martin E, Fiorino C, et al. Comparing 3DCRT and inversely optimized IMRT planning for head and neck cancer: equivalence between step-and-shoot and sliding window techniques. Radiother Oncol 2005;77:148–56.

[37] Miles EA, Clark CH, Guerrero Urbano MT, et al. The impact of introducing intensity modulated radiotherapy into routine clinical practice. Radiother Oncol 2005;77:241–6.

[38] Mohan R, Wu Q, Manning M, Schmidt-Ullrich R. Radiobiological considerations in the design of fractionation strategies for intensity-modulated radiation therapy of head and neck cancers. Int J Radiat Oncol Biol Phys 2000;46:619–30.

[39] Pugachev A, Ruan S, Carlin S, et al. Dependence of FDG uptake on tumor microenvironment. Int J Radiat Oncol Biol Phys 2005; 62:545–53.

[40] Rajendran JG, Mankoff DA, O'Sullivan F, et al. Hypoxia and glucose metabolism in malignant tumors. Evaluation by [^{18}F]fluoromisonidazole and [^{18}F]fluorodeoxyglucose positron emission tomography imaging. Clin Cancer Res 2004;10:2245–52.

[41] Rudoltz MS, Perkins RS, Luthmann RW, et al. High-dose-rate brachytherapy for primary carcinomas of the oral cavity and oropharynx. Laryngoscope 1999;109:1967–73.

[42] Saarilahti K, Kouri M, Collan J, et al. Intensity modulated radiotherapy for head and neck cancer: evidence for preserved salivary gland function. Radiother Oncol 2005;74:251–8.

[43] Tate DJ, Adler JR, Chang SD, et al. Stereotactic radiosurgical boost following radiotherapy in primary nasopharyngeal carcinoma: impact on local control. Int J Radiat Oncol Biol Phys 1999;45:915–21.

[44] Van de Wiele C, Lahorte C, Oyen W, et al. Nuclear medicine imaging to predict response to radiotherapy: a review. Int J Radiat Oncol Biol Phys 2003;55:5–15.

[45] Vrieze O, Haustermans K, De Wever W, et al. Is there a role for FGD-PET in radiotherapy planning in esophageal carcinoma? Radiother Oncol 2004;73:269–75.

[46] Wu Q, Mohan R, Morris M, Lauve A, Schmidt-Ullrich R. Simultaneous integrated boost intensity-modulated radiotherapy for locally advanced head-and-neck squamous cell carcinomas. I: dosimetric results. Int J Radiat Oncol Biol Phys 2003;56:573–85.

[47] Zhao S, Kuge Y, Mochizuki T, et al. Biologic correlates of intratumoral heterogeneity in ^{18}F-FDG distribution with regional expression of glucose transporters and hexokinase-II in experimental tumor. J Nucl Med 2005;46:675–82.

Chapter 5

Publication 3:

Accuracy of patient dose calculation for lung IMRT: A comparison of Monte Carlo, convolution/superposition, and pencil beam computations

Barbara Vanderstraeten[1,2], Nick Reynaert[1], Indira Madani[2], Leen Paelinck[2], Carlos De Wagter[2], Werner De Gersem[2], Wilfried De Neve[2], Hubert Thierens[1]

[1] *Department of Medical Physics, Ghent University, Gent, Belgium*

[2] *Department of Radiotherapy, Ghent University Hospital, Gent, Belgium*

Medical Physics 2006;33:3149-3158

Abstract

The accuracy of dose computation within the lungs depends strongly on the performance of the calculation algorithm in regions of electronic disequilibrium that arise near tissue inhomogeneities with large density variations. There is a lack of data evaluating the performance of highly developed analytical dose calculation algorithms compared to Monte Carlo computations in a clinical setting. We compared full Monte Carlo calculations (performed by our Monte Carlo dose engine MCDE) with two different commercial convolution/superposition (CS) implementations (Pinnacle-CS and Helax-TMS's collapsed cone model Helax-CC) and one pencil beam algorithm (Helax-TMS's pencil beam model Helax-PB) for 10 intensity modulated radiation therapy (IMRT) lung cancer patients. Treatment plans were created for two photon beam qualities (6 and 18 MV). For each dose calculation algorithm, patient, and beam quality, the following set of clinically relevant dose-volume values was reported: (i) minimal, median, and maximal dose (D_{min}, D_{50}, and D_{max}) for the gross tumor and planning target volumes (GTV and PTV); (ii) the volume of the lungs (excluding the GTV) receiving at least 20 and 30 Gy (V_{20} and V_{30}) and the mean lung dose; (iii) the 33rd percentile dose (D_{33}) and D_{max} delivered to the heart and the expanded esophagus; and (iv) D_{max} for the expanded spinal cord. Statistical analysis was performed by means of one-way analysis of variance for repeated measurements and Tukey pairwise comparison of means. Pinnacle-CS showed an excellent agreement with MCDE within the target structures, whereas the best correspondence for the organs at risk (OARs) was found between Helax-CC and MCDE. Results from Helax-PB were unsatisfying for both targets and OARs. Additionally, individual patient results were analyzed. Within the target structures, deviations above 5% were found in one patient for the comparison of MCDE and Helax-CC, while all differences between MCDE and Pinnacle-CS were below 5%. For both Pinnacle-CS and Helax-CC, deviations from MCDE above 5% were found within the OARs: within the lungs for two (6 MV) and six (18 MV) patients for Pinnacle-CS, and within other OARs for two patients for Helax-CC (for D_{max} of the heart and D_{33} of the expanded esophagus) but only for 6 MV. For one patient, all four algorithms were used to recompute the dose after replacing all computed tomography voxels within the patient's skin contour by water. This made all differences above 5% between MCDE and the other dose calculation algorithms disappear. Thus, the observed deviations mainly arose from differences in particle transport modeling within the lungs, and the commissioning of the algorithms was adequately performed (or the commissioning was less important for this type of treatment). In conclusion, not one pair of the dose calculation algorithms we investigated could provide results that were consistent within 5% for all 10 patients for the set of clinically relevant dose-volume indices studied. As the results from both CS algorithms differed significantly, care should be taken when evaluating treatment plans as the choice of dose calculation algorithm may influence clinical results. Full Monte Carlo provides a great benchmarking tool for evaluating the performance of other algorithms for patient dose computations.

Key words: Monte Carlo, convolution/superposition, pencil beam, lung cancer, intensity modulated radiation therapy (IMRT)

I. INTRODUCTION

The level of refinement of dose calculation algorithms used for clinical radiotherapy treatment planning has increased highly over the past decades. The accuracy of patient dose predictions has continuously improved by moving from simple scatter- and inhomogeneity corrections over pencil beam algorithms to point kernel-based convolution/ superposition (CS) methods. Calculating dose distributions for lung cancer makes great demands on computational engines, as regions of electronic disequilibrium arise in the presence of tissue inhomogeneities, for example, at the tumor-lung interface. Due to the steep slopes of tumor control probability (TCP) and normal tissue complication probability (NTCP) curves, a dose error of 5% may lead to a change in TCP of 10 to 20% and to an even larger change in NTCP.[1,2] Therefore, we must obviously try to avoid any (systematic) differences between the planned and delivered dose distributions.

By explicitly modeling the particle transport, full Monte Carlo (MC) simulations are expected to result in the highest dose calculation accuracy. Experiments involving phantom measurements have already shown that MC calculations are clearly superior to conventional systems, including CS algorithms, near low density materials and around air cavities.[3-7] For pencil beam algorithms, deviations from MC calculations and measurements larger than 10% have been reported. All of these experiments study the effect of a single beam on a large air or lung cavity. Transferring these results to a clinical setting is not at all obvious.

Therefore, it is important to evaluate the accuracy of dose calculation algorithms directly within their ultimate field of application: the computation of patient dose distributions for clinical treatment plans. This will enable us to evaluate their performance for a variety of tissue inhomogeneity shapes and sizes, as well as for a large number of small and irregularly shaped beam segments for a combination of beam incidences.

Several studies have compared MC computations with pencil beam calculations for clinical cases, especially demonstrating the latter's shortcomings in regions with tissue heterogeneities.[8–14] Data on the comparison of MC with CS algorithms are more scarce[15–17] and to our knowledge no such study has been devoted to intensity modulated radiation therapy (IMRT) for lung cancer yet. By reducing the dose to critical organs relative to the tumor prescription dose, IMRT techniques allow dose escalation with the aim to improve local control. However, the use of a large number of irregularly shaped segments implies the need for an accurate dose calculation algorithm. The purpose of the present study was to compare full MC calculations of patient dose distributions with results from two different commercial CS implementations and one pencil beam algorithm for 10 clinical lung IMRT cases for two photon beam qualities (6 and 18 MV). This also allowed for a comparison between both CS algorithms.

II. MATERIALS AND METHODS

A. Patients and IMRT treatment planning

Ten non-small-cell lung cancer patients with various tumor locations were randomly selected for this study. For each patient, a median dose of 70 Gy was prescribed to the planning target volume (PTV). This PTV results from a 5-mm-wide isotropic expansion of the clinical target volume (CTV), which is derived from the macroscopic gross tumor volume (GTV). To deal with conflicting dose objectives during the optimization, a 6-mm-wide expansion of all organs at risk (OARs) is excluded from the PTV.[18] The lungs, heart, esophagus, and spinal cord were delineated as OARs. The lungs include both the ipsilateral and contralateral lung, but they exclude the GTV. The esophagus was expanded by a 3-mm-wide isotropic margin, while the spinal cord was expanded by a 5-mm-wide isotropic margin. Treatment planning objectives for the OARs were formulated as follows. For the lungs, V_{20} and V_{30} should not exceed 30 and 20%, respectively, while the mean lung dose (MLD) should not exceed 27 Gy. V_x is the relative lung volume (percentage) that receives at least x Gy. For the heart, the maximal dose (D_{max}) should not exceed 62 Gy, while D_{33}, D_{67}, and the minimal dose (D_{min}) should not exceed 55 Gy, 50 Gy, and 40 Gy, respectively. A dose of at least D_x is received by x% of the OAR's volume. D_{max} and D_{min} are represented by D_2 and D_{98}.[19] For the expanded esophagus D_{max}, D_{33}, D_{67}, and D_{min} should not exceed 68 Gy, 60 Gy, 54 Gy, and 50 Gy, respectively. For the expanded spinal cord, D_{max} should not exceed 50 Gy.

For each patient, two IMRT treatment plans were created with photon beam qualities of 6 MV and 18 MV. A class solution of nine non-coplanar beams with a single isocenter was applied. A combination of GRATIS (Sherouse Systems, Inc, Chapel Hill, NC, USA) and in-house developed software was used for planning. For every template beam, initial beam segments were created by the anatomy-based segmentation tool (ABST), taking into account the presence of OARs and the distance to the skin.[20] Segment weights and multileaf collimator (MLC) leaf positions were optimized by the segment outline and weight adapting tool (SOWAT); the optimization uses a biophysical cost function.[21] Dose computation between optimization cycles was performed by Pinnacle version 6.2b (Philips Medical Systems, Best, The Netherlands). The 6 MV and 18 MV plans were optimized independently.

B. Dose calculation algorithms

Four different calculation algorithms were used to recompute the final dose for all plans. MCDE (Monte Carlo dose engine) is an accurate MC code for IMRT dose computations. Based on the BEAMnrc/DOSXYZnrc system,[22] MCDE uses the most recent EGSnrc electron transport algorithms.[23] Reynaert *et al.*[24] have described the working of MCDE. The commissioning of the 6 MV and 18 MV photon beams of the Elekta SL*i*plus linear accelerator at Ghent University Hospital has been reported in detail elsewhere,[25,26] including data on the comparison of simulations and measurements. The MLC was modeled using BEAMnrc's MLCE component module (CM), which takes into account the tongue-and-groove design of the MLC as well as the air gap between the leaves. A phase space file scored below the mirror is used as input in MCDE. By having DOSXYZnrc reprogrammed as an additional CM, MCDE handles the beam modifiers and the patient in one process. Pinnacle version 6.2b and Helax-TMS version 6.1A (Nucletron, Veenendaal, The Netherlands) are two commercial treatment planning systems which incorporate CS algorithms. These algorithms convolve the energy released by a photon per unit mass with energy deposition kernels.[27] For inhomogeneous media, the energy deposition kernels are scaled with density. Pinnacle's CS model (Pinnacle-CS) is based on the work of Mackie *et al.* and Papanikolaou *et al.*[28–30] Just like Pinnacle-CS, Helax-TMS's collapsed cone model (Helax-CC) involves point kernels,[31] while its simpler pencil beam model (Helax-PB) is based on pencil kernels.[32] We did not introduce bias by including the algorithm used by the optimization engine (Pinnacle-CS) in our comparison, as we directly compared the resulting dose distributions with each other and did not evaluate their individual compatibility with the planning objectives.

Beam and computed tomography (CT) data for all plans were interchanged between MCDE, Pinnacle-CS, Helax-CC, and Helax-PB through a DICOM interface. A common scoring grid with an equal spacing of 5 mm in the x, y, and z directions was used. For each MCDE calculation, 25 million particles were transported through the patient-dependent part of the linac head and the patient geometry. To convert CT numbers into elemental composition data, six material bins were introduced (air, lung, adipose, muscle, cartilage, and cortical bone), while the mass density was calibrated continuously against the CT number. Each MCDE scoring voxel had a radius of 2 mm.[33] The resulting dose grids were converted from dose-to-medium to dose-to-water.[34] As the same set of commissioning measurements was used to customize the beams for clinical use for both Pinnacle and Helax-TMS, a fair comparison could be made.

To eliminate the effect of differences in particle transport modeling within the patient, additional computations for each of the dose calculation algorithms and for both energies were performed for one patient after setting all CT voxels within the skin contour to water (density=1 g/cm^3).

C. Dose reporting and evaluation

For each patient, dose-volume histograms (DVHs) were created with the PLUNC software (Plan UNC, University of North Carolina) for the dose distributions of both the 6 MV and 18 MV plans calculated by all four-dose calculation algorithms for the following structures: GTV, PTV, lungs, heart, expanded esophagus, and expanded spinal cord. Individual dose-volume points were also recorded. D_{min}, D_{50}, and D_{max} were evaluated for the GTV and PTV. For the lungs, V_{30}, V_{20}, and MLD were reported. D_{33} and D_{max} were evaluated for the expanded esophagus and for the heart. D_{max} was recorded for the expanded spinal cord. In the case of steep DVHs, volume points (V_x) have a greater variability than dose points (D_x). Therefore, comparison of dose engines should preferably be based directly on dose point differences and not on the extrapolation of volume point differences. For the lungs, however, we report values of V_{30} and V_{20} because of their importance in clinical treatment plan evaluation; typically, the relevant part of the DVH is reasonably flat.

To detect systematic differences between the dose calculation algorithms, one-way analysis of variance (ANOVA) for repeated measurements[35] was performed for each dose-volume point, structure, and beam energy combination. Tukey's method was used to perform pairwise comparison of means. *P* values below 5% were considered significant. Although the ANOVA method efficiently allows us to gain insight in systematic deviations, it is questionable whether all patients can be considered random samples from the same population, considering their differences in anatomy, tumor location, and tumor size. Therefore, and due to the limited number of patients in our study, it is essential to evaluate differences observed in individual patients as well. For this purpose, relative dose-volume differences (percentage) between the results from the different dose calculation algorithms were computed for each patient, dose-volume point, structure, and beam energy combination. Whenever relative dose-volume differences are reported, this is done by dividing the absolute difference by the prescription dose (70 Gy) for target structures or by the maximally tolerable value indicated by the treatment planning objectives for the OARs.

III. RESULTS

A. ANOVA and pairwise comparison of means

Tables I and II show the results of the statistical analysis for the 6 MV and 18 MV plans, respectively. Each table row corresponds to a certain dose-volume point for a certain target or OAR. The *p* value of the one-way ANOVA for repeated measurements (for the same dose-volume point for all 10 patients) is reported. For all six possible pairs of dose calculation algorithms, the mean value (averaged over all patients) of the relative difference in dose-volume value between each pair is presented, as well as the corresponding *p* value according to Tukey's multiple comparison procedure. *P* values below 5% are printed in bold.

For 6 MV (Table I), there are significant differences between at least two of the dose calculation algorithms for all dose-volume points. When comparing MCDE to the other three algorithms, Pinnacle-CS certainly shows the best correspondence within the target structures (within 2% for all dose-volume points), although MCDE reports significantly higher D_{max}-values (+1.5% for the GTV and +1.7% for the PTV). Helax-CC and Helax-PB both deviate significantly from MCDE within the target structures, but in opposite directions: Helax-PB reports higher doses than MCDE (up to +3.2% for PTV-D_{min}), while Helax-CC reports lower dose values (up to −3.1% for PTV-D_{max}). As expected due to the correspondence between MCDE and Pinnacle-CS within the targets, Pinnacle-CS also reports significantly higher doses than Helax-CC (up to +3.1% for PTV-D_{min}), and significantly lower doses than Helax-PB (up to −4.4% for PTV-D_{max}). Consequently, both Helax algorithms differ significantly for all target dose-volume points (up to 5.9% for PTV-D_{min}).

TABLE I. Results of the statistical analysis for 6 MV. For each target or OAR and for every dose-volume point, one-way ANOVA for repeated measurements was performed. For each pair of dose calculation algorithms studied, results of the pairwise comparison of means according to Tukey's method are reported. Significant *p* values (<5%) are printed in bold.

			MCDE - Pinnacle-CS		MCDE – Helax-CC		MCDE – Helax-PB		Pinnacle-CS – Helax-CC		Pinnacle-CS – Helax-PB		Helax-CC – Helax-PB	
6 MV		p-value ANOVA	Mean Rel. Diff. (%)	p	Mean Rel. Diff. (%)	p	Mean Rel. Diff. (%)	p	Mean Rel. Diff. (%)	p	Mean Rel. Diff. (%)	p	Mean Rel. Diff. (%)	p
Targets														
GTV	D_{min}	**0.001**	-0.60	0.547	0.49	0.701	-1.45	**0.014**	1.09	0.092	-0.85	0.251	-1.94	**0.001**
	D_{50}	**0.000**	0.19	0.954	1.69	**0.000**	-0.49	0.542	1.50	**0.001**	-0.68	0.263	-2.18	**0.000**
	D_{max}	**0.000**	1.54	**0.002**	2.82	**0.000**	-0.24	0.928	1.27	**0.012**	-1.78	**0.000**	-3.06	**0.000**
PTV	D_{min}	**0.000**	-0.47	0.918	2.63	**0.005**	-3.24	**0.001**	3.10	**0.001**	-2.77	**0.003**	-5.87	**0.000**
	D_{50}	**0.000**	0.13	0.986	1.96	**0.000**	-1.99	**0.000**	1.83	**0.000**	-2.12	**0.000**	-3.95	**0.000**
	D_{max}	**0.000**	1.71	**0.018**	3.06	**0.000**	-2.70	**0.000**	1.35	0.082	-4.41	**0.000**	-5.76	**0.000**
Organs at risk														
Lungs	V_{30}	**0.000**	1.84	0.138	-0.12	0.999	-2.53	**0.021**	-1.96	0.103	-4.37	**0.000**	-2.41	**0.030**
	V_{20}	**0.000**	2.89	**0.000**	-0.29	0.968	0.51	0.846	-3.17	**0.000**	-2.37	**0.003**	0.80	0.588
	MLD	**0.000**	3.05	**0.000**	1.06	**0.011**	-1.46	**0.000**	-1.99	**0.000**	-4.51	**0.000**	-2.52	**0.000**
Heart	D_{33}	**0.000**	1.20	**0.002**	-0.06	0.997	-1.11	**0.005**	-1.27	**0.001**	-2.31	**0.000**	-1.04	**0.008**
	D_{max}	**0.036**	0.86	0.755	0.33	0.980	-1.71	0.217	-0.53	0.928	-2.57	**0.026**	-2.04	0.105
Expanded esophagus	D_{33}	**0.022**	-0.07	1.000	1.19	0.670	-2.26	0.155	1.26	0.629	-2.19	0.175	-3.45	**0.011**
	D_{max}	**0.000**	0.69	0.612	1.45	0.063	-2.22	**0.002**	0.76	0.532	-2.90	**0.000**	-3.66	**0.000**
Expanded spinal cord	D_{max}	**0.000**	2.48	**0.001**	0.46	0.869	-0.43	0.894	-2.01	**0.011**	-2.91	**0.000**	-0.89	0.465

On the other hand, the statistical analysis indicates an excellent correspondence between MCDE and Helax-CC for the organs at risk (within 1.5% for all dose-volume points), although there is a small but significant underestimation of MLD by Helax-CC (−1.1%). Pinnacle-CS strongly underestimates the dose to critical structures compared to MCDE and Helax-CC, in particular for the lungs (−2.9% for V_{20} and −3.1% for MLD), the heart (−1.2% for D_{33}), and the expanded spinal cord (−2.5% for D_{max}). Helax-PB, on the other hand, has a tendency to overestimate the dose delivered to the organs at risk compared to MCDE (up to +2.5% for lungs-V_{30}) and Helax-CC (up to +3.7% for expanded esophagus-D_{max}), although for some dose-volume points its reported values show good correspondence, for example, V_{20} for the lungs (−0.5% compared to MCDE and −0.8% compared to Helax-CC) and D_{max} for the expanded spinal cord (+0.4% compared to MCDE and +0.9% compared to Helax-CC). Unsurprisingly, the dose-volume values of Helax-PB are significantly higher than those of Pinnacle-CS (up to +4.5% for MLD).

TABLE II. Results of the statistical analysis for 18 MV. For each target or OAR and for every dose-volume point, one-way ANOVA for repeated measurements was performed. For each pair of dose calculation algorithms studied, results of the pairwise comparison of means according to Tukey's method are reported. Significant *p* values (<5%) are printed in bold.

			MCDE - Pinnacle-CS		MCDE – Helax-CC		MCDE – Helax-PB		Pinnacle-CS – Helax-CC		Pinnacle-CS – Helax-PB		Helax-CC – Helax-PB	
6 MV		p-value ANO-VA	Mean Rel. Diff. (%)	p	Mean Rel. Diff. (%)	p	Mean Rel. Diff. (%)	p	Mean Rel. Diff. (%)	p	Mean Rel. Diff. (%)	p	Mean Rel. Diff. (%)	p
Targets														
GTV	D_{min}	**0.000**	-2.18	**0.000**	0.65	0.238	-1.56	**0.000**	2.83	**0.000**	0.63	0.265	-2.20	**0.000**
	D_{50}	**0.000**	-1.08	**0.014**	2.25	**0.000**	-0.58	0.320	3.33	**0.000**	0.50	0.454	-2.83	**0.000**
	D_{max}	**0.000**	0.71	0.878	3.32	**0.007**	-3.31	**0.007**	2.61	**0.044**	-4.02	**0.001**	-6.64	**0.000**
PTV	D_{min}	**0.000**	-0.92	0.583	0.86	0.635	-3.72	**0.000**	1.79	0.082	-2.80	**0.002**	-4.58	**0.000**
	D_{50}	**0.000**	-1.03	0.067	2.03	**0.000**	-2.66	**0.000**	3.07	**0.000**	-1.63	**0.001**	-4.70	**0.000**
	D_{max}	**0.000**	0.90	0.863	3.35	**0.032**	-7.95	**0.000**	2.44	0.169	-8.85	**0.000**	-11.30	**0.000**
Organs at risk														
Lungs	V_{30}	**0.000**	2.81	**0.000**	0.25	0.969	0.19	0.986	-2.56	**0.000**	-2.62	**0.000**	-0.06	0.999
	V_{20}	**0.000**	8.05	**0.000**	0.38	0.992	4.40	**0.013**	-7.67	**0.000**	-3.65	**0.049**	4.02	**0.026**
	MLD	**0.000**	3.73	**0.000**	1.20	0.053	-0.87	0.238	-2.52	**0.000**	-4.59	**0.000**	-2.07	**0.000**
Heart	D_{33}	**0.000**	0.88	**0.001**	0.48	0.142	-0.29	0.539	-0.41	0.261	-1.18	**0.000**	-0.77	**0.006**
	D_{max}	0.149	1.02	0.469	0.66	0.783	-0.52	0.879	-0.37	0.952	-1.54	0.141	-1.17	0.348
Expanded esophagus	D_{33}	**0.014**	0.59	0.800	0.58	0.804	-1.40	0.151	-0.01	1.000	-1.98	**0.020**	-1.98	**0.020**
	D_{max}	**0.000**	0.11	0.995	1.44	**0.014**	-2.30	**0.000**	1.33	**0.026**	-2.40	**0.000**	-3.73	**0.000**
Expanded spinal cord	D_{max}	**0.001**	2.14	**0.000**	0.89	0.227	0.88	0.233	-1.25	**0.045**	-1.26	**0.044**	-0.01	1.000

For 18 MV (Table II), only for D_{max} of the heart is there no significant difference between all four dose calculation algorithms (p=0.149). Again, MCDE and Pinnacle-CS show the best correspondence within the target structures (within 1% for the dose-volume points within the PTV), although Pinnacle-CS reports significantly higher values of the minimal and median dose within the GTV (+2.2% and +1.1%, respectively). As with 6 MV, Helax-PB reports higher target dose values than MCDE (up to +8.0% for PTV-D_{max}) and Pinnacle-CS (up to +8.9% for PTV-D_{max}), while Helax-CC reports lower values (up to −3.4% for PTV-D_{max} compared to MCDE and up to −3.3% for PTV-D_{50} compared to Pinnacle-CS). Helax-PB and Helax-CC differ significantly for all dose-volume points within the GTV (up to 6.6% for D_{max}) and PTV (up to 11.3% for D_{max}).

Except for the maximal dose delivered to the expanded esophagus (p=0.014), the statistical analysis indicates an excellent agreement between MCDE and Helax-CC for all OAR dose-volume points (within 1.5%), whereas Pinnacle-CS again underestimates dose-volume values within most critical structures (up to −8.1% for lungs-V_{20} compared to MCDE). Helax-PB has a tendency to overestimate OAR doses compared to Helax-CC (up to +3.7% for expanded esophagus-D_{max}), although its results still agree well with those of MCDE (within 1.5%, except for lungs-V_{20} :−4.4% and expanded esophagus-D_{max}: +2.3%).

B. Individual patients

Figure 1 summarizes the comparison results for individual patients. The upper-right corner of the matrix plot represents the 6 MV results, while the 18 MV results are shown in the lower-left corner. Each individual plot contains data on the relative dose-volume differences between the two dose calculation algorithms indicated by each plot's row and column headers. Each bar within a plot corresponds to a certain dose-volume point for a certain target or OAR, in the same order as found in Tables I and II. For every dose-volume point the patients were divided into three categories, where the absolute value of the relative difference was either below 2% (white), between 2% and 5% (light gray), or above 5% (dark gray).

For 6 MV, it is clear that the best correspondence between target dose-volume values can be found between MCDE and Pinnacle-CS, in agreement with the results of our statistical analysis. The difference between MCDE and Helax-CC is above 5% (9.0%) for only one patient (for D_{min} of the PTV), which puts the obtained statistically significant differences into perspective. On the other hand, while our statistical analysis indicates a good resemblance between MCDE and Helax-CC for the OAR dose-volume points, Fig. 1 shows two patient/dose-volume point combinations where the observed difference is above 5% (−6.1% for D_{max} of the heart and +11.1% for D_{33} of the expanded esophagus). A similar situation can be found in Fig. 1 for the OAR differences between MCDE and Pinnacle-CS, with deviations of +6.1 and +5.3% occurring for V_{20} of the lungs. Helax-PB shows unacceptably great deviations from the other three dose calculation algorithms for both targets and OARs. For 18 MV MCDE, Pinnacle-CS, and Helax-CC correspond very well with regard to the target structures. Only for one patient, a deviation larger than 5% occurred between MCDE and Helax-CC (+5.2% for D_{max} of the PTV). For the OARs, the difference in dose-volume value between MCDE and Helax-CC is within 5% in all cases, while Pinnacle-CS clearly shows larger deviations: both for the comparison with MCDE and Helax-CC, differences above 5% are reported for 11 patient/dose-volume point combinations, mainly within the lungs. Again, Helax's pencil beam algorithm is clearly inferior to the other CS algorithms and to MCDE.

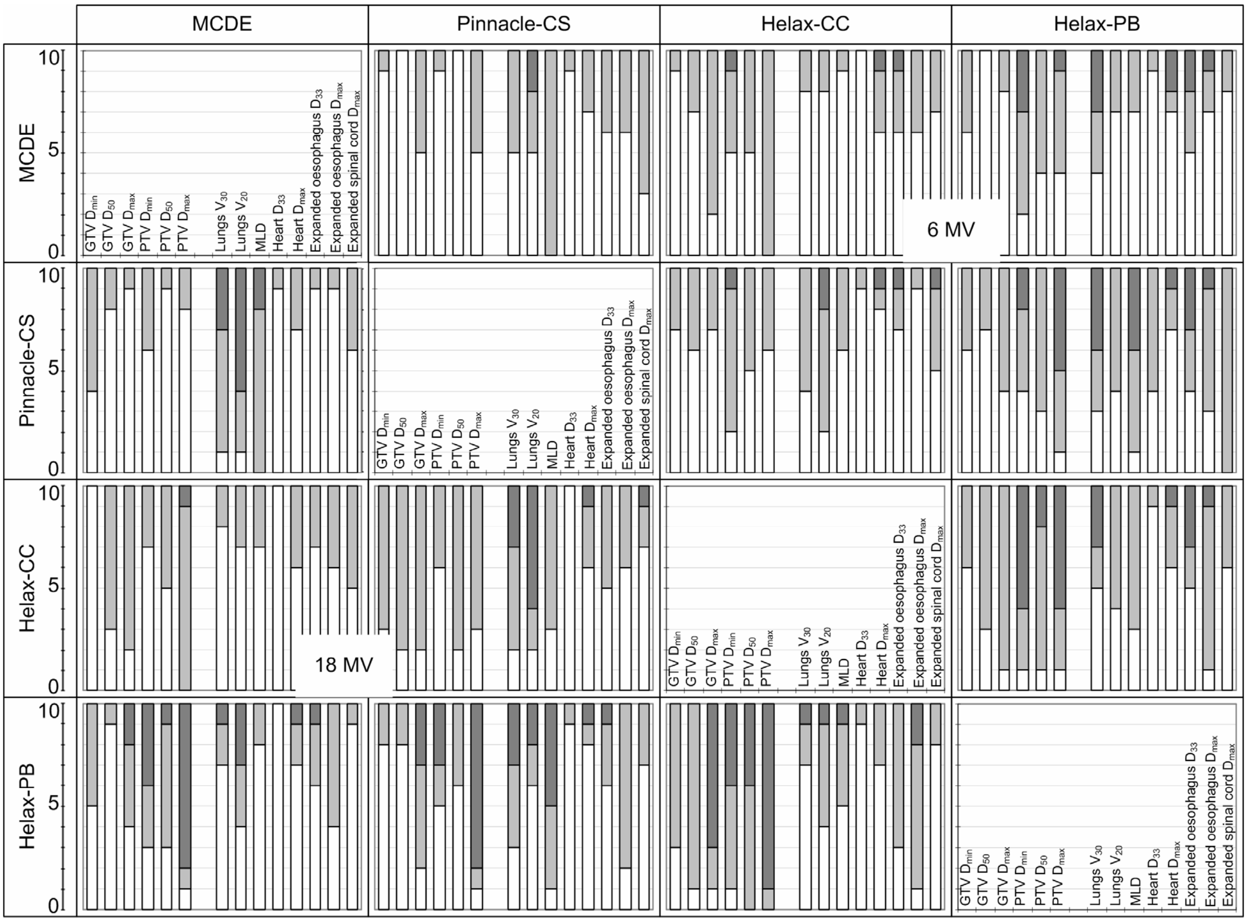

FIG. 1. Individual patient results for 6 MV (upper-right corner) and 18 MV (lower-left corner). For each pair of dose calculation algorithms and for each dose-volume point corresponding to a certain target or organ at risk, the number of patients for which the absolute value of the observed relative dose-volume difference was below 2% (white), between 2% and 5% (light gray), and above 5% (dark gray) is shown.

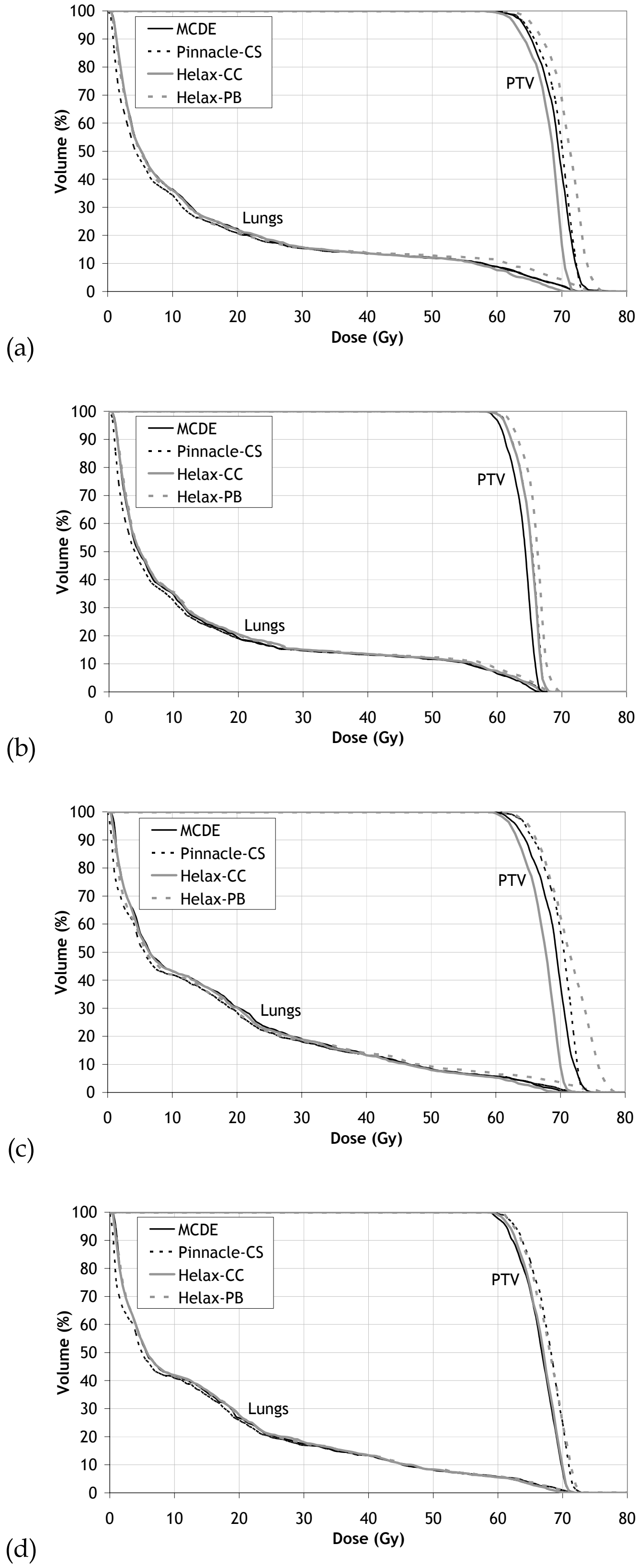

FIG. 2. Dose-volume histograms of the PTV and the lungs for patient number 4, computed by our MCDE, Pinnacle's CS algorithm, and Helax-TMS's collapsed cone and pencil beam algorithms: (a) for 6 MV, (b) for 6 MV and after replacing all CT voxels within the skin contour with water, (c) for 18 MV, and (d) for 18 MV and after replacing all CT voxels within the skin contour with water.

To illustrate the observed differences for individual patients, Fig. 2 shows an exemplary set of DVHs (for patient number 4) of the PTV and of the lungs for all four dose calculation algorithms for 6 MV (a) and 18 MV (c). For 6 MV, both Helax-CC and Helax-PB deviate up to 3% from MCDE within the PTV, but in opposite directions, while the Pinnacle-CS curve stays within 1% from the MCDE curve. For the lungs, Pinnacle-CS underestimates the observed dose-volume values compared to MCDE (up to −5.3% for V_{20}), while the deviations between Helax-PB and MCDE are more moderate (up to −4.0% for V_{20}). The clinically relevant dose-volume values of Helax-CC correspond within 2% with those of MCDE within the lungs. For 18 MV, Pinnacle-CS still shows the best correspondence with MCDE within the PTV (up to +2.1% for D_{min}), followed by Helax-CC (up to −3.9% for D_{max}). D_{max} within the PTV is overestimated by Helax-PB compared to MCDE by 5.6%. For the lungs, Pinnacle-CS underestimates V_{30} and V_{20} by 5.5 and 6.4%, respectively. Deviations between Helax-PB and MCDE are also over 4% (−4.4% for V_{30} and −4.3% for V_{20}); while for Helax-CC, the clinically relevant dose-volume values again stay within 2% of those reported by MCDE.

C. Calculations in water

All four dose calculation algorithms were used to recompute the dose for patient number 4 after replacing all CT voxels with water within the patient's skin contour. The DVHs of the PTV and the lungs are shown in Fig. 2 for 6 MV (b) and 18 MV (d). For 6 MV both the Pinnacle-CS and Helax-CC curves now stay within 2% from the MCDE curve for the PTV, while the differences between MCDE and Helax-PB become slightly larger compared to the calculations in medium (up to +3.5% for D_{min}). For the lungs, the deviations of Pinnacle-CS from MCDE for the clinically relevant dose-volume points greatly decrease compared to the calculations in medium (−0.7% instead of −5.3% for V_{20}). The deviation between Helax-PB and MCDE for V_{20} is reduced to +3.1%. For 18 MV all algorithms agree within 2.2% with MCDE within the PTV for the calculations in water (+2.2% instead of +5.6% for the difference in D_{max} between Helax-PB and MCDE). For the reported dose-volume points within the lungs, Pinnacle-CS differs much less from MCDE compared to the calculations in medium (−2.7% instead of −5.5% for V_{30} and −2.4% instead of −6.4% for V_{20}). Deviations between Helax-PB and MCDE are reduced from −4.4% to −0.1% for V_{30} and from −4.3% to +1.9% for V_{20}.

IV. DISCUSSION

Both from the statistical analysis and the evaluation of individual patient cases, it is clear that large deviations occur between the different dose calculation algorithms. Therefore, substantial errors can be made when an insufficiently accurate dose computation engine is selected. For treatment planning of lung cancer, it is highly important to take into account differences in tissue density during dose computation and to model secondary electron transport accurately.[36] If the lower attenuation of photon beams within lung tissue is not considered, the dose to tissues downstream will be underestimated. Furthermore, as the electron path length within lung amounts to several centimeters, the beam penumbra widens, exposing larger volumes of lung to significant doses and reducing the dose near the beam edge.[37,38] Additionally, an imbalance between the number of produced and absorbed electrons arises near the interface between low and high density tissues, causing the dosage to build up.[4,39,40] The electronic disequilibrium occurring in these cases will again cause an underestimation of the dose to the lung if its effect is not taken into account. Moreover, these effects are expected to become more pronounced for higher photon energies, smaller field sizes, and decreased lung densities.[3,41,42] Both Helax-CC and Pinnacle-CS apply three-dimensional (3D) density scaling of their kernels for inhomogeneous media,[31] whereas Helax-PB only employs a one-dimensional inhomogeneity correction through depth scaling.[32] Helax-CC also uses kernel tilting and accounts for beam hardening and off-axis softening,[43,44] like Pinnacle-CS. Electron transport is modeled most accurately in MCDE through the EGSnrc code.[23]

Although measurement data may be helpful in establishing the ground truth between the four dose calculation algorithms, the accuracy of 3D gel dosimetry or radiochromic film in anthropomorphic phantoms is presently limited around 3%, which is comparable to the differences that were observed in our study. Research on establishing measurement protocols for dose verification of clinical (lung) cases is ongoing, and we may certainly benefit from experimental verification in the future. On the other hand, comparison with measurements has shown that MCDE performs excellently even for narrow offset fields.[16] Details on the commissioning and validation of the 6 MV and 18 MV photon beams have been published as well.[25,26] Moreover, none of the data presented in this paper indicate that any systematic errors may still be present when MCDE is used to perform patient dose calculations. The calculations in water that were performed for patient number 4 show that the observed differences mainly arise from differences in particle transport modeling within the patient, as the observed deviations between MCDE and the other dose calculation algorithms strongly decreased compared to the calculations in medium. Because MCDE incorporates the most accurate electron transport of the four dose calculation algorithms, we believe it is safe to assume that MCDE is the system that is the closest to the ground truth in our study.

By performing a one-way ANOVA for repeated measurements, we can detect systematic differences between dose calculation algorithms. Pairwise comparison of means is performed by averaging dose-volume differences between two algorithms over all patients. Consequently, if the difference between two algorithms is a large positive value for one patient and a large negative value for another patient, both values will cancel each other out in the final evaluation and will cause the test to conclude that there is no evidence of significant difference between both algorithms. However, such a situation would be unacceptable for clinical practice. An example can be found in our data set for D_{33} of the expanded esophagus comparing Pinnacle-CS to Helax-PB for 6 MV. On the other hand, if deviations are small but in the same direction (positive or negative) for all patients, the test may conclude that both algorithms differ significantly. At the same time, looking at individual patient results may show that all the observed differences are within 5%, which could certainly be considered acceptable for clinical use. An example of this can be seen in our data set for comparison between MCDE and Helax-CC within the target structures. While the statistical analysis is valuable for gaining initial insight in systematic differences, additional analysis of individual patient results remains indispensable for evaluating the practicability of the different dose calculation algorithms. In principle, if only one patient shows an unacceptably large deviation for one dose calculation algorithm, this algorithm is no longer suitable for clinical use (for this type of patient).

From our data set, Pinnacle-CS could be considered the best CS algorithm for dose determination within the target structures, whereas Helax-CC yields better results for the OARs. As illustrated by Figs. 2(a) and 2(c), Helax-CC typically underestimates the dose to the PTV (and other target structures), while Pinnacle-CS has a tendency to underestimate the dose to the lungs. For individual patients, both algorithms show deviations over 5% from MCDE (except for Pinnacle-CS within the targets). As the algorithms behind the commercial treatment planning systems are not known in detail to the user, it is not so easy to explain the observed differences. To investigate this, it is advisable to distinguish effects related to differences in beam modeling from effects related to the particle transport within the patient.[45] For a proper comparison, an accurate beam model is required, which provides an excellent agreement between calculations and measurements in homogeneous phantoms. By recomputing the dose after setting all CT voxels within the skin contour to water for patient number 4 as an exemplary patient case, we could eliminate the influence of particle transport within the patient. The results are shown in Figs. 2(b) and 2(d). The DVHs of the different dose calculation algorithms clearly lay closer together for the calculations in water compared to those in medium. Analysis of the clinically relevant dose-volume values shows that all deviations above 5% between MCDE and the other dose calculation algorithms disappear, for example, the difference between Pinnacle-CS and MCDE for V_{20} within the lungs decreases from −5.3% to −0.7% for 6 MV and from −6.4% to −2.4% for 18 MV. Thus, for this patient, the observed differences were mainly due to the modeling of the particle transport within the patient by the different dose calculation algorithms. The remaining differences are all clinically acceptable and are either due to slight discrepancies in the commissioning process or to differences in the beam model. Due to the relatively large fields involved in lung cancer treatments, the accuracy of the beam model is less important here than, for example, in cases of treatments of head and neck tumors close to or within the oral or nasal cavity. As the differences between the calculations in medium mainly arise from the modeling of secondary electron transport within the lungs, the deviations are the most striking within the PTV and the lungs and not so much within the other OARs.

To maximize the accuracy while commissioning a treatment planning system, it is important to consider the specific field of application of future dose calculations. In the case of IMRT, which involves the use of a large number of small and irregularly shaped fields, one should attach great importance to the similarity between simulations and measurements for small offset fields, rather than focus on large central fields. Indeed, when commissioning a commercial treatment planning system, limitations of the beam model require a compromise, as it is generally not possible to achieve perfect agreement for both large and small fields, central and off-axis. Moreover, attention should be paid to the fact that the commissioning process should take place based on fields shaped by the MLC only, that is, with the jaws retracted. Again, this aims to mimic the clinical reality, because large parts of a highly irregular field contour will be created by the MLC leaves and not by the jaws.

The treatment plan configuration (number of beams or beam segments, shapes and angles) may influence dose calculation errors in various ways. As IMRT typically combines a large number of beam angles (in our case, 9) as well as a large number of segments for each beam angle, the superposition of dose contributions from the individual beam segments may wipe out differences between dose calculation algorithms. Indeed, it has been stated that larger differences are observed when comparing individual fields.[9] Therefore, 3D conformal treatment plans may be more crucial when it comes to evaluating the performance of the inhomogeneity correction of a certain dose calculation algorithm, because of the smaller number of treatment fields. On the other hand, the fact that IMRT beam segments will generally be smaller than 3D field shapes will potentially increase dose errors for IMRT. Larger errors may also arise for IMRT treatments due to increased MLC transmission in the presence of irregularly shaped beam segments. It is obvious that the type of treatment machine and the way in which leaf sequencing is performed also contribute to the entire treatment plan configuration; hence these factors may also influence the magnitude of dose errors. The way in which the treatment plan configuration affects the accuracy of dose calculation within inhomogeneous patient geometries is certainly worth further investigation. It is clear that care should be taken not to generalize the results presented in this paper toward other treatment configurations.

Moreover, inhomogeneity effects are expected to become more distinct for higher photon energies. Figure 1 clearly illustrates the presence of more large deviations (over 5%) between the dose-volume values reported within the lungs for 18 MV than for 6 MV. Again, analysis of individual segments may allow us to study the influence of beam quality in more detail, as differences will become more pronounced.

From the large variety in deviations observed for the same dose-volume parameter in different patients, it follows that individual patient anatomy plays an important role. Together with a profound knowledge of the causes of the observed dose-volume differences between algorithms, extensive patient data sets may allow us to formulate guidelines concerning the appropriate dose calculation algorithm based on tumor location and size. If a particular anatomy is more “difficult” or “critical”, for example, because the tumor is located close to the edge of the lungs, a more accurate (but time-consuming) dose calculation algorithm could be recommended. Research focusing on individual segments may give us more insight into the strengths and weaknesses of different dose calculation algorithms. At the moment, dose engines like MCDE are not suitable for use in routine clinical practice, due to the present limitations in computer power. Faster MC solutions, which include several approximations and simplifications to increase calculation speed, are commercially available. Like any other dose calculation algorithm, these practical MC codes need to be benchmarked before clinical use. Full MC provides a great tool for benchmarking the performance of other dose calculation algorithms within patients (where measurements are difficult or even impossible), as it models particle transport most accurately.

V. CONCLUSIONS

We compared full Monte Carlo calculations (performed by our Monte Carlo dose engine MCDE) with two different commercial CS implementations (Pinnacle-CS and Helax-TMS's collapsed cone model Helax-CC) and one pencil beam algorithm (Helax-TMS's pencil beam model Helax-PB) for 10 IMRT lung cancer patients and two photon beam qualities (6 and 18 MV). Statistical analysis was performed by means of one-way ANOVA for repeated measurements and pairwise comparison of means according to Tukey's method. Pinnacle-CS showed an excellent correspondence with MCDE for dose evaluation within the target structures, whereas the best correspondence for the OARs was found between Helax-CC and MCDE. Results from Helax-PB were unsatisfying for both target and OARs. As the statistical analysis averages pairwise differences over all patients, it is valuable for gaining insight in systematic differences. However, additional analysis of individual patient results remains indispensable.

Not one pair of the dose calculation algorithms we investigated could provide results that were consistent (within 5%) for all 10 patients for the set of clinically relevant dose-volume indices studied. This was even true for both CS algorithms: Pinnacle-CS and Helax-CC. The choice of dose calculation algorithm may thus influence treatment planning as well as clinical results. After setting all CT voxels within the skin contour to water for one patient, all differences above 5% between MCDE and the other dose calculation algorithms disappeared. Thus, the deviations observed for the calculations in medium mainly arose from the differences between the algorithms in secondary electron transport modeling within the lungs. As it directly models particle transport, full Monte Carlo provides a great benchmarking tool for evaluating the performance of other algorithms for patient dose computations.

ACKNOWLEDGMENTS

This work was supported by Ghent University (GOA Grant No. 12050401). Services regarding Helax-TMS provided by Nucletron B.V. (Veenendaal, The Netherlands) are acknowledged with appreciation. Barbara Vanderstraeten is a Research Assistant (Aspirant) of the Research Foundation-Flanders (FWO-Vlaanderen). Leen Paelinck is a Post-Doctoral Research Fellow of the FWO-Vlaanderen.

[1] N. Papanikolaou, J. Battista, A. Boyer, C. Kappas, E. Klein, T. R. Mackie, M. Sharpe, and J. Van Dyk, *Tissue Inhomogeneity Corrections for Megavoltage Photon Beams*, AAPM Report No 85, Task Group No 65 of the Radiation Therapy Committee of the American Association of Physicists in Medicine (Medical Physics Publishing, Madison, WI, 2004).

[2] B. A. Fraass, J. Smathers, and J. Deye, "Summary and recommendations of a National Cancer Institute workshop on issues limiting the clinical use of Monte Carlo dose calculation algorithms for megavoltage external beam radiation therapy," Med. Phys. **30**, 3206–3216 (2003).

[3] M. R. Arnfield, C. H. Siantar, J. Siebers, P. Garmon, L. Cox, and R. Mohan, "The impact of electron transport on the accuracy of computed dose," Med. Phys. **27**, 1266–1274 (2000).

[4] C. Martens, N. Reynaert, C. De Wagter, P. Nilsson, M. Coghe, H. Palmans, H. Thierens, and W. De Neve, "Underdosage of the upper-airway mucosa for small fields as used in intensity-modulated radiation therapy: A comparison between radiochromic film measurements, Monte Carlo simulations, and collapsed cone convolution calculations," Med. Phys. **29**, 1528–1535 (2002).

[5] G. Crammer-Sargison, W. A. Beckman, and J. Popescu, "Modelling an extreme water-lung interface using a single pencil beam algorithm and the Monte Carlo method," Phys. Med. Biol. **49**, 1557–1567 (2004).

[6] L. Paelinck, N. Reynaert, H. Thierens, W. De Neve, and C. De Wagter, "Experimental verification of lung dose with radiochromic film: comparison with Monte Carlo simulations and commercially available treatment planning systems," Phys. Med. Biol. **50**, 2055–2069 (2005).

[7] T. Krieger and O. A. Sauer, "Monte Carlo-versus pencil-beam-/collapsed-cone-dose calculation in a heterogeneous multi-layer phantom," Phys. Med. Biol. **50**, 859–868 (2005).

[8] L. Wang, C. S. Chui, and M. Lovelock, "A patient-specific Monte Carlo dose-calculation method for photon beams," Med. Phys. **25**, 867–878 (1998).

[9] L. Wang, E. Yorke, and C. S. Chui, "Monte Carlo evaluation of 6 MV intensity modulated radiotherapy plans for head and neck and lung treatments," Med. Phys. **29**, 2705–2717 (2002).

[10] W. Laub, M. Alber, M. Birkner, and F. Nusslin, "Monte Carlo dose computation for IMRT optimization," Phys. Med. Biol. **45**, 1741–1754 (2000).

[11] W. U. Laub, A. Bakai, and F. Nüsslin, "Intensity modulated irradiation of a thorax phantom: comparisons between measurements, Monte Carlo calculations and pencil beam calculations," Phys. Med. Biol. **46**, 1695–1706 (2001).

[12] A. Leal, F. Sanchez-Doblado, R. Arrans, J. Rosello, C. E. Pavon, and J. I. Lagares, "Routine IMRT verification by means of an automated Monte Carlo simulation system," Int. J. Radiat. Oncol., Biol., Phys. **56**, 58–68 (2003).

[13]J. Yang, J. Li, L. Chen, R. Price, S. McNeeley, L. Qin, L. Wang, W. Xiong, and C. M. Ma, "Dosimetric verification of IMRT treatment planning using Monte Carlo simulations for prostate cancer," Phys. Med. Biol. **50**, 869–878 (2005).

[14]C. Boudreau, E. Heath, J. Seuntjens, O. Ballivy, and W. Parker, "IMRT head and neck treatment planning with a commercially available Monte Carlo based planning system," Phys. Med. Biol. **50**, 879–890 (2005).

[15]P. Francescon, C. Cavedon, S. Reccanello, and S. Cora, "Photon dose calculations of a three-dimensional treatment planning system compared to the Monte Carlo code BEAM," Med. Phys. **27**, 1579–1587 (2000).

[16]N. Reynaert, M. Coghe, B. De Smedt, L. Paelinck, B. Vanderstraeten, W. De Gersem, B. Van Duyse, C. De Wagter, W. De Neve, and H. Thierens, "The importance of accurate linear accelerator head modelling for IMRT Monte Carlo calculations," Phys. Med. Biol. **50**, 831–846 (2005).

[17]J. Seco, E. Adams, M. Bidmead, M. Partridge, and F. Verhaegen, "IMRT treatments assessed with a Monte Carlo dose calculation engine," Phys. Med. Biol. **50**, 817–830 (2005).

[18]W. De Neve, Y. Wu, and G. Ezzell, "Practical IMRT planning," in *Image-Guided IMRT*, edited by T. Bortfeld, R. Schmidt-Ullrich, W. De Neve, and D. E. Wazer (Springer, Berlin, 2006), pp. 49–54.

[19]Q. Wu, R. Mohan, M. Morris, A. Lauve, and R. Schmidt-Ullrich, "Simultaneous integrated boost intensity-modulated radiotherapy for locally advanced head-and-neck squamous cell carcinomas. I: dosimetric results," Int. J. Radiat. Oncol., Biol., Phys. **56**, 573–585 (2003).

[20]W. De Gersem, F. Claus, C. De Wagter, and W. De Neve, "An anatomy-based beam segmentation tool for intensity-modulated radiation therapy and its application to head-and-neck cancer," Int. J. Radiat. Oncol., Biol., Phys. **51**, 849–859 (2001).

[21]W. De Gersem, F. Claus, C. De Wagter, B. Van Duyse, and W. De Neve, "Leaf position optimization for step-and-shoot IMRT," Int. J. Radiat. Oncol., Biol., Phys. **51**, 1371–1388 (2001).

[22]D. W. O. Rogers, C. M. Ma, B. Walters, G. X. Ding, D. Sheikh-Bagheri, and G. Zang, *Beamnrc User Manual* (National Research Council of Canada, Ottawa, 2002).

[23]I. Kawrakow and D. W. O. Rogers, *The EGSnrc Code System: Monte Carlo Simulation of Electron and Photon Transport*, NRCC Report PIRS-701 (National Research Council of Canada, Ottawa, 2000).

[24]N. Reynaert, B. De Smedt, M. Coghe, L. Paelinck, B. Van Duyse, W. De Gersem, C. De Wagter, W. De Neve, and H. Thierens, "MCDE: a new Monte Carlo dose engine for IMRT," Phys. Med. Biol. **49**, N235–N241 (2004).

[25]J. Van de Walle, C. Martens, N. Reynaert, H. Palmans, M. Coghe, W. De Neve, C. De Wagter, and H. Thierens, "Monte Carlo model of the Elekta Sl*i*plus accelerator: Validation of a new MLC component module in BEAM for a 6 MV beam," Phys. Med. Biol. **48**, 371–385 (2003).

[26]B. De Smedt, N. Reynaert, F. Flachet, M. Coghe, M. G. Thompson, L. Paelinck, G. Pittomvils, C. De Wagter, W. De Neve, and H. Thierens, "Decoupling initial electron beam parameters for Monte Carlo photon beam modelling by removing beam-modifying filters from the beam path," Phys. Med. Biol. **50**, 5935–5951 (2005).

[27]A. Ahnsejö and M. M. Aspradakis, "Dose calculations for external photon beams in radiotherapy," Phys. Med. Biol. **44**, R99–R155 (1999).

[28]T. R. Mackie, J. W. Scrimger, and J. J. Battista, "A convolution method of calculating dose for 15-MV x rays," Med. Phys. **12**, 188–196 (1985).

[29]T. R. Mackie, A. F. Bielajew, D. W. O. Rogers, and J. J. Battista, "Generation of photon energy deposition kernels using the EGS Monte Carlo code," Phys. Med. Biol. **33**, 1–20 (1988).

[30]N. Papanikolaou, T. R. Mackie, C. Meger-Wells, M. Gehring, and P. Reckwerdt, "Investigation of the convolution method for polyenergetic spectra," Med. Phys. **20**, 1327–1336 (1993).

[31]A. Ahnesjö, "Collapsed cone convolution of radiant energy for photon dose calculation in heterogeneous media," Med. Phys. **16**, 577–592 (1989).

[32]A. Ahnesjö, M. Saxner, and A. Trepp, "A pencil beam model for photon dose calculation," Med. Phys. **19**, 263–273 (1992).

[33]B. De Smedt, B. Vanderstraeten, N. Reynaert, W. De Neve, and H. Thierens, "Investigation of geometrical and scoring grid resolution for Monte Carlo dose calculations for IMRT," Phys. Med. Biol. **50**, 4005–4019 (2005).

[34]J. V. Siebers, P. J. Keall, A. E. Nahum, and R. Mohan, "Converting absorbed dose to medium to absorbed dose to water for Monte Carlo based photon beam dose calculations," Phys. Med. Biol. **45**, 983–995 (2000).

[35]J. Neter, M. Kutner, C. Nachtsheim, and W. Wasserman, *Applied Linear Statistical Models*, 4th ed. (McGraw-Hill, New York, 1996).

[36]W. De Neve and C. De Wagter, "Lethal pneumonitis in a phase I study of chemotherapy and IMRT for NSCLC: The need to investigate the accuracy of dose computation," Radiother. Oncol. **75**, 246–247 (2005).

[37]R. O. Kornelsen and M. E. J. Young, "Changes in the dose-profile of a 10 MV x-ray beam within and beyond low density material," Med. Phys. **9**, 114–116 (1982).

[38]R. C. Miller, J. A. Bonner, and R. W. Kline, "Impact of beam energy and field margin on penumbra at lung tumor-lung parenchyma interfaces," Int. J. Radiat. Oncol., Biol., Phys. **41**, 707–713 (1998).

[39]B. L. Werner, I. J. Das, F. M. Khan, and A. S. Meigooni, "Dose perturbations at interfaces in photon beams," Med. Phys. **14**, 585–595 (1987).

[40]B. J. Mijnheer, R. K. Rice, and L. M. Chin, "Lead-polystyrene transition zone dosimetry in high-energy photon beams," Radiother. Oncol. **11**, 379–386 (1988).

[41]T. R. Mackie, E. El-Kathib, J. Battista, J. Scrimger, J. Van Dyk, and J. R. Cunningham, "Lung dose corrections for 6- and 15-MV x rays," Med. Phys. **12**, 327–332 (1985).

[42]R. K. Rice, B. J. Mijnheer, and L. M. Chin, "Benchmark measurements for lung dose corrections for X-ray beams," Int. J. Radiat. Oncol., Biol., Phys. **15**, 399–409 (1988).

[43]P. W. Hoban, "Accounting for the variation in collision kerma-to-terma ratio in polyenergetic photon beam convolution," Med. Phys. **22**, 2035–2044 (1995).

[44] R. C. Tailor, V. M. Tello, C. B. Schroy, M. Vossler, and W. F. Hanson, “A generic off-axis energy correction for linac photon beam dosimetry,” Med. Phys. **22**, 662–667 (1998).

[45] I. J. Chetty, M. Rosu, D. L. McShan, B. A. Fraass, and R. K. Ten Haken, “The influence of beam model differences in the comparison of dose calculation algorithms for lung cancer treatment planning,” Phys. Med. Biol. **50**, 801–815 (2005).

Chapter 6

Publication 4:

Comparison of 6 MV and 18 MV photons for IMRT treatment of lung cancer

Indira Madani[1], Barbara Vanderstraeten[1,2], Samuel Bral[1], Marc Coghe[1], Werner De Gersem[1], Carlos De Wagter[1], Hubert Thierens[2], Wilfried De Neve[1]

[1] *Department of Radiotherapy, Ghent University Hospital, Gent, Belgium*

[2] *Department of Medical Physics, Ghent University, Gent, Belgium*

Radiotherapy and Oncology 2007;82:63-69

Abstract

Background and purpose: To compare 6 MV and 18 MV photon intensity modulated radiotherapy (IMRT) for non-small cell lung cancer.

Materials and methods: Doses for a cohort of 10 patients, typical for our department, were computed with a commercially available convolution/superposition (CS) algorithm. Final dose computation was also performed with a dedicated IMRT Monte Carlo dose engine (MCDE).

Results: CS plans showed higher $D_{95\%}$ (Gy) for the GTV (68.13 vs 67.36, $p = 0.004$) and CTV (67.23 vs 66.87, $p = 0.028$) with 18 than with 6 MV photons. MCDE computations demonstrated higher doses with 6 MV than 18 MV in $D_{95\%}$ for the PTV (64.62 vs 63.64, $p = 0.009$), $\mathrm{PTV}_{\mathrm{optim}}$ (65.48 vs 64.83, $p = 0.014$) and CTV (66.22 vs 65.64, $p = 0.027$). Dose inhomogeneity was lower with 18 than with 6 MV photons for GTV (0.08 vs 0.09, $p = 0.007$) and CTV (0.10 vs 0.11, $p = 0.045$) in CS but not MCDE plans. 6 MV photons significantly ($D_{33\%}$; $p = 0.045$) spared the esophagus in MCDE plans. Observed dose differences between lower and higher energy IMRT plans were dependent on the individual patient.

Conclusions: Selection of photon energy depends on priority ranking of endpoints and individual patients. In the absence of highly accurate dose computation algorithms such as CS and MCDE, 6 MV photons may be the prudent choice.

Keywords: Intensity modulated radiotherapy; Non-small cell lung cancer; Loss of electronic equilibrium

High-energy photons for treatment of deep targets improve dose uniformity and skin sparing. However, loss of electronic equilibrium may reduce target coverage. Furthermore, lateral scatter of high-energy electrons results in an extended path in low-density tissues such as the lung, causing increase of beam penumbra, larger volumes of lung irradiated and reduced target dose near the beam edge [15]. High-energy photons have a pronounced rebuild-up dose at lung–tissue, tissue–bone interfaces and behind air cavities [18,19,27]. With higher photon energy, smaller field sizes and decreased lung density this effect becomes more pronounced [1,17,23]. Thus, low-energy photons were advised for radiotherapy of lung cancer to minimize lateral electronic disequilibrium and to reduce the irradiated volume of the normal lung [13]. Protocol 91-05 of Radiation Therapy Oncology Group (RTOG) has recommended the use of photons of energy in the range 4–12 MV for radiotherapy of non-small cell lung cancer (NSCLC) [21].

Our current clinical practice still uses 18 MV photon beams for intensity modulated radiotherapy (IMRT) of lung cancer. This practice has originated from experience where the optimization tool was allowed to apply 6 MV as well as 18 MV photons, using a convolution/superposition (CS) dose engine. The use of 6 MV photons in patients with extended anteroposterior diameter may result in inadequate target coverage along the central axis and high dose in superficial structures. Photon beam energy is less critical when multiple beams are used [2]. There are data supporting the use of high-energy photons in particular clinical settings [28]. Moreover, the use of 18 MV in IMRT of lung cancer has been shown not to influence the quality of treatment plans [16].

The goal of the present study was to determine if 6 MV photon beams result in better treatment plans, as obtained with the CS algorithm than 18 MV beams. We evaluated the dose coverage of the targets and sparing of the organs at risk (OARs) in IMRT plans from 10 patients with inoperable NSCLC. We also compared final dose calculations with CS and the Monte Carlo dose engine (MCDE).

Materials and methods

Patient characteristics

All patients, as characterized in Table 1, were scheduled for IMRT in accordance with the protocol adopted by the Radiotherapy Department of the Ghent University Hospital. They underwent helical CT scanning throughout the thorax with 5 mm width between slices in a supine position under normal free breathing.

Table 1. Patient characteristics

Patient			Tumor							Target volume (cc)	
Number	Age	Gender	Side	Location	Histology	T	N	M	Stage	CTV	PTV
1	54	M	Right	Middle lobe	SCC	4	2	0	IIIB	136.62	292.36
2	70	M	Left	Upper lobe	SCC	3	2	0	IIIA	272.14	481.64
3	60	M	Right	Middle lobe	SCC	2	2	0	IIIA	115.35	248.05
4	70	M	Left	Upper lobe	Adeno	4	2	0	IIIB	185.32	354.15
5	67	M	Right	Lower lobe	SCC	2	0	0	IB	572.93	912.18
6	68	M	Left	Upper lobe	SCC	4	3	0	IIIB	69.03	228.88
7	76	F	Right	Lower lobe	Adeno	1	2	0	IIIA	96.06	205.11
8	57	M	Right	Upper lobe	SCC	2	2	0	IIIA	116.99	238.59
9	74	M	Left	Hilum	SCC	3	2	0	IIIA	108.74	229.27
10	69	M	Right	Lower lobe	SCC	4	0	0	IIIB	115.19	231.88

CTV, clinical target volume; PTV, planning target volume; M, male; F, female; SCC, squamous cell carcinoma; Adeno, adenocarcinoma.

Target and OAR delineation and volumes

The gross tumor volume (GTV), including the tumor and enlarged lymph nodes, was expanded by a 5 mm margin to yield the clinical target volume (CTV). In the case of nodal disease, adjacent intact lymph nodes were included in the CTV. A margin of 5 mm for upper and middle lobe tumors and 8 mm for tumors in the lower lobes was added to create the Planning Target Volume (PTV). PTV-fragmentation was performed to obtain the PTV without build-up (PTV_{whbu}), a part of the PTV beneath the skin resulting from subtraction of a 6-mm wide build-up region from the PTV [10]. Subtraction of expanded OARs from the PTV_{whbu} resulted in the optimization PTV (PTV_{optim}), a structure used in optimization.

OARs include heart, esophagus, lungs (ipsilateral and contralateral without the GTV) and spinal cord. To obtain the respective planning risk volumes (PRVs), the esophagus was expanded by a 3-mm (esophagus_exp_3 mm) and the spinal cord by a 5-mm margin (spinal_cord_exp_5 mm); expansion was not applied to the lungs.

Treatment planning objectives

A total dose of 70 Gy in 35 fractions of 2.0 Gy was prescribed to the PTV. Maximum dose of 50, 62 and 68 Gy was allowed to the spinal cord (PRV), heart, esophagus (PRV), respectively. $D_{33\%}$ and $D_{67\%}$ should not exceed 60 and 54 Gy, respectively, to the esophagus (PRV). Dose–volume constraints for the lungs were set as follows: $V_{20} < 30\%$, $V_{30} < 20\%$ and mean lung dose <27 Gy.

Treatment planning

The algorithm and tools used for IMRT planning of lung tumors were described before [9]. Briefly, identical beam angles and conformal beam shapes were used for both the 6 MV and 18 MV plans. The beam configuration was based on a class solution of 9 non-coplanar beams with a single isocenter where every beam was adjusted for each individual patient to meet the set dose–volume constraints for OARs. These adjustments sometimes resulted in a change in the number of beams, beam shape, gantry, couch and collimator angles. For every conformal beam, initial multileaf collimator defined beam segments were generated from the beam's eye view projections of the PTVs and OARs with an in-house developed Anatomy Based Segmentation Tool (ABST) [3]. The conformal beams and segments were passed as multileaf collimated beams to the convolution/superposition dose engine at the Pinnacle planning system (version 6.2 b, Philips Medical Systems, Andover, MA), which returned beam and segment-specific 3-D dose distributions. Initial beam and segment weights for the optimization process were generated using an in-house developed segment weight optimization tool (SWOT) [4]. The full set of dose distributions was passed to the in-house developed segment outline and weight adapting tool (SOWAT) [5] for segment weight and leaf position optimization. Dose computations between optimization cycles were performed by the collapse cone convolution/superposition dose engine at the Pinnacle planning system. The dose fall-off of the beamlets that are used to account for leaf position changes during optimization is too steep to incorporate effectively changes in distant scatter. The weight optimization of SOWAT takes into account wide scatter as optimization uses dose distributions that are computed per segment by the Pinnacle planning system. The optimization algorithm involves a bio-physical objective function [5,7].

When the treatment plan fulfilled the acceptance criteria, the CRASH (combine, reorder and step and shoot) tool resulted in a prescription file for the linear accelerator [6]. Six and 18 MV photons of the Elekta SL*i*plus linear accelerator were commissioned and validated previously [11,25].

MCDE was used for recomputation of the dose of the final plan [24]. For MCDE, DOSXYZnrc was reprogrammed as a component module within BEAMnrc [22]. Use of the DOSXYZnrc module allows one to combine the physical properties of the patients (e.g., the electron densities from the planning CTs) with the phase space files of the treatment machine generated by BEAMnrc. The result is a highly accurate dose engine that uses the electron transport algorithms of the EGSnrc Monte Carlo code.

Dose reporting and evaluation

We evaluated 2%, 95% and 98% dose levels ($D_{2\%}$, $D_{95\%}$ and $D_{98\%}$) and dose inhomogeneity for the following target structures: the GTV, CTV, PTV and $\mathrm{PTV}_{\mathrm{optim}}$; $D_{2\%}$, $D_{33\%}$, and $D_{67\%}$ were assessed for the heart, esophagus and esophagus_exp_3 mm; $D_{2\%}$ for the spinal cord and spinal_cord_exp_5 mm; mean lung dose, V_{20} and V_{30} for the lungs. $D_{2\%}$ and $D_{98\%}$ are used as surrogate for dose maximum and dose minimum, respectively [10]. Dose inhomogeneity has been calculated as $(D_{2\%} - D_{98\%})/D_{\mathrm{median}}$. Two-tailed paired sample *t*-test was used for comparison of numerical data between the two energies. A value of $p < 0.05$ was considered statistically significant.

Results

Comparison of dose distributions

Mean dose–volume parameters of the targets and OARs calculated for 6 MV and 18 MV photons with the CS algorithm and MCDE are presented in Tables 2 and 3, respectively. The tables also show the statistical significance of the differences using a two-tailed paired sample *t*-test. It can be seen from Table 2 that the PTV was underdosed in CS plans when 18 MV photons were used ($p > 0.05$ for $D_{2\%}$, $D_{98\%}$ and $D_{95\%}$). Eighteen MV photons provided significantly higher $D_{95\%}$ for the GTV and CTV comparing with 6 MV ($p = 0.004$ and 0.028 correspondently). However, this difference was not confirmed by MCDE computations (Table 3).

Table 2. Mean dose-volume parameters computed with the CS algorithm

End point		18 MV		6 MV		
		Mean	SD	Mean	SD	p
	Target					
$D_{2\%}$ (Gy)	GTV	72.64	0.88	72.92	1.58	0.422
	CTV	72.73	0.82	72.97	1.47	0.491
	PTV	72.61	0.74	72.84	1.37	0.479
	PTV_{optim}	72.63	0.74	72.85	1.37	0.488
$D_{98\%}$ (Gy)	GTV	66.80	3.34	66.30	2.40	0.252
	CTV	65.62	5.69	65.37	4.72	0.527
	PTV	62.92	5.94	63.37	5.13	0.296
	PTV_{optim}	63.58	5.42	64.27	4.32	0.154
$D_{95\%}$ (Gy)	**GTV**	**68.13**	**1.39**	**67.36**	**1.44**	**0.004**
	CTV	**67.23**	**3.00**	**66.87**	**2.83**	**0.028**
	PTV	64.49	5.30	64.83	4.48	0.372
	PTV_{optim}	65.63	3.86	65.78	3.39	0.607
Inhomogeneity	**GTV**	**0.08**	**0.05**	**0.09**	**0.06**	**0.007**
	CTV	**0.10**	**0.09**	**0.11**	**0.09**	**0.045**
	PTV	0.14	0.09	0.14	0.09	0.576
	PTV_{optim}	0.13	0.08	0.12	0.08	0.217
	Organ at risk					
$D_{2\%}$ (Gy)	Heart	28.62	19.05	31.07	16.63	0.401
	Esophagus	60.60	10.47	60.91	9.77	0.824
	Esophagus_exp_3 mm	62.53	8.16	63.14	6.82	0.549
	Spinal cord	30.18	12.97	26.59	13.63	0.313
	Spinal cord_exp_5 mm	33.07	12.20	29.41	13.61	0.294
$D_{33\%}$ (Gy)	Heart	11.49	12.21	9.66	11.82	0.423
	Esophagus	41.59	16.48	39.50	18.84	0.129
	Esophagus_exp_3 mm	40.99	17.00	38.96	19.41	0.161
$D_{67\%}$ (Gy)	Heart	6.23	8.63	5.00	7.22	0.241
	Esophagus	6.01	6.58	5.68	6.39	0.504
	Esophagus_exp_3 mm	5.69	5.88	5.60	6.21	0.839
V_{20} (%)	Lungs	27.14	12.89	26.99	14.63	0.899
V_{30} (%)	Lungs	14.28	6.75	13.03	6.59	0.252
Mean lung dose (Gy)	Lungs	14.55	4.80	14.55	4.69	0.997

SD, standard deviation; GTV, gross tumor volume; CTV, clinical target volume; PTV, planning target volume; PTV_{optim}, PTV for optimization; $D_{2\%}$, $D_{67\%}$, $D_{95\%}$ and $D_{98\%}$, dose levels on the DVHs above which lay 2%, 67%, 95% and 98% of the contoured volume; V_{20}, relative volume of the lung receiving at least 20 Gy; V_{30}, relative volume of the lung receiving at least 30 Gy. Significant differences ($p < 0.05$) are in bold.

Table 3. Mean dose-volume parameters computed with Monte Carlo dose engine

End point		18 MV		6 MV		
		Mean	SD	Mean	SD	p
	Target					
$D_{2\%}$ (Gy)	GTV	73.17	1.21	73.98	1.43	0.053
	CTV	73.33	1.12	74.13	1.49	0.093
	PTV	73.22	1.14	74.03	1.38	0.067
	$\text{PTV}_{\text{optim}}$	73.26	1.19	74.05	1.39	0.077
$D_{98\%}$ (Gy)	GTV	65.18	3.46	65.74	3.01	0.116
	CTV	64.03	5.96	64.90	4.87	0.071
	PTV	**62.31**	**6.25**	**63.27**	**5.47**	**0.015**
	$\text{PTV}_{\text{optim}}$	**62.94**	**5.73**	**63.94**	**4.87**	**0.028**
$D_{95\%}$ (Gy)	GTV	66.56	1.71	67.00	1.87	0.258
	CTV	**65.64**	**3.42**	**66.22**	**3.61**	**0.027**
	PTV	**63.64**	**5.78**	**64.62**	**4.99**	**0.009**
	$\text{PTV}_{\text{optim}}$	**64.83**	**3.94**	**65.48**	**3.84**	**0.014**
Inhomogeneity	GTV	0.11	0.05	0.12	0.06	0.642
	CTV	0.13	0.09	0.13	0.09	0.434
	PTV	0.16	0.09	0.15	0.09	0.081
	$\text{PTV}_{\text{optim}}$	0.15	0.08	0.14	0.09	0.081
	Organ at risk					
$D_{2\%}$ (Gy)	Heart	29.26	18.61	31.60	16.30	0.408
	Esophagus	60.55	10.61	61.34	9.89	0.523
	Esophagus_exp_3 mm	62.61	8.12	63.61	7.25	0.250
	Spinal cord	31.41	12.67	27.89	13.50	0.310
	Spinal cord_exp_5 mm	34.15	12.17	30.65	13.52	0.310
$D_{33\%}$ (Gy)	Heart	12.03	11.98	10.36	11.61	0.452
	Esophagus	**42.49**	**16.54**	**39.72**	**18.64**	**0.045**
	Esophagus_exp_3 mm	41.83	16.91	39.43	19.37	0.116
$D_{67\%}$ (Gy)	Heart	6.68	8.57	5.64	7.32	0.316
	Esophagus	6.82	6.68	6.27	5.98	0.315
	Esophagus_exp_3 mm	6.43	5.94	6.16	5.82	0.516
V_{20} (%)	Lungs	24.63	9.72	23.32	8.77	0.272
V_{30} (%)	Lungs	18.50	7.62	17.46	7.34	0.057
Mean lung dose (Gy)	Lungs	15.37	4.70	15.27	4.65	0.730

SD, standard deviation; GTV, gross tumor volume; CTV, clinical target volume; PTV, planning target volume; $\text{PTV}_{\text{optim}}$, PTV for optimization; $D_{2\%}$, $D_{67\%}$, $D_{95\%}$ and $D_{98\%}$, dose levels on the DVHs above which lay 2%, 67%, 95% and 98% of the contoured volume; V_{20}, relative volume of the lung receiving at least 20 Gy; V_{30}, relative volume of the lung receiving at least 30 Gy. Significant differences ($p < 0.05$) are in bold.

MCDE computations demonstrated superiority of 6 MV over 18 MV in dose coverage ($D_{95\%}$ and $D_{98\%}$) of the PTV (p = 0.009 and 0.015) (Fig. 1), PTV$_{\text{optim}}$ (p = 0.014 and 0.028) and $D_{95\%}$ in the CTV (p = 0.027). Dose inhomogeneity in the PTV did not differ between the two energies for both the CS and MCDE calculations. Dose inhomogeneity in the GTV and CTV for CS but not for MCDE was lower with 18 MV than with 6 MV photons (Tables 2 and 3). There was no significant difference between both energies in sparing of the lungs – V_{20}, V_{30} and mean lung dose did not exceed the set planning constraints (Table 2). In comparison with MCDE there was overestimation in V_{20} for individual patients whose plans did not meet lung dose–volume constraints (Fig. 2). V_{30} was at the border of significance (p = 0.057). Change of energy did not affect $D_{33\%}$ for the esophagus in CS plans but MCDE revealed a significantly (p = 0.045) higher value for 18 MV photons. As can be seen from Tables 2 and 3 and Fig. 1, the differences between other target and OAR dose–volume parameters were smaller than uncertainty for the two energies and both computation algorithms.

Dose distributions and tumor location

We studied the influence of target location on dose coverage of the targets and OARs in individual patients (Table 1 and patient numbers in Figs. 1 and 2). All treatment planning objectives for the targets and all OARs with the lowest V_{20} and V_{30} were achieved for the two energies and for CS and MCDE in patients number 4 and 8 bearing a peripheral middle sized tumor in the left and right upper lobe, respectively. Though, all treatment plans of patient number 1 met dose–volume constraints. Treatment plans of 3 patients did not meet the lung dose–volume constraints V_{20} and/or V_{30}. In patients number 5 and 7 with tumors in the lower lobe V_{20} exceeded the planning objectives for both energies and for the two calculation algorithms (Fig. 2). The index V_{30} was less than 20 Gy in CS plans for both energies in patient number 5 (data not shown). Patient number 6 had two separate tumor lesions located in the same lobe that resulted in irradiation of the large lung volume and thus making impossible to keep V_{20} (Fig. 2) and V_{30} (data not shown) below the set values. In the rest of patients with tumors located centrally or in the lower lobe, $D_{2\%}$ exceeded the constraints for the heart (patient number 2, CS plans with 6 MV and 18 MV photons), esophagus and/or esophagus_exp_3 mm (patients number 3, 9, 10 in CS plans regardless the energy; patients number 2 and 9 with the two energies and patient number 10 MV with 18 MV photons in MCDE plans) (data not shown).

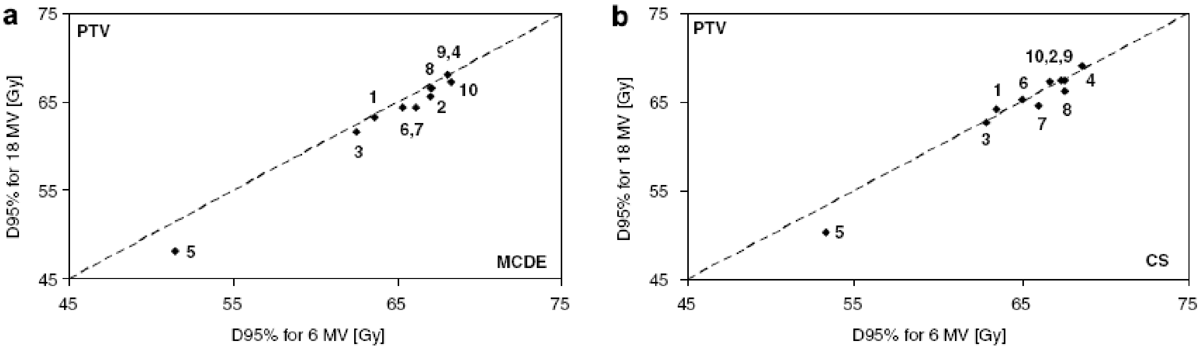

Fig. 1. Comparison of $D_{95\%}$ in the PTV computed with MCDE (a) and with the CS algorithm (b) for 6 MV (abscissa) and 18 MV photons (ordinate). Each diamond represents data of an individual patient indicated by Arabic numbers. The dashed line indicates the line of identity. If the diamonds fall below the diagonal identity line then they show an advantage for the 6 MV plans, while if they lie above the diagonal identify line they show an advantage for the 18 MV plans.

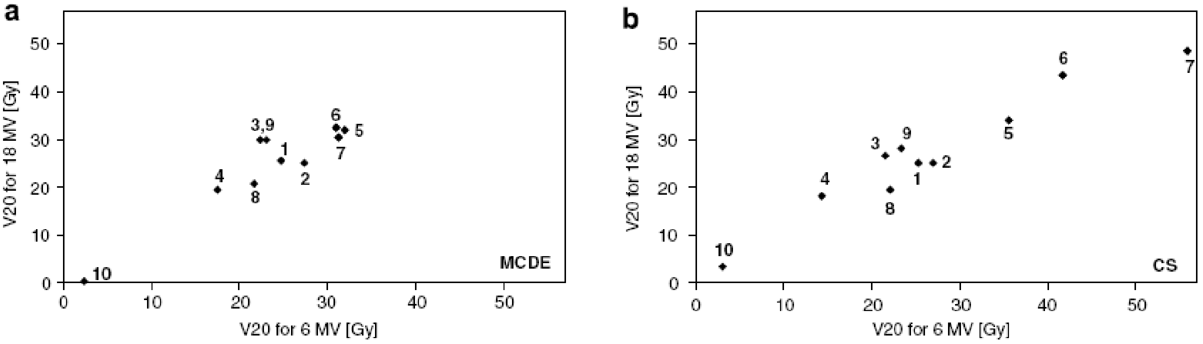

Fig. 2. Comparison of V_{20} computed with MCDE (a) and with the CS algorithm (b) for 6 MV (abscissa) and 18 MV photons (ordinate). Symbols represent data of an individual patient indicated by Arabic numbers.

Discussion

In this study, we compared IMRT treatment plans for a typical NSCLC cohort with middle to large size tumors with 6 MV and 18 MV photon beams. The observed differences in dose coverage of the targets and OARs between the 6 MV and 18 MV plans were insignificant except higher $D_{95\%}$ for the CTV and GTV, lower inhomogeneity in the CTV and GTV and underdosage of PTV in 18 MV plans. PTV underdosage may be explained by differences in secondary electron transport in low density tissues caused by lower- and higher-energy photons. Loss of electronic equilibrium in the lungs results in enlarged beam penumbra and blurring of the dose at the beam edge, compromising dose homogeneity and irradiating larger volumes of the lung [12,20]. In case of conflict between the underdosage to the PTV and dose–volume constraints for OARs such as lungs and spinal cord, it is our policy to give priority to dose–volume constraints for OARs with the aim to achieve the prescribed dose in the CTV or GTV.

It appears that benefit from 6 MV photon beams may not be so obvious when different beam arrangements are applied. Beam configuration can influence the effects of electronic equilibrium and increase them with increase in number of beams that may favor higher energies, particularly in dose escalation [2]. To exclude influence of beam configuration, the same beam arrangements were used for higher and lower energy IMRT treatment plans. We did not find advantage of 6 MV over 18 MV photons in dose coverage of the targets.

Any calculation algorithm used for dose computation in IMRT planning of lung cancer should take into account tissue density and secondary electron transport [8]. We wanted to evaluate the observed dose deviations between lower- and higher-energy treatment plans using MCDE for final dose calculations. A detailed comparison of different dose calculation algorithms, including CS and MCDE, for IMRT of lung cancer was published by Vanderstraeten et al. [24]. They described differences between MCDE and other algorithms putting forward MCDE as a benchmarking tool. For our treatment plans, MCDE generally favored 6 MV photons while for CS 18 MV was better. Still, the observed deviations were quite small. MCDE calculations performed in the present study are based on the most accurate EGSnrc electron transport algorithms [14]. Possibly incomplete account for loss of electronic equilibrium in the lungs by the CS algorithm compared to MCDE has resulted in discrepancy between both calculations. Moreover, using the CS dose engine might have misled the optimization tool. Due to present limitations in computer power, MCDE calculations were only performed for recomputing the dose of the final plan. If MCDE computation had been used as start of optimization, the results might have been different from those observed. In absence of fast Monte Carlo algorithms, Monte Carlo may still be used to verify target coverage in case of applying other algorithms [26].

Our results are in agreement with the report of Liu et al. who did not find any noticeable difference in the quality of IMRT plans applying 6 MV and 18 MV photons, though 18 MV were less preferable due to greater loss of lateral electronic equilibrium [16]. Nevertheless, target location may influence selection of photon energy. The peripheral or cranially located PTV may be planned to higher doses as its location appears to compromise dose-volume constraints less than the PTVs with more central or caudal location [9]. In our study, independently of energy and dose computation algorithm, patients with peripheral tumors in the upper lobes showed the best dose distributions in all targets and best sparing OARs. In other cases of the cranially sited tumors dose coverage was not as good as expected due to target complexity; central location of tumor may advocate use of lower energy. Photon energy may not have significant impact on dose distribution in peripheral cranially located tumors. More caution should be taken in selecting photon energy in case of central and lower lobe tumors.

Conclusions

We have compared 6 MV and 18 MV photons for IMRT treatment of NSCLC, as applied in the Radiotherapy Department of the Ghent University Hospital. IMRT of NSCLC resulted in dose degradation and higher inhomogeneity in the PTV when using 18 MV as compared to 6 MV photon beams. Using for final dose calculation MCDE algorithm also favored 6 MV in dose coverage of the PTV. Selection of 18 MV or 6 MV photons for IMRT of lung cancer depends on priority ranking of the endpoints as well as the individual patient. In the absence of highly accurate and, therefore, acceptable dose computation algorithms such as MCDE and CS, 6 MV photons may be the prudent choice.

Acknowledgements

The project ''Conformal Radiotherapy Ghent University Hospital'' is supported by the Stichting tegen Kanker (Grants 51AC8904, FBC2003/2006 and ZKB2747), Fund of Scientific Research – Flanders (Grant G.0183.03), Ghent University (Grants GOA 12050401, BOF 01112300, 011VO497, 011B3300), and the Centrum voor Studie en Behandeling van Gezwelziekten. B. Vanderstraeten is a research assistant (aspirant) of the FWO.

Nick Reynaert and Bart De Smedt are acknowledged for supporting the Monte Carlo simulations.

References

[1] Arnfield MR, Siantar CH, Siebers J, et al. The impact of electron transport on the accuracy of computed dose. Med Phys 2000;27:1266–74.

[2] Blomquist M, Li J, Ma CM, et al. Comparison between a conventional treatment energy and 50 MV photons for the treatment of lung tumours. Phys Med Biol 2002;47:889–97.

[3] De Gersem W, Claus F, De Wagter C, et al. An anatomy-based beam segmentation tool for intensity-modulated radiation therapy and its application to head-and-neck cancer. Int J Radiat Oncol Biol Phys 2001;51:849–59.

[4] De Gersem WR, Derycke S, Colle CO, et al. Inhomogeneous target-dose distributions: a dimension more for optimization? Int J Radiat Oncol Biol Phys 1999;44:461–8.

[5] De Gersem W, Claus F, De Wagter C, et al. Leaf position optimization for step-and-shoot IMRT. Int J Radiat Oncol Biol Phys 2001;51:1371–88.

[6] De Neve W, De Gersem W, Derycke S, et al. Clinical delivery of intensity modulated conformal radiotherapy for relapsed or second-primary head and neck cancer using a multileaf collimator with dynamic control. Radiother Oncol 1999;50:301–14.

[7] De Neve W, De Gersem W, De Meerleer G, et al. In response to Drs. Vaarkamp and Krasin. Int J Radiat Oncol Biol Phys 2001;49:1519–20.

[8] De Neve W, De Wagter C. Lethal pneumonitis in a phase I study of chemotherapy and IMRT for NSCLC: the need to investigate the accuracy of dose computation. Radiother Oncol 2005;75:246–7.

[9] De Neve W, Chaltin M, Vandecasteele K, et al. Intensitymodulated radiation therapy for lung cancer. In: Jeremic B, editor. Advances in Radiation Oncology in Lung Cancer. Berlin, Heidelberg, New York: Springer; 2005. p. 423–34.

[10] De Neve W, Wu Y, Ezzel G. Practical IMRT planning. In: Bortfeld T, Schmidt-Ulrich R, De Neve W, Wazer D, editors. Image-guided IMRT. Berlin, Heidelberg: Springer; 2006. p. 47–59.

[11] De Smedt B, Reynaert N, Flachet F, et al. Decoupling initial electron beam parameters for Monte Carlo photon beam modelling by removing beam-modifying filters from the beam path. Phys Med Biol 2005;50:5935–51.

[12] Dirkx ML, Heijmen BJ, Korevaar GA, et al. Field margin reduction using intensity-modulated X-ray beams formed with a multileaf collimator. Int J Radiat Oncol Biol Phys 1997;38:1123–9.

[13] Ekstrand KE, Barnes WH. Pitfalls in the use of high energy X rays to treat tumors in the lung. Int J Radiat Oncol Biol Phys 1990;18:249–52.

[14] Kawrakow I, Rogers DWO. The EGSnrc code system: Monte Carlo simulation of electron and photon transport. 2000, NRCC Report PIRS-701, National Research Council of Canada, Ottawa.

[15] Kornelsen RO, Young ME. Changes in the dose-profile of a 10 MV X-ray beam within and beyond low density material. Med Phys 1982;9:114–6.

[16] Liu HH, Wang X, Dong L, et al. Feasibility of sparing lung and other thoracic structures with intensity-modulated radiotherapy for non-small-cell lung cancer. Int J Radiat Oncol Biol Phys 2004;58:1268–79.

[17] Mackie TR, el-Khatib E, Battista J, et al. Lung dose corrections for 6- and 15-MV X rays. Med Phys 1985;12:327–32.

[18] Martens C, Reynaert N, De Wagter C, et al. Underdosage of the upper-airway mucosa for small fields as used in intensitymodulated radiation therapy: a comparison between radiochromic film measurements, Monte Carlo simulations, and collapsed cone convolution calculations. Med Phys 2002;29:1528–35.

[19] Mijnheer BJ, Rice RK, Chin LM. Lead–polystyrene transition zone dosimetry in high-energy photon beams. Radiother Oncol 1988;11:379–86.

[20] Miller RC, Bonner JA, Kline RW. Impact of beam energy and field margin on penumbra at lung tumor-lung parenchyma interfaces. Int J Radiat Oncol Biol Phys 1998;41:707–13.

[21] Radiation Therapy Oncology Group, Int. No. 105, Prospective randomised trial of postoperative adjuvant therapy in patients with completely resected stage II and stage IIIa non-small cell lung cancer, RTOG 91-05 revised edition, August 24, 1992.

[22] Reynaert N, De Smedt B, Coghe M, et al. MCDE: a new Monte Carlo dose engine for IMRT. Phys Med Biol 2004;49:241–53.

[23] Rice RK, Mijnheer BJ, Chin LM. Benchmark measurements for lung dose corrections for X-ray beams. Int J Radiat Oncol Biol Phys 1988;15:399–409.

[24] Vanderstraeten B, Reynaert N, Paalinck L, et al. Accuracy of patient dose calculation for lung IMRT: A comparison of Monte Carlo, convolution/superposition, and pencil beam computations. Med Phys 2006;33:3149–58.

[25] Van de Walle J, Martens C, Reynaert N, et al. Monte Carlo model of the Elekta SLiplus accelerator: validation of a new MLC component module in BEAM for a 6 MV beam. Phys Med Biol 2003;48:371–85.

[26] Wang L, Yorke E, Desobry G, et al. Dosimetric advantage of using 6 MV over 15 MV photons in conformal therapy of lung cancer: Monte Carlo studies in patient geometries. J Appl Clin Med Phys 2002;3:51–9.

[27] Werner BL, Das IJ, Khan FM, et al. Dose perturbations at interfaces in photon beams. Med Phys 1987;14:585–95.

[28] White PJ, Zwicker RD, Huang DT. Comparison of dose homogeneity effects due to electron equilibrium loss in lung for 6 MV and 18 MV photons. Int J Radiat Oncol Biol Phys 1996;34:1141–6.

Chapter 7

Publication 5:

Conversion of CT numbers into tissue parameters for Monte Carlo dose calculations: a multi-centre study

Barbara Vanderstraeten[1], Pik Wai Chin[2], Michael Fix[3], Antonio Leal[4], Grisel Mora[5], Nick Reynaert[1], Joao Seco[6], Martin Soukup[7], Emiliano Spezi[8], Wilfried De Neve[9] and Hubert Thierens[1]

[1] *Department of Medical Physics, Ghent University, Gent, Belgium*
[2] *Department of Medical Physics, Velindre Cancer Centre, Cardiff, United Kingdom*
[3] *Division of Medical Radiation Physics, Inselspital-University of Berne, Berne, Switzerland*
[4] *Department of Medical Physiology and Biophysics, University of Seville and Virgen Macarena Hospital, Seville, Spain*
[5] *Nuclear Physics Centre, University of Lisbon, Lisbon, Portugal*
[6] *Department of Radiation Oncology, Massachusetts General Hospital and Harvard Medical School, Boston, MA, USA*
[7] *Section for Biomedical Physics, University Hospital Tuebingen, Tuebingen, Germany*
[8] *Servizio di Fisica Sanitaria, Policlinico S.Orsola Malpighi, Bologna, Italy*
[9] *Department of Radiotherapy, Ghent University Hospital, Gent, Belgium*

Physics in Medicine and Biology 2007;52:539-562

Abstract

The conversion of computed tomography (CT) numbers into material composition and mass density data influences the accuracy of patient dose calculations in Monte Carlo treatment planning (MCTP). The aim of our work was to develop a CT conversion scheme by performing a stoichiometric CT calibration. Fourteen dosimetrically equivalent tissue subsets (bins), of which ten bone bins, were created. After validating the proposed CT conversion scheme on phantoms, it was compared to a conventional 5 bin scheme with only 1 bone bin. This resulted in dose distributions D_{14} and D_5 for nine clinical patient cases in a European multi-centre study. The observed local relative differences in dose to medium were mostly smaller than 5%. The dose–volume histograms of both targets and organs at risk were comparable, although within bony structures D_{14} was found to be slightly but systematically higher than D_5. Converting dose to medium to dose to water (D_{14} to D_{14wat} and D_5 to D_{5wat}) resulted in larger local differences as D_{5wat} became up to 10% higher than D_{14wat}. In conclusion, multiple bone bins need to be introduced when Monte Carlo (MC) calculations of patient dose distributions are converted to dose to water.

1. Introduction

In Monte Carlo treatment planning (MCTP), the conversion of computed tomography (CT) numbers into material properties is one of the main factors that determine the accuracy of patient dose calculations (du Plessis *et al* 1998). To interrelate the CT number and the electron density (or stopping power for protons) of a tissue, the CT number scale is often divided into a number of subsets (DeMarco *et al* 1998, Hartmann Siantar *et al* 1997, Ma *et al* 1999, Wang *et al* 1998). Typically, six or less different media are defined, e.g. air, lung, fat, water, muscle and bone. Certain Monte Carlo (MC) implementations use a larger number of materials, e.g. MCV (Siebers *et al* 2000a) and the commercial implementation by Nucletron of the VMC++ code (Kawrakow 2001). These systems use over 50 and over 20 materials, respectively. Verhaegen and Devic (2005) have shown that the misassignment of media can lead to large dose errors in MCTP (up to 10% for MV photons). The CT scanner is often calibrated using tissue equivalent materials. However, the elemental composition of those tissue substitutes differs from that of real tissues, resulting in significantly different calibration curves of CT number to electron density (or proton stopping power). For an accurate extraction of tissue properties from CT data, a stoichiometric calibration method was proposed by Schneider *et al* (1996). First, a set of materials (which do not necessarily have to be tissue equivalent) with known elemental compositions and physical densities is scanned to measure the corresponding CT numbers. Next, the results are fitted to a theoretical parameter equation interrelating the CT number and the physical density and atomic number (Z) of each material, at the effective energy of the kV imaging spectrum. Finally, the fitted parameters can be used to calculate the CT numbers of real tissues using tabulated composition data.

The influence of differences in tissue composition on MC dose calculations has been investigated by du Plessis *et al* (1998). They combined the 16 most common human tissue types into dosimetrically equivalent subsets with constant elemental composition by performing MC calculations within homogeneous phantoms. Using a clinical 8 MV photon beam, seven subsets were found to be sufficient to obtain a dose calculation accuracy of 1%. However, for lung and bone further subdivision turned out to be necessary by varying the physical density while keeping the elemental composition constant. The disadvantage of the method of du Plessis *et al* (1998) is that the application of the resulting CT conversion is limited to the beam quality under consideration. Schneider *et al* (2000) therefore proposed a CT conversion method for MC simulations based on the stoichiometric calibration method. Considering

71 human tissues, they created 24 different subsets with constant elemental composition based on the estimated accuracy of the calculated CT numbers.

Instead of converting CT numbers into tissue parameters like elemental composition and mass density, one could also directly extract interaction probabilities from the CT number. This approach is used by the electron MC code VMC (Kawrakow *et al* 1996) and its photon extension XVMC (Fippel 1999). The main advantage is that there is no need to specify any boundaries separating tissue subsets. However, most MC codes explicitly need the elemental composition within each patient voxel to obtain interaction data for dose calculations. Therefore, the VMC/XVMC approach is more difficult to implement in such codes.

The aim of our work was to propose a CT conversion method that is based on the stoichiometric calibration method and that makes use of dosimetrically equivalent tissue subsets based on a clinical 6 MV photon beam, in order to combine the methods of Schneider *et al* (2000) and du Plessis *et al* (1998). Evaluations were performed by means of a MC slab phantom and the Gammex RMI 461A head/body CT phantom using inserts from the Gammex RMI 465 electron density CT phantom (Gammex RMI, Middleton, WI, USA). Furthermore, the effect of selecting a different photon beam quality (15 MV photons) or a different beam modality (electrons) was investigated. The resulting 6 MV photon binning scheme was compared to a conventional scheme with only 5 bins. For this purpose a multi-centre study was set up. A stoichiometric CT calibration was performed at seven European centres. Finally, our investigation was focused towards the clinical evaluation of patient treatment plans. Attention was paid to the conversion from dose to medium to dose to water.

2. Materials and methods

2.1. Influence of material composition on photon attenuation and energy deposition

The elemental composition of a material influences dose calculation both through its attenuation and energy deposition characteristics. To determine for which types of human tissue an accurate CT conversion is important and why, mass attenuation coefficients and mass stopping power values were studied for a set of materials (air, water, lung, adipose, muscle, cartilage and cortical bone) as well as for the individual elements that are present within these materials. The attenuation coefficients of the individual elements were taken from the National Institute of Standards and Technology (NIST) photon cross sections (XCOM) database[10] (Hubbell and Seltzer 2004). The mass attenuation coefficient of a mixture can be calculated as the weighted sum of the coefficients of the constituent elements (Jackson and Hawkes 1981). The elemental composition of the human tissues was obtained from ICRU report 44 (ICRU 1989). Mass stopping power values for both the individual elements and human tissues were computed using the NIST electron stopping power and range (ESTAR) database[11].

2.2. Stoichiometric calibration

The following set of materials with known elemental composition was used to calibrate the Siemens Somatom Plus 4 CT scanner at Ghent University Hospital (GUH): PMMA, polystyrene, Gammex RMI solid water, Gammex RMI lung equivalent material and $CaCl_2$ solutions in water of 5, 10, 15, 20, 25, 30 and 35% by weight (maximum solubility around 40%). Table 1 reports their mass density and elemental composition data. A scan protocol used routinely for radiotherapy treatment planning was selected; the tube voltage was 120 kV. For each material the average CT number and standard deviation were determined within a manually drawn region of interest (ROI) on the CT image. Depending on the shape of each material sample, a circular or rectangular ROI was used in order to cover an area as large as possible within the homogeneous material. The stoichiometric calibration procedure of Schneider *et al* (1996) was applied. It makes use of the following empirical formula for parametrization of the total attenuation coefficient μ of a mixture of elements (with elemental weights w_i , atomic numbers Z_i and atomic masses A_i) provided by Jackson and Hawkes (1981):

$$\mu = \rho N_A \sum_{i=1}^{n} \left(\frac{w_i}{A_i} \left(K^{ph} Z_i^{4.62} + K^{coh} Z_i^{2.86} + K^{KN} Z_i \right) \right). \quad (1)$$

In this formula ρ is the mass density and N_A is the Avogadro constant. K^{ph} characterizes the cross section of photoelectric absorption, while K^{coh} characterizes the cross sections of both the coherent scattering and the binding correction for the incoherent scattering. K^{KN} represents the Klein–Nishina coefficient. K^{ph}, K^{coh} and K^{KN} depend on the effective energy of the CT scanner spectrum. The CT number H is expressed in Hounsfield units (HU) and calculated as follows:

---

[10] Available online: http://physics.nist.gov/PhysRefData/Xcom/Text/XCOM.html.

[11] Available online: http://physics.nist.gov/PhysRefData/Star/Text/ESTAR.html.

Table 1. Mass density ρ and elemental weights w_i of the set of materials used for the stoichiometric calibration of the Siemens Somatom Plus 4 CT scanner at Ghent University Hospital.

Material	ρ (g cm^{-3})	w_H	w_C	w_N	w_O	w_{Mg}	w_{Si}	w_{Cl}	w_{Ca}
PMMA	1.190	0.081	0.599	0	0.320	0	0	0	0
Polystyrene	1.040	0.077	0.923	0	0	0	0	0	0
Gammex RMI solid water[a]	1.035	0.081	0.673	0.024	0.198	0	0	0.001	0.023
Gammex RMI lung equivalent material[a]	0.300	0.085	0.593	0.020	0.181	0.112	0.008	0.001	0
$CaCl_2$ solution 5%	1.035	0.106	0	0	0.844	0	0	0.032	0.018
$CaCl_2$ solution 10%	1.080	0.101	0	0	0.799	0	0	0.064	0.036
$CaCl_2$ solution 15%	1.126	0.095	0	0	0.755	0	0	0.096	0.054
$CaCl_2$ solution 20%	1.171	0.090	0	0	0.710	0	0	0.128	0.072
$CaCl_2$ solution 25%	1.216	0.084	0	0	0.666	0	0	0.160	0.090
$CaCl_2$ solution 30%	1.261	0.078	0	0	0.622	0	0	0.192	0.108
$CaCl_2$ solution 35%	1.307	0.073	0	0	0.577	0	0	0.224	0.126

[a] As supplied by the manufacturer.

$$H = 1000\left(\frac{\mu}{\mu_{water}} - 1\right). \qquad (2)$$

As we only need the attenuation coefficient relative to water to calculate the CT number, only two parameters (K^{ph}/K^{KN} and K^{coh}/K^{KN}) have to be determined by a fit of the measured CT numbers to equations (1) and (2).

The above-mentioned set of calibration materials allowed us to perform a CT scanner calibration for a large range of CT number values through the range of $CaCl_2$ solutions. However, the fact that these solutions need to be fabricated in-house complicated the calibration of CT scanners at other centres. Therefore, a Gammex RMI 465 electron density CT phantom was sent around to perform the stoichiometric calibration. This phantom consists of a 33 cm diameter disc made out of Gammex RMI solid water that includes a matrix of twenty 2.8 cm diameter holes. Interchangeable rods of various tissue and water substitutes can be fitted into these holes. For the calibrations 17 different material inserts were used: LN-300 and LN-450 lung equivalent materials, AP6 adipose, polyethylene, breast, CT solid water, CB3 resin, CT solid water, brain, liver, IB1 inner bone, CB4 resin, acrylic, B200 bone mineral, CB2–10% $CaCO_3$, CB2–30% $CaCO_3$, CB2–50% $CaCO_3$ and SB3 cortical bone. Their mass density and elemental composition data were reported by Watanabe

(1999). Circular ROIs with a diameter of approximately 2.5 cm were drawn manually on the CT images to determine the average CT number and its standard deviation for each insert. So, the ROIs were approximately the same among the centres. To evaluate the stoichiometric calibration using the Gammex RMI 465 phantom, the phantom was first scanned on the Siemens Somatom Plus 4 CT scanner at GUH and the measured CT numbers for each insert were compared to calculations based on the original stoichiometric calibration (using the set of materials listed in table 1). The same scan protocol was used for both calibrations. Next, the phantom was sent to seven different centres in Europe. A list of the studied CT scanner types and their respective locations can be found in table 2. Each centre used a different scan protocol, depending on the local radiotherapy treatment planning procedure.

Table 2. Results of the stoichiometric calibration using the Gammex RMI 465 electron density CT phantom. All measurements were performed at a tube voltage of 120 kV.

CT scanner	Location	K^{ph}/K^{KN}	K^{coh}/K^{KN}
Siemens Somatom Plus 4	Ghent University Hospital, Belgium	4.24×10^{-5} [a]	-1.77×10^{-3} [a]
Philips Gemini GXL PET/CT	Ghent University Hospital, Belgium	1.99×10^{-5}	9.26×10^{-4}
Siemens Somatom Sensation Open	University Hospital Tübingen, Germany	2.11×10^{-5}	3.70×10^{-4}
Siemens Somatom Sensation Open	Velindre Cancer Centre, Cardiff, UK	2.30×10^{-5}	3.49×10^{-5}
Siemens Somatom Sensation Cardiac 64	Clinica Quadrantes, Lisbon, Portugal	2.65×10^{-5}	-2.84×10^{-4}
Toshiba Xvision/EX	HUV Macarena, Seville, Spain	3.89×10^{-5}	-8.37×10^{-4}
GE HiSpeed QX/i	Royal Marsden Hospital, London, UK	2.78×10^{-5}	-3.98×10^{-4}
GE ProSpeed	Inselspital Radioonkologie, Bern, Switzerland	1.11×10^{-5}	4.79×10^{-3}

[a] Stoichiometric calibration using the set of materials from table 1 instead of the Gammex RMI 465 phantom.

2.3. *Dosimetrically equivalent tissue subsets*

After the stoichiometric calibration of each CT scanner, the fitted values of K_{ph}/K_{KN} and K_{coh}/K_{KN} were used to calculate the CT numbers of the 71 human tissues that were also considered by Schneider *et al* (2000, tables 3–

5). Mass density and elemental composition data were taken from literature (Woodard and White 1986, White *et al* 1987, ICRU 1989).

The mass density was calibrated continuously in terms of the CT number, as a different value can be assigned to each individual voxel of a MC scoring grid in the BEAMnrc/DOSXYZnrc system (Rogers *et al* 2002). A mass density calibration curve consisting of three separate linear least-squares fits (for air and lung, soft tissues, and bone tissues) was created for each of the CT scanners listed in table 2.

To extract the elemental composition data, the CT number scale was divided into dosimetrically equivalent tissue subsets (bins). To determine the necessary number of subsets, DOSXYZnrc calculations were performed within homogeneous phantoms with dimensions of $31 \times 31 \times 20$ cm^3. The incident beam was a 10×10 cm^2 6 MV photon field produced by the Elekta SL*i*plus linear accelerator at GUH (Van de Walle *et al* 2003). The dimensions of the scoring grid voxels on the central axis were 1 cm in the X and Y directions for all voxels, and 2 mm (voxels 1–20), 4 mm (voxels 21–25) and 1 cm (voxels 26–39) in the Z direction. For each voxel on the central axis, our aim was to keep the maximum deviation between the depth dose curves calculated within two materials representing adjacent tissue subsets below 1%. The statistical uncertainty (1σ) of the MC calculations was less than 0.5% within each voxel on the central axis. Depth dose curves were calculated for air, lung, soft tissues and bone tissues. Each tissue subset was represented by the elemental composition that corresponds with the mean CT number of the subset. As suggested by Schneider *et al* (2000), the elemental composition of human adipose, muscle or bone tissues can be interpolated in good approximation between either adipose tissue 3 and adrenal gland, GI tract and connective tissue, or bone marrow and cortical bone, depending on the CT number. Starting from a conventional 5 bin scheme (air, lung, adipose, muscle and bone), additional bins were inserted and the corresponding depth dose curves were calculated until the above-mentioned accuracy requirement was fulfilled. To eliminate the influence of mass density on the determination of the number of subsets, it was set to 1 g cm^{-3} for all materials. The number of tissue subsets necessary to achieve dosimetric equivalence within 1% was determined for the Siemens Somatom Plus 4 CT scanner at GUH. An equal number of bins were created for the other CT scanners listed in table 2, taking into account their individual stoichiometric calibration.

To evaluate whether the proposed binning scheme for 6 MV photons is also sufficient for MC calculations using another beam modality and/or a different energy, similar depth dose curves were calculated for the proposed bone subset materials of the Siemens Somatom Plus 4 CT scanner at GUH using a 15 MV photon beam and a 6.6 MeV electron beam (Gaussian energy spectrum with a full width at half maximum value of 0.2 MeV), respectively.

2.4. MC slab phantoms

To evaluate our division of the human bone tissues into a number of subsets, we first performed DOSXYZnrc calculations within MC phantoms. Two heterogeneous slab geometries were defined, consisting of a 0.1 cm and a 1 cm thick layer of bone, respectively, embedded within adipose tissue. The phantom dimensions were 31 × 31 × 16 cm^3. The bone layers were located perpendicularly to the Z-axis either between $Z = 5$ cm and $Z = 5.1$ cm depth or between $Z = 5$ cm and $Z = 6$ cm depth. The incident beam was the 10 × 10 cm^2 6MV photon field produced by the Elekta SL*i*plus linear accelerator at GUH. The dimensions of the scoring grid voxels on the central axis were 1 cm in the X and Y directions for all voxels, and down to 0.5 mm in the Z direction for the voxels close to the interfaces between the adipose tissue and the bone layer.

The vertebral column was used to represent the bone layer. Its CT number was calculated using the stoichiometric calibration data of the Siemens Somatom Plus 4 CT scanner at GUH; the elemental composition data were taken from White *et al* (1987). For each geometry (with a 0.1 cm or a 1 cm bone layer), depth dose curves were calculated with the bone layer represented according to the new binning scheme (with multiple bone bins) on the one side, and a conventional binning scheme with a single bone bin representing the material composition of ICRU cortical bone (ICRU 1989) on the other side. For both calculations equal values of the mass density were assigned to the bone layer. The value was derived from the calculated CT number using the mass density calibration curve of the Siemens Somatom Plus 4 CT scanner at GUH. The resulting depth dose curves were compared voxel by voxel along the Z-axis as well as by calculating differences in area below the curves within the bone layer.

2.5. Gammex RMI 461A head/body CT phantom

In addition to the MC slab phantoms, the accuracy of our CT conversion procedure was evaluated on the Gammex RMI 461A phantom. This phantom consists of a 33 cm outer diameter annulus made out of RMI solid water with a central hole into which the inserts of the Gammex RMI 465 tissue calibration phantom can be fitted. The following six inserts were used: LN-300 and LN-450 lung equivalent materials, B200 bone mineral, CB2–10% $CaCO_3$, CB2–30% $CaCO_3$ and CB2–50% $CaCO_3$.

DOSXYZnrc was used to calculate dose profiles within a large water phantom positioned 100 cm below the source of the Elekta Precise linear accelerator. The incident beam was a 6MV photon field with dimensions of 10×10 cm^2 at the phantom surface. The Gammex RMI 461A phantom was placed just below the water surface and the dose profiles were determined along the X-axis at depths of 12 cm and 15 cm below the phantom. The phantom was scanned on the Siemens Somatom Plus 4 scanner at GUH with the different inserts specified above. For each insert, the average CT number was determined within a manually drawn circular ROI with a diameter of approximately 2.5 cm. Next, the CT number was converted into a homogeneous material composition and mass density. Two sets of DOSXYZnrc calculations were performed, one using the material properties derived from our CT conversion and another by modelling the phantom with the exact material properties. The dimensions of the scoring grid voxels along the calculated dose profiles were 0.25 × 1 × 4 cm^3.

2.6. Patient dose calculations

Finally, our CT conversion procedure was evaluated on patients. Nine patient cases were selected at four different centres (patient numbers 1, 2–3, 4–6 and 7–9, respectively), of which three oropharyngeal cancer patients (patient numbers 1, 3 and 8), three laryngeal cancer patients (5, 6 and 9), one lung cancer patient (2), one breast cancer patient (4) and one patient with a brain tumour (7). Patients 7 and 8 were treated using a 3D conformal treatment technique, while patients 1–3, 4–5 and 9 received intensity-modulated radiation therapy (IMRT) treatment. For the breast cancer patient a single field was evaluated. The selection of patients was based on the presence of bony structures close to or within the high dose region, since this is what our CT conversion focuses on as will be explained in section 3.1. For each patient two MC calculations were performed: the material composition of every voxel was determined once applying the proposed CT conversion scheme and once using a conventional 5 bin scheme. This 5 bin scheme was derived from the proposed 14 bin scheme by keeping the first 4 bins and replacing bins 5–14 by a single bin representing the material composition of ICRU cortical bone. The mass density was derived directly from the CT number in the same, continuous manner for both sets of calculations. In this way two dose distributions were generated for each patient, which will further be referred to as D_{14} and D_5. Dose difference maps (DD) were created by calculating the local relative difference in dose between D_{14} and D_5. Values of DD were only assigned to voxels for which the local value of D_{14} was higher than 50% of the isocentric value of D_{14}. This was done to avoid the occurrence of large local relative dose differences corresponding to small absolute dose differences within the low dose regions, which are not clinically relevant and may thus lead to misinterpretation. Additionally, dose–volume histograms (DVHs) of the relevant target structures and organs at risk were created for each patient.

Whereas conventional dose calculations for photon beam treatment planning report dose to water, MC dose engines calculate dose to medium. When comparing MC results with results obtained by conventional systems, the MC dose distributions must thus be converted to dose to water. Additionally, dosimetry calibration protocols are generally based on absorbed dose to water standards. Although it would be possible to convert measurements and conventional dose results to dose to medium, the most important reason for converting dose to medium to dose to water is that tumour control probability (TCP) and normal tissue complication probability (NTCP) data are usually given in terms of dose to water and it will take a lot of effort and time before biological data can be made available in terms of dose to medium. Liu and Keall (2002) have elaborated on this issue in a point-counterpoint discussion.

Siebers *et al* (2000b) have proposed a method to convert dose to medium to dose to water by applying Bragg–Gray cavity theory. They have shown that a single correction factor can be used for each material—as long as it is not air—throughout the field for a given photon energy. Their post-processing method proved to be equally valid as performing the conversion online during the MC simulations. We have computed the conversion factor for each material of the proposed CT conversion scheme of each CT scanner as the ratio of the water and medium mass stopping powers at an effective electron energy of 1 MeV. As will be shown in section 3.1 and figure 2, the conversion factor of cortical bone amounts up to almost 1.13, while the conversion factors for lung and soft tissues differ only 1 or a few % from 1, respectively. Hence, large errors may arise when converting dose to medium to dose to water if the wrong bone composition is assigned. To evaluate the effect of possible conversion errors caused by taking into account an insufficient number of bone bins in a clinical situation, we have converted the above-mentioned MC dose distributions D_{14} and D_5 of each of the nine selected patient cases from dose to medium to dose to water. The converted dose distributions are referred to as D_{14wat} and D_{5wat}. Dose to water difference maps (DD_{wat}) were created by calculating the local relative dose difference between D_{14wat} and D_{5wat}, but values were only assigned to voxels for which the local value of D_{14} was greater than 50% of the isocentric value of D_{14}.

Again, DVHs of the relevant target structures and organs at risk were created for each patient.

Finally, to illustrate the influence of using a wrong CT conversion scheme (e.g. from another CT scanner) on patient dose calculations, an additional oropharyngeal patient case treated using a 3D conformal technique was selected. Two CT scanners were chosen from table 2 based on the differences between their mass density calibration curves: the Siemens Somatom Plus 4 CT scanner at GUH (A) and the Siemens Somatom Sensation Open CT scanner at the University Hospital of Tuebingen (B). For the selected patient MC dose calculations were performed using the proposed 14 bin CT conversion schemes of both CT scanners A and B, resulting in the dose distributions D_A and D_B. These dose distributions were compared by means of isodifference plots in transversal planes.

3. Results and discussion

3.1. Influence of material composition on photon attenuation and energy deposition

Figure 1(a) shows the mass attenuation coefficient of each material relative to that of water as a function of the photon energy in the range of 100 keV to 20 MeV. The attenuation properties of tissues like lung, adipose, muscle and cartilage are more or less water equivalent. However, the curves for air and cortical bone clearly deviate. This is due to the H- and Ca-content of those tissues: figure 1(b) shows the mass attenuation coefficient of the individual elements. Lung tissue contains 10.3% by weight of hydrogen, whereas dry air does not contain any hydrogen. This is the main cause of the discrepancy between the mass attenuation coefficients of lung and air, the latter being about 10% lower than the former. The 'cartilage–high Ca' curve in figure 1(a) illustrates the influence of calcium. This curve was created by setting the calcium content of cartilage to that of cortical bone, i.e. 22.5% by weight, while rescaling the other elemental weights. Additionally, the hydrogen content of cartilage (9.6% by weight) is higher than that of cortical bone (3.4% by weight), which accounts for the remaining shift. Therefore, an accurate conversion of CT numbers into elemental H- and Ca-weights is of high importance, as these weights strongly influence photon attenuation (Seco and Evans 2006). Figure 2(a) shows the water-to-material relative mass stopping power as a function of the electron energy in the range of 100 keV to 30 MeV; values for the individual elements are shown in figure 2(b). The energy deposition depends primarily on the hydrogen content.

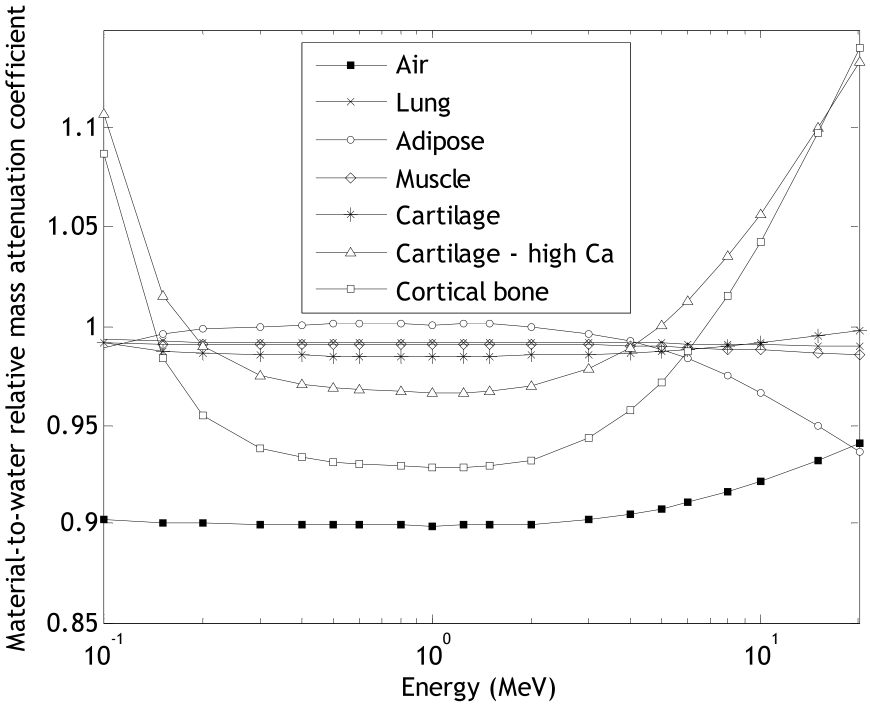

(a)

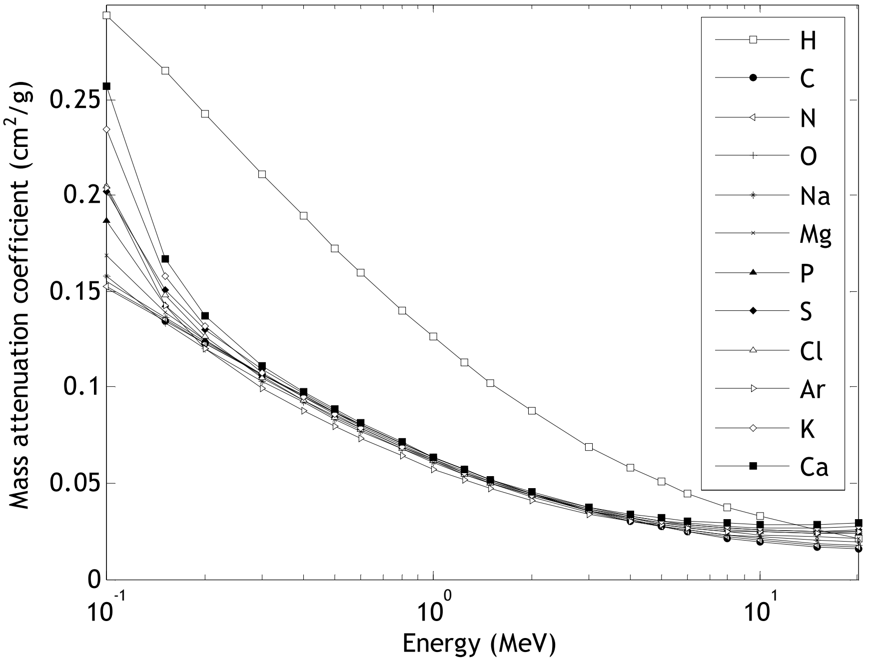

(b)

Figure 1. (a) Mass attenuation coefficients of different materials relative to that of water as a function of photon energy (MeV). The 'cartilage–high Ca' curve was created by setting the calcium content of cartilage to that of cortical bone, i.e. 22.5% by weight, while rescaling the other elemental weights. (b) Mass attenuation coefficients of individual elements (cm^2 g^{-1}) as a function of photon energy (MeV).

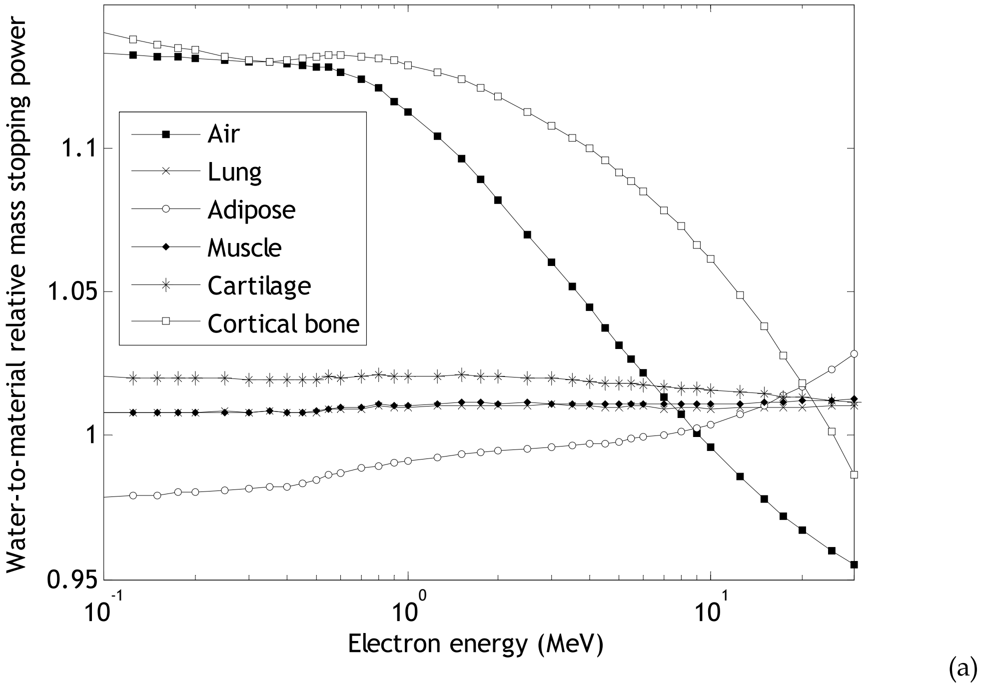

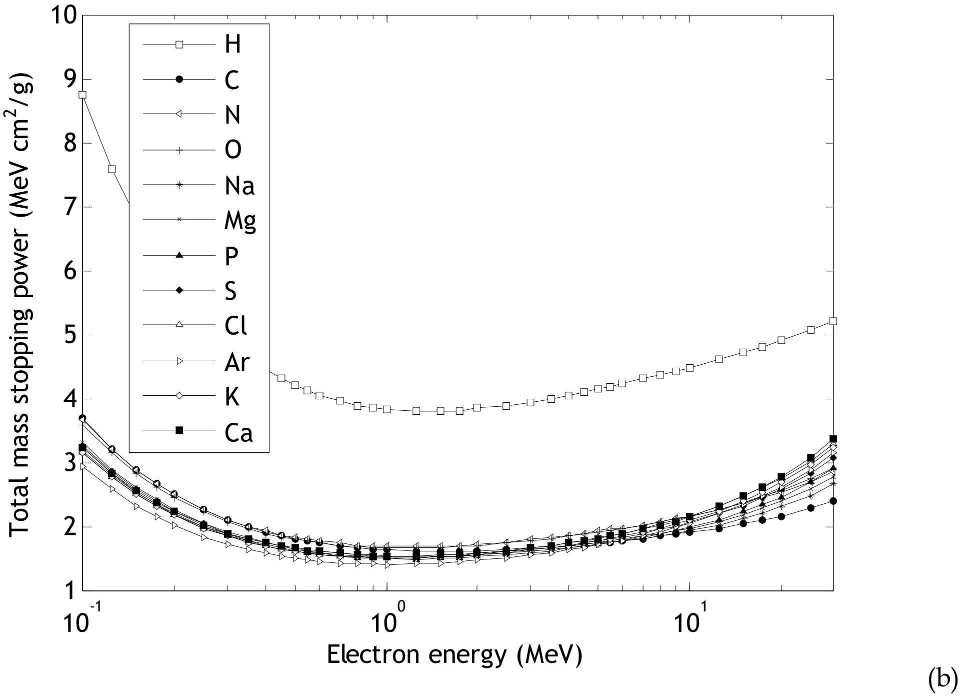

Figure 2. (a) Mass stopping power of water relative to that of different materials as a function of electron energy (MeV). (b) Mass stopping powers of individual elements (MeV cm² g⁻¹) as a function of electron energy (MeV).

For radiotherapy beams with photon energies between 0.1 and 10 MeV the Compton effect is the dominant interaction process. As the probability for Compton interaction is proportional to the electron density of a material, it will depend significantly on the hydrogen content (Seco and Evans 2006). At diagnostic imaging energies, however, the calcium content of a material will strongly increase the importance of the photo-electric and Rayleigh scattering terms because of their strong Z-dependence. Because dose calculations use material property data extracted from CT images, the calcium content may indirectly influence the dose calculations if not properly accounted for when converting CT numbers into electron density. Thus, it is particularly important to be able to distinguish lung from air (different H-content) as well as different bone compositions from each other (different H- and Ca-contents) to perform accurate MC patient dose calculations. Magnetic resonance imaging (MRI) techniques may allow us to visualize the H-content within patients, e.g. throughout the lungs. However, the resulting images are generally characterized by a low signal-to-noise ratio and poor resolution. At present, the most practical approach seems to be the selection of a different CT number boundary between air and lung depending on the tumour site, i.e. lower for lung tumours (to assign lung to patient voxels with low CT numbers) and higher for head and neck tumours (to avoid the assignment of lung to patient voxels with low CT numbers, which is anatomically impossible). This matter will not be examined any further in this paper. Instead, our CT conversion procedure will focus on the division of the human bone tissues into a sufficient number of subsets.

3.2. Stoichiometric calibration

A fit of the measured CT number data to equations (1) and (2) for the set of materials listed in table 1 resulted in values of K^{ph}/K^{KN} and K^{coh}/K^{KN} of 4.24×10^{-5} and -1.77×10^{-3}, respectively, for the Siemens Somatom Plus 4 CT scanner at GUH. The R^2-value of the fit was 0.999. The occurrence of a negative value for K^{coh}/K^{KN} has been addressed by de Kock and Schreuder (1996). In his reply, Schneider has suggested repeated air calibration measurements and separate scans for each material to obtain a positive K^{coh}. We performed all scans in a clinical setting, i.e. in the same circumstances as for real patients. In any case, the negative K^{coh} yields excellent results. The possibility of decreasing the number of fitting parameters to avoid the occurrence of a negative K^{coh} value is discussed in an appendix to this paper.

Figure 3 shows calculated versus measured CT numbers for the inserts of the Gammex RMI 465 phantom for the same CT scanner. The calculations were performed using the stoichiometric calibration curve based on the set of materials from table 1. The R^2-value of the 1:1 fit was 0.983. The largest deviations occur for B200 bone mineral, CB2–50% $CaCO_3$ and SB3 cortical bone (and to a lesser extent for AP6 adipose). AP6 adipose and B200 bone mineral are the only material inserts containing fluorine (3.1% and 16.7%, respectively), while CB2–50% $CaCO_3$ and SB3 cortical bone are the inserts with the highest calcium content (20.0% and 27.0%, respectively).

Verhaegen and Devic (2005) have already pointed out problems with the use of tissue substitutes containing fluorine, e.g. Teflon, to perform CT calibrations for MC dose calculations. None of the human body tissues contains fluorine. On the other hand, the stoichiometric calibration procedure should be able to accurately predict the CT number of every material with a known composition, on the condition that equation (1) is a valid approximation. The difference between the attenuation coefficient of elemental fluorine calculated through this equation and the value of the same coefficient according to the NIST database (Hubbell and Seltzer 2004) is about−1.5% for an effective CT scanner energy around 70 keV, which cannot account for the large discrepancies observed in figure 4. Possibly there is a difference between the elemental composition data of our calibration materials and the data available in the literature.

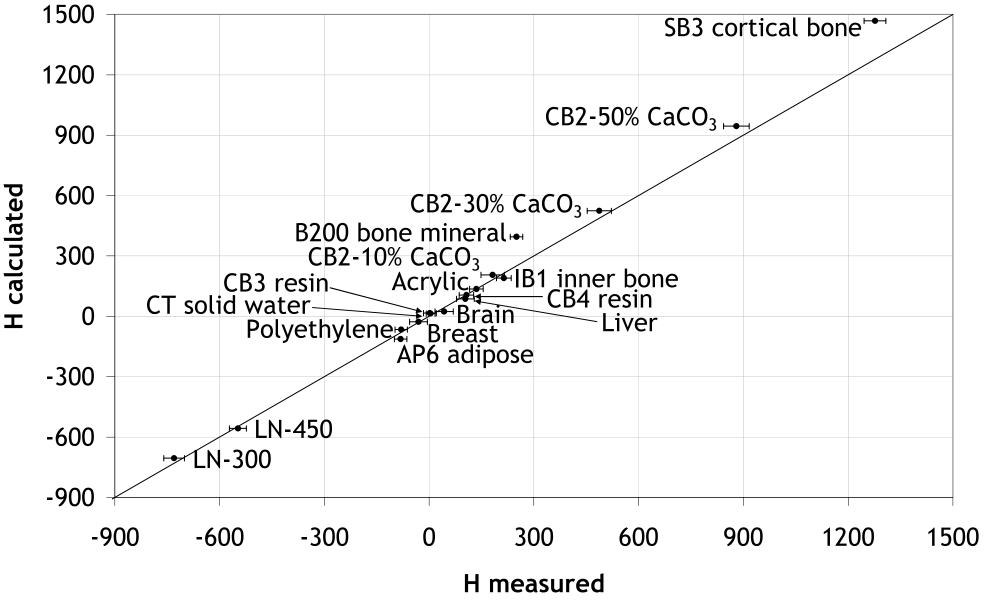

Figure 3. Calculated versus measured CT numbers for the inserts of the Gammex RMI 465 phantom listed in section 1.2 for the Siemens Somatom Plus 4 CT scanner at Ghent University Hospital. Calculations were performed using the stoichiometric calibration based on the set of materials from table 1. The half width of each error bar is equal to one standard deviation of the measured CT number.

The inaccuracy of attenuation coefficients of materials containing considerable amounts of calcium calculated through equation (1) has been reported by de Kock and Schreuder (1996). Schneider *et al* (2000) have provided an interpolation formula for the CT number of a medium that is composed of only two components. We used this formula to compute additional 'measurement' data for artificial $CaCl_2$ and $CaCO_3$ solutions with a high calcium content (up to 40% by weight). From a comparison between these interpolated and the calculated (using the stoichiometric calibration curve based on the set of materials from table 1) CT numbers it was clear that equation (1) overestimated the CT number for materials with a high calcium content. Moreover, the deviations increased as the calcium content became higher. For materials with w_{Ca} greater than 20%, the R^2-value of the fit was equal to 0.711. The difference between the attenuation coefficient of elemental calcium calculated through equation (1) and the value of the same coefficient according to the NIST database (Hubbell and Seltzer 2004) is about 4.1% for an effective CT scanner energy around 70 keV, while the observed discrepancies were clearly larger.

We extended the equation used to predict CT numbers from material properties with two purely empirical fitting parameters a and b, in addition to K^{ph}/K^{KN} and K^{coh}/K^{KN}. We thus allowed a linear decrease of the calculated CT number with respect to the CT number calculated according to the original equation, for materials with w_{Ca} greater than 20%: $H = (1 - a)H_{\text{original}} + b$. In this way, an excellent correspondence between calculated and measured CT numbers could be obtained for these materials ($a = 0.297$, $b = 242$, $R^2 = 0.996$). Only for the artificial $CaCO_3$ solution containing 40% by weight of calcium the result still was not satisfactory. However, the maximum calcium content of even the most dense human bone is at most 30%. We investigated the dosimetric relevance of this empirical extension by calculating the CT number for 27 human bone tissues based on both the original and the extended fit. We determined the corresponding tissue bins according to the binning scheme based on the original fit, which will be presented in section 3.3. For 23 tissues the bin number was the same; for the other four tissues the difference was 1 bin. As the dose difference between adjacent bins is less than 1%, we conclude that the empirical extension of the calibration equation was not dosimetrically relevant. Hence, the observed differences between calculated and measured CT numbers for materials with a high calcium content are acceptable for our purposes.

The Gammex RMI 465 phantom was sent around to different centres to perform a stoichiometric calibration of the CT scanner. Because of the observed discrepancies between the calculated and measured CT numbers of the inserts containing fluorine (AP6 adipose and B200 bone mineral), these data were omitted to fit the measured data to equations (1) and (2). The resulting values of K^{ph}/K^{KN} and K^{coh}/K^{KN} are listed in table 2. This table illustrates the variety in stoichiometric calibration results found for the investigated scan protocols at different centres. It is absolutely necessary to perform an individual stoichiometric calibration for each CT scanner and scan protocol used for radiotherapy treatment planning. The same scan protocol has to be selected to calibrate the CT scanner and to scan patients. If several scan protocols are used depending on the tumour site, several CT conversion schemes will need to be created at each institution, as different values of the fitted parameters will occur for the same CT scanner using different protocols.

3.3. Dosimetrically equivalent tissue subsets

The mass density calibration curve for the Siemens Somatom Plus 4 scanner at GUH is shown in figure 4. Compared to air/lung and bone, the fit for the soft tissues is clearly worse. This is due to the limited ability to distinguish soft tissues by means of their CT number in the range between 0 and 100 HU as shown by Schneider *et al* (2000), figure 3. It appears that the first two linear regression curves could be combined into a single curve representing air, lung and soft tissues together. Because the individual fits were performed separately, there is a discontinuity between the regression curves of soft and bone tissues. Its effect was evaluated through the comparison of depth dose curves calculated within homogeneous phantoms, corresponding to the soft and bone tissues just left and right of the discontinuity at $H = 100$, respectively. The maximal deviation was equal to 1.07% found at 0.3 cm depth. Therefore, the potential misassignment of a voxel with a CT number close to 100 HU to the last soft tissue bin or first bone tissue bin will not have severe consequences for the performed dose calculations, and the discontinuity between the mass density calibration curves is acceptable.

For the other CT scanners listed in table 2, similar curves were obtained.

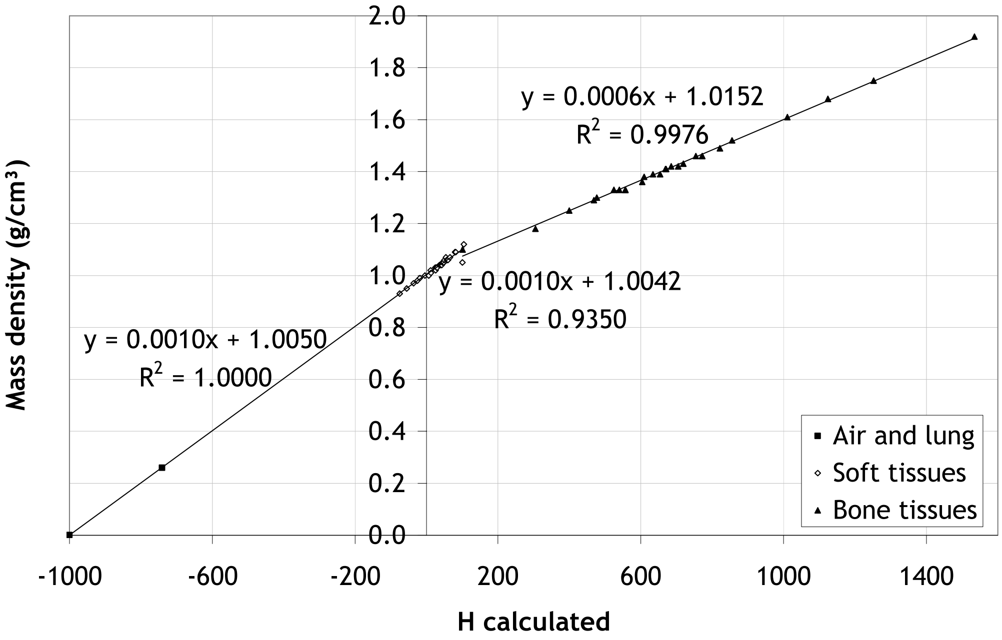

Figure 4. Mass density calibration curve of the Siemens Somatom Plus 4 CT scanner at Ghent University Hospital. The equation of each linear regression curve is displayed as well as the corresponding correlation coefficient.

The proposed conversion of CT numbers into elemental composition data is presented in table 3 for the Siemens Somatom Plus 4 scanner at GUH. Air and lung were assigned an individual bin each. Two bins were created for soft tissue, i.e. for adipose- and muscle-like tissues. The maximal deviation between the depth dose curves of both subset representatives was 0.97% (found at 2.9 cm depth). Ten equidistant bins were created for bone. The maximal deviation between the depth dose curves of two adjacent subsets was found between the first two bins, and was equal to 1.01% (found at 3.5 cm depth). Based on these findings, 14 tissue subsets were created for each of the CT scanners listed in table 2.

For 15 MV photons, the deviation between the depth dose curves of the first and last bone bin was below 1% at all calculated depths. Indeed, figure 2 clearly shows an intersection between the mass stopping power curves of cartilage and cortical bone at an electron energy of about 20 MeV. Thus, for high energy photon beams used for radiation therapy it will not be necessary to introduce as many bone bins as for low energy beams. The proposed binning scheme can therefore be used for 6 MV beams as well as for higher energies.

Table 3. Proposed conversion of CT numbers into elemental weight data w_i for the Siemens Somatom Plus 4 CT scanner at Ghent University Hospital. H_l and H_u are the lower and upper boundaries of each CT number interval.

H_l	H_u	w_H	w_C	w_N	w_O	w_{Na}	w_{Mg}	w_P	w_S	w_{Cl}	w_{Ar}	w_K	w_{Ca}
	-900			0.755	0.232						0.013		
-900	-100	0.103	0.105	0.031	0.749	0.002		0.002	0.003	0.003		0.002	
-100	20	0.112	0.533	0.011	0.341	0.001			0.001	0.001			
20	100	0.101	0.156	0.040	0.693	0.003		0.001	0.003	0.002		0.001	
100	250	0.095	0.453	0.025	0.355	0.001		0.021	0.002	0.001		0.001	0.046
250	400	0.084	0.401	0.028	0.369	0.001	0.001	0.036	0.002	0.001		0.001	0.077
400	550	0.075	0.355	0.030	0.381	0.001	0.001	0.048	0.002	0.001		0.001	0.105
550	700	0.067	0.316	0.033	0.392	0.001	0.001	0.059	0.002	0.001			0.128
700	850	0.060	0.281	0.035	0.401	0.001	0.001	0.068	0.002				0.149
850	1000	0.053	0.250	0.037	0.410	0.001	0.001	0.077	0.003				0.168
1000	1150	0.048	0.223	0.038	0.417	0.001	0.002	0.084	0.003				0.184
1150	1300	0.043	0.198	0.040	0.423	0.001	0.002	0.091	0.003				0.199
1300	1450	0.038	0.176	0.041	0.429	0.001	0.002	0.097	0.003				0.212
1450		0.034	0.156	0.042	0.435	0.001	0.002	0.103	0.003				0.224

For 6.6 MeV electrons, the maximal deviation between the depth dose curves of two adjacent bone bins was found between the first two bins, and was equal to 2.2% (found at 2.3 cm depth), whereas approximately 85% and 95% of all bone bins differ less than 1% and 2%, respectively. The larger than 1% differences are possibly due to a larger effect of electron elastic scattering in the dose deposition for electron beams compared to photon beams. Additionally, there is a large dose gradient at this depth (18.9% mm^{-1} for the depth dose curve of the first bone bin), which affects the comparison of the two bone bins. In the first part of the depth dose curve, which is reasonably flat and which is the part that is most relevant to radiotherapy treatment planning, the maximal deviation between the depth dose curves of two adjacent bone bins is again found between the first two bins but only amounts to 0.7%. We therefore consider our proposed CT conversion scheme suitable for photons as well as for electrons. For high energy electrons used for radiotherapy the proposed CT conversion scheme will be satisfactory *a fortiori*, due to the smaller difference between the mass stopping power values of different bone compositions at higher electron energies.

3.4. MC slab phantoms

For the elemental composition of the vertebral column a CT number value of 520 HU was calculated. Thus, the vertebral column would be modelled as the third bone bin by our proposed 14 bin CT conversion scheme (table 3) and as ICRU cortical bone by the conventional 5 bin scheme. The calculated mass density value was 1.323 g cm^{-3}. Figure 5 shows the resulting depth dose curves for both values of the bone layer thickness (0.1 cm and 1 cm). Local absolute dose differences up to 4.1% (0.1 cm) and 6.4% (1 cm) were observed within the bone layer, and up to 3.3% (0.1 cm) and 4.0% (1 cm) within the adjacent adipose tissue. The differences in area below the depth dose curves within the bone layer were more limited: 2.3% (0.1 cm) and 2.4% (1 cm), respectively.

The calculations for the 0.1 cm thick layer of bone allow us to study energy deposition effects around bony structures embedded within soft tissue, while the calculations for the 1 cm thick layer additionally allow us to study attenuation effects within the bony structure itself. The results indicate that although large dose deviations may be observed locally in or around bony structures within patients, the influence of introducing a larger number of bone bins on integrated dose quantities, e.g. DVHs, is likely to remain limited.

3.5. Gammex RMI 461A head/body CT phantom

Both sets of DOSXYZnrc calculations were compared by averaging the absolute value of the dose difference over the 13 central voxels along the *X*-axis and by normalizing the result using the average dose calculated within the central voxel. The following results were obtained at 12 cm and 15 cm depth, respectively: 1.0% and 1.1% for LN-300, 0.5% and 0.6% for LN-450, 1.4% and 1.5% for B200 bone mineral, 0.6% and 0.5% for CB2–10% $CaCO_3$, 0.4% and 0.6% for CB2–30% $CaCO_3$ and 0.2% and 0.2% for CB2–50% $CaCO_3$. These numbers confirm the adequacy of our CT conversion procedure. Because the average CT number was converted into a homogeneous material composition and mass density for each insert, the influence of scanning artefacts on the calculations was excluded.

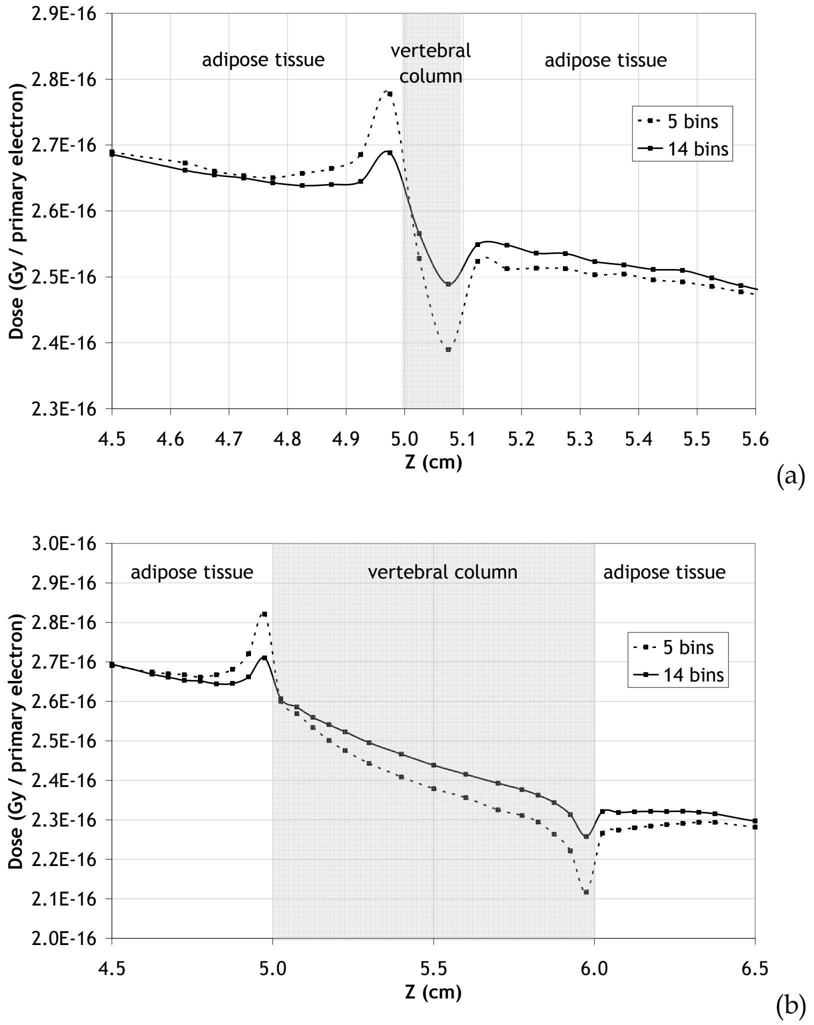

Figure 5. Depth dose curves within MC slab phantoms consisting of a 0.1 cm (a) and a 1 cm (b) thick layer of vertebral column (520 HU) embedded within adipose tissue. Calculations were performed with the vertebral column layer represented according to a conventional 5 bin CT conversion scheme (dotted lines) and our proposed 14 bin CT conversion scheme (solid lines) for the Siemens Somatom Plus 4 CT scanner at Ghent University Hospital. The mass density of the bone layer was equal to 1.323 g cm^{-3}.

3.6. Patient dose calculations

Figure 6 illustrates the attributed material numbers for the proposed 14 bin conversion scheme for patient 3 in a sagittal slice through the isocentre (a), as well as the D_{14} (b) and DD (c) distributions. The material numbers of the 5 bin conversion scheme result from the 14 bin conversion scheme by replacing all numbers greater than or equal to 5 by 5. Figure 7 shows DD as a histogram for each patient. It is clear that the observed relative differences between D_{14} and D_5 are spread approximately symmetrically around DD = 0% and are mostly smaller than 5%. The largest local dose differences were reported for patient number 1, which was the patient with the smallest voxel size, i.e. 2 × 2 ×5 mm^3. The voxel size of the dose calculation grid was 5 × 5 × 5 mm^3 for patients 2–4, 4 × 4 ×

3 mm³ for patients 5–6 and 4 × 4 × 4 mm³ for patients 7–9. Despite the observed local differences for each patient, the D_{14}- and D_5-DVHs of the target structures and relevant organs at risk were hardly distinguishable from each other. However, for bony structures like the mandible, maxilla or parts of the PTV for certain patients D_{14} was found to be slightly but systematically higher than D_5. This is due to the higher mass stopping power values of soft bony tissues compared to hard ones like cortical bone as shown in figure 2. Figure 8(a) illustrates the DVHs of D_{14} and D_5 for patient 3.

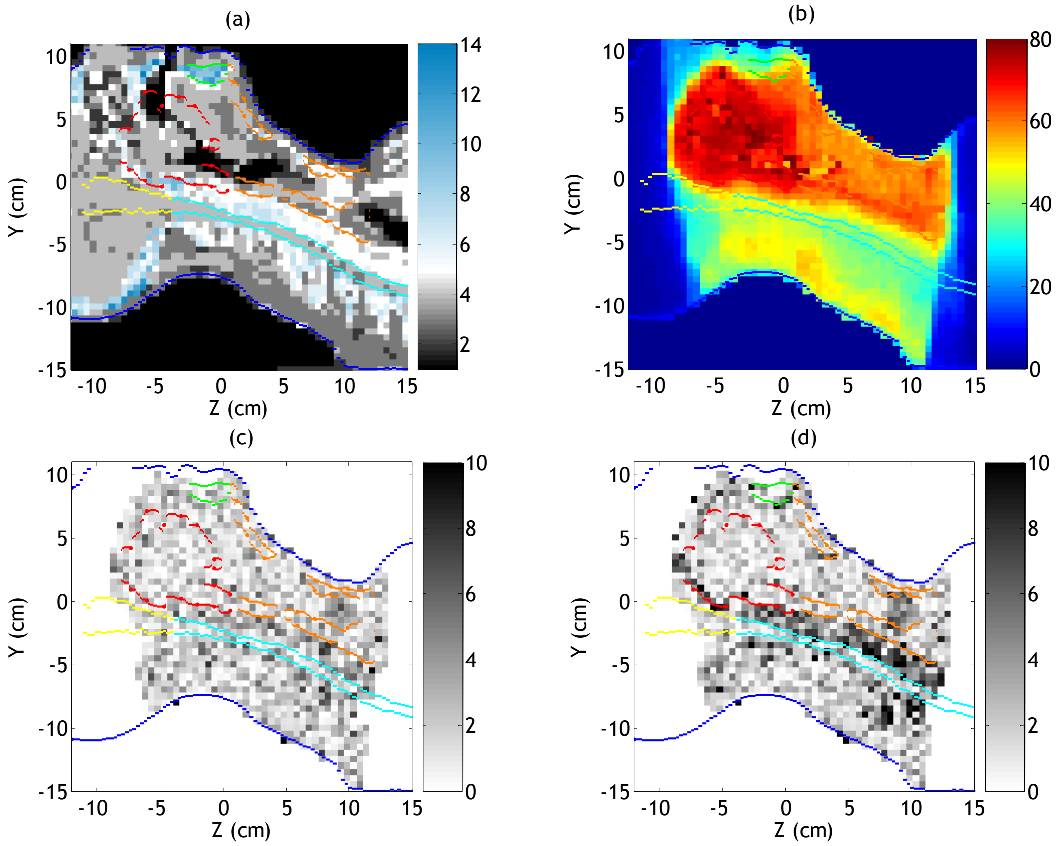

Figure 6. Sagittal views through the isocentre (0, 0, 0) for patient 3, showing the material numbers for the 14 bin conversion scheme (a), the dose distribution D_{14} in Gy (b) and the absolute value (%) of the local dose difference distributions DD (c) and DD_{wat} (d). Contoured structures: PTV_1 (red), PTV_2 (orange), skin (blue), brainstem (yellow), mandible (green) and the spinal cord (cyan).

Table 4 shows the dose to medium to dose to water conversion factors for each material of the proposed CT conversion scheme of the Siemens Somatom Plus 4 CT scanner at GUH. For the other CT scanners listed in table 2, similar tables were obtained. Siebers *et al* (2000b) have associated errors up to 1.3% with these conversion factors, provided that a sufficient number of materials are included in the conversion process (Fippel and Nuesslin 2000, Siebers *et al* 2000c). Figure 6(d) illustrates the dose to water difference distribution DD_{wat} for patient 3 in a sagittal slice through the isocentre. Compared to $DD_{(med)}$ shown in figure 6(c), it is clear that the observed differences were larger, particularly in the bony tissue surrounding the spinal cord. Similar observations were made for the other patients in case of bony structures close to or within the high dose regions, but not for the lung and breast cancer patients.

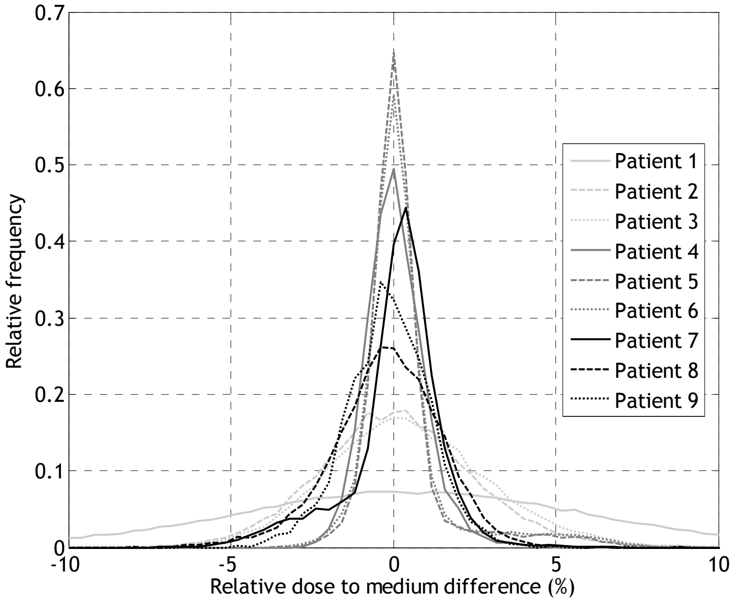

Figure 7. Histograms of the relative dose to medium differences DD (%) between the MC dose distributions D_{14} and D_5, which were calculated based on a 14 bin and a 5 bin CT conversion scheme, respectively. Each histogram was plotted using a bin width of 0.4%.

Table 4. Dose to medium to dose to water conversion factors for the proposed CT conversion scheme of the Siemens Somatom Plus 4 CT scanner at Ghent University Hospital. The CT number interval and elemental composition corresponding to each material number are summarized in table 3.

Material number	Conversion factor
1	1.110
2	0.996
3	0.995
4	1.013
5	1.024
6	1.040
7	1.054
8	1.068
9	1.079
10	1.090
11	1.100
12	1.117
13	1.125
14	1.129

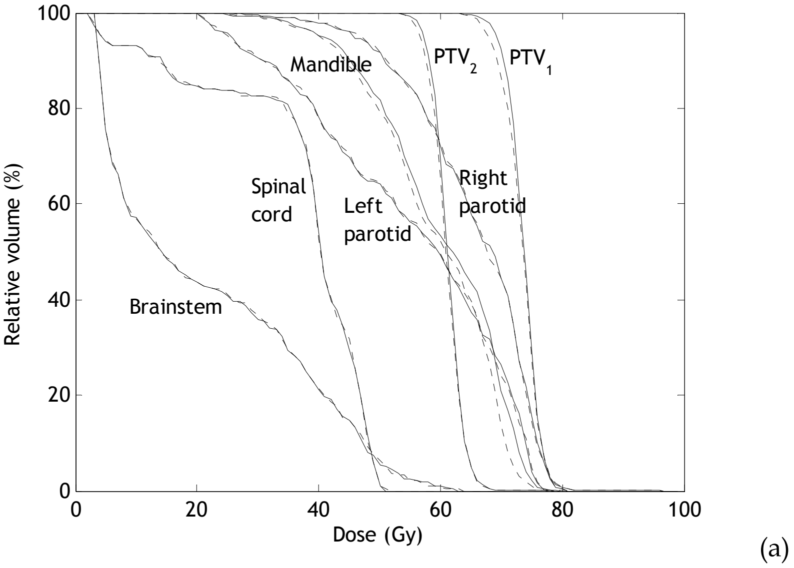

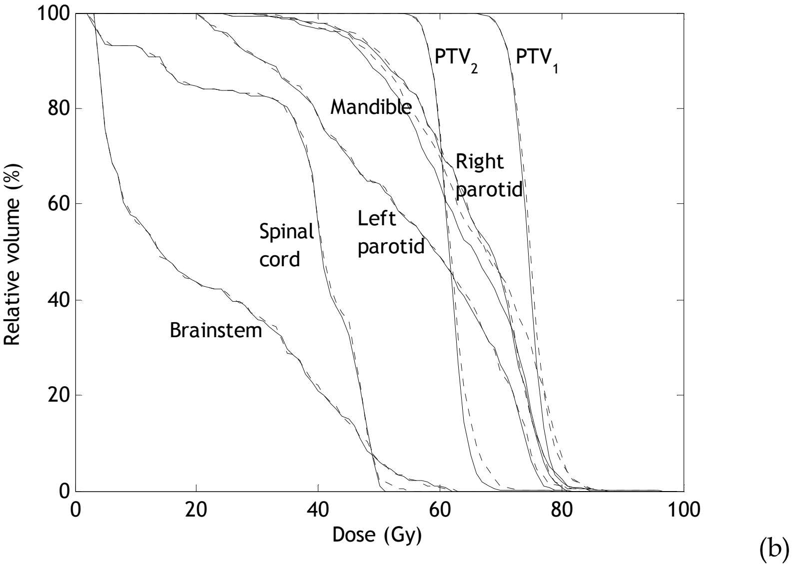

Figure 8. Dose–volume histograms of relevant target structures and organs at risk for patient 3 for D_{14} (solid lines) and D_5 (dashed lines) (a) and for D_{14wat} (solid lines) and D_{5wat} (dashed lines) (b).

Figure 9 shows DD_{wat} histograms for each patient. Unlike for DD, there is a distinct asymmetry in the histograms towards negative dose difference values, i.e. D_{5wat} is higher than D_{14wat}. This is due to the fact that for the 5 bin CT conversion scheme all bony tissues are classified as cortical bone and therefore the dose to water is over 10% higher than the dose to medium within those voxels. For the 14 bin CT conversion scheme, the dose to medium to dose to water correction is only a few % for the first bone bin, while this number quickly rises for the next bone bins. Therefore, possible errors during the conversion from dose to medium to dose to water, caused by considering an insufficient number

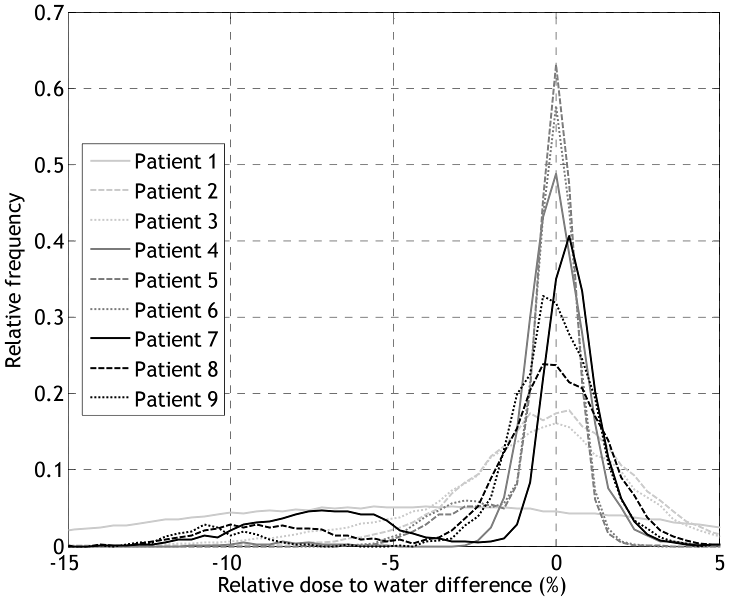

Figure 9. Histograms of the relative dose to water differences DD_{wat} (%) between the MC dose distributions D_{14wat} and D_{5wat}. D_{14wat} and D_{5wat} result from the conversion of D_{14} and D_5 from dose to medium to dose to water. Each histogram was plotted using a bin width of 0.4%.

of bone subsets, will naturally be most apparent within the voxels of which the real composition differs the most from the assigned composition, in our case within the softest bone tissues for the 5 bin CT conversion scheme. The clear lump around −11% in the DD_{wat} histogram of patient number 9 was caused by the cartilage tissue of the larynx and the spinal cord; for other patients the lumps visible in the histograms were primarily due to the skull (patient 7), the skull base (patients 5, 6 and 8), the mandible (patients 5 and 8) and the spinal cord (patient 5). For patient 1, the large amount of bony tissue present within the high dose region caused a shift of the maximum of the histogram of about 5% towards negative dose difference values.

Although histograms are a good means to visualize the dose difference distribution, attention should also be paid to the clinical significance of the observed differences, i.e. to take into account their location with respect to the tumour and organs at risk. Indeed, if considerable errors are encountered within bony tissue that is not part of or close to any relevant structures there is less cause for concern with regard to the patient's treatment. To evaluate the effect of the observed dose differences on the dose delivered to relevant structures it is best to look at DVHs. Figure 8(b) shows the DVHs of D_{14wat} and D_{5wat} for patient 3. The most apparent differences occur between the curves of both PTVs and the mandible. Note that—in contrast to figure 8(a)—D_{5wat} is higher than D_{14wat} within the bony structures. While the presence of soft bony tissues in the 14 bin CT conversion scheme increases the calculated dose to medium compared to the 5 bin CT conversion scheme because of the higher mass stopping power values, the DVHs change sides when the dose is converted to dose to water because the conversion factors for soft bony tissues are smaller. These opposite effects somewhat limit the observed dose to water differences between the 14 and 5 bin CT conversion schemes. Similar observations were made for the DVHs of bony structures within other patients. The largest difference was observed for patient 9, for whom the minimal dose received by 5% of the PTV volume was 10% higher for D_{5wat} than for D_{14wat}. It is thus highly important to use a CT conversion scheme that discriminates between different bone compositions when evaluating the dose to water.

With regard to the comparison of MC calculations using CT conversion schemes of different CT scanners, the dose difference distribution between D_A and D_B was calculated as $200\% - D_A/D_B$ for each patient voxel. The results are shown in figure 10. It is clear that the differences are almost everywhere within 2% and mostly even within 1%. Despite the quite large difference of 268 HU between the calculated CT numbers of cortical bone for both CT calibrations (1535 HU for CT scanner A versus 1267 HU for CT scanner B), the influence on dose errors is apparently limited. This finding is in agreement with the statement of Constantinou *et al* (1992) that heterogeneity correction factors used by conventional dose engines for photon beam calculations are relatively insensitive to small changes in the CT number.

4. Conclusions

The conversion of CT numbers into material properties strongly influences the accuracy of patient dose calculations in Monte Carlo treatment planning. By studying the attenuation and energy deposition properties of human tissues as well as individual elements, we have shown that it is particularly important to distinguish lung from air and different bone compositions from each other. The aim of our work was to develop a CT conversion scheme by performing a stoichiometric calibration of the CT scanner and by creating dosimetrically equivalent tissue subsets or bins. While each subset corresponds to a fixed material composition, the mass density could be calibrated continuously against the CT number. The proposed CT conversion scheme consisted of 14 bins: air, lung, adipose, muscle and 10 bone bins. It was validated by performing MC calculations within virtual MC slab phantoms and within a real CT phantom containing different inserts. While the proposed CT conversion scheme was developed for a clinical 6 MV photon beam, it is also suitable for higher energy photons and for electrons.

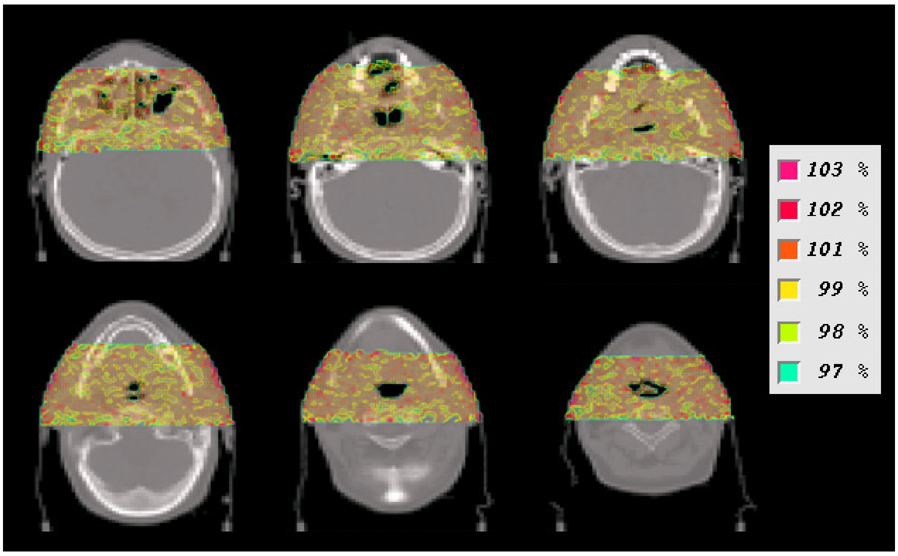

Figure 10. Isodifference plots showing values of 200%−D_A/D_B for several transversal slices for an oropharyngeal cancer patient case. D_A and D_B are the MC dose distributions calculated based on the CT conversion schemes of two different CT scanners. Values were only assigned to voxels that received more than 10% of the target prescription dose; voxels with a mass density value below 0.1 g cm^{-3} were not taken into account.

The main focus of our work was to evaluate the proposed CT conversion scheme on patient treatment plans by means of a European multi-centre study. Nine patient cases with different tumour locations were selected. The proposed 14 bin CT conversion scheme was compared to a conventional 5 bin CT conversion scheme. The observed local relative differences in dose to medium were mostly smaller than 5%. The DVHs of the target and organs at risk were similar for both conversion schemes; only within certain bony structures D_{14} was found to be slightly but systematically higher than D_5. However, after converting the results to dose to water D_{5wat} became up to 10% higher than D_{14wat}. Indeed, the correction factor for cortical bone exceeds 1.10, while it only deviates a few % from 1 for soft bony tissues. It is clear that multiple bone bins need to be introduced when MC calculations of patient dose distributions are converted to dose to water. A comparison of the CT conversion schemes of different CT scanners showed that the influence of selecting the wrong conversion scheme is limited as the local dose to medium errors were below 2%.

Acknowledgments

Frank De Bisschop (Ghent University, Belgium) is acknowledged for preparing the $CaCl_2$ solutions. A Ferri and L Pierotti (Policlinico S.Orsola-Malpighi, Bologna, Italy) are acknowledged for their support with the Gammex RMI phantoms. Barbara Vanderstraeten is a Research Assistant (Aspirant) of the Fund for Scientific Research-Flanders (FWO-Vlaanderen).

Appendix. Stoichiometric calibration: fitting parameters

The stoichiometric calibration procedure of Schneider *et al* (1996) involves the determination of two parameters ($K^{\mathrm{ph}}/K^{\mathrm{KN}}$ and $K^{\mathrm{coh}}/K^{\mathrm{KN}}$) through a least-squares fit of measured CT numbers to equations (1) and (2). In this way, however, negative $K^{\mathrm{coh}}/K^{\mathrm{KN}}$ values were obtained for several CT scan protocols of our multi-centre study (table 2). Although the good quality of the fits based on these parameter values was shown in section 3.2, the occurrence of non-meaningful $K^{\mathrm{coh}}/K^{\mathrm{KN}}$ values may indicate that the model of Schneider *et al* is overdetermined. Indeed, $K^{\mathrm{ph}}/K^{\mathrm{KN}}$ and $K^{\mathrm{coh}}/K^{\mathrm{KN}}$ are both functions of energy and are thus interrelated. The fits were repeated using this relationship instead of treating $K^{\mathrm{ph}}/K^{\mathrm{KN}}$ and $K^{\mathrm{coh}}/K^{\mathrm{KN}}$ as independent free parameters.

According to the parametrization of the total elemental attenuation coefficient by Rutherford *et al* (1976) (Schneider *et al* 1996, equation (7)), the ratio between $K^{\mathrm{ph}}/K^{\mathrm{KN}}$ and $K^{\mathrm{coh}}/K^{\mathrm{KN}}$ can be determined as follows:

$$\frac{K^{ph}/K^{KN}}{K^{coh}/K^{KN}} = \frac{\left(\mu/\rho\right)^{ph}}{\left(\mu/\rho\right)^{coh}} Z^{(1.86-3.62)}. \quad \text{(A.1)}$$

In this equation, $(\mu/\rho)^{\mathrm{ph}}$ and $(\mu/\rho)^{\mathrm{coh}}$ are the mass attenuation coefficients for photoelectric absorption and coherent scattering, respectively. While $K^{\mathrm{ph}}/K^{\mathrm{KN}}$ and $K^{\mathrm{coh}}/K^{\mathrm{KN}}$ are assumed to depend only on energy, the mass attenuation coefficients depend both on the element (Z) and energy. Values for $(\mu/\rho)^{\mathrm{ph}}$ and $(\mu/\rho)^{\mathrm{coh}}$ can be obtained as a function of photon energy from the NIST XCOM database (Hubbell and Seltzer 2004). Although the location-dependent energy spectrum of the CT scanner is unknown, an excellent linear relationship was obtained between the logarithms in base 10 of both parameters for the entire range of CT photon energies (20–120 keV). For oxygen (the most abundant element in human tissues) and calcium (the second most abundant element in cortical bone, after oxygen), respectively:

$$O\colon\ \log\left(\frac{K^{ph}}{K^{KN}}\right) = 0.53\log\left(\frac{K^{coh}}{K^{KN}}\right) - 0.45 \qquad (R^2 = 1.00) \ \text{(A.2)}$$

$$Ca\colon\ \log\left(\frac{K^{ph}}{K^{KN}}\right) = 0.54\log\left(\frac{K^{coh}}{K^{KN}}\right) - 0.51 \qquad (R^2 = 1.00). \ \text{(A.3)}$$

Clearly, the assumption that energy- and material-dependent factors can be separated is not entirely exact. Taking relationship (A.2) into account during the fit of measured CT data for the set of materials listed in table 1, resulted in values of $K^{\mathrm{ph}}/K^{\mathrm{KN}}$ and $K^{\mathrm{coh}}/K^{\mathrm{KN}}$ of 2.94×10^{-5} and 1.44×10^{-3}, respectively, for the Siemens Somatom Plus 4 CT scanner at GUH. Similarly, the use of (A.3) resulted in $K^{\mathrm{ph}}/K^{\mathrm{KN}}$ and $K^{\mathrm{coh}}/K^{\mathrm{KN}}$ values equal to 3.08×10^{-5} and 1.09×10^{-3}, respectively. The R^2-values of the fits based on (A.2) and (A.3) were both 0.998. The fits were thus hardly worse compared to the original fit (R^2 = 0.999), which treated $K^{\mathrm{ph}}/K^{\mathrm{KN}}$ and $K^{\mathrm{coh}}/K^{\mathrm{KN}}$ as independent free parameters.

Alternatively, the mass attenuation coefficient of a mixture can be calculated as the weighted sum of the coefficients of the constituent elements (Jackson and Hawkes 1981):

$$\left(\frac{\mu}{\rho}\right)=\sum_{i=1}^{n} w_i\left(\frac{\mu}{\rho}\right)_i . \quad \text{(A.4)}$$

For each element i, values of $(\mu/\rho)_i$ are available as a function of photon energy from the NIST XCOM database (Hubbell and Seltzer 2004). A quadratic fit can be performed through the 60, 80 and 100 keV data points. We assume that the unknown location-dependent energy spectrum of the CT scanner can be represented by a sole effective energy value E_{eff}. In this way, the CT number can be calculated as a function of E_{eff} through equations (A.4) and (2). The parametrization of the attenuation coefficient (1) is thus abandoned. The CT scanner can then be calibrated by determining the value of E_{eff} through a least-squares fit of measured against calculated CT numbers. As in the previous approach, only one fitting parameter is used. For the set of materials listed in table 1, this approach resulted in a value of E_{eff} equal to 73.0 keV, for the Siemens Somatom Plus 4 CT scanner at GUH. The R^2-value of the fit was 0.998.

In conclusion, in addition to the stoichiometric calibration procedure with two fitting parameters proposed by Schneider *et al* (1996), two alternative approaches were presented in this appendix. Both methods use only one fitting parameter, either $K^{\mathrm{coh}}/K^{\mathrm{KN}}$ or E_{eff}. By decreasing the number of independent fitting parameters, the unphysical negative $K^{\mathrm{coh}}/K^{\mathrm{KN}}$ values disappeared. For both alternative approaches, the quality of the stoichiometric calibration fit was hardly affected compared to the original two-parameter approach. However, both alternative methods require the use of experimental data from the NIST database. For the second alternative approach, fits of $(\mu/\rho)_i$ against E_{eff} had to be performed for all constituent elements of the calibration materials and human tissues, compared to only one fit of K^{ph}/K^{KN} against K^{coh}/K^{KN} for the first alternative approach, thus introducing more uncertainty. On the other hand, the second alternative approach does not require the assumption that the mass attenuation coefficient can be parametrized by separating energy- and material-dependent factors. Throughout our paper, we have applied the original stoichiometric calibration procedure of Schneider *et al*, because it leads to very good results in practice. The occurrence of negative K^{coh}/K^{KN} values has no impact on our proposed CT conversion method.

References

Constantinou C, Harrington J C and DeWerd L A 1992 An electron density calibration phantom for CT-based treatment planning computers *Med. Phys.* **19** 325–7

de Kock E A and Schreuder A N 1996 Comments on 'The calibration of CT Hounsfield units for radiotherapy treatment planning' *Phys. Med. Biol.* **41** 1524–7

DeMarco J J, Solberg T D and Smathers J B 1998 A CT-based Monte Carlo simulation tool for dosimetry planning and analysis *Med. Phys.* **25** 1–11

du Plessis F C P, Willemse C A and Lötter M G 1998 The indirect use of CT numbers to establish material properties needed for Monte Carlo calculation of dose distributions in patients *Med. Phys.* **25** 1195–201

Fippel M 1999 Fast Monte Carlo dose calculations for photon beams based on the VMC electron algorithm *Med. Phys.* **26** 1466–75

Fippel M and Nuesslin F 2000 Comments on 'Converting absorbed dose to medium to absorbed dose to water for

Monte Carlo based photon beam dose calculations' *Phys. Med. Biol.* **45** L17–8

Hartmann Siantar C L *et al* 1997 *Lawrence Livermore National Laboratory's PEREGRINE Project Report* UCRL-JC-126732

Hubbell J H and Seltzer S M 2004 Tables of x-ray mass attenuation coefficients and mass energy-absorption coefficients (version 1.4). National Institute of Standards and Technology, Gaithersburg, MD. Available online at http://physics.nist.gov/xaamdi (May 2006)

ICRU (International Commission on Radiation Units and Measurements) 1989 Tissue Substitutes in Radiation Dosimetry and Measurement *ICRU Report 44* (Washington, DC: ICRU)

Jackson D F and Hawkes D J 1981 X-ray attenuation coefficients of elements and mixtures *Phys. Rep.* **70** 169–233

Kawrakow I 2001 VMC++, electron and photon Monte Carlo calculations optimized for radiation treatment planning *Advanced Monte Carlo for Radiation Physics, Particle Transport Simulation and Applications: Proceedings of the Monte Carlo 2000 Meeting (Lisbon)* ed A Kling *et al* (Berlin: Springer) pp 229–36

Kawrakow I, Fippel M and Friedrich K 1996 3D electron dose calculations using a voxel based Monte Carlo algorithm (VMC) *Med. Phys.* **23** 445–57

Liu H H and Keall P 2002 D_m rather than D_w should be used in Monte Carlo treatment planning *Med. Phys.* **29** 922–4

Ma C M, Mok E, Kapur A, Pawlicki T, Findley D, Brain S, Forster K and Boyer A L 1999 Clinical implementation of a Monte Carlo treatment planning system *Med. Phys.* **26** 2133–43

Rogers D W O, Ma C M,Walters B, Ding G X, Sheikh-Bagheri D and Zang G 2002 *BEAMnrc Users Manual* (Ottawa, Canada: National Research Council of Canada)

Schneider U, Pedroni E and Lomax A 1996 The calibration of CT Hounsfield units for radiotherapy treatment planning *Phys. Med. Biol.* **41** 111–24

Schneider W, Bortfeld T and Schlegel W 2000 Correlation between CT numbers and tissue parameters needed for Monte Carlo simulations of clinical dose distributions *Phys. Med. Biol.* **45** 459–78

Seco J and Evans P M 2006 Assessing the effect of electron density in photon dose calculations *Med. Phys.* **33** 540–52

Siebers J V, Keall P J, Kim J and Mohan R 2000a Performance benchmarks of the MCV Monte Carlo system *13th Int. Conf. on the Use of Computers in Radiation Therapy (XIIIth ICCR)* ed W Schlegel and T Bortfeld (Heidelberg: Springer) pp 129–31

Siebers J V, Keall P J, Nahum A E and Mohan R 2000b Converting absorbed dose to medium to absorbed dose to water for Monte Carlo based photon beam dose calculations *Phys. Med. Biol.* **45** 983–95

Siebers J V, Keall P J, Nahum A E and Mohan R 2000c Reply to 'Comments on 'Converting absorbed dose to medium to absorbed dose to water for Monte Carlo based photon beam dose calculations" *Phys. Med. Biol.* **45** L18–9

Van de Walle J, Martens C, Reynaert N, Palmans H, Coghe M, De Neve W, De Wagter C and Thierens H 2003 Monte Carlo model of the Elekta Sl*i*plus accelerator: validation of a new MLC component module in BEAM for a 6 MV beam *Phys. Med. Biol.* **48** 371–85

Verhaegen F and Devic S 2005 Sensitivity study for CT image use in Monte Carlo treatment planning *Phys. Med. Biol.* **50** 937–46

Wang L, Chui C S and Lovelock M 1998 A patient-specific Monte Carlo dose-calculation method for photon beams *Med. Phys.* **25** 867–78

Watanabe Y 1999 Derivation of linear attenuation coefficients from CT numbers for low-energy photons *Phys. Med. Biol.* **44** 2201–11

White D R,Woodard H Q and Hammond M S 1987 Average soft-tissue and bone models for use in radiation dosimetry *Br. J. Radiol.* **60** 907–13

Woodard H Q and White D R 1986 The composition of body tissues *Br. J. Radiol.* **59** 1209–19

Chapter 8

Publication 6:

Evaluation of uncertainty-based stopping criteria for Monte Carlo calculations of intensity-modulated radiotherapy and arc therapy patient dose distributions

Barbara Vanderstraeten[1,2], Ana Maria Luiza Olteanu[2], Nick Reynaert[1], Antonio Leal[3], Wilfried De Neve[2] and Hubert Thierens[1]

[1] *Department of Medical Physics, Ghent University, Gent, Belgium*
[2] *Department of Radiotherapy, Ghent University Hospital, Gent, Belgium*
[3] *Department of Medical Physiology and Biophysics, University of Seville and Virgen Macarena Hospital, Sevilla, Spain*

International Journal of Radiation Oncology, Biology, Physics 2007;69: 628-637

Abstract

Purpose: To formulate uncertainty-based stopping criteria for Monte Carlo (MC) calculations of intensity-modulated radiotherapy and intensity-modulated arc therapy patient dose distributions and evaluate their influence on MC simulation times and dose characteristics.

Methods and Materials: For each structure of interest, stopping criteria were formulated as follows: $\sigma_{rel} \leq \sigma_{rel,tol}$ or $D\sigma_{rel} \leq D_{lim}\sigma_{rel,tol}$ within ≥95% of the voxels, where σ_{rel} represents the relative statistical uncertainty on the estimated dose, D. The tolerated uncertainty ($\sigma_{\mathrm{rel,tol}}$) was 2%. The dose limit (D_{lim}) equalled the planning target volume (PTV) prescription dose or a dose value related to the organ at risk (OAR) planning constraints. An intensity-modulated radiotherapy–lung, intensity-modulated radiotherapy–ethmoid sinus, and intensity-modulated arc therapy–rectum patient case were studied. The PTV-stopping criteria–based calculations were compared with the PTV+OAR-stopping criteria–based calculations.

Results: The MC dose distributions complied with the PTV-stopping criteria after 14% (lung), 21% (ethmoid), and 12% (rectum) of the simulation times of a 100 million histories reference calculation, and increased to 29%, 44%, and 51%, respectively, by the addition of the OAR-stopping criteria. Dose–volume histograms corresponding to the PTV-stopping criteria, PTV+OAR-stopping criteria, and reference dose calculations were indiscernible. The median local dose differences between the PTV-stopping criteria and the reference calculations amounted to 1.4% (lung), 2.1% (ethmoid), and 2.5% (rectum).

Conclusion: For the patient cases studied, the MC calculations using PTV-stopping criteria only allowed accurate treatment plan evaluation. The proposed stopping criteria provided a flexible tool to assist MC patient dose calculations. The structures of interest and appropriate values of $\sigma_{rel,tol}$ and D_{lim} should be selected for each patient individually according to the clinical treatment planning goals.

INTRODUCTION

Highly conformal dose distributions can be created using intensity-modulated radiotherapy (IMRT) or intensity-modulated arc therapy (IMAT) (1, 2). Monte Carlo (MC) techniques simulate the random trajectories (''histories'') of individual photons and electrons in material. MC techniques can provide highly accurate patient dose distributions, particularly in the presence of tissue inhomogeneities. Unlike analytical algorithms for dose calculations, MC calculations provide an average dose value and a value for the statistical uncertainty on the average dose within each scoring voxel. The statistical uncertainty decreases as the number of simulated histories increases. The clinical evaluation of a radiotherapy plan will thus depend on the number of histories used for the MC calculation of the patient dose distribution. From a practical viewpoint, it is important to determine the optimal (*i.e.*, minimal) number of histories at which a clinical treatment plan can be evaluated adequately.

Several investigators have studied the effect of statistical uncertainties on the evaluation of dose distributions. Keall *et al*. (3) reported that a statistical uncertainty of 2% at the maximal dose point did not significantly affect the isodose lines, dose–volume histograms (DVHs), or biologic dose indexes for a calculated lung treatment plan. By performing simulations within a water and lung computed tomography phantom, Buffa and Nahum (4) showed that the tumor control probability estimates ceased to change as a function of the number of histories when the standard deviation of the dose became <1.5–2%. The normal tissue complication probability estimates for organs at risk (OARs) were not considered. A more general analysis of the effect of statistical uncertainties on treatment plan evaluation was performed by Kawrakow (5), who showed that random dose uncertainties lead to statistical and systematic uncertainties on a ''well-behaved'' cost function defining the suitability of a treatment plan. The desired accuracy on the cost function can thus provide a stopping criterion for the MC calculation. Although a relative uncertainty of 2% within the planning target volume (PTV) is often assumed to be sufficient for accurate clinical treatment plan evaluation, Chetty *et al*. (6) have addressed the importance of considering the tradeoffs between uncertainties in doses to targets and ''serial'' or ''parallel'' critical organs to determine the acceptable levels of statistical uncertainty. To remove the effect of statistical uncertainties on DVHs, de-noising techniques have been developed (7, 8). Apart from the final treatment plan evaluation, statistical uncertainties can also influence the inverse MC treatment planning process by introducing noise convergence errors, as shown by Jeraj and Keall (9). Ma *et al*. (10) have provided an overview of the effect of statistical uncertainties on MC treatment planning.

The aim of our work was to evaluate the 2% tolerance level while paying attention to critical organs. For this purpose, we implemented uncertainty-based stopping criteria into our MC dose calculation software. For each structure of interest, upper limits were imposed on the relative and absolute statistical uncertainties. Calculations were performed taking into account the PTV only, and the PTV and a set of critical organs. Both approaches were compared for three clinical treatment plans: an IMRT lung cancer case, an IMRT ethmoid sinus cancer case, and an IMAT rectum cancer case. The evaluation of the observed dose differences was performed locally, as well as according to the DVHs.

METHODS AND MATERIALS

Uncertainty-based stopping criteria

MC calculations of patient dose distributions result in values for the estimated dose D and the corresponding relative statistical uncertainty σ_{rel} within each patient voxel. The absolute uncertainty on the estimated dose is equal to $D\sigma_{rel}$. In the BEAMnrc/DOSXYZnrc system used for the MC calculations in this study, the uncertainties were estimated using a history-by-history method (11, 12). The larger the number of histories used to perform the MC simulation, the lower the uncertainty will be within each patient voxel. To determine the simulation time that is necessary from a clinical viewpoint, we formulated general uncertainty-based stopping criteria. Within each patient voxel, the following Boolean expression was evaluated:

$$\sigma_{rel} \leq \sigma_{rel,tol} \text{ OR } D\sigma_{rel} \leq D_{lim}\sigma_{rel,tol} \quad (1)$$

The values for the tolerated relative uncertainty $\sigma_{rel,tol}$ and the dose limit D_{lim} were defined separately for each target or OAR. We proposed stopping the MC simulation as soon as Expression 1 is true for ≥95% of the patient voxels within each structure of interest.

For a specific patient case, the structures of interest were first listed. Next, the values of $\sigma_{rel,tol}$ and D_{lim} were assigned to each structure. Typically, $\sigma_{rel,tol}$ was equal to 2%. For D_{lim}, we selected the prescription dose for a target structure or a dose value related to the treatment planning constraints for an OAR. The rationale behind this approach is explained in the "Discussion." During the MC simulation, the fraction of voxels for which Expression 1 is true was evaluated regularly for each structure of interest. As soon as all evaluations resulted in fractions of ≥95%, the simulation was stopped. Details on the MC calculations and the implementation of the uncertainty-based stopping criteria are provided below.

MC calculations

All MC calculations for this study were performed using the MC dose engine MCDE, developed by Reynaert *et al.* (13). By reprogramming DOSXYZnrc as a component module within BEAMnrc, MCDE uses the EGSnrc photon and electron transport algorithms (14). Because it uses no additional variance reduction techniques or approximations, MCDE is an accurate MC code for IMRT patient dose calculations. The possibility of simulating IMAT plans was recently included in MCDE (15). For this study, treatment plans were created using an in-house developed version (16–18) of the GRATIS software package (Sherouse Systems, Chapel Hill, NC). MCDE is able to simulate all beams in a single process, requiring only one input file. For each history, the beam angle of the simulated particle is randomly sampled according to the treatment plan's monitor unit configuration. The MC sampling process ensures that the total number of simulated histories is the only quantity of interest, regardless of the beam angle selection.

To incorporate the uncertainty-based stopping criteria in MCDE, the phantom component module was modified. In practice, the user can enter a list of structures of interest into the simulation input file, together with structure-specific values of $\sigma_{rel,tol}$ and D_{lim}. Each structure entry refers to the location of the corresponding GRATIS structure file, which can be imported from the treatment planning system. Additionally, the user can provide a density (grams per cubic centimeter) cutoff value to exclude air voxels from the structures of interest. All calculations were performed on a Linux PC cluster consisting of 31 nodes (2.4-GHz Intel Pentium IV dual processors with 2-GB RAM). Each time a total number of 10^6 histories was simulated on an individual cluster node, MCDE evaluated the fraction of voxels complying with Expression 1 for each structure and wrote these data to the simulation log file. $\sigma_{rel,tol}$ was multiplied before-hand by the square root of the number of cluster nodes in use. As soon as the evaluated fractions exceeded the 95% limit for all structures, the simulation was stopped. For each node, the simulation was halted in any case after 100 × 10^6 histories, even if not all stopping criteria had been fulfilled. In the remainder of this report, the numbers of simulated histories always refer to each individual cluster node.

Patient cases

Three patients with various tumor locations were selected: a lung case, an ethmoid sinus case, and a rectal case. For the lung and ethmoid sinus cases, IMRT plans consisting of nine non–coplanar 6-MV photons beams with 25 and 42 beam segments in total were created. An IMAT plan consisting of 56 coplanar 18-MV photon beams organized in four arcs was created for the rectal case (18).

For each patient, a 100 × 10^6-history reference dose distribution D_{ref} was calculated. This simulation is referred to as MC_{ref}. Two additional simulations were performed taking into account uncertainty-based stopping criteria. In the first run (MC_{PTV}), only the PTV was included as the structure of interest. In the second run (MC_{all}), several OARs were added to the list of structures. The resulting dose distribution—obtained after simulating N_{PTV} and N_{all} histories—is referred to as D_{PTV} and D_{all}, respectively. For each patient case, the structures of interest and the corresponding D_{lim} values are listed in Table 1; $\sigma_{rel,tol}$ was equal to 2%. The rim and surroundings were shell-shaped critical structures created to avoid dose littering within the noncontoured normal tissue for the rectal case (19). The rim represents a region of 2 cm around the PTV, and the ''surroundings'' is the region between the rim and the skin. Each MCDE scoring voxel had a radius of 2 mm. To eliminate air from the PTV, the density cutoff value was set to 0.5 g/cm^3 in the simulation input file for the ethmoid sinus case.

Table 1. Structures of interest and corresponding dose limit (D_{lim}) values for studied patient cases. Overview of total numbers of simulated histories N resulting from the MC_{PTV}, MC_{all}, and MC_{ref} simulations.

Lung case		Ethmoid sinus case		Rectum case	
Structure	D_{lim} (Gy)	Structure	D_{lim} (Gy)	Structure	D_{lim} (Gy)
PTV	70	PTV	70	PTV	45
Lungs	27	Left retina	30	Bladder	18
Heart	55	Right retina	30	Small bowel	10
Liver	30	Left optic nerve	45	Rim	30
Esophagus	55	Right optic nerve	45	Surroundings	8.5
Spinal cord	25	Optic chiasm	40		
No. of simulated histories (× 10^6)					
N_{PTV}	14	N_{PTV}	21	N_{PTV}	12
N_{all}	29	N_{all}	44	N_{all}	51
N_{ref}	100	N_{ref}	100	N_{ref}	100

Abbreviations: PTV = planning target volume; MC = Monte Carlo.

Reporting and evaluation

From the log file of the D_{all} MC simulation, the fraction of voxels complying with Expression 1 was set out against the number of simulated histories for each structure of interest. The GRATIS structure files and MCDE dose distributions resulting from the MC_{PTV}, MC_{all}, and MC_{ref} simulations were imported into MATLAB (The MathWorks, Natick, MA). Additional data analysis was performed using in-house created MATLAB scripts.

For each patient and for each structure of interest, (D,σ_{rel}) scatterplots after N_{PTV}, N_{all}, and 100 × 10^6 histories were created (3). The influence of the number of simulated histories on the resulting dose distributions was evaluated by comparing the DVHs of D_{PTV}, D_{all}, and D_{ref}. Additionally, dose difference distributions were computed between D_{PTV} and D_{ref} and D_{all} and D_{ref}. Within each structure of interest, the dose difference (in percentages) between a dose distribution D and D_{ref} was calculated as follows (6):

$$100\frac{\left|D-D_{ref}\right|}{\max\left(D_{ref},D_{\lim}\right)} \quad (2)$$

Finally, the gain in simulating N_{all} instead of N_{PTV} histories was evaluated. For the structures of interest that did not satisfy the uncertainty-based stopping constraints after N_{PTV} histories, σ_{rel}–volume histograms of MC_{PTV} and MC_{all} were plotted. Only the voxels that did not meet the constraints were taken into account.

RESULTS

Lung case

Figure 1a shows the fraction of voxels complying with the relative ($\sigma_{rel} \leq \sigma_{rel,tol}$) or absolute ($D\sigma_{rel} \leq D_{lim}\sigma_{rel,tol}$) stopping constraints (see Expression 1) as a function of the number of simulated histories for each structure of interest. The MC_{PTV} and MC_{all} simulations were stopped after $N_{PTV} = 14 \times 10^6$ and $N_{all} = 29 \times 10^6$ histories, respectively (Table 1). The 95% limit was reached first for the liver and last for the lungs. Only 36% of the ipsilateral lung satisfied the uncertainty-based stopping criteria after N_{PTV} histories. Figure 2 shows (D,σ_{rel}) scatterplots of MC_{PTV}, MC_{all}, and MC_{ref} for the liver, PTV, and lungs. Because of the low dose delivered to the liver (relative to the planning dose constraint), the absolute constraint was easily met for all voxels. After N_{PTV} histories, 82% of the PTV voxels satisfied the constraint $\sigma_{rel} \leq \sigma_{rel,tol}$, 84% satisfied $D\sigma_{rel} \leq D_{lim}\sigma_{rel,tol}$, and

97% satisfied either the relative or absolute constraint. For the lungs, the corresponding values were 5%, 63% and 69%; after N_{all} histories, these values were 19%, 77%, and 96%. After 100×10^6 histories, the uncertainty-based stopping criteria were met within all voxels for each structure of interest. Figure 1b compares the DVHs of D_{PTV}, D_{all}, and D_{ref} for all structures of interest. Almost no differences could be observed among the three sets of DVHs. In Table 2, the median (DD_{50}) and fifth percentile (DD_5) values of the dose difference distributions D_{PTV}-D_{ref} and D_{all}-D_{ref}, calculated according to Expression 2, are presented for each structure of interest. The reported values of D_{all}-D_{ref} were systematically lower than those of D_{PTV}-D_{ref}, as one would expect from the use of a greater number of histories. For DD_5, the largest differences were encountered for the lungs (4.0% for D_{PTV}-D_{ref} and 3.0% for D_{all}-D_{ref}), especially within the ipsilateral lung, followed by the PTV and spinal cord, heart, and, finally,

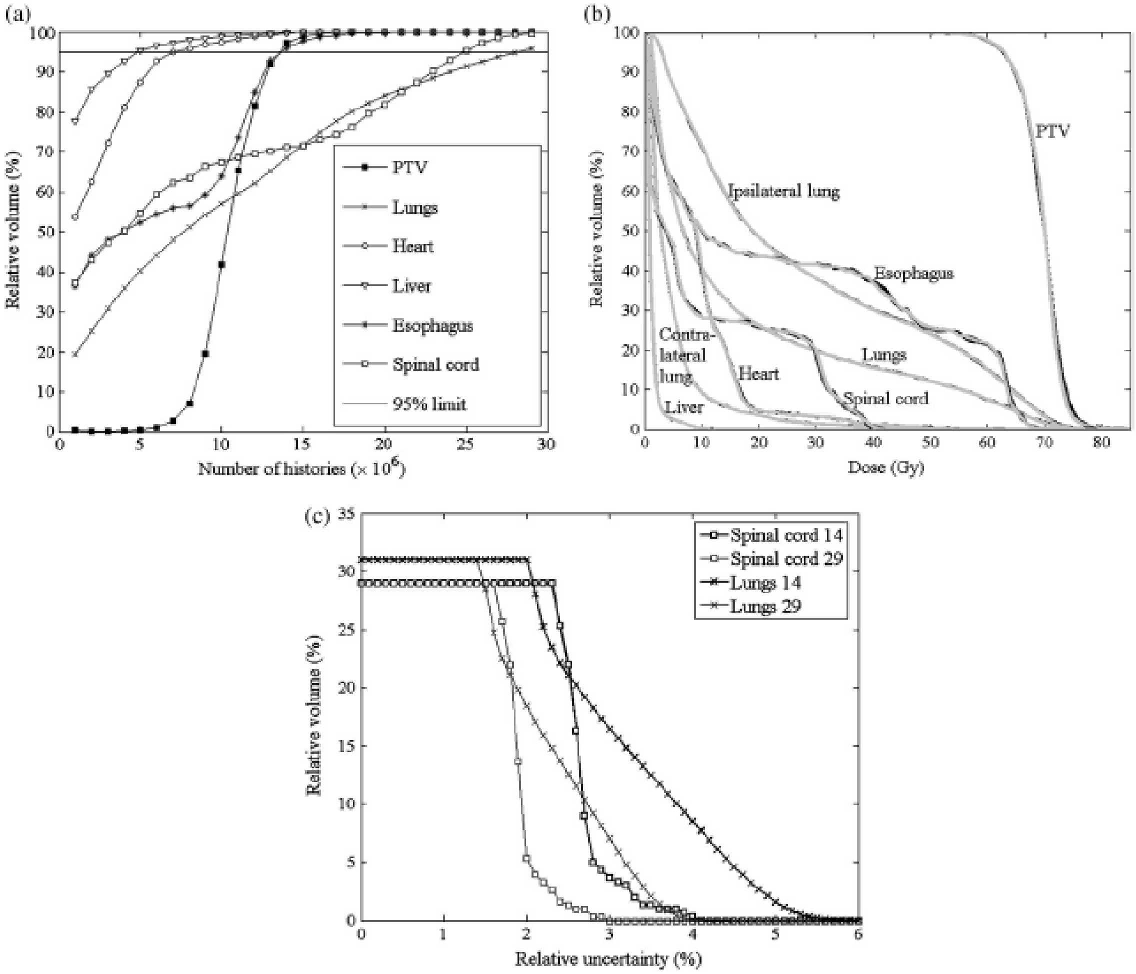

Fig. 1. Lung case. (a) Fraction of voxels complying with proposed uncertainty-based stopping constraint for each structure of interest, as function of total number of simulated histories. (b) Dose–volume histograms after simulation of 14 × 10^6 (black), 29 × 10^6 (dark gray), and 100 × 10^6 (light gray) histories for all structures of interest. (c) Relative uncertainty–volume histograms after simulation of 14 × 10^6 (bold curves) and 29 × 10^6 (regular curves) histories for spinal cord and lungs. Only voxels that did not comply with uncertainty-based stopping criteria after 14 × 10^6 histories were taken into account. PTV = planning target volume.

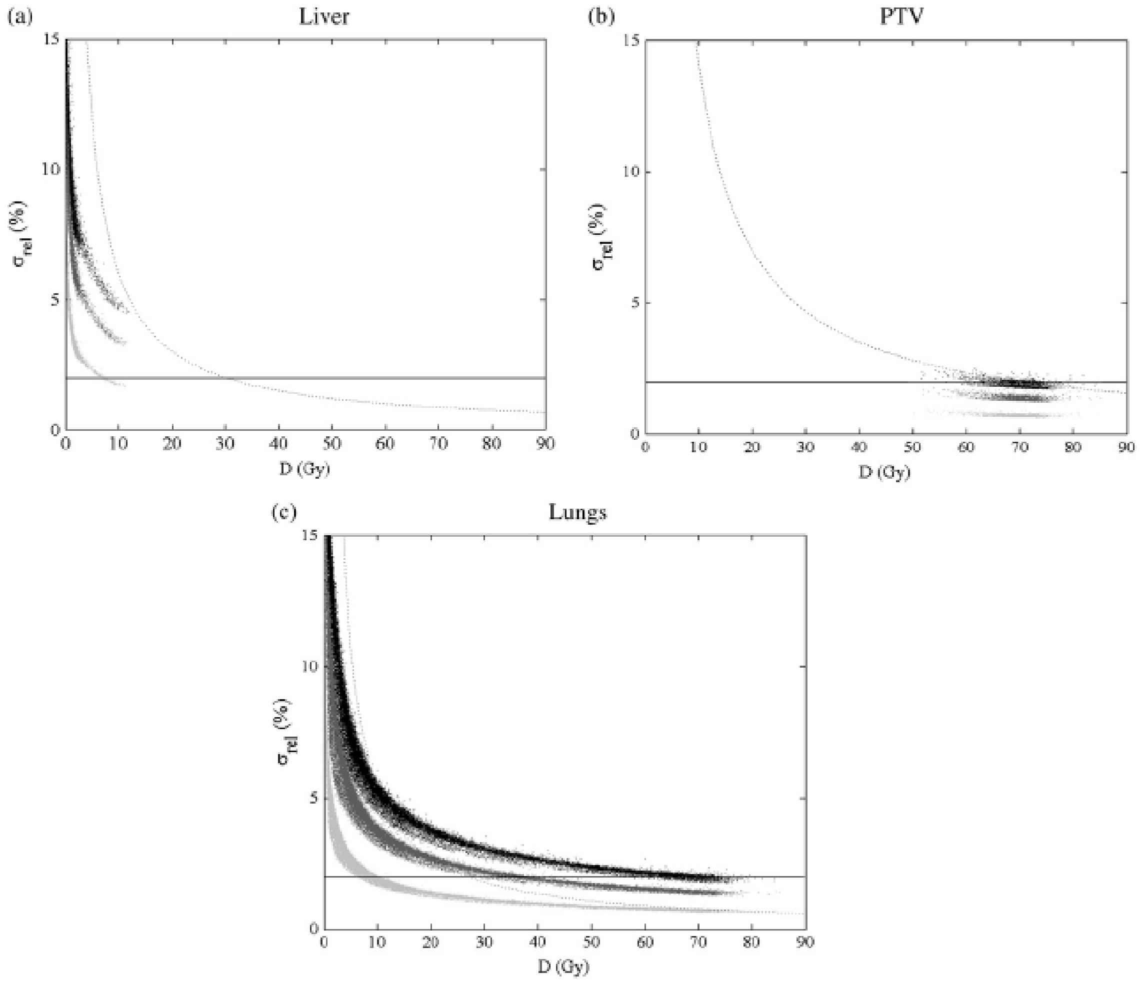

Fig. 2. Lung case. (D,σ_{rel}) scatterplots after simulation of 14×10^6 (black), 29×10^6 (dark gray), and 100×10^6 (light gray) histories for (a) liver, (b) planning target volume (PTV), and (c) lungs. Solid and dotted lines represent relative ($\sigma_{rel} \leq \sigma_{rel,tol}$) and absolute ($D\sigma_{rel} \leq D_{lim}\sigma_{rel,tol}$) uncertainty-based stopping criteria, respectively.

liver (0.9% for D_{PTV}-D_{ref} and 0.7% for D_{all}-D_{ref}). This order was similar to the order in which the structures of interest satisfied the uncertainty-based stopping criteria (Fig. 1). Considering DD_5, it is important to keep in mind that these values represent the minimal dose difference encountered in only 5% of the structure voxels and an equal fraction of voxels was allowed to violate Expression 1 for each structure without compromising the acceptance of the uncertainty-based stopping criteria. Analogously, the order encountered for DD_{50} is similar to the order in which each structure reached the 50% limit in Fig. 1. The largest differences were encountered for the PTV (1.3% for D_{PTV}-D_{ref} and 1.0% for D_{all}-D_{ref}), followed by the lungs (0.9% for D_{PTV}-D_{ref} and 0.7% for D_{all}-D_{ref}) and other structures of interest, for which all DD_{50} values were <0.5%. Finally, Fig. 1c shows the σ_{rel}–volume histograms of MC_{PTV} and MC_{all} for the structures of interest that did not satisfy the uncertainty-based stopping criteria after N_{PTV} histories (*i.e.*, the spinal cord and lungs). For each structure, only the voxels that did not comply with the relative or absolute stopping constraint after N_{PTV} histories were taken into account (*i.e.*, 29% of the spinal cord voxels and 31% of the lung voxels). For 9% of the lung voxels, the relative uncertainty on the estimated dose was >4% after N_{PTV} histories. After N_{all} histories, this was no longer the case (<1% of the voxels). For 16% of the lung voxels and 4% of the spinal cord voxels, σ_{rel} was >3% after N_{PTV} histories. After *Nall* histories, this was still the case for 7% of the lung voxels, but not for the spinal cord (<1% of the voxels).

Table 2. Median (DD_{50}) and 5th percentile (DD_5) values of dose difference distributions D_{PTV}-D_{ref} and D_{all}-D_{ref} for each structure of interest of studied patient cases.

	DD_{50} (%)		DD_5 (%)	
Structure of interest	D_{PTV}-D_{ref}	D_{all}-D_{ref}	D_{PTV}-D_{ref}	D_{all}-D_{ref}
Lung case				
PTV	1.3	1.0	3.7	2.9
Lungs	0.9	0.7	4.0	3.0
Ipsilateral lung	1.4	1.0	4.7	3.5
Contralateral lung	0.7	0.5	2.8	2.1
Heart	0.4	0.3	1.7	1.3
Liver	0.2	0.2	0.9	0.7
Esophagus	0.4	0.3	2.9	2.0
Spinal cord	0.5	0.4	3.8	2.8
Ethmoid sinus case				
PTV	1.4	1.0	4.0	3.1
Left retina	2.0	1.4	5.5	4.1
Right retina	1.8	1.4	5.1	3.7
Left optic nerve	1.6	1.1	4.8	4.0
Right optic nerve	2.1	1.3	5.4	3.9
Optic chiasm	1.5	1.2	4.5	3.4
Rectum case				
PTV	1.2	0.4	3.5	1.3
Bladder	2.5	0.9	7.7	2.7
Small bowel	1.4	0.5	9.4	3.4
Rim	1.5	0.5	4.5	1.6
Surroundings	1.9	0.7	9.7	3.5

Dose differences computed according to Expression 2.

Dose distributions D_{PTV}, D_{all} and D_{ref} obtained after Monte Carlo simulations of N_{PTV}, N_{all} and 100×10^6 histories, respectively (see Table 1).

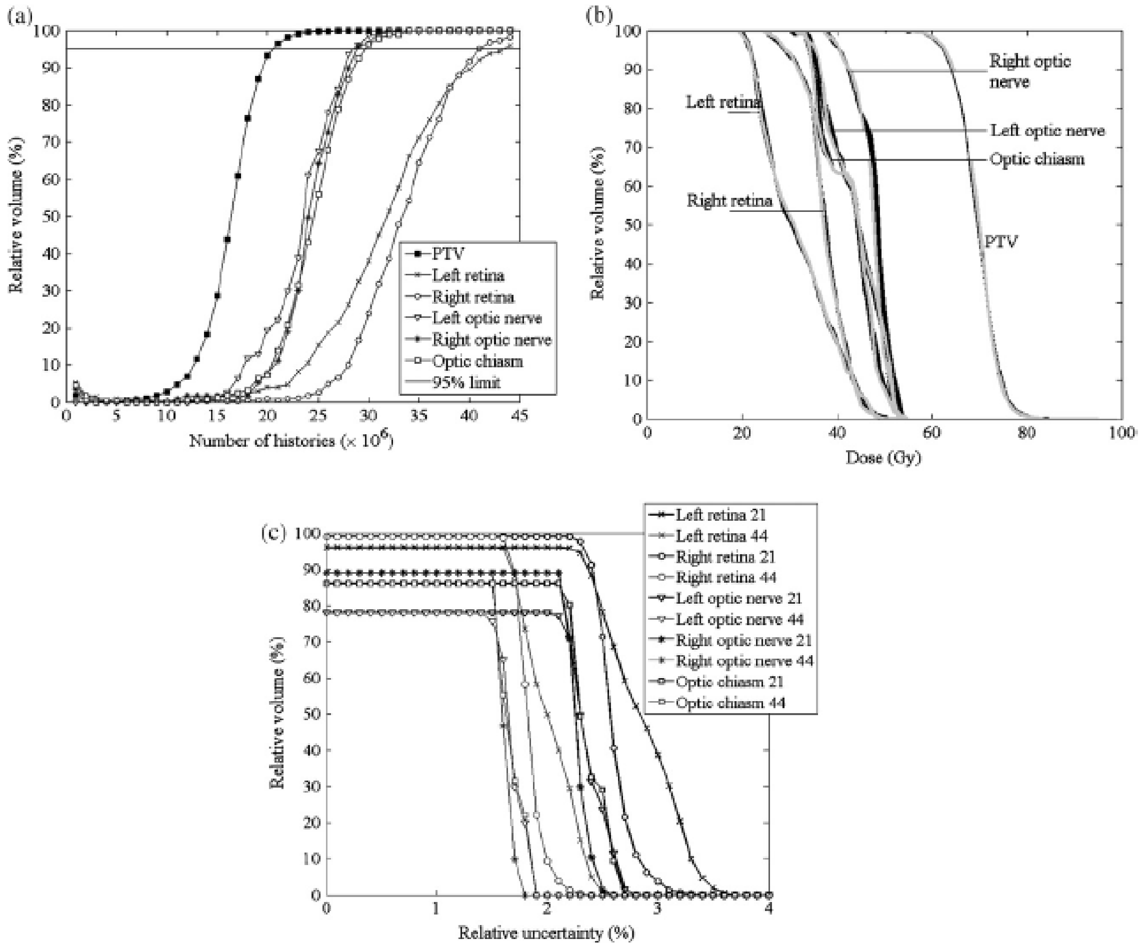

Fig. 3. Ethmoid sinus case. (a) Fraction of voxels complying with proposed uncertainty-based stopping constraint for each structure of interest, as function of total number of simulated histories. (b) Dose–volume histograms after simulation of 21 × 10^6 (black), 44 × 10^6 (dark gray), and 100 × 10^6 (light gray) histories for all structures of interest. (c) Relative uncertainty–volume histograms after simulation of 21 × 10^6 (bold curves) and 44 × 10^6 (regular curves) histories for optical structures. Only voxels that did not comply with uncertainty-based stopping criteria after 21 × 10^6 histories were taken into account. PTV = planning target volume.

Ethmoid sinus case

The fraction of voxels complying with the relative ($\sigma_{rel} \leq \sigma_{rel,tol}$) or absolute ($D\sigma_{rel} \leq D_{lim}\sigma_{rel,tol}$) stopping constraints as a function of the number of simulated histories is shown in Fig. 3a for each structure of interest. The MC_{PTV} and MC_{all} simulations were stopped after $N_{PTV} = 21 \times 10^6$ and $N_{all} = 44 \times 10^6$ histories, respectively (Table 1). The PTV reached the 95% limit before all optical structures; the left retina reached it the last. Only 4% of the left retina (and even only 1% of the right retina) satisfied the uncertainty-based stopping criteria after N_{PTV} histories. After N_{PTV} histories, 83% of the PTV voxels satisfied the constraint $\sigma_{rel} \leq \sigma_{rel,tol}$, 84% satisfied $D\sigma_{rel} \leq D_{lim}\sigma_{rel,tol}$, and 97% satisfied either the relative or absolute constraint. After N_{all} histories, all PTV voxels satisfied both constraints, and 49% of the voxels within the left retina satisfied $\sigma_{rel} \leq \sigma_{rel,tol}$, 47%

satisfied $D\sigma_{rel} \leq D_{lim}\sigma_{rel,tol}$, and 96% satisfied either the relative or absolute constraint. The uncertainty-based stopping criteria were met within all voxels for each structure of interest after 100 × 10^6 histories.

Figure 3b shows the DVHs of D_{PTV}, D_{all}, and D_{ref} for all structures of interest. Again, only very slight differences could be observed among the three sets of DVHs. The curves obtained after simulation of N_{PTV} histories were already sufficiently accurate to evaluate the treatment plan. Table 2 presents the median and fifth percentile values of the dose difference distributions D_{PTV}-D_{ref} and D_{all}-D_{ref}, calculated according to Expression 2, for each structure of interest. For DD_5, the largest differences were encountered for the left retina (5.5% for D_{PTV}-D_{ref} and 4.1% for D_{all}-D_{ref}), followed by the right optic nerve, right retina, left optic nerve, optic chiasm, and, finally, the PTV (4.0% for D_{PTV}-D_{ref} and 3.1% for D_{all}-D_{ref}). A similar order was encountered for DD_{50}, with values ranging from 2.1% (for D_{PTV}-D_{ref} within the right optic nerve) to 1.0% (for D_{all}-D_{ref} within the PTV).

Finally, Fig. 3c shows σ_{rel}–volume histograms of MC_{PTV} and MC_{all} for the structures of interest that did not satisfy the uncertainty-based stopping criteria after N_{PTV} histories (*i.e.*, all optical structures). For each structure, only the voxels that did not comply with the relative or absolute stopping constraints after N_{PTV} histories were taken into account (*i.e.*, 96% of the left retina, 99% of the right retina, 78% of the left optic nerve, 89% of the right optic nerve, and 86% of the optic chiasm voxels). For 39% of the left retina voxels and 4% of the right retina voxels, the relative uncertainty on the estimated dose was >3% after N_{PTV} histories; for the other structures, σ_{rel} was <3% within all voxels. After N_{all} histories, σ_{rel} was still >2% for 50% of the left retina voxels and 9% of the right retina voxels, but for none of the voxels within the other structures.

Rectum case

Figure 4a shows the fraction of voxels complying with the relative ($\sigma_{rel} \leq \sigma_{rel,tol}$) or absolute ($D\sigma_{rel} \leq D_{lim}\sigma_{rel,tol}$) stopping constraints as a function of the number of simulated histories for each structure of interest. The MC_{PTV} and MC_{all} simulations were stopped after $N_{PTV} = 12 \times 10^6$ and $N_{all} = 51 \times 10^6$ histories, respectively (Table 1). The 95% limit was reached first for the PTV and last for the surroundings. After N_{PTV} histories, 99% of the PTV voxels satisfied the constraint $\sigma_{rel} \leq \sigma_{rel,tol}$, 97% satisfied $D\sigma_{rel} \leq D_{lim}\sigma_{rel,tol}$, and 99% satisfied either the relative or absolute constraint. For the surroundings, the corresponding values were 0%, 32%, and 32%; after N_{all} histories, these values were 44%, 52%, and 96%. After 100 × 10^6 histories, the uncertainty-based stopping criteria were met within all voxels for each structure of interest, except for 0.3% of the voxels within the surroundings.

Figure 4b compares the DVHs of D_{PTV}, D_{all}, and D_{ref} for all structures of interest. Again, almost no differences could be observed among the three sets of DVHs. Table 2 presents the median and fifth percentile values of the dose difference distributions D_{PTV}-D_{ref} and D_{all}-D_{ref}, calculated according to Expression 2, for each structure of interest. For DD_5, the largest differences were encountered for the surroundings (9.7% for D_{PTV}-D_{ref} and 3.5% for D_{all}-D_{ref}), followed by the small bowel, bladder, rim, and, finally, the PTV (3.5% for D_{PTV}-D_{ref} and 1.3% for D_{all}-D_{ref}). This order was similar to the order in which the structures of interest satisfied

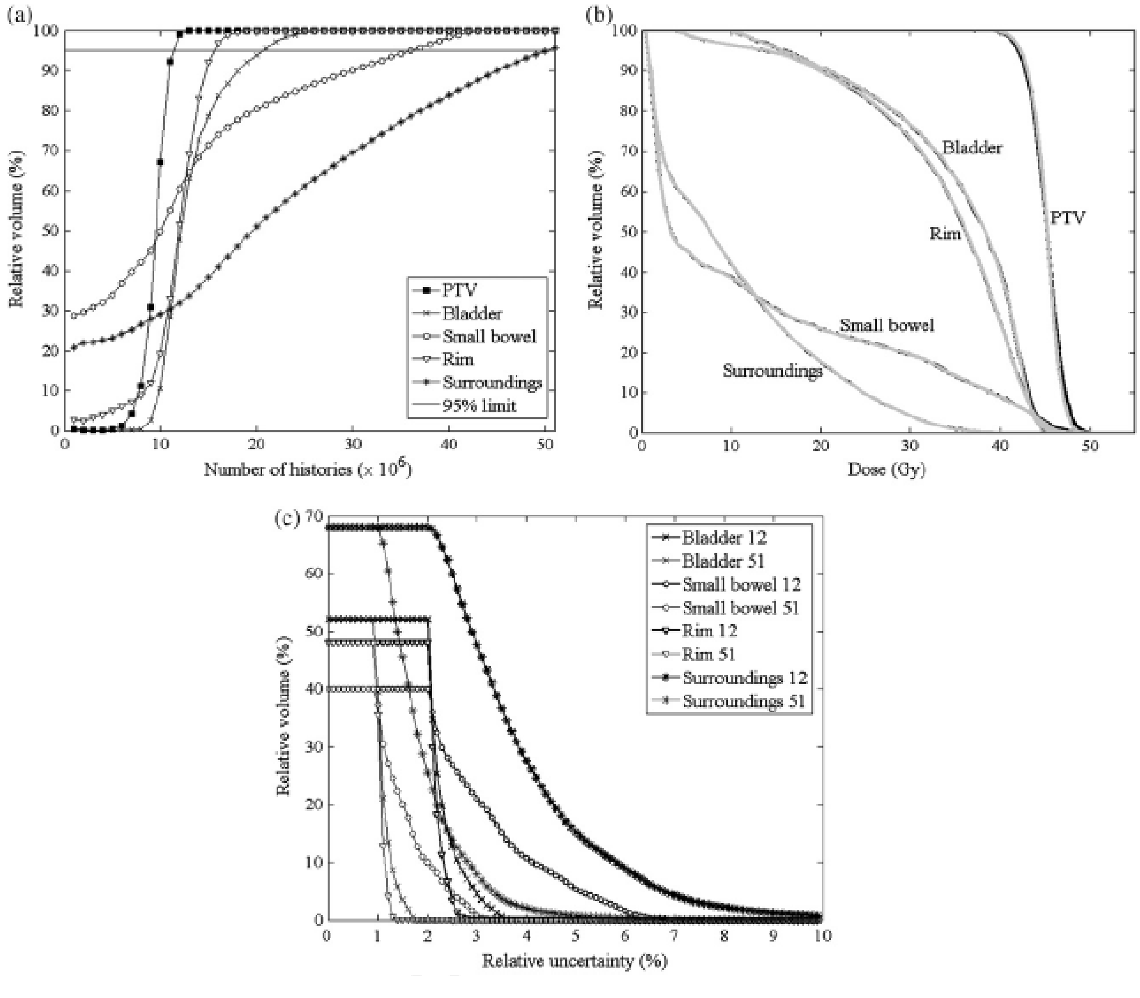

Fig. 4. Rectal case. (a) Fraction of voxels complying with proposed uncertainty-based stopping constraint for each structure of interest, as function of total number of simulated histories. (b) Dose–volume histograms after simulation of 12 × 10^6 (black), 51 × 10^6 (dark gray), and 100 × 10^6 (light gray) histories for all structures of interest. (c) Relative uncertainty–volume histograms after simulation of 12 × 10^6 (bold curves) and 51 × 10^6 (regular curves) histories for bladder, small bowel, rim and surroundings. Only voxels that did not comply with uncertainty-based stopping criteria after 12 × 10^6 histories were taken into account. PTV = planning target volume.

the uncertainty-based stopping criteria (Fig. 4a). Again, differences of this magnitude were only encountered within 5% of the structure voxels. For DD_{50}, the largest differences were encountered for the bladder (2.5% for D_{PTV}-D_{ref} and 0.9% for D_{all}-D_{ref}), followed by the surroundings, rim, small bowel, and, finally, the PTV (1.2% for D_{PTV}-D_{ref} and 0.4% for D_{all}-D_{ref}).

Finally, Fig. 4c shows σ_{rel}–volume histograms of MC_{PTV} and MC_{all} for the structures of interest that did not satisfy the uncertainty-based stopping criteria after N_{PTV} histories (*i.e.*, all OARs). For each structure, only the voxels that did not comply with the relative or absolute stopping constraints after N_{PTV} histories were taken into account (*i.e.*, 52% of the bladder voxels, 40% of the small bowel voxels, 48% of the rim voxels, and 68% of the surroundings voxels). For 15% of the surroundings voxels and 5% of the small bowel voxels, the relative uncertainty on the estimated dose was >5% after N_{PTV} histories. After N_{all} histories, this was no longer the case (<1% of the voxels for both structures). For 48% of the surroundings voxels, 21% of the small bowel voxels and 5% of the bladder voxels, σ_{rel} was >3% after N_{PTV} histories. After N_{all} histories, this was still the case for 8% of the surroundings voxels, but not for the small bowel or bladder (<1% of the voxels).

DISCUSSION

The proposed uncertainty-based stopping criteria were based on the evaluation of Expression 1 within each patient voxel. This Boolean expression consists of two separate constraints for the relative (σ_{rel}) and absolute uncertainty ($D\sigma_{rel}$), combined into an "OR" statement. Because of the stochastic nature of MC calculations, the aberrant behavior of the dose calculation results within individual voxels cannot be ruled out. For this reason, we allowed the statement to remain unfulfilled within no >5% of the voxels for each structure of interest. Similar conditions have been incorporated into all practical MC treatment planning systems. Because σ_{rel} is inversely proportional to $D^{1/2}$ (3, 7), the relative constraint $\sigma_{rel} \leq \sigma_{rel,tol}$ will be satisfied last within the low-dose regions. From a clinical viewpoint, however, it is rarely desirable to determine dose values far below the tolerance level with great accuracy. If the stopping criteria would be based on relative constraints only, the corresponding MC calculations would take unnecessarily long. For this reason, the absolute constraint $D\sigma_{rel} \leq D_{lim}\sigma_{rel,tol}$ was added to Expression 1. This constraint allowed the absolute uncertainty to be compared with the product of the tolerated relative uncertainty and a dose limit value. Thus, for dose values less than D_{lim}, we allowed the relative uncertainty to exceed $\sigma_{rel,tol}$. In contrast, for dose values greater than D_{lim}, the absolute constraint becomes more difficult to satisfy than the relative constraint. Therefore, it is necessary to combine both constraints into an "OR" statement. This is illustrated by the presented lung case. Even after simulation of 100×10^6 histories, the relative constraint was satisfied only for a few of the voxels within the liver, and the absolute constraint was still not satisfied within all lung voxels. However, from a clinical perspective, there was clearly no point in simulating more histories.

The values of D_{lim} are assigned to each structure of interest individually. It is important to establish a link between the way clinical treatment plans are prescribed and evaluated and the selected values of D_{lim}.

For target structures, we propose to select the homogeneous target prescription dose for D_{lim}. Because D will be approximately equal to D_{lim} within each target voxel, the relative and absolute constraint will be more or less equivalent.

For OARs, the added value of the absolute constraint $D\sigma_{rel} \leq D_{lim}\sigma_{rel,tol}$ was clearly more significant. It is important to discriminate between so-called parallel and serial OARs (3, 6). For parallel organs, such as the lungs, treatment planning constraints are often formulated in terms of the mean dose within the organ. Therefore, we selected this mean dose constraint for D_{lim}. For serial organs, such as the spinal cord, it is important to limit the maximal dose delivered to the organ. Because point doses are generally more sensitive to statistical fluctuations than derived dose metrics (6), the planning constraints for serial organs should be formulated in terms of a dose percentile such as D_2 or D_5, instead of the maximal dose. In its new report in progress, the International Commission on Radiological Units will recommend the use of D_2 instead of the maximal dose for both target volumes and OARs (Vincent Grégoire, personal communication, 13 February 2007). The absolute stopping constraint $D\sigma_{rel} \leq D_{lim}\sigma_{rel,tol}$ requires a value for D_{lim} representative of the average dose within the structure of interest, because the relative constraint $\sigma_{rel} \leq \sigma_{rel,tol}$ should still prevail within the high-dose regions to secure the meaning of $\sigma_{rel,tol}$. For lack of a planning constraint value for the mean or median dose for serial organs, we selected a typical value of one of these dose indexes for D_{lim}. The exact value was not so critical, because MC simulation times will primarily be influenced by how fast the high-dose voxels will fulfill the relative constraint. For example, values of D_{lim} can be obtained by retrospective dose–volume analysis of treatment plans for patients with the same tumor site. For the ethmoid sinus and rectal patient cases, the values of D_{lim} for the optical structures, small bowel, rim, and surroundings were thus selected. Alternatively, values of D_{lim} can be easily obtained by halving the planning constraint value of the maximal dose for the structure of interest. For the lung cancer patient case, the value of D_{lim} for the spinal cord was thus selected.

Alternatively, Kawrakow (5) has presented a termination criterion for MC patient dose calculations using the evaluation of a cost function that quantifies the suitability of a treatment plan. The implementation of his approach requires knowledge of the acceptable uncertainty on the cost function. However, it is not clear how this can be determined from a clinical perspective. The purpose of the present study was to provide a practical tool capable of determining the number of histories necessary for accurate clinical treatment plan evaluation. Within this framework, the formulated uncertainty-based stopping criteria are easy to understand, implement, and use.

Considering the data in Figs. 1a, 3a, and 4a, it is important to note that the proposed uncertainty-based stopping criteria lead to substantial differences in simulation time for the PTV and different OARs of interest. Moreover, clear differences can be observed between the shapes of the curves. The more homogeneous the dose delivered to a structure, the steeper the curve will be, because all voxels will satisfy the stopping criteria at approximately the same time. The most obvious example is the PTV, but the dose delivered to small optical structures, such as the right retina and right optic nerve, was also quite homogeneous. Other structures, such as the lungs, small bowel, and surroundings, received a highly inhomogeneous dose, resulting in the flat curves shown in Figs. 1a and 4a.

Moreover, because of the lower density of lung tissue, σ_{rel} will be greater within the lung voxels compared with the other structures of interest. Therefore, accurate dose computation within the lungs will cause the total MC simulation time to increase.

Because of the inclusion of the absolute stopping constraint $D\sigma_{rel} \leq D_{lim}\sigma_{rel,tol}$, the uncertainty-based stopping criteria were easily satisfied within the low-dose regions. This is illustrated by the scatterplots in Fig. 2. For certain structures of interest, such as the liver and heart, the value of the delivered dose was well below D_{lim} within each voxel.

Figures 1c, 3c, and 4c show the gain in simulating N_{all} instead of N_{PTV} histories. Only within the lungs, small bowel, and surroundings, were values of σ_{rel} >5% encountered after N_{PTV} histories. For the other structures, it seems to be less essential to increase the MC simulation time.

The presence of a lot of statistical noise in the lungs resulted from the low density of the lung tissue. For the rectal patient case, N_{PTV} was only one-quarter of N_{all}, explaining the large σ_{rel} values encountered within the small bowel and surroundings. Although it is not shown by the DVHs because of the large volume of these structures, the noise will be evident from other dose distribution evaluation methods (e.g., isodose or gamma evaluation plots).

For the studied patient cases, the uncertainty-based stopping criteria were met within all voxels for all structures of interest after simulating 100×10^6 histories. This justified our consideration of D_{ref} as the reference dose distribution, and we expect this to be valid for similar patient cases as well. Therefore, considering Figs. 1b, 3b, and 4b, it is clear that all treatment plans could be accurately evaluated using the DVHs obtained after N_{PTV} histories, even for low-density OARs such as the lungs. In contrast, the evaluation of the uncertainty-based stopping criteria could depend on the treatment plan configuration. IMRT typically involves the delivery of a large number of small beam segments with relatively few monitor units per segment. In contrast to traditional inverse planning techniques, IMRT plans at Ghent University Hospital are created by direct aperture optimization (16, 17). This typically results in an overlapping set of small and large segments for each beam angle; segments created by inverse planning will generally be smaller and involve less overlap. For the studied patient cases, large beam segments will thus generally contribute more to the patient dose than for inversely planned cases. The influence of treatment plan configuration on the stopping criteria for MC dose calculations is worth additional investigation; however, this was beyond the scope of the present study.

Considering the studied patient cases, the MC calculations could be stopped as soon as the uncertainty-based stopping criteria were satisfied within the PTV only, taking into account a tolerated relative uncertainty of 2% and a dose limit value equal to the PTV prescription dose. Simulating more histories did not change the DVHs of the structures of interest. The formulated uncertainty-based stopping criteria could be used to determine the MC calculation times necessary for accurate clinical IMRT or IMAT plan evaluations. By formulating the absolute stopping constraint, characteristic differences in the dose response of target volumes and serial and parallel OARs can be taken into account by including a meaningful dose limit value. Users can define their own structures of interest for each patient case individually and select appropriate values of the tolerated relative uncertainty and of the dose limit according to their treatment planning goals. The proposed uncertainty-based stopping criteria thus provide a flexible tool to assist MC patient dose calculations.

REFERENCES

1. Bortfeld T. IMRT: A review and preview. *Phys Med Biol* 2006;51:R363–R379.

2. Yu CX. Intensity-modulated arc therapy with dynamic multileaf collimation: An alternative to tomotherapy. *Phys Med Biol* 1995;40:1435–1449.

3. Keall PJ, Siebers JV, Jeraj R, *et al*. The effect of dose calculation uncertainty on the evaluation of radiotherapy plans. *Med Phys* 2000;27:478–484.

4. Buffa FM, Nahum AE. Monte Carlo dose calculations and radiobiological modelling: Analysis of the effect of the statistical noise of the dose distribution on the probability of tumour control. *Phys Med Biol* 2000;45:3009–3023.

5. Kawrakow I. The effect of Monte Carlo statistical uncertainties on the evaluation of dose distributions in radiation treatment planning. *Phys Med Biol* 2004;49:1549–1556.

6. Chetty IJ, Rosu M, Kessler ML, *et al*. Reporting and analyzing statistical uncertainties in Monte Carlo-based treatment planning. *Int J Radiat Oncol Biol Phys* 2006;65:1249–1259.

7. Sempau J, Bielajew AF. Towards the elimination of Monte Carlo statistical fluctuation from dose volume histograms for radiotherapy treatment planning. *Phys Med Biol* 2000;45:131–157.

8. Jiang SB, Pawlicki T, Ma CM. Removing the effect of statistical uncertainty on dose–volume histograms from Monte Carlo dose calculations. *Phys Med Biol* 2000;45:2151–2161.

9. Jeraj R, Keall P. The effect of statistical uncertainty on inverse treatment planning based on Monte Carlo dose calculation. *Phys Med Biol* 2000;45:3601–3613.

10. Ma CM, Li JS, Jiang SB, *et al*. Effect of statistical uncertainties on Monte Carlo treatment planning. *Phys Med Biol* 2005;50:891–907.

11. Rogers DWO, Ma CM, Walters B, *et al*. BEAMnrc users manual. Ottawa, Canada: National Research Council of Canada;2002.

12. Walters BRB, Kawrakow I, Rogers DWO. History by history statistical estimators in the BEAM code system. *Med Phys* 2002;29:2745–2752.

13. Reynaert N, De Smedt B, Coghe M, *et al*. MCDE: A new Monte Carlo dose engine for IMRT. *Phys Med Biol* 2004;49:N235–N241.

14. Kawrakow I, Rogers DWO. The EGSnrc code system: Monte Carlo simulation of electron and photon transport. NRCC Report PIRS-701. Ottawa, Canada: National Research Council of Canada; 2000.

15. Olteanu AML, Reynaert N, De Gersem W, *et al*. Monte Carlo simulation of intensity-modulated arc therapy plans. In: Abstract Book of the First European Workshop on Monte Carlo Treatment Planning; 2006. p. 75.

16. De Gersem W, Claus F, De Wagter C, *et al*. An anatomy-based segmentation tool for intensity-modulated radiation therapy and its application to head-and-neck cancer. *Int J Radiat Oncol Biol Phys* 2001;51:849–859.

17. De Gersem W, Claus F, De Wagter C, *et al*. Leaf position optimization for step-and-shoot IMRT. *Int J Radiat Oncol Biol Phys* 2001;51:1371–1388.

18. Duthoy W, De Gersem W, Vergote K, *et al*. Clinical implementation of intensity-modulated arc therapy (IMAT) for rectal cancer. *Int J Radiat Oncol Biol Phys* 2004;60:794–806.

19. De Neve W, Wu Y, Ezzell G. Practical IMRT planning. In: Bortfeld T, Schmidt-Ullrich R, De Neve W, *et al*., editors. Image-guided IMRT. Berlin: Springer; 2006. p. 54.

Chapter 9

Publication 7:

The influence of air cavities within the PTV on Monte Carlo-based IMRT optimization

Bart De Smedt[1], Barbara Vanderstraeten[1,2], Nick Reynaert[1], Werner De Gersem[2], Wilfried De Neve[2] and Hubert Thierens[1]

[1] *Department of Medical Physics, Ghent University, Gent, Belgium*
[2] *Department of Radiotherapy, Ghent University Hospital, Gent, Belgium*

Journal of Physics: Conference Series 2007;74:012003

Abstract

Integrating Monte Carlo calculated dose distributions into an iterative aperture-based IMRT optimization process can improve the final treatment plan. However, the influence of large air cavities in the planning target volume (PTV) on the outcome of the optimization process should not be underestimated. To study this influence, the treatment plan of an ethmoid sinus cancer patient, which has large air cavities included in the PTV, is iteratively optimized in two different situations, namely when the large air cavities are included in the PTV and when these air cavities are excluded from the PTV. Two optimization methods were applied to integrate the Monte Carlo calculated dose distributions into the optimization process, namely the 'Correction – method' and the 'Per Segment – method'. The 'Correction – method' takes the Monte Carlo calculated global dose distribution into account in the optimization process by means of a correction matrix, which is in fact a dose distribution that is equal to the difference between the Monte Carlo calculated global dose distribution and the global dose distribution calculated by a conventional dose calculation algorithm. The 'Per Segment – method' uses directly the Monte Carlo calculated dose distributions of the individual segments in the optimization process. Both methods tend to converge whether or not large air cavities are excluded from the PTV during the optimization process. However, the 'Per Segment – method' performs better than the 'Correction – method' in both situations and the 'Per Segment – method' in the case where the large air cavities are excluded from the PTV leads to a better treatment plan then when these air cavities are included. Therefore we advise to exclude large air cavities and to apply the 'Per Segment – method' to integrate the Monte Carlo dose calculations into an iterative aperture-based optimization process. Nevertheless, the 'Correction – method' provides a good alternative in the case when the external dose engine is not able to generate individual dose distributions for the individual segments.

1. Introduction

In the standard approach of intensity modulated radiotherapy (IMRT) treatment plan optimization, the intensity pattern for each IMRT beam is modelled as a 2D map of energy fluence incident on a patient. This intensity pattern is divided into discrete uniform beam elements (beamlets or bixels) and an inverse planning or automated optimization system is then used to generate a set of beamlets that will produce, as closely as possible, the desired dose distributions.

To produce practically deliverable treatment fields, these elementary beamlets are regrouped into larger fields during a process called 'leaf sequencing'. However, the obtained treatment fields are only an approximation of the ideal intensity distribution and this usually leads to a reduced quality of the treatment plan. Nevertheless, there are several approaches to overcome the sequencer problems in IMRT optimization (Alber and Nüsslin 2001, Litzenberg *et al* 2002, Siebers *et al* 2002) and one of these approaches is the method of aperture-based optimization.

Aperture-based optimization (Shepard *et al* 2002, De Gersem *et al* 2001) is a technique for IMRT that is designed to reduce the complexity of intensity modulated treatment plans and to facilitate the application of IMRT in clinical practice. This is achieved by avoiding the optimization of intensity maps. Instead, the planning process is based on a small, preset number of multileaf collimator (MLC) shapes (apertures or segments) per beam direction. The optimization is then either limited to calculate optimal weights for predefined apertures (which can be, for example, derived from the patient's anatomy), or it can be extended to a simultaneous optimization of the shapes and weights of the apertures.

The aim of this work is to investigate whether the final treatment plan obtained by an iterative aperture-based optimization process that incorporates a conventional dose calculation algorithm could be improved by integrating Monte Carlo calculated dose distributions into this optimization process and to illustrate the influence of large air cavities on the outcome of the optimization process. Two alternative methods are examined to integrate these Monte Carlo calculated dose distributions into the aperture-based optimization process applied at Ghent University Hospital (GUH).

2. Methods and materials

2.1. IMRT optimization system

At GUH, a segmentation-based inverse planning approach is used to create IMRT treatment plans for step-and-shoot delivery with a MLC. Starting from an initial set of beam segments, as illustrated in figure 1, the corresponding set of segment dose distributions is calculated by an external dose engine. Generally the differential scatter-air ratio dose calculation algorithm of GRATIS (Sherouse *et al* 1989) is used. As illustrated in a recent paper (Paelinck *et al* 2006) the accuracy of this system cannot be guaranteed, as for individual cases deviations above 10% were obtained when comparing GRATIS DVHs to MCDE results. During the optimization process, a bio-physical objective function is maximized starting with the in-house developed Segment Weight Optimization Tool (SWOT) cycle, which only optimizes the weights of the beam segments and leaves all segment shapes unchanged. After the first SWOT cycle, the Segment Outline and Weight Adapting Tool (SOWAT) optimizes the MLC settings and weights of these segments (De Gersem *et al* 2001) and an additional SWOT cycle is performed. When the plan acceptance criteria are not fulfilled, a new optimization cycle is performed (SOWAT + SWOT). This is repeated until the plan acceptance criteria are fulfilled.

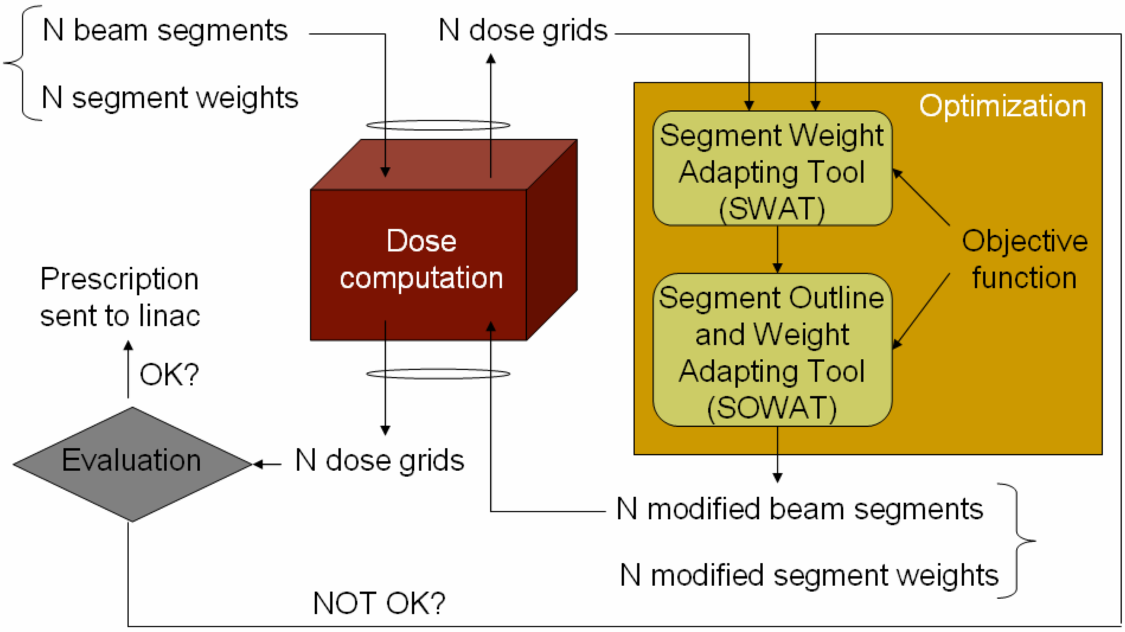

Figure 1. Overview of the iterative optimization cycle and the different optimization algorithms used at Ghent University Hospital.

The aim of our study was to investigate whether the final treatment plan could be improved by integrating our Monte Carlo Dose Engine MCDE (Reynaert *et al* 2004) into the iterative optimization process and to illustrate the influence of large air cavities on the outcome of this optimization process.

2.2. Dose computation method: 'Correction – method'

The initial treatment plan calculated with GRATIS (providing a global dose distribution D_{GRATIS}) is recalculated with MCDE resulting in a global dose distribution D_{MCDE}. The values of the voxels in the correction matrix R are determined by $R = D_{MCDE} - D_{GRATIS}$, which results in a dose distribution that is equal to the difference between the global GRATIS and MCDE results.

To take this correction matrix into account during the optimization process, an additional beam ('patch-beam') was created of which the weight (set to unity) and MLC settings were locked. Both SOWAT and SWOT cycles used the GRATIS dose distributions of the individual segments, plus the dose distribution of this 'patch-beam' to evaluate the outcome of the treatment plan.

It can be expected that this method will introduce small systematic errors during the optimization process, because the correction matrix R (and inherently the dose distribution of the 'patch-beam') remains constant, while the GRATIS results for the individual beam segments are modified during an optimization iteration (as the MLC settings and weights of the individual segments are changed). Nevertheless, the 'Correction – method' is very useful if the Monte Carlo dose engine that has to be integrated into the optimization software is only capable of delivering a global dose distribution.

2.3. Dose computation method: 'Per Segment – method'

With the 'Per Segment – method', the Monte Carlo calculated dose distributions of the individual segments are used directly by the SOWAT and SWOT algorithms instead of the GRATIS dose distributions. No 'patch-beam' has to be created. It is therefore a more accurate method of integrating Monte Carlo results into the optimization process. However, this method requires a Monte Carlo dose engine to be capable of delivering the dose distributions of the individual segments.

2.4. Clinical case

An ethmoid sinus cancer patient case was studied with large air cavities present in the planning target volume (PTV). The patient was treated with 42 6 MV beam segments impinging from 9 different directions. Starting from the initial plan generated by the GRATIS dose calculation algorithm, five additional optimization cycles (SOWAT and SWOT) were performed. Before the start of each cycle, a MCDE calculation was performed for both the 'Correction – method' and the 'Per Segment – method', thus providing a global dose distribution and a set of dose distributions of the individual segments.

To determine the influence of the air cavities, both methods were applied while including/excluding the large air cavities from the original PTV. This allows the study of the influence of statistical noise from the MCDE calculations on the optimization process. The exclusion of the air cavities of the PTV leads to a newly defined structure and is accomplished by delineating these air cavities in the PTV and by subtracting these air cavities from the original PTV using in-house developed software.

Treatment plans were compared by means of dose volume histograms (DVHs) and their corresponding values of the objective function are used to illustrate the convergence of the iterative optimization process.

3. Results and discussion

3.1. Calculation times

The MCDE calculation times of the treatment plans obtained in the iterative optimization cycles with the 'Per Segment – method' and the 'Correction – method' were almost identical, namely 4 hours on a cluster consisting of 34 2.4 GHz Xeon processors.

However, to obtain the correction matrix ('patch-beam') for the 'Correction – method', the individual dose distributions of the different beam segments had to be calculated first by the GRATIS dose computation algorithm, which requires an additional calculation time of about half an hour before a new optimization cycle can be started.

With the 'Per Segment – method', there is no need for an extra dose calculation with GRATIS since these individual Monte Carlo calculated dose distributions are used directly in the optimization cycle.

3.2. Convergence of the value of the objective function

For the initial treatment plan, the values of the objective function for the dose distribution calculated by GRATIS were respectively -6.2 when including the large air cavities in the PTV and -6.8 when excluding these air cavities. A recalculation of this initial treatment plan with the Monte Carlo dose engine MCDE provided a dose distribution from which the values of the objective function were equal to -14.9 and -12.6 respectively, as illustrated in figure 2.

Both the 'Correction – method' and the 'Per Segment – method' tend to converge in both situations. However, when the air cavities are included in the PTV, the convergence isn't obtained as fluently as in the situation without the air cavities as the values of the objective function don't increase continuously.

Figure 2 also illustrates that the results obtained with both the 'Correction – method' as well as the 'Per Segment – method' are quite similar when the air cavities are included in the PTV. However, excluding the air cavities from the PTV clearly leads to a larger difference between both methods, which leads to the conclusion that a better treatment plan is obtained by applying the 'Per Segment – method'.

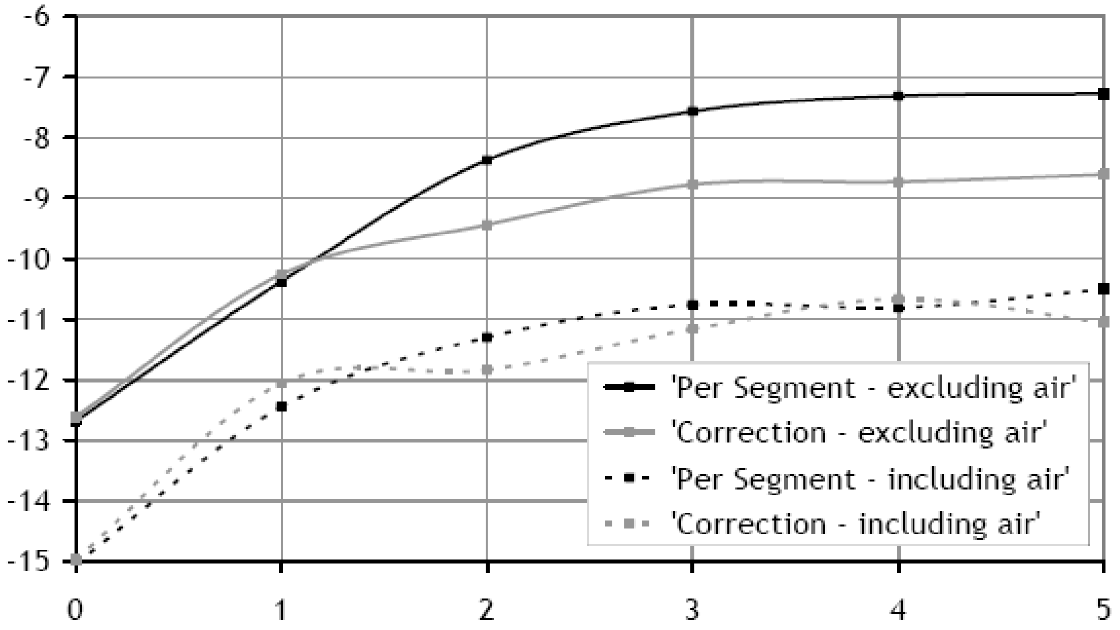

Figure 2. Illustration of the convergence of the value of the objection function (OF) after five optimization cycles for both the 'Correction – method' and 'Per Segment – method' when applied in two situations: one situation in which the large air cavities are included in the PTV and the other situation in which these air cavities are excluded from the PTV.

3.3. Comparison of DVHs

As the quantitative values of the objective function strongly depend on the choice of this function, the quality of the resulting treatment plan was also evaluated by looking at the DVHs for both methods in both situations (inclusion or exclusion of the air cavities from the PTV).

A. Excluding the air cavities from the PTV.

Looking at the DVHs for both optimization methods in the situation where the air cavities are excluded from the PTV in figure 3, one can conclude that the initial treatment plan is improved by integrating Monte Carlo calculated dose distributions into the iterative aperture-based optimization process. Moreover, in accordance to the values of the objective function in figure 2, the 'Per Segment – method' provides a better treatment plan compared to the 'Correction – method' and is therefore a more favourable method of integrating Monte Carlo calculated dose distributions into the optimization process. Nevertheless, not all dose engines are able to produce dose distributions for the individual beam segments and therefore the 'Correction – method' provides a good alternative, especially in the case when the air cavities are excluded from the PTV.

B. Including the air cavities from the PTV.

Figure 4 shows the DVHs for the 'Per Segment – method' applied to both situations (including and excluding the air cavities from the PTV). It's clear that the initial treatment plan is improved in both cases. However, excluding the air cavities from the PTV during the optimization process provides a better treatment plan. This is mainly caused by the presence of high statistical noise on the Monte Carlo calculated dose in these air cavities, since relatively fewer particles will interact in air compared to the surrounding tissues.

If acceptable statistical uncertainties on the dose values in these air voxels are required, e.g. to compute the value of the objective function, the calculation time of the Monte Carlo dose engine should be increased dramatically (by a factor of thousand) to compensate for the low density of air, which is not realistic at all. Denoising cannot solve this problem as the noise in the air cavities is too severe. Denoising techniques can decrease the calculation time by a factor of ten (Kawrakow 2002, El Naqa *et al* 2005), which is still not sufficient for the air voxels.

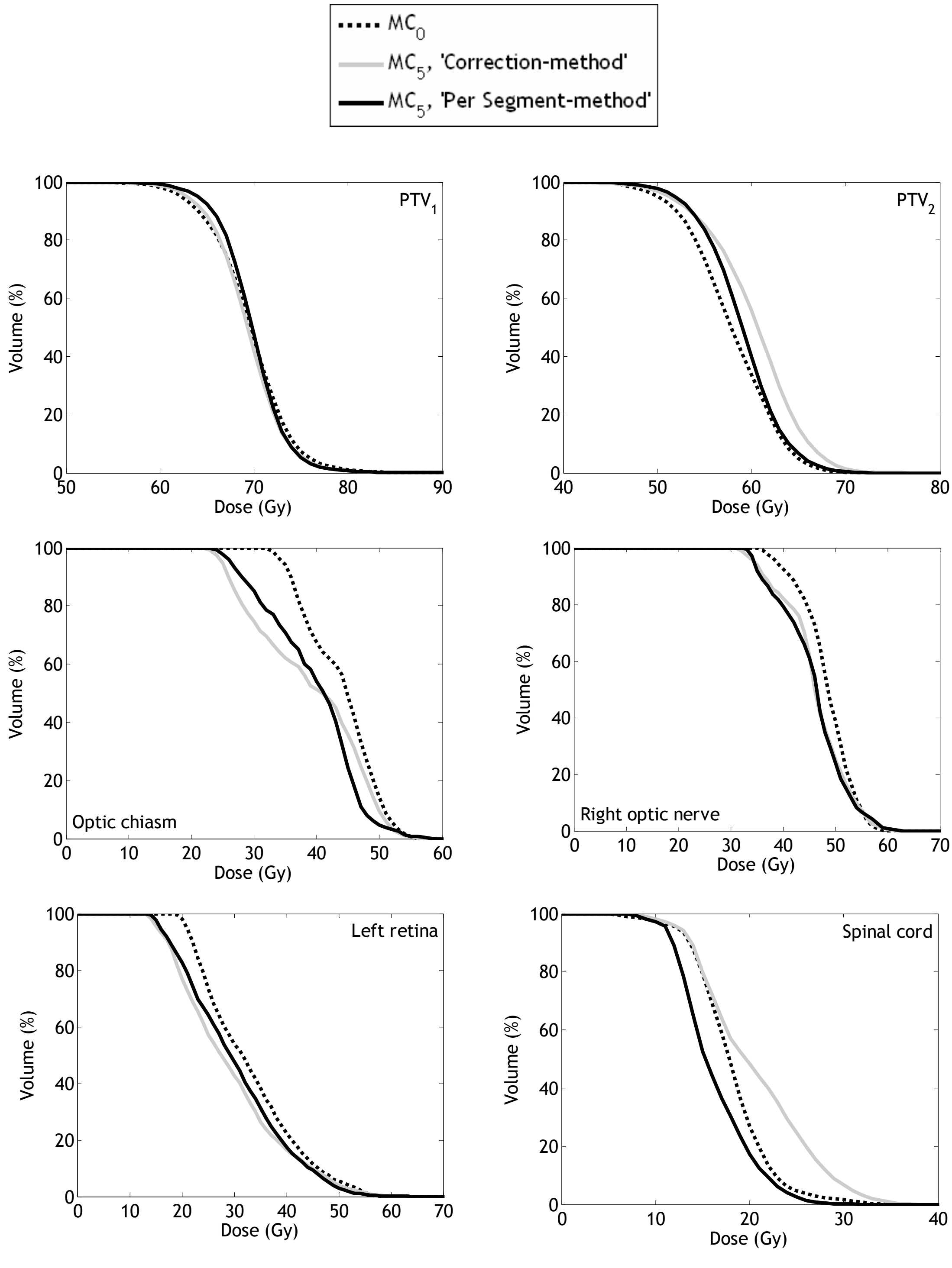

Figure 3. Comparison between the 'Correction – method' and 'Per Segment – method' of the DVHs of the initial treatment plan and the treatment plan after the fifth optimization cycle obtained in the situation where the air cavities are excluded from the PTV.

Therefore each dose calculation algorithm will have to deal with the concept 'dose to air' in some way. There are several possible methods to achieve this. For instance, one can apply a KERMA approximation in the air voxels. Another possibility is to transport track-end electrons on straight lines by their range (Kawrakow and Fippel 2000) in these air regions, instead of locally depositing the track-end electrons, as is the case

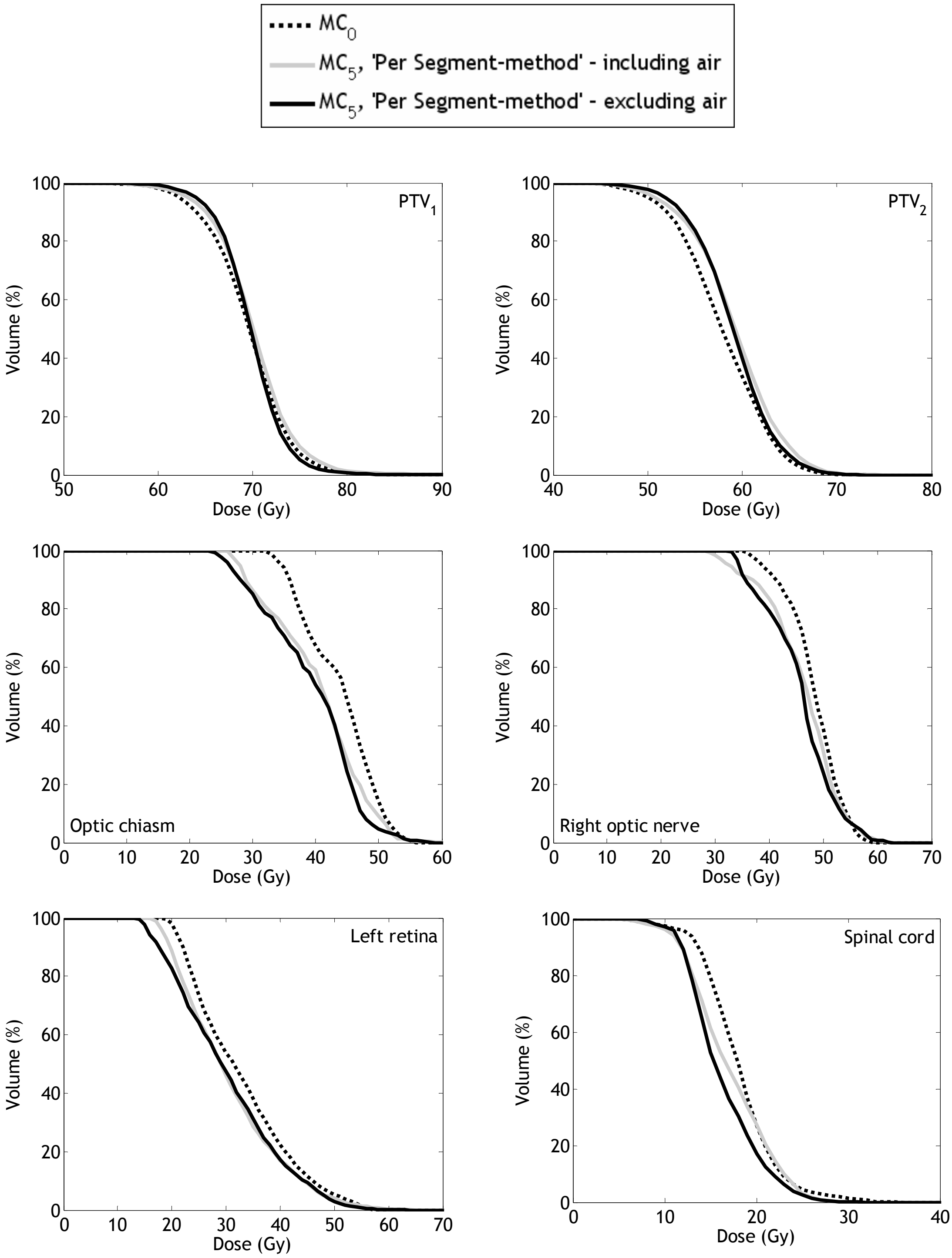

Figure 4. Comparison of the DVHs of the initial treatment plan and the treatment plan after the fifth optimization cycle obtained for the 'Per Segment – method' in the cases where the air cavities are included or excluded from the PTV.

with EGS-based Monte Carlo dose calculation algorithms. However, lowering the ECUT value to 0.521 MeV in our patient calculations did not have a significant effect on the noise in these air voxels.

In this paper, subtracting the volume of the air from the volume of the PTV (the volume of air measured 30% of the volume of the PTV) leads to a dose distribution in the PTV containing less statistical noise. An advantage of this method is that some commercially available treatment planning systems are provided with software to subtract structures. A disadvantage is that the delineation of all air cavities leads to a higher workload. However, one could question the subtraction of air cavities from the PTV on principle, as they are in fact part of the PTV. Nevertheless, we are interested in the dose to the tissue within the PTV and not in the dose to the air cavities.

Another possible method is to adapt the DVH software and the calculation of the value of the objective function by the optimization software in such a manner that all voxels with a Hounsfield number less than, for instance, -500 Hounsfield units are neglected or are given a lower weight so they have less influence. The disadvantage of this method is that it is not always possible to manipulate commercially available DVH software or the optimization algorithm. Therefore, it is recommended that commercial treatment planning systems provide at least one of these aforementioned methods, especially those treatment planning systems that implement a Monte Carlo dose calculation algorithm.

4. Conclusions

By integrating Monte Carlo dose calculations into the IMRT optimization process the treatment plan can be further improved. Both the 'Correction – method' and 'Per segment – method' could be applied. However, the 'Per Segment – method' performed better than the 'Correction – method' when the air cavities are excluded from the PTV. When the air cavities are included, both methods converge to a similar treatment plan, which is indeed an improvement of the initial treatment plan, although not fully optimized. Therefore we advise to not include air cavities and to apply the 'Per Segment – method' to integrate the Monte Carlo dose calculations into the optimization process. However, the 'Correction – method' provides also a good alternative when the Monte Carlo dose engine is not able to generate individual dose distributions.

Acknowledgments

This research work was supported by the Ghent University grant GOA 12050401. Barbara Vanderstraeten is a Research Assistant (Aspirant) of the Fund for Scientific Research – Flanders (FWO-Vlaanderen).

References

Alber M and Nüsslin F 2001 Optimization of intensity modulated radiotherapy underd constraints for static and dynamic MLC delivery *Phys. Med. Biol.* **46** 3229-3239

De Gersem W, Claus F, De Wagter C, Van Duyse B and De Neve W 2001 Leaf position optimization for step-and-shoot IMRT, *Int. J. Radiat. Oncol. Biol. Phys.* **51** 1371-1388

De Vlamynck K, Palmans H, Verhaegen F, De Wagter C, De Neve W and Thierens H 1999 Dose measurements compared with Monte Carlo simulations of narrow 6 MV multileaf collimator shaped photon beams, *Med. Phys.* **26** 1874-1882

El Naqa I, Kawrakow I, Fippel M, Siebers J V, Lindsay P E, Wickerhauser M V, Vicic M, Zakarian K, Kauffmann N and Deasy J O 2005 A comparison of Monte Carlo dose calculation denoising techniques, *Phys. Med. Biol.* **50** 909-922

Kawrakow I 2002 On the de-noising of Monte Carlo calculated dose distributions, *Phys. Med. Biol.* **47** 3087-3103

Kawrakow I and Fippel M 2000 Investigation of variance reduction techniques for Monte Carlo photon dose calculations using XVMC, *Phys. Med. Biol.* **45** 2163-2183

Kawrakow I and Rogers D W O 2000 The EGSnrc code system: Monte Carlo simulation of electron and photon transport, *NRCC Report PIRS-701*, National Research Council of Canada, Ottawa

Litzenberg D W, Moran J M and Fraass B A 2002 Incorporation of realistic delivery limitations into dynamic MLC treatment delivery, *Med. Phys.* **29** 810-820

Paelinck L, De Smedt B, Reynaert N, Coghe M, De Gersem W, De Wagter C, Vanderstraeten B, Thierens H, De Neve W. 2006 Comparison of dose-volume histograms of IMRT treatment plans for ethmoid sinus cancer computed by advanced treatment planning systems including Monte Carlo. *Radiother. Oncol.* **81(3)** 250-256

Reynaert N, De Smedt B, Coghe M, Paelinck L, Van Duyse B, De Gersem W, De Wagter C, De Neve W and Thierens H 2004 MCDE: a new Monte Carlo Dose Engine for IMRT with an efficient scoring method, *Phys. Med. Biol.* **49** N235-N241

Rogers D W O, Ma C-M, Walters B, Ding G X, Sheikh-Bagheri D and Zang G. 2002 BEAMnrc user manual, National Research Council of Canada.

Siebers J V, Lauterbach M, Keall P J, Mohan R 2002 Incorporating multi-leaf collimator leaf sequencing into iterative IMRT optimization, *Med. Phys.* **29** 952-959

Shepard D M, Earl M and Yu C 2002 Direct aperture optimization: A turnkey solution for step-andshoot IMRT, *Med. Phys.* **29** 1007-1018

Sherouse G W, Thorn J, Novins K, Margolese-Malin J and Mosher C 1989 A portable 3D radiotherapy design system (abstract), *Med. Phys.* **16** 466

Chapter 10

Discussion

10.1 Rationale for BCRT

By targeting the most radiation resistant regions inside the tumor while maximally preserving the functionality of critical organs, BCRT may improve the local control versus toxicity ratio. However, a new set of problems and questions arise with the integration of biological imaging information into the IMRT treatment planning process. Indeed, the exact meaning of the biological imaging information remains insufficiently known, as well as how the radiobiological factors should be transformed into the desired dose prescription. Moreover, it is not clear what should be the optimal radiation treatment schedule.

It has been suggested that the rationale for inhomogeneous dose prescription should be further investigated through fundamental radiobiological research and pre-clinical evaluations using animal models, before proceeding towards clinical implementation [1]. On the other hand, clinical investigations may already contribute to address some of the above-mentioned issues [2,3]. For a variety of tumor sites, phase I trials are first needed to study the dose/volume/toxicity relationship. Next, phase II trials with local control and site of recurrence as primary endpoints might test the validity of the approach. While pre-clinical research is required to formulate stable hypotheses for safe and well-designed clinical trials, the results of these trials may in turn raise new questions and provide guidance to the fundamental research. Pre-clinical, translational and clinical research can thus be conducted simultaneously. To conduct clinical trials, the appropriate technology for the planning and delivery of BCRT is required [4]. In this thesis, a technical solution was provided for the clinical implementation of BCRT.

10.2 Technical solution

10.2.1 Relationship between signal intensity and dose

An important task in the implementation of BCRT is to quantify the tumor burden from the available biological imaging data and to relate it to the desired radiation dose. The most fundamental and logical approach would be to generate the dose prescription based on a biological model. This involves two steps: (i) translating the biological image signal intensity values into meaningful radiobiological parameters and (ii) determining the inhomogeneous dose prescription pattern from the known biology distribution.

Unfortunately, for many biological imaging techniques it is not at all obvious which fundamental radiobiological properties are represented in the image and how they can be quantified. Additionally, due to technical limitations and the presence of image artefacts the biological image signal does not always accurately reflect the actual biological characteristics over the entire imaging volume. Provided all necessary biological parameters are known, radiobiological models can generate the most desirable dose distribution by optimizing the cell killing through maximization of the TCP [5-8].

As data on fundamental radiobiological parameters are sparse and not easily extracted from the available biological images, a more practical approach seems to be the best option at present. Several authors have suggested the use of a linear relationship between the biological image signal intensity I and the radiation dose D to be delivered in every image voxel [9-12]. This linear relationship is used as a reasonable starting point [5].

In the first two publications of this thesis [13,14], the prescription dose was escalated linearly between D_{low} and D_{high}, respectively corresponding to I_{low} and I_{high}. The values of I_{low}, I_{high}, D_{low} and D_{high} can be chosen freely. For FDG-PET guided BCRT in head and neck cancer, we wanted to achieve a maximal intensity range for dose escalation, while minimizing the influence of noise. For this purpose, I_{low} and I_{high} were set equal to 25% and 100% of the 95th percentile PET intensity value within the PTV. For D_{low}, the PTV prescription dose of the standard IMRT treatment was selected, *i.e.* 69 Gy in 32 fractions or 2.16 Gy per fraction. The radiation dose used in current clinical practice with "intent to cure" seems to be an acceptable value for $\mathrm{D}_{\mathrm{low}}$ of the BCRT dose prescription [5].

In principle, the dose prescription for BCRT can be determined experimentally by analyzing animal data or hypothesis-driven clinical data. This is similar to the establishment of the empirical dose prescriptions for different disease sites in current clinical practice. In this thesis, the choice of D_{high} was determined by the dose escalation levels applied in the FDG-PET guided dose painting phase I clinical trial, *i.e.* 2.5 and 3 Gy per fraction [15].

10.2.2 Treatment plan optimization

BCRT has been implemented into the inverse treatment planning process at several institutions [10,11,16]. Once the desired BCRT dose prescription distribution is determined, IMRT optimization can proceed. The algorithmic segmentation-based inverse IMRT planning approach of GUH involves the creation of initial beam segments, followed by optimization of the segment weights and leaf positions [17,18].

To implement BCRT at GUH, a biology-based segmentation tool was first developed to generate initial beam segments based on the projected biological images [13]. The optimization engine uses an objective function that consists of a physical and a biological part. The physical part is entirely target-related and refers to target inhomogeneity and prescription dose values. To implement BCRT, a physical term was added to the objective function, which minimizes the root mean square deviation between the obtained and intended dose values in every PTV voxel [13].

The biological part of the objective function numerically maximizes the TCP while maintaining the NTCP below a certain limit. If fundamental radiobiological parameters could be extracted from the biological images, they could be used to modify the conventional TCP and NTCP formula to take into account a heterogeneous biology distribution. In this way, a biological model-based approach would allow BCRT optimization through the biological part of the objective function. Truly biological optimization of BCRT is a great challenge at present, because there is a lack of data that allow the development of biological models, linking the biological imaging information to treatment outcome. One could also take a “hybrid” approach, by calculating the intended dose within every patient voxel by means of a biological model and entering this data into the physical part of the objective function. The influence of the biology-based segmentation tool and optimization settings on BCRT treatment planning was studied in the first publication of this thesis [13].

10.2.3 Treatment plan evaluation

The large volume of information inherent to 3D treatment design makes it difficult to display and assess the corresponding dose distributions in an objective way. The spatial characteristics of a 3D dose distribution can be examined in detail by means of 2D isocurves in a slice-by-slice fashion. However, this is only quasi-quantitative, time-consuming and not an efficient way to compare competing treatment plans even for conventional IMRT. The additional degrees of freedom provided by the biological images complicate BCRT treatment plan evaluation even more, as a homogeneous dose distribution is no longer the goal within the PTV.

Data reduction techniques are commonly used to quantitatively assess treatment plans. By presenting the fractional volume of a structure of interest (target or OAR) receiving doses above a certain value, DVHs have become the most widely used IMRT treatment plan evaluation tool. Unfortunately, due to the non-uniform biology distribution within the tumor, they are not very useful for evaluating BCRT treatment plans. For this reason, Q-volume histograms (QVHs) were introduced in the first publication of this thesis [13]. Within each target voxel, Q is defined as the ratio of the obtained dose and the intended dose, which is calculated from the biological image signal intensity value. By display of the fractional volume for which Q is greater than each abscissa value, a QVH essentially is a DVH of the dose ratio distribution. In the ideal case, a QVH curve drops down steeply at $Q = 1$. To compress the quality of the obtained biologically conformal dose distribution into a single figure, the quality factor QF was introduced. QF was defined as the average absolute deviation of Q to 1 within the PTV. In case of a perfect biologically conformal dose distribution, $QF = 0$. QVHs can also be used for the comparison of BCRT with conventional IMRT treatment planning. In the latter case Q becomes equal to the ratio of the obtained dose and the uniform prescription dose within each target voxel.

10.3 Treatment planning studies

The feasibility of achieving deliberately inhomogeneous dose distributions in accordance with biological imaging information can be demonstrated by performing treatment planning studies. Examples of FMISO-PET guided BCRT for a base-of-tongue cancer case [10], FDG-PET and SPECT guided BCRT for 2 lung cancer cases [11], and FDG-PET guided BCRT for an oropharyngeal cancer case [13] have been reported.

In the second publication of this thesis, FDG-PET guided BCRT was used to create treatment plans for 15 head and neck cancer patients [14]. Two different levels of dose escalation were applied. While BCRT or dose painting-by-numbers ("FDG-PET voxel intensity-based IMRT") had a large impact on the dose distribution within the PTV compared to regular dose painting ("FDG-PET contour-based IMRT"), only small effects were observed on the dose distribution outside the PTV, especially on the dose delivered to the organs at risk. The resulting BCRT plans complied with the OAR planning constraints for all patients.

Thorwarth *et al.* [19] have confirmed dose escalation using BCRT to be feasible in head and neck cancer under the constraint of limiting normal tissue doses to the level of conventional IMRT. In their planning study incorporating 13 patients, hypoxia dose painting-by-numbers was realized according to a map of dose escalation factors calculated from dynamic FMISO-PET data. Compared to a dose painting strategy delivering a 110% uniform dose escalation to a contoured FDG-PET lesion, improved target coverage was achieved using dose painting-by-numbers. Moreover, an increase in TCP of 14.3% was reported for FMISO-PET guided dose painting-by-numbers, compared to only 1.8% for the uniform FDG-PET guided dose escalation. The TCP model was established by relating dynamic FMISO data with therapy outcome [20].

10.4 Current issues in BCRT

10.4.1 Biological imaging

One of the main challenges for BCRT in the future will be the selection of one or more adequate biological imaging modalities for each treatment site. In the ideal case, several biological image sets will be available for each patient. Together, they will enable us to visualize biological tumor characteristics that influence RT response (metabolism, proliferation, oxygenation, vascularization), as well as provide data on normal tissue functionality. A spatially heterogeneous biology profile can thus be created for each patient.

In order to achieve this, efforts should be made to explore new tracers for biological imaging, or – at first instance – to develop adequate image acquisition protocols for RT treatment planning (including image reconstruction and post-processing) and image quantification of existing and available tracers. Because of the high spatial accuracy desired for BCRT, image resolution is an important issue.

At present, PET and fMRI seem to be the most powerful imaging techniques to assess biological tumor properties non-invasively. FDG-PET can be used to identify regions of enhanced glucose metabolism. Using human FaDu head and neck squamous cell carcinomas in nude mice, Schütze *et al.* recently observed a greater effect on local control by increasing the radiation dose in tumors with higher FDG uptake, where the dose-response relationship appears to be steep, than in tumors with lower FDG uptake, where the dose-response relationship seems to be very shallow [21].

FLT is preferentially used to image tumor cell proliferation. Figure 4.3 illustrates the qualitative differences between CT, FDG-PET and FLT-PET images for a rectal cancer patient [22]. To visualize hypoxic regions within tumors, a variety of different PET tracers, such as FMISO and Cu-ATSM, is available. Each of them is of potential use for BCRT planning purposes [23,24]. In order to preserve maximal lung function, ^{99m}Tc-labelled macro-aggregated albumin (MAA) SPECT perfusion imaging can be used to divert dose from well-functioning regions within the lungs towards less perfused regions [25].

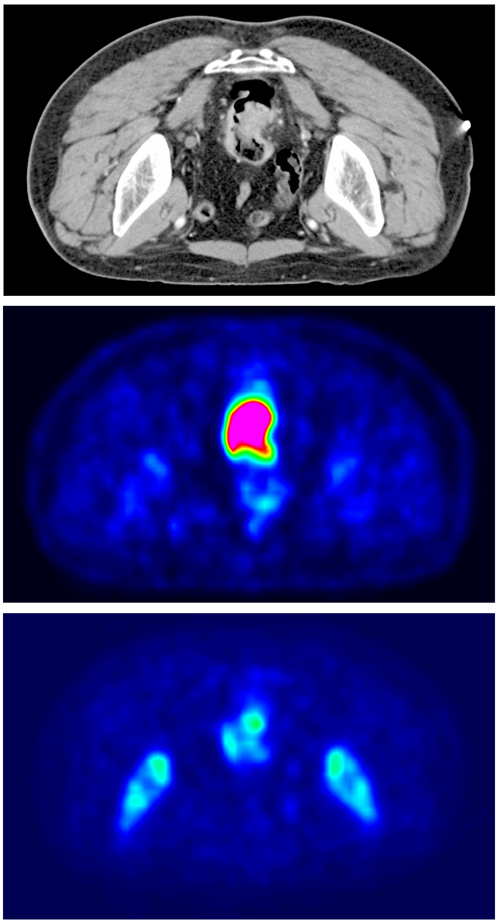

Figure 4.3: Illustration of pre-treatment CT (top), FDG-PET (centre) and FLT-PET (bottom) transversal images for a rectal cancer patient case (reprinted with permission from Sarah Roels).

Conventional MRI lacks the metabolic information that can accurately define the presence and spatial extent of active tumor. By correlating DCE-MRI with histopathological and clinical outcome data, however, the potential application of DCE-MRI as a predictor of radiation response has been shown [26]. Next to FMISO-PET and Cu-ATSM-PET, blood oxygen level dependent (BOLD) MRI is a promising technique for the assessment of tumor hypoxia [27].

For prostate tumors, the (choline + creatine)/citrate ratio can be determined using MRSI to mark active disease with a high degree of specificity [28]. For brain gliomas, the use of the choline to N-aceltylaspartate index (CNI) determined by MRSI has been suggested to be more reliable in defining the location and volume of microscopic and actively growing disease compared to conventional MRI [29,30]. Although the clinical application of MRSI for RT is most developed for gliomas and prostate cancer, it will probably be useful in many other areas of the body too [31].

10.4.2 Requirement for precise treatment delivery

BCRT does not only increase the degree of complexity of treatment planning, but also the level of difficulty of safe and effective treatment delivery. While planning is performed based on pre-treatment imaging data, the location of the target volume and critical organs is generally different at the time of delivery, both due to patient set-up variations and organ motion, caused by breathing for example. The highly structured BCRT dose distributions (see, for example, Fig. 5 on page 69) require highly precise treatment delivery techniques. Image-guided RT (IGRT) allows imaging of the patient geometry both before and during irradiation and the correction of set-up errors. A variety of in-room medical imaging techniques were developed to facilitate IGRT.

Electronic portal imaging devices (EPIDs) were developed early in the 1980s to enable the verification of treatment field positions relative to the patient’s anatomy. At present, they are an option on all commercial linear accelerators. Amorphous silicon flat panel devices have been reported to yield an image quality superior to that of films [32], with the added convenience of digital recording and image processing.

Cone-beam CT (CBCT) uses a 2D detector, for example an EPID, to reconstruct CT images from a single rotation of a point source on the linac [33]. MV CBCT uses the therapeutic beam as a source, whereas kV CBCT uses an X-ray tube mounted on the linac. While it was believed initially that the soft-tissue visualization of CBCT could be sufficient for online

IGRT, even strong promoters of this technique have now started to use implanted fiducials for prostate RT (Ben Heijmen, personal communication, 11 November 2007). At GUH, the Elekta Synergy linac is equipped with a kV CBCT device. Figure 4.4 shows an example of matched planning CT and kV CBCT images for a clinical prostate case. In The Netherlands, the potential of MRI for IGRT by integration of a 1.5 Tesla MRI scanner with a 6 MV linac is being investigated [34].

Finally, optical tracking systems may be used to measure the position of external infrared markers fixed to the patient's surface relative to a fixed coordinate system in the treatment room. While sub-millimeter spatial resolution, facilitating verification and on-line correction of the patient set-up within the treatment room, has been claimed to be achievable in real time [35], it cannot be obtained in practice in some cases, e.g. to accurately quantify internal prostate motion. The relationship between the positions of the external markers and internal structures of interest is established from the planning CT. Combinations with other imaging devices like ultrasound are also possible, to determine the exact location of internal structures relative to the treatment room coordinates [36].

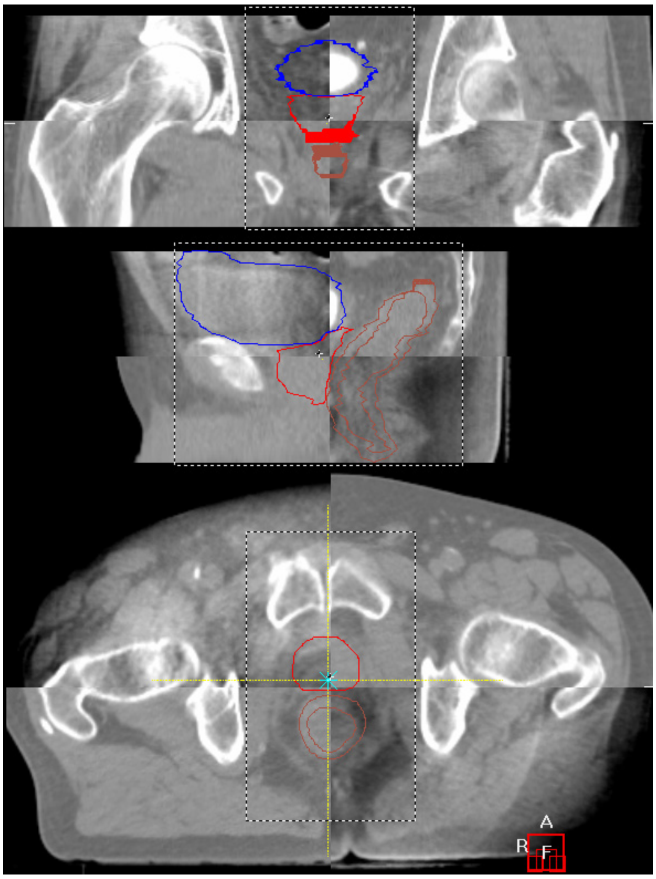

Figure 4.4. Match of planning CT and CBCT images for a clinical prostate case. Top: coronal view, centre: sagittal view, bottom: transverse view. Red line: PTV, blue line: bladder, inner brown line: rectum, outer brown line: expanded rectum, dashed line: user-defined region of interest for matching purposes.

In case of non-gated biological imaging investigations, the use of BCRT could come as a relative advantage with regard to organ motion [37]. CT scanning can be performed fast, i.e. during a single breath-hold of the patient. RT delivery, however, takes several minutes. Breathing motion can thus cause severe problems in the delivery of conventional IMRT for lung cancer [38,39]. To solve this, 4D CT scanning may be performed at several instances of the breathing cycle to determine the exact extent of the breathing motion [40] and the PTV and OAR margins for treatment planning may be increased [41]. Several 4D techniques are available to take breathing motion into account during RT delivery, including respiratory control [42], gating and tracking [43]. Using respiratory control, irradiation is only performed during assisted or voluntary respiratory pauses at selected phases of the respiratory cycle. Gating involves switching the treatment beam on when the amplitude of the breathing motion coincides with a pre-selected sector of the breathing cycle. Using intra-fraction tumor tracking, the treatment beam is intentionally moved to follow the movement of the tumor.

Most biological imaging examinations last much longer than CT scanning. PET imaging, for example, may take 30 to 45 minutes. As a consequence, the image is smeared out across the breathing cycle. By using the resulting average image signal within each patient voxel to guide the dose prescription, BCRT may therefore cope better with reproducible patient motion than conventional IMRT. Ultimately, however, gating and intra-fraction tumor tracking remain the best way to deal with breathing motion for lung cancer treatment.

10.4.3 Inter-fraction tumor tracking

Apart from variations in positioning and organ motion, patient anatomy and biological tumor characteristics themselves may also change. Indeed, fractionated RT typically spans about 6 weeks; during this time many anatomical changes may occur. First of all, the tumor will hopefully shrink. Both inflammation and oedema can resolve. Moreover, weight loss, which is a common consequence of acute treatment toxicity, can lead to muscle wasting and shifting of both normal tissue and tumor positions. A detailed study performed by Barker *et al.* showed significant changes in the position (GTV: up to 17.3 mm) and volume (GTV: medianly -1.8% daily or -70% in total; parotid glands: -28%) of both the GTV and OARs during RT for head and neck cancer [44]. When it comes to biological changes during therapy, the situation is even more complex as variations in tumor metabolism, oxygenation and vascularization may occur [45]. Usually, these changes do not occur in a predictable way.

The use of repeated imaging during RT to adjust the treatment to the observed changes in tumor location and extent, is called inter-fraction tumor tracking - a particular case of adaptive RT (ART). Ultimately, IGRT technology may be used to provide per-treatment images and perform re-planning for immediate delivery while the patient is in the treatment room. Time and effort could be saved by using algorithms capable of deforming treatment plans according to anatomical deformations, instead of re-planning entirely from the start [46,47].

Phase I study on adaptive FDG-PET guided BCRT in head and neck cancer

Several investigations have demonstrated changes in tumor glucose utilization during the first weeks of chemotherapy, suggesting that effective therapy decreases FDG uptake in the tumor [48-50]. Several studies have indicated the usefulness of pre-treatment FDG-PET images for predicting the response to RT treatment of head and neck cancer [51-57]. By performing FDG-PET investigations before pre-operative (chemo-) radiotherapy and after a dose of 36 Gy, local tumor control and survival could be predicted for patients with oral squamous cell carcinoma [58]. These data support the use of consecutive pre- and per-treatment FDG-PET imaging to adapt BCRT treatment plans during a fractionated course of RT for head and neck cancer.

As re-planning more than once or twice during treatment is not practical at present, only small day-to-day variations need to be assumed. Especially for the biological images, there exists no profound evidence to support this hypothesis. In a future study, the magnitude of these day-to-day changes should preferably be investigated in detail. The results are expected to depend not only on the investigated biological imaging modality and tracer, but also on the tumor type and site and even on the individual patient. The best timing for the per-treatment FDG-PET investigation is not obvious, as radiation-induced inflammation causes increased FDG uptake. By hypothesizing that FDG-PET imaging at the end of the second week of RT may detect non-responding, radioresistant intra-tumor regions that require a higher radiation dose, a phase I study on adaptive FDG-PET guided BCRT in head and neck cancer was set up at GUH.

The main objective of the study is to establish the maximum tolerated dose MTD) for dose escalation. The MTD is defined as the maximal escalation dose causing dose-limiting toxicity (DLT). DLT is defined as any grade 4 toxicity observed in the treated patient group during RT or within 3 months after the end of treatment. Secondary objectives of the study are to report on acute, subacute and late toxicity, recurrence and site of recurrence, and tumor control rates. Acute, subacute and late toxicity are scored during treatment, 3 months after treatment and 6 months (and later) after treatment, respectively. To assess (sub)acute toxicity, the common toxicity criteria (CTC) version 2.0 are used [59]. The study is prospective, non-controlled and non-randomized. In total, 12 patients are planned to be included. Table 4.1 summarizes patient inclusion criteria.

Table 4.1: Patient inclusion criteria of the Phase I clinical trial on adaptive FDG-PET guided BCRT in head and neck cancer.

Inclusion criteria
- Histologically confirmed squamous cell carcinoma of oral cavity, oro- and hypopharynx and larynx
- Primary unresectable tumor and/or patients refusing surgery
- Stage T2-4 N0 M0 or T_{any} N+ M0 for laryngeal cancer
- Decision of radio(chemo)therapy by Multidisciplinary Group of Head and Neck Tumors at GUH
- Karnofsky performance status ≥70%
- No prior irradiation to the head and neck region
- No other malignancies

The total treatment consists of 32 fractions (6 weeks and 2 days). In the standard IMRT treatment for these patients at GUH, a total dose of 69.12 Gy (2.16 Gy per fraction) is prescribed homogeneously to the PTV derived from the macroscopic tumor including a margin for microscopic disease. For the study, two levels of dose escalation (I and II) are defined, and 6 patients are included at each dose level. FDG-PET/CT scanning is performed before the start of RT (PET/CT 1) and on Thursday of the second week of treatment (PET/CT 2). The total treatment is divided into 3 separate phases (dose level I):

- Phase 1 (25 Gy, 10 fx): FDG-PET guided BCRT based on PET/CT 1
- Phase 2 (30 Gy, 10 fx): FDG-PET guided BCRT based on PET/CT 2
- Phase 3 (25.92 Gy, 12 fx): standard IMRT based on PET/CT 2

BCRT treatment planning during phases 1 and 2 is performed using values of I_{low} and I_{high} equal to 25% and 100% of the 95th percentile PET intensity value within the PTV. D_{low} and D_{high} are equal to 2.16 and 2.5 Gy per fraction (phase 1) and 2.5 and 3.5 Gy per fraction (phase 2).

At dose level II, the escalation dose of phase 1 is 30 Gy instead of 25 Gy (D_{low} and D_{high} equal to 2.5 and 3.5 Gy per fraction); the other dose levels remain unchanged. Due to the large size of the treatment fields, treatment phases 1 and 2 are both delivered on 2 treatment machines at GUH: the Elekta SL18 and Elekta Synergy linear accelerators. Five separate treatment plans are thus created for each patient. The treatment delivery at dose level I is summarized in table 4.2. The application of CBCT and a high-resolution MLC on the Elekta Synergy linac ensure a highly accurate delivery of BCRT.

Table 4.2: Treatment delivery for dose level I of the Phase I clinical trial on adaptive FDG-PET guided BCRT in head and neck cancer.

	SL 18	Synergy
Phase 1: FDG-PET guided BCRT 25 Gy (10 x 2.5 Gy)	21.6 Gy	3.4 Gy
Phase 2: FDG-PET guided BCRT 30 Gy (10 x 3 Gy)	21.6 Gy	8.4 Gy
Phase 3: standard IMRT 25.92 Gy (12 x 2.16 Gy)	-	25.92 Gy
Total dose: 80.92 Gy	43.2 Gy	37.72 Gy

In March 2007, 6 patients enrolled the trial at dose level I. So far, the observed maximal CTC grades of acute dysphagia and mucositis are, respectively, 2 and 3 (1 patient), 3 and 2 (4 patients) and 3 and 3 (1 patient). No events of DLT have occurred yet. Figure 4.1 shows transverse pre- and per-treatment FDG-PET images of a 57-year old female hypopharyngeal cancer patient included in the study. The QVHs and QFs of each treatment plan for this patient are shown in figure 4.2.

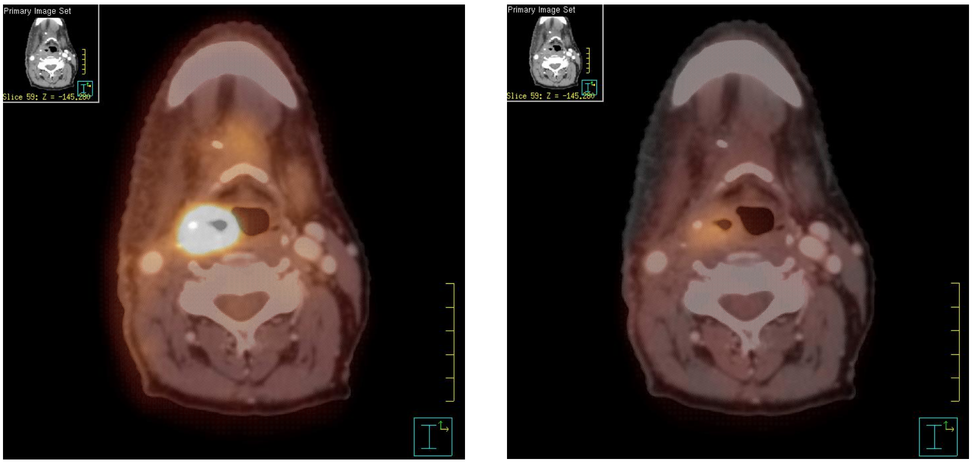

Figure 4.1: Transverse slices of pre- and per-treatment FDG-PET images registered to the pre-treatment CT of a patient included in the Phase I clinical trial on adaptive FDG-PET guided BCRT at GUH.

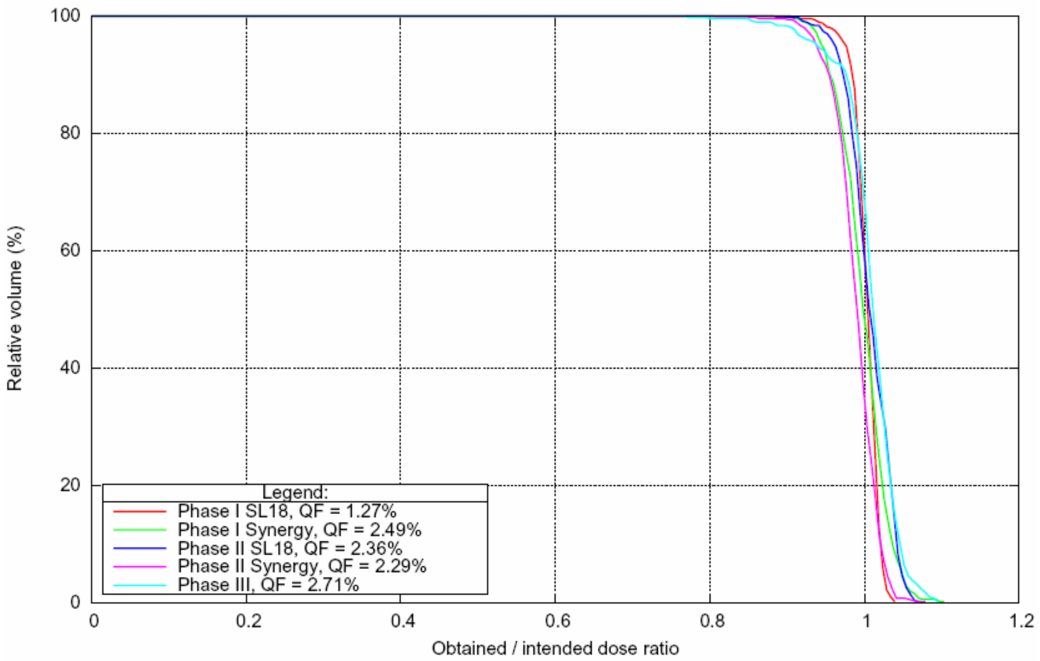

Figure 4.2: QVHs and QFs for each treatment plan of a patient included in the Phase I clinical trial on adaptive FDG-PET guided BCRT at GUH.

10.5 Patient dose calculations

10.5.1 The added value of Monte Carlo

Analytical models have traditionally been used to estimate dose distributions for RT treatment planning. Their accuracy has increased steadily from measurement-based calculations to PB and CS algorithms, together with the available computer power in the clinic. At present, vendors have started to incorporate MC dose engines into their commercial TP software. Several investigators have evaluated the added value of MC compared to analytical dose calculation algorithms.

In a number of phantom studies, MC has been reported to be superior to conventional techniques near low density volumes and air cavities [60-65]. MC was compared to two different CS algorithms by Paelinck *et al.* for a 6 MV photon beam incident on a phantom with a lung insert [62]. While one CS algorithm systematically underestimated the dose within the lung-equivalent cavity by 6%, the other one overestimated the dose behind the cavity by 4%, as shown in figure 4.5.

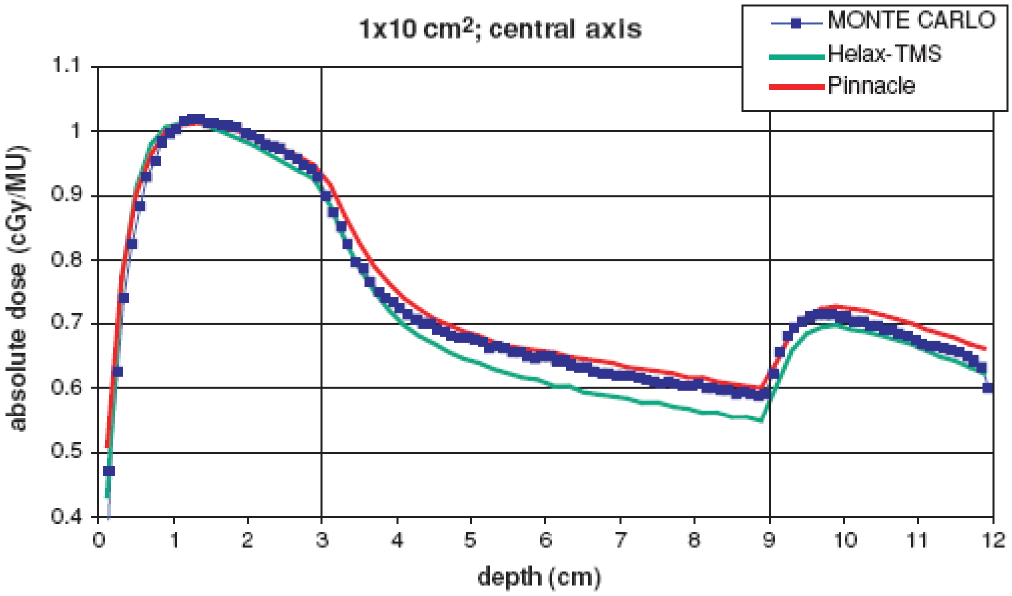

Figure 4.5: Comparison of MC (BEAMnrc/DOSXYZnrc) and 2 CS algorithms (Helax-TMS version 6.1A, Nucletron, Veenendaal, The Netherlands and Pinnacle version 6.2b, Philips Medical Systems, Best, The Netherlands) for a 1x10 cm² 6 MV photon field incident on a polystyrene phantom containing a lung-equivalent cavity [62].

It is not obvious how to extrapolate findings for single beams crossing large air or lung cavities within phantoms towards clinical practice. MC therefore has to be compared to conventional dose calculation algorithms for realistic clinical cases. While it has been shown that MC is clearly superior to broad beam and PB algorithms for patient dose calculations [66-72], only a limited number of studies has been devoted to the comparison of MC and CS in a clinical setting. For mediastinal and breast treatments restricted to large fields, Francescon *et al.* [73] only observed small differences, even for single fields and large inhomogeneities. Reynaert *et al.* compared two MC and 1 CS dose calculation algorithm for a head and neck case [74]. While CS results were in acceptable agreement with MCDE, systematic errors in the DVH of the optic chiasm were encountered for the other MC algorithm, due to an error in the leaf projection. Finally, Seco *et al.* [75] compared PB, CS and MC for a head and neck case. Differences up to 10% were reported for important dose-volume parameters of the critical structures.

There is still a lack of studies investigating whether clinical treatment plans may benefit from replacing CS by MC algorithms for dose calculation. For this purpose, two studies were set up at Ghent University and GUH [76,77]. In the third publication of this thesis, MCDE was compared to two commercial CS algorithms and one PB algorithm for 6 MV and 18 MV IMRT treatment plans of ten lung cancer patients [75]. Of both CS algorithms, one clearly performed better within the PTV, while the other one performed better within the OARs. It was shown that the results from PB were unsatisfactory within both the PTV and OARs. In such a study, the analysis of individual patient results is indispensable. None of the studied dose calculation algorithms were consistent within 5% in all ten patients. The choice of dose calculation algorithm may influence treatment planning, and thus also clinical results. If an algorithm leads to large deviations in one particular patient, it may no longer be considered suitable for clinical use. However, the possible disposal of a dose calculation algorithm depends on several factors, including the institution's internal accuracy requirements, the accuracy of the dose calculation algorithm used as the reference (in this case, MCDE) and the availability of a practicable alternative. Of course, whatever algorithm one uses, it should be optimally commissioned and adequately benchmarked.

In the fourth publication of this thesis, results from the previous study were applied to investigate an important clinical question, namely whether 6 MV or 18 MV photons should be preferred for IMRT treatment of non-small cell lung cancer [78]. Although the observed deviations were quite small, 6 MV photons were generally favoured by MCDE. It was shown that the location of the tumor and the priority ranking of the endpoints may influence the selection of photon beam quality. Whereas 18 MV photons may lead to better dose uniformity within the PTV and improved skin sparing, 6 MV photons may reduce the irradiated volume of normal lung by reducing the extent of lateral electron disequilibrium.

A second study comparing MCDE to two commercial CS algorithms was performed at GUH for IMRT treatment of ten ethmoid sinus cancer patients [77]. The PTV typically contained large natural and surgical air cavities, causing electron disequilibrium at the interface with the tumor tissue. For individual patients, large differences (>10%) were reported between the maximal PTV dose calculated by the different algorithms. In case of MCDE, the air within the PTV produced a lot of noise on the resulting dose distribution. Differences above 5% between the different algorithms were encountered within the OARs.

When comparing MC to conventional dose calculation algorithms in a clinical setting, it is interesting to distinguish between effects related to differences in the beam model and effects related to the particle transport within the patient [79]. This may help to reveal the cause of the observed differences. Beam model accuracy can be evaluated by comparing calculations within a homogeneous phantom. Chetty *et al.* compared MC with two versions of a broad beam algorithm, one with an approximate beam model and one with an accurate beam model [79]. For 6 MV photons incident on a homogeneous phantom, the agreement between

MC and the accurate beam model algorithm was very good. For 15 MV photons incident on a heterogeneous lung phantom, however, the mean lung dose differed 30%. The authors concluded that the importance of accurate particle transport becomes much greater in case of inhomogeneities, especially at high energies. In the third publication of this thesis, the influence of particle transport within the patient was eliminated by recomputing the dose after setting all CT voxels within the skin contour to water for one patient case [75]. The remaining dose differences between the algorithms were all clinically acceptable, and either due to slight discrepancies in the commissioning process or to differences in the beam model.

The ultimate way of evaluating the added value of MC, is to link clinical outcome to the (retrospectively) observed dose differences between MC and the conventional dose calculation algorithm used for treatment planning. Possible recurrences may be linked to PTV underdosage (as reported by MC), while possible side effects and normal tissue complications may be linked to OAR overdosage. However, no such data are currently available for MC yet.

10.5.2 Advancements in MCDE

The calculation of patient dose distributions with MC is associated with specific issues such as linear accelerator modelling, scoring grids, variance reduction techniques and CT conversion. For MCDE [80], several of these topics had been addressed before the start of the research presented in this thesis. The treatment head of the Elekta SL*i*plus linear accelerator at GUH had been modelled in detail to commission 6 and 18 MV photon beams [81,82]. By introducing a separate scoring grid and two different stepping algorithms, dose scoring was accelerated substantially [83]. The optimal scoring grid resolution was also investigated for clinical head and neck, and lung cancer cases [82]. Variance reduction techniques have deliberately been kept out of MCDE, to preserve maximal accuracy at the cost of calculation speed. This thesis has addressed some unresolved issues related to the use of MCDE for patient dose calculations.

An accurate CT conversion scheme was developed in the fifth publication of this thesis, in which great importance was attached to the dosimetric relevance of introducing additional tissue composition subsets [84]. A collaboration between 7 different European centres was set up to investigate several associated issues, such as CT calibration and conversion of dose to medium to dose to water. As a result, a CT conversion scheme incorporating 14 bins (air, lung, fat, muscle and 10 bone bins) was proposed. The mass density can be calibrated continuously against the CT number. Especially for skeletal tissue, it is important to define a sufficiently large number of subsets with different chemical compositions, due to the effects resulting from the conversion from dose to medium to dose to water. Each CT scanner should be calibrated individually and a stoichiometric calibration method should be used [85].

Due to the nature of the method, dose calculation using MC is very time-consuming. The time needed to calculate patient dose distributions in the clinic should be as short as possible but long enough to ensure sufficiently accurate results. For this purpose, uncertainty-based stopping criteria were implemented into MCDE in the sixth publication of this thesis [86]. For each structure of interest, upper limits were imposed on the relative or absolute uncertainty on the dose within each voxel. Two clinical IMRT cases and one clinical IMAT case were investigated. The tolerated relative uncertainty was equal to 2% [87,88]. The tolerated absolute uncertainty should be determined taking into account the absolute dose prescription for the PTV and the planning constraints for the OARs. The proposed stopping criteria provide a practical and flexible tool for automatic determination of the appropriate number of histories when simulating patient dose distributions using MCDE.

10.6 Monte Carlo treatment planning

10.6.1 Monte Carlo-based IMRT optimization

The use of inaccurate dose calculation for inverse IMRT treatment planning introduces two errors, a systematic error and a convergence error [89]. The systematic error is due to the inaccuracy of the dose calculation algorithm itself, while the convergence error appears because the beam settings resulting from optimization are different from the optimal settings obtained with a highly accurate dose calculation algorithm. Jeraj *et al.* compared PB, CS and MC algorithms for three clinical cases (lung, prostate and head and neck). The systematic error was about 1% of the maximal dose within the PTV and slightly larger outside for CS, and about 5% for PB. The convergence error was found to be very sensitive to the objective function and only slightly correlated to the systematic error. The authors concluded that the accuracy of PB is insufficient for IMRT optimization and CS or preferably MC should be used instead.

The presence of statistical uncertainties (noise) on the calculated MC dose distributions can disturb the MC-based IMRT optimization process, especially if dose inhomogeneity within the PTV is penalized [90]. Moreover, the MC dose engine cannot just replace the conventional dose calculation algorithm, because the total number of time-consuming MC calculations that can be performed is limited from a practical viewpoint. To introduce MC calculations in the optimization of IMRT, MC can be used in combination with a conventional dose calculation algorithm [68,91,92] or independently by specifically adapting the optimization software to the MC dose engine [93-95]. In both cases, a conventional dose calculation algorithm can still be used to obtain an initial treatment plan.

Because as few approximations as possible are applied in MCDE, it is a highly accurate but rather slow MC dose engine. It was mainly developed as a benchmarking tool and was not specifically designed for routine use in the clinic. However, in the seventh publication of this thesis MCDE was used to investigate the feasibility of incorporating MC calculations into the IMRT optimization process at GUH [91]. As proof of principle, an ethmoid sinus patient case was considered. By computing individual MC dose distributions for each beam in between optimization cycles, the best final plan could be obtained. However, not all MC dose engines allow the generation of such individual dose distributions. By computing the full MC dose distribution in between optimization cycles, the initial treatment plan could still be improved. Moreover, the optimization process was severely disturbed by statistical noise generated by the air cavities within the PTV.

10.6.2 Commercial MCTP systems

It is obvious that RT patients may benefit from the improvements in dose calculation accuracy using full MC. In the third publication of this thesis, highly accurate dose calculations with MCDE resulted in clinically meaningful dose differences compared to commercial CS algorithms [76]. However, in many clinics the available computer power may still not allow full MC calculations. Nevertheless, vendors of RT TPSs have recently started to offer MC systems. To reduce the calculation time, many approximations and simplifications are often included, which may cause substantial dose inaccuracies. The importance of accurate linear accelerator modelling has been illustrated before [74]. Moreover, the simplification of photon or electron transport, or other techniques like denoising of dose distributions, may lead to loss of accuracy. Geometrical and scoring voxel size should also be evaluated critically [96]. In any case, like any other TPS commercial MC systems need to be benchmarked carefully before bringing them into clinical use. This can be done either by means of measurements or by comparison with accurate MC dose engines containing only a few approximations, like MCDE.

The introduction of BEAM/DOSXYZ was an important step towards the practical implementation of MCTP. Although this package already enabled actual MCTP calculations, the high calculation times presented a major drawback. Therefore, Kawrakow *et al.* [97] developed the Voxel Monte Carlo (VMC) code as a fast MC dose engine for electron beams based on a set of sophisticated variance reduction techniques. For photon beams, Peregrine [98] was introduced as a MC dose engine using multiple variance reduction techniques. Later, VMC was also extended for photon beams, resulting in the fast X-ray Voxel Monte Carlo (XVMC) [99]. Together, Kawrakow and Fippel optimized XVMC [100], and each of them developed his own C++ version of the original Fortran code, called VMC++ and XVMC, respectively [101,102]. XVMC/VMC++ and Peregrine are the only MC dose engines implemented into commercial TPSs for photon RT. For electrons, the MC dose engines Dose Planning Method (DPM) [103], Macro Monte Carlo (MMC) [104] and PENetration and Energy Loss of Positrons and Electrons (PENELOPE) [105,106] were also implemented commercially. Table 4.3 summarizes the (future) availability of MC dose calculation engines in commercial TPSs, resulting from a survey carried out by the subcommittee on MTCP of the Netherlands Commission on Radiation Dosimetry [102].

Table 4.3: Overview of MC dose engines implemented into commercial TPSs [102].

Company	Treatment planning system	Photon MC code	Electron MC code
BrainLab	iPlan RT Dose 4.0	XVMC	XVMC
CMS	XiO 4.3.0	XVMC	XVMC
	Monaco 4.3.0	XVMC	-
Elekta	Elekta-Plan 1.1	XVMC	-
	Elekta-Plan 1.2	XVMC	XVMC
	Elekta-Plan 2.0	XVMC	XVMC
Nucletron	DCM (now OTP) 2.0	-	VMC
	OTP 1.4	VMC++	VMC++
	PLATO	-	-
	TMS	-	-
Philips	Pinnacle3 v6.9c	-	DPM (modified)
Varian	Cadplan	-	-
	Eclipse 7.2.X	-	MMC
Siemens	KonRad v2.1	-	-
Dosisoft	Isogray	-	PENELOPE
North American Scientific	Corvus, Peacock v5	Peregrine	-

10.7 Current issues in MCTP

10.7.1 Particle therapy

Photons rapidly lose energy by ionization as they travel through tissue, whereas charged particles deposit most of their energy at a specific depth. The location of this so-called Bragg peak can be precisely calculated as a function of the particle's initial energy. Compared to conventional external photon beam RT, particle therapy may therefore deliver high doses directly to the target volume. By combining particles with different energies into a single beam, the Bragg peak can be spread-out into a plateau. A high dose of radiation may thus be deposited throughout the depth of the tumor, while the tissue in front of the tumor is exposed to far less radiation and the tissue behind the tumor remains virtually damage-free. Figure 4.6 illustrates the dose distributions resulting from proton and photon intensity-modulated therapy for a paranasal sinus cancer patient. Particle therapy is particularly appropriate in situations where photon RT includes high risks for the patients. Deep-seated tumors, tumors in the vicinity of OARs, radiation resistant tumors and paediatric tumors are particularly in favour of particle therapy.

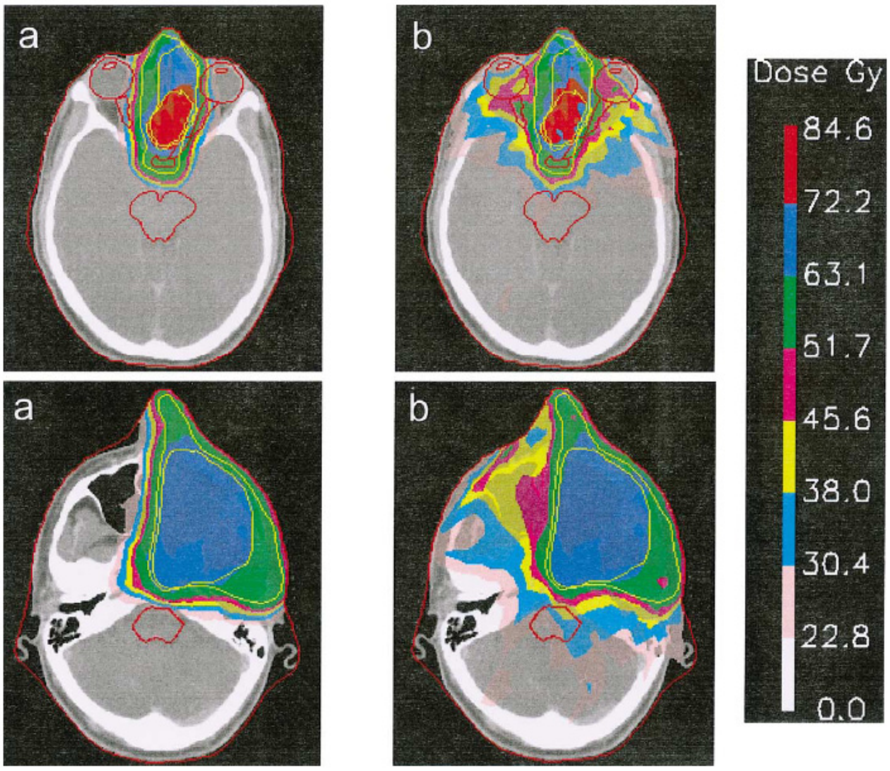

Figure 4.6: Dose distributions of proton (a) and photon (b) intensity-modulated therapy for a paranasal sinus cancer patient at the level of the globes (top) and petrous ridge (bottom) [107]. Dose levels of 76, 66 and 54 Gy were prescribed to three target volumes. The globes, the optic nerves and the brainstem were considered as critical structures.

As particle therapy delivers conformal dose distributions with very high precision, and steep dose gradients can be located near critical structures, accurate dose calculation is important. PB algorithms are usually applied for proton therapy calculations [108-110]. However, the 1D density scaling of proton pencil beams in water limits the accuracy of the PB calculations [111]. Although more sophisticated scaling methods have been introduced [111,112], the results still differ from MC dose distributions, because PB algorithms can only approximately deal with multiple elastic Coulomb scattering in heterogeneous media, and elastic and inelastic nuclear reactions [113].

The general purpose MC codes GEANT4 [114], FLUKA [115,116] and MCNP [117] can be used for proton therapy treatment planning. However, the requirement of a large material database for the cross sections slows down simulations in patient geometries. For this reason, Fippel and Soukup developed VMCpro [113], a fast MC code for proton therapy dose calculations based on VMC for electrons and photons [97,99].

Protons lose their energy by ionization, multiple Coulomb scattering and nuclear reactions. Hence, accurate conversion of CT data into mass density and elemental composition information is even more important for proton MC dose calculations than for photons. Jiang *et al.* [118] have studied the effect of three different CT conversion methods on proton MC simulations. Two clinical proton plans were selected for their tissue variety, namely a lung and a paranasal sinus cancer case. Small but significant differences were observed.

Intensity-modulated proton therapy (IMPT) [119] can be achieved by modulating the intensity and energy of narrow beam spots that are delivered to the patient in a scanned pattern [120,121]. Optimization of IMPT is currently based on analytical dose calculation algorithms with limited accuracy, resulting in suboptimal dose distributions. Soukup and Alber recently implemented VMCpro into IMPT treatment planning [122]. Treatment plans for 6 clinical cases obtained using a PB algorithm were recalculated using MC to determine the size of the convergence error. For prostate cases, values up to 1% were reported for the target, which was caused mainly by the nuclear interactions. Although the use of MC highly increased calculation times, it was shown that MC-based optimization of IMPT could significantly improve the optimal dose distribution for specific patient cases.

Physical dose optimization for IMPT generally assumes a constant relative biological effectiveness (RBE), whereas in reality the biological effect caused by proton beams does not depend on the physical dose alone, but also on the local energy spectrum [123]. By including RBE variations in the inverse planning process, Wilkens and Oelfke illustrated the importance of biological optimization for IMPT [124].

10.7.2 4D Monte Carlo

Motion issues are a challenge in RT dose calculations. Time dependence in RT may arise from the linear accelerator or from the patient. Unlike conventional dose calculation algorithms, MC can take into account motion just through sampling. This will not greatly increase calculation time, because it is the total number of simulated histories that will determine the uncertainty on the final dose distribution. Indeed, a major advantage of MC over conventional dose engines is that the uncertainties are independent of the treatment set-up.

The linear accelerator may be the source of time dependence when a dynamic MLC is used [125], or in case of IMAT treatment [126]. To take into account dynamic MLC movement, MC simulations can randomize the leaf positions from their known time-dependent distributions [127-129]. IMAT was implemented into MCDE by Olteanu *et al.* [130], and a comparison between MCDE and CS for clinical prostate and rectum cases is ongoing.

Patient-related motion may arise from set-up errors, inter-fraction organ motion and intra-fraction organ movement [131]. The main source of intra-fraction organ movement is breathing motion. Several investigators have integrated breathing motion into MC dose calculations. Ding *et al.* [131] used CT scans at total inhalation and total exhalation to interpolate scans at intermediate breathing phases. By performing a weighted sum of the corresponding dose maps, the actual dose distribution delivered to the patient was determined. However, the treatment itself stayed unaffected. Keall *et al.* [132], on the other hand, used the same beam directions for each CT dataset but each time confined the MLC settings to the PTV of the dataset (tumor tracking). The resulting dose maps were then combined into a so-called 4D treatment plan. A 4D MC calculation does not take more time than a 3D calculation, as it is the summed dose map that needs to be sufficiently accurate. Each individual dose map thus requires only a limited number of histories, whereas for a conventional dose calculation algorithm, the calculation time would be proportional to the number of breathing phases. A different approach to take into account the interplay effects between linear accelerator motion and patient motion, was introduced by Paganetti *et al.* [133]. They included motion into the MC calculation geometry by deformation of the patient voxels according to the 4D CT data. Heath and Seuntjens [134] developed a so-called voxel tracking algorithm to take into account internal and external contour changes by deforming the voxels.

With the introduction of IGRT in the clinic, set-up errors and anatomy changes in the course of treatment can be imaged on a daily basis. Intra-fraction organ motion can even be imaged in real time. Moreover, the treatment plans can be adapted based on the observed changes (ART). 4D MC calculations could be used to determine the actual total dose distribution received by the patient based on the acquired image sets and delivered treatment plans.

10.7.3 MCDE for treatment plan verification

Just like conventional TPSs, commercial MCTP systems should be benchmarked to detect possible errors arising from systematic errors in the code, problems with the beam model, CT conversion and the use of variance reduction techniques and de-noising methods. To commission MC dose engines, calculation results can be compared with measurements in a phantom or with calculations from an independent, accurate MC dose engine [74,99,135-138].

In the future, the Lab for Standard Dosimetry (LSD) in Ghent is likely to add treatment plan verification using MCDE to its service package. Hospitals could use this service to benchmark their commercial (conventional or MC-based) TPS for clinical cases.

10.8 References

1. K Tanderup, DR Olsen and C Grau. Dose painting: art or science? *Radiother Oncol* 2006;79:245-8.

2. AL Grosu, M Piert, WA Weber, B Jeremic, M Picchio, U Schratzenstaller, FB Zimmerman, M Schwaiger and M Molls. Positron emission tomography for radiation treatment planning. *Strahlenther Onkol* 2005;8:483-99.

3. W De Neve. IMRT and focused radiotherapy. *Radiother Oncol* 2007;82:S12 (Abstract).

4. JM Galvin and W De Neve. Intensity modulating and other radiation therapy devices for dose painting. *J Clin Oncol* 2007;25:924-30.

5. L Xing, Y Yang and DM Spielman. Molecular/functional image-guided intensity-modulated radiation therapy. In: T Bortfeld, R Schmidt-Ullrich, W De Neve and DE Wazer, editors. Image-guided IMRT. Berlin: Springer. 2006;187-98.

6. A Brahme. Individualizing cancer treatment: biological optimization models in treatment planning and delivery. *Int J Radiat Oncol Biol Phys* 2001;49:327-37.

7. JA Penagaricano, N Papanikolaou, CA Wu and YL Yan. Assessment of biologically-based optimization (BORT) in the IMRT era. *Med Dosim* 2005;30:12-9.

8. Y Kim and WA Tome. Risk-adaptive optimization: Selective boosting of high-risk tumor subvolumes. *Int J radiat Oncol Biol Phys* 2006;66:1528-42.

9. L Xing, C Cotrutz, S Hunjan, AL Boyer, E Adalsteinsson and D Spielman. Inverse planning for functional image-guided intensity-modulated radiation therapy. *Phys Med Biol* 2002;47:3567-78.

10. M Alber, F Paulsen, SM Eschmann and HJ Machulla. On biologically conformal boost dose optimization. *Phys Med Biol* 2003;48:N31-5.

11. SK Das, MM Miften, S Zhou, M Bell, MT Munley, CS Whiddon, O Craciunescu, AH Baydush, T Wong, JG Rosenman, MW Dewhirst and LB Marks. Feasibility of optimizing the dose distribution in lung tumors using fluorine-18-fluorodeoxyglucose positron emission tomography and single photon emission computed tomography guided dose prescription. *Med Phys* 2004;31:1452-61.

12. S Bowen, R Flynn, S Bentzen and R Jeraj. Effect of a biologically-based prescription function in IMRT dose optimization. *Med Phys* 2007;34:2524 (Abstract).

13. B Vanderstraeten, W De Gersem, W Duthoy, W De Neve and H Thierens. Implementation of biologically conformal radiation therapy (BCRT) in an algorithmic segmentation-based inverse planning approach. *Phys Med Biol* 2006;51:N277-86.

14. B Vanderstraeten, W Duthoy, W De Gersem, W De Neve and H Thierens. [^{18}F]fluoro-deoxy-glucose positron emission tomography ([^{18}F]FDG-PET) voxel intensity-based intensity-modulated radiation therapy (IMRT) for head and neck cancer. *Radiother Oncol* 2006;79:249-58.

15. I Madani, W Duthoy, C Derie, W De Gersem, T Boterberg, M Saerens, F Jacobs, V Grégoire, M Lonneux, L Vakaet, B Vanderstraeten, W Bauters, K Bonte, H Thierens and W De Neve. Positron emission tomography-guided, focal-dose escalation using intensity-modulated radiotherapy for head and neck cancer. *Int J Radiat Oncol Biol Phys* 2007;58:126-35.

16. Y Yang and L Xing. Towards biologically conformal radiation therapy (BCRT): selective IMRT dose escalation under the guidance of spatial biology distribution. *Med Phys* 2005;32:1473-84.

17. W De Gersem, F Claus, C De Wagter and W De Neve. An anatomy-based beam segmentation tool for intensity-modulated radiation therapy and its application to head-and-neck cancer. *Int J Radiat Oncol Biol Phys* 2001;51:849-59.

18. W De Gersem, F Claus, C De Wagter, B Van Duyse and W De Neve. Leaf position optimization for step-and-shoot IMRT. *Int J Radiat Oncol Biol Phys* 2001;51:1371-88.

19. D Thorwarth, SM Eschmann, F Paulsen and M Alber. Hypoxia dose painting by numbers: a planning study. *Int J Radiat Oncol Biol Phys* 2007;68:291-300.

20. D Thorwarth, SM Eschmann, J Scheiderbauer, F Paulsen and M Alber. Kinetic analysis of dynamic ^{18}F-fluoromisonidazole PET correlates with radiation treatment outcome in head-and-neck cancer. *BMC Cancer* 2005;5:152.

21. C Schütze, R Bergmann, A Yaromina, F Hessel, J Kotzerke, J Steinbach, M Baumann and B Beuthien-Baumann. Effect of increase of radiation dose on local control relates to pre-treatment FDG uptake in FaDu tumours in nude mice. *Radiother Oncol* 2007;83:311-5.

22. S Roels, P Slagmolen, V Vandecaveye, S Stroobants, S Dymarkowski, F Penninckx and K Haustermans. Bio-image guided optimisation of radiotherapy in rectal cancer. *Radiother Oncol* 2006;81:S86-7 (Abstract).

23. SM Bentzen. Theragnostic imaging for radiation oncology: dose-painting by numbers. *Lancet Oncol* 2005;6:112-7.

24. S Apisarnthanarax and KS Clifford Chao. Current imaging paradigms in radiation oncology. *Radiat Res* 2005;163:1-25.

25. JA Christian, M Partridge, E Nioutsikou, G Cook, HA McNair, B Cronin, F Courbon, JL Bedford and M Brada. The incorporation of SPECT functional lung imaging into inverse radiotherapy planning for non-small cell lung cancer. *Radiother Oncol* 2005;77:271-7.

26. MA Zahra, KG Hollingsworth, E Sala, DJ Lomas and LT Tan. Dynamic contrast-enhanced MRI as a predictor of tumour response to radiotherapy. *Lancet Oncol* 2007;8:63-74.

27. AR Padhani, KA Krohn, JS Lewis and M Alber. Imaging oxygenation of human tumours. *Eur radiol* 2007;17:861-72.

28. J Kurhanewicz, DB Vigneron, H Hricak, P Narayan, P Carroll and SJ Nelson. Three-dimensional H-1 MR spectroscopic imaging of the in situ human prostate with high (0.24 - 0.7) spatial resolution. *Radiology* 1996;198:795-805.

29. A Pirzkall, TR McKnight, EE Graves, MP Carol, PK Sneed, WW Wara, SJ Nelson, LJ Verhey and DA Larson. MR-spectorscopy guided target delineation for high-grade gliomas. *Int J Radiat Oncol Biol Phys* 2001;50:915-28.

30. A Pirzkall, XJ Li, JM Oh, S Chang, MS Berger, DA Larson, LJ Verhey, WP Dillon and SJ Nelson. 3D MRSI for resected high-grade gliomas before RT: Tumor extent according to metabolic activity in relation to MRI. *Int J Radiat Oncol Biol Phys* 2004;59:126-37.

31. LJ Verhey, C Chuang and A Pirzkall. Magnetic resonance imaging for IMRT. In: T Bortfeld, R Schmidt-Ullrich, W De Neve and DE Wazer, editors. Image-guided IMRT. Berlin: Springer. 2006;177-86.

32. JJ Kruse, MG Herman, CR Hagness, BJ Davis, YI Garces, MG Haddock, KR Olivier, SL Stafford and TM Pisansky. Electronic and film portal images: a comparison of landmark visibility and review accuracy. *Int J Radiat Oncol Biol Phys* 2002;54:584-91.

33. DA Jaffray. Emergent technologies for 3-dimensional image-guided radiation delivery. *Semin Radiat Oncol* 2005;15:208-16.

34. J Lagendijk and W Raaymakers. The potential of MRI for IGRT. *Radiother Oncol* 2006;81:S6 (Abstract).

35. SL Meeks, WA Tome, TR Willoughby, PA Kupelian, TH Wagner, JM Buatti and FJ Bova. Optically guided patient positioning techniques. *Semin Radiat Oncol* 2005;15:192-201.

36. WA Tome, SL Meeks, NP Orton, LG Bouchet and FJ Bova. Commissioning and quality assurance of an optically guided three-dimensional ultrasound target localization system for radiotherapy. *Med Phys* 2002;29:1781-8.

37. CB Caldwell, K Mah, M Skinner and CE Danjoux. Can PET provide the 3D extent of tumor motion for individualized internal target volumes? A phantom study of the limitations of CT and the promise of PET. *Int J Radiat Oncol Biol Phys* 2003;55:1381-93.

38. T Bortfeld, SB Jiang and E Rietzel. Effects of motion on the total dose distribution. *Semin Radiat Oncol* 2004;14:41-51.

39. J Seco, GC Sharp, J Turcotte, D Gierga, T Bortfeld and H Paganetti. Effects of organ motion on IMRT treatments with segments of few monitor units. *Med Phys* 2007;34:923-34.

40. EC Ford, GS Mageras, E Yorke and CC Ling. Respiration-correlated sprial CT: a method of measuring respiratory-induced anatomic motion for radiation treatment planning. *Med Phys* 2003;30:88-97.

41. M van Herk. Errors and margins in radiotherapy. *Semin Radiat Oncol* 2004;14:52-64.

42. JW Wong, MB Sharpe, DA Jaffray, VR Kini, JM Robertson, JS Stromberg and AA Martinez. The use of active breathing control (ABC) to reduce margin for breathing motion. *Int J Radiat Oncol Biol Phys* 1999;44:911-9.

43. P Giraud, E Yorke, S Jiang, L Simon, K Rosenzweig and G Mageras. Reduction of organ motion effects in IMRT and conformal 3D radiation delivery by using gating and tracking techniques. *Cancer Radiother* 2006;10:269-82.

44. JL Barker, AS Garden, KK Ang, JC O'Daniel, H Wang, LE Court, WH Morrison, DI Rosenthal, KS Chao, SL Tucker, R Mohan and L Dong. Quantification of volumetric and geometric changes occurring during fractionated radiotherapy for head-and-neck cancer using an integrated CT/linear accelerator system. *Int J Radiat Oncol Biol Phys* 2004;59:960-70.

45. R Jeraj, U Simoncic, D Barbee, J Nickles, M Avila-Rodriguez and L Forrest. Cell proliferation and tumor hypoxia during radiation therapy. *Med Phys* 2006;33:2289 (Abstract).

46. R Mohan, X Zhang, H Wang, Y Kang, X Wang, H Liu, KK Ang, D Kuban and L Dong. Use of deformed intensity distributions for on-line modification of image-guided IMRT to account for interfractional anatomic changes. *Int J Radiat Oncol Biol Phys* 2005;61:1258-66.

47. H Wang, L Dong, J O'Daniel, R Mohan, AS Garden, KK Ang, DA Kuban, M Bonnen, JY Chang and R Cheung. Validation of an accelerated 'demons' algorithm for deformable image registration in radiation therapy. *Phys Med Biol* 2005;50:2887-905.

48. RL Wahl, K Zasadny, M Helvie, GD Hutchins, B Weber and R Cody. Metabolic monitoring of breast cancer chemohormonotherapy using positron emission tomography – initial evaluation. *J Clin Oncol* 1993;11:2101-11.

49. T Jansson, JE Westlin, H Ahlstrom, A Lilja, B Langstrom and J Bergh. Positron emission tomography studies in patients with locally advanced and/or metastatic breast cancer – a method for early therapy evaluation? *J Clin Oncol* 1995;13:1470-7.

50. M Findlay, H Young, D Cunningham, A Iveson, B Cronin, T Hickish, B Pratt, J Husband M Flower and R Ott. Noninvasive monitoring of tumor metabolism using fluorodeoxyglucose and positron emission tomography in colorectal cancer liver metastases: correlation with tumor response to fluorouracil. *J Clin Oncol* 1996;14:700-8.

51. AS Allal, DO Slosman, T Kebdani, M Allaoua, W Lehmann and P Dulguerov. Prediction of outcome in head-and-neck cancer patients using the standardized uptake value of 2-[^{18}F]fluoro-2-deoxy-D-glucose. *Int J Radiat Oncol Biol Phys* 2004;59:1295-300.

52. Y Kitagawa, K Sano, S Nishizawa, M Nakamura, T Ogasawara, N Sadato and Y Yonekura. FDG-PET for prediction of tumor aggressiveness and response to intra-arterial chemotherapy and radiotherapy in head and neck cancer. *Eur J Nucl Med Mol Imaging* 2003;30:63-71.

53. S Chaudry, M Natwa, J Lavarino, P Anne, W Keane, C Intenzo and M Machtay. Utility of FDG-PET scans in staging and prediction of outcome inhead and neck cancer. *Int J Radiat Oncol Biol Phys* 2006;66:S446 (Abstract).

54. W Halfpenny, SF Hain, L Biassoni, MN Maisey, JA Sherman and M McGurk. FDG-PET. A possible prognostic factor in head and neck cancer. *Br J Cancer* 2002;86:512-6.

55. H Minn, M Lapela, PJ Klemi, R Grénman, S Leskinen, P Lindholm, J Bergman, E Eronen, M Haaparanta and H Joensuu. Prediction of survival with fluorine-18-fluoro-deoxyglucose and PET in head and neck cancer. *J Nucl Med* 1997;38:1907-11.

56. JL Roh, KH Pae, SH Choi, JS Kim, S Lee, SB Kim, SY Nam and SY Kim. 2-[^{18}F]-Fluoro-2-deoxy-D-glucose positron emission tomography as guidance for primary treatment in patients with advanced-stage resectable squamous cell carcinoma of the larynx and hypopharynx. *EJSO* 2007;33:790-5.

57. DL Schwartz, J Rajendran, B Yueh, MD Coltrera, M LeBlanc, J Eary and K Krohn. FDG-PET prediction of head and neck squamous cell cancer outcomes. *Arch Otolaryngol Head Neck Surg* 2004;130:1361-7.

58. M Kunkel, GJ Forster, TE Reichert, J Kutzner, P Benz, P Bartenstein and W Wagner. Radiation response non-invasively imaged by [^{18}F]FDG-PET predicts local tumor control and survival in advanced oral squamous cell carcinoma. *Oral Oncol* 2003;39:170-7.

59. National Cancer Institute. The revised common toxicity criteria, version 2. CTEP website: http://ctep.info.nih.gov/reporting/ctc.html

60. R Mohan. Why Monte Carlo? In: DD Leavitt and D Starkshall, editors. Proc. 12th Int. Conf. on the Use of Computers in Radiation Therapy. Madison, WI: Medical Physics Publishing. 1997;16-8.

61. CM Ma, E Mok, A Kapur, T Pawlicki, D Findley, S Brain, K Forster and AL Boyer. Clinical implementation of a Monte Carlo treatment planning system. *Med Phys* 1999;26:2133–43.

62. L Paelinck, N Reynaert, H Thierens, W De Neve and C De Wagter. Experimental verification of lung dose with radiochromic film: comparison with Monte Carlo simulations and commercially available treatment planning systems. *Phys Med Biol* 2005;50:2055–69.

63. G Crammer-Sargison, WA Beckman and J Popescu. Modelling an extreme water-lung interface using a single pencil beam algorithm and the Monte Carlo method. *Phys Med Biol* 2004;49:1557-67.

64. MR Arnfield, CH Siantar, JV Siebers, P Garmon, L Cox and R Mohan. The impact of electron transport on the accuracy of computed dose. *Med Phys* 2000;27:1266-74.

65. T Krieger and OA Sauer. Monte Carlo- versus pencil-beam-/collapsed-cone-dose calculation in a heterogeneous multi-layer phantom. *Phys Med Biol* 2005;50:859-68.

66. L Wang, C S Chui and M Lovelock. A patient-specific Monte Carlo dose-calculation method for photon beams. *Med Phys* 1998;25:867–78.

67. L Wang, E Yorke and C S Chui. Monte Carlo evaluation of 6 MV intensity modulated radiotherapy plans for head and neck and lung treatments. *Med Phys* 2002;29:2705–17.

68. W Laub, M Alber, M Birkner and F Nusslin. Monte Carlo dose computation for IMRT optimization. *Phys Med Biol* 2000;45:1741–54.

69. WU Laub, A Bakai and F Nüsslin. Intensity modulated irradiation of a thorax phantom: comparisons between measurements, Monte Carlo calculations and pencil beam calculations. *Phys Med Biol* 2001;46:1695–1706.

70. A Leal, F Sanchez-Doblado, R Arrans, J Rosello, CE Pavon and JI Lagares. Routine IMRT verification by means of an automated Monte Carlo simulation system. *Int J Radiat Oncol Biol Phys* 2003;56:58–68.

71. J Yang, J Li, L Chen, R Price, S McNeeley, L Qin, L Wang, W Xiong and CM Ma. Dosimetric verification of IMRT treatment planning using Monte Carlo simulations for prostate cancer. *Phys Med Biol* 2005;50:869–78.

72. C Boudreau, E Heath, J Seuntjens, O Ballivy and W Parker. IMRT head and neck treatment planning with a commercially available Monte Carlo based planning system. *Phys Med Biol* 2005;50:879–90.

73. P Francescon, C Cavedon, S Reccanello and S Cora. Photon dose calculations of a three-dimensional treatment planning system compared to the Monte Carlo code BEAM. *Med Phys* 2000;27:1579–87.

74. N Reynaert, M Coghe, B De Smedt, L Paelinck, B Vanderstraeten, W De Gersem, B Van Duyse, C De Wagter, W De Neve and H Thierens. The importance of accurate linear accelerator head modelling for IMRT Monte Carlo calculations. *Phys Med Biol* 2005;50:831–46.

75. J Seco, E Adams, M Bidmead, M Partridge and F Verhaegen. IMRT treatments assessed with a Monte Carlo dose calculation engine. *Phys Med Biol* 2005;50: 817–30.

76. B Vanderstraeten, N Reynaert, I Madani, L Paelinck, C De Wagter, W De Gersem, W De Neve and H Thierens. Accuracy of patient dose calculation for lung IMRT: A comparison of Monte Carlo, convolution/superposition, and pencil beam computations. *Med Phys* 2006;33:3149-58.

77. L Paelinck, B De Smedt, N Reynaert, M Coghe, W De Gersem, C De Wagter, B Vanderstraeten, H Thierens and W De Neve. Comparison of dose-volume histograms of IMRT treatment plans for ethmoid sinus cancer computed by advanced treatment planning systems including Monte Carlo. *Radiother Oncol* 2006;81:250-6.

78. I Madani, B Vanderstraeten, S Bral, M Coghe, W De Gersem, C De Wagter, H Thierens and W De Neve. Comparison of 6 MV and 18 MV photons for IMRT treatment of lung cancer. *Radiother Oncol* 2007;82:63-9.

79. IJ Chetty, M Rosu, DL McShan, BA Fraass and RK Ten Haken. The influence of beam model differences in the comparison of dose calculation algorithms for lung cancer treatment planning. *Phys Med Biol* 2005;50:802-15.

80. N Reynaert, B De Smedt, M Coghe, L Paelinck, B Van Duyse, W De Gersem, C De Wagter, W De Neve and H Thierens. MCDE: a new Monte Carlo dose engine for IMRT. *Phys Med Biol* 2004;49:N235-41.

81. J Van de Walle, C Martens, N Reynaert, H Palmans, M Coghe, W De Neve, C De Wagter and H Thierens. Monte Carlo model of the Elekta SL*i*plus accelerator: Validation of a new MLC component module in BEAM for a 6 MV beam. *Phys Med Biol* 2003;48:371-85.

82. B De Smedt, N Reynaert, F Flachet, M Coghe, MG Thompson, L Paelinck, G Pittomvils, C De Wagter, W De Neve and H Thierens. Decoupling initial electron beam parameters for Monte Carlo photon beam modelling by removing beam-modifying filters from the beam path. *Phys Med Biol* 2005;50 :5935-51.

83. B De Smedt, N Reynaert, W De Neve and H Thierens. DOSSCORE: an accelerated DOSXYZnrc code with an efficient stepping algorithm and scoring grid. *Phys Med Biol* 2004;49:4623-35.

84. B Vanderstraeten, PW Chin, M Fix, A Leal, G Mora, N Reynaert, J Seco, M Soukup, E Spezi, W De Neve and H Thierens. Conversion of CT numbers into tissue parameters for Monte Carlo dose calculations: a multi-centre study. *Phys Med Biol* 2007;52:539-62.

85. U Schneider, E Pedroni and A Lomax. The calibration of CT Hounsfield units for radiotherapy treatment planning. *Phys Med Biol* 1996;41:111-24.

86. B Vanderstraeten, AML Olteanu, N Reynaert, A Leal, W De Neve and H Thierens. Evaluation of uncertainty-based stopping criteria for Monte Carlo calculations of intensity-modulated radiotherapy and arc therapy patient dose distributions. *Int J Radiat Oncol Biol Phys* 2007;69:628-37.

87. PJ Keall, JV Siebers, R Jeraj and R Mohan. The effect of dose calculation uncertainty on the evaluation of radiotherapy plans. *Med Phys* 2000;27:478-84.

88. FM Buffa and AE Nahum. Monte Carlo dose calculations and radiobiological modelling: analysis of the effect of the statistical noise of the dose distribution on the probability of tumour control. *Phys Med Biol* 2000;45:3009-23.

89. R Jeraj, PJ Keall and JV Siebers. The effect of dose calculation accuracy on inverse treatment planning. *Phys Med Biol* 2002;47:391-407.

90. R Jeraj and P Keall. The effect of statistical uncertainty on inverse treatment planning based on Monte Carlo dose calculation. *Phys Med Biol* 2000;45:3601-13.

91. B De Smedt, B Vanderstraeten, N Reynaert, W De Gersem, W De Neve and H Thierens. The influence of air cavities within the PTV on Monte Carlo-based IMRT optimization. *Journal of Physics: Conference Series* 2007;73:012003.

92. Hyperion treatment planning system, Universitätsklinikum Tübingen, Tübingen, Germany

93. R Jeraj and P Keall. Monte Carlo-based inverse treatment planning. *Phys Med Biol* 1999;44:1885-96.

94. L Bogner, J Scherer and M Herbst. An inverse Monte Carlo optimisation algorithm for conformal radiotherapy. *Phys Medica* 1999:15:111-19.

95. TT He. Implementation of a Monte Carlo based inverse planning model for clinical IMRT with MCNP code, Ph.D. thesis (Univ. Michigan, USA). *Med Phys* 2003;30:482 (Abstract).

96. JE Cygler, C Lochrin, GM Dalaskov, M Howard, R Zohr, B Esche, L Eapen, L Grimard and JM Caudrelier. Clinical use of a commercial Monte Carlo treatment planning system for electron beams. *Phys Med Biol* 2005;50:1029-34.

97. I Kawrakow, M Fippel and K Friedrich. 3D electron dose calculations using a voxel based Monte Carlo algorithm (VMC). *Med Phys* 1996;23:445–57.

98. CL Hartmann-Siantar, PM Bergstrom Jr., WP Chandler, L Chase, LJ Cox, TP Daly, D Garrett, SM Hornstein, RK House, EI Moses, RW Patterson, JA Rathkopf and AE Schach von Wittenau. Lawrence Livermore National Laboratory's PEREGRINE project. In: Proceedings of the XIIth Conference on the Use of Computers in Radiotherapy. Madison: Medical Physics Publishing. 1997;19-22.

99. M Fippel. Fast Monte Carlo dose calculations for photon beams based on the VMC electron algorithm. *Med Phys* 1999;26:1466–75.

100. I Kawrakow and M Fippel. Investigation of variance reduction techniques for Monte Carlo photon dose calculations using XVMC. *Phys Med Biol* 2000;45:2163-83.

101. I Kawrakow. Accurate condensed history Monte Carlo simulation of electron transport I. EGSnrc, the new EGS4 version. *Med Phys* 20000;27:485-98.

102. N Reynaert, SC van der Marck, DR Schaart, W Van der Zee, C Van Vliet-Vroegindeweij, M Tomsej, J Jansen, B Heijmen, M Coghe and C De Wagter. Monte Carlo treatment planning for photon and electron beams (Review). *Rad Phys Chem* 2007;76:643-86.

103. J Sempau, SJ Wilderman and AF Bielajew. DPM, a fast, accurate Monte Carlo code optimized for photon and electron radiotherapy treatment planning dose calculations. *Phys Med Biol* 2000;45:2263-91.

104. H Neuenschwander, TR Mackie and PJ Reckwerdt. MMC – a high-performance Monte Carlo code for electron beam treatment planning. *Phys Med Biol* 1995;40:543-74.

105. J Sempau, E Acosta, J Baro, JM Fernandez-Varea and F Salvat. An algorithm for Monte Carlo simulation of coupled electron-photon transport. *Nucl Instrum Meth B* 1997;132:377-90.

106. F Salvat, JM Fernández-Varea and J Sempau. Penelope – a code system for Monte Carlo simulation of electron and photon transport. Workshop Proceedings. Issey-les-Moulineaux, France, 7-10 July 2003.

107. AJ Lomax, M Goitein and J Adams. Intensity modulation in radiotherapy: photons versus protons in the paranasal sinus. *Radiother Oncol* 2003;66:11-8.

108. P Petti. Differential-pencil-beam dose calculations for charged particles. *Med Phys* 1992;19:137-49.

109. L Hong, M Goitien, B Bucciolini, R Comiskey, B Gottschalk, S Rosenthal, C Serago and M Urie. A pencil beam algorithm for proton dose calculations. *Phys Med Biol* 1996;41:1305-30.

110. AK Carlsson, P Andreo and A Brahme. Monte Carlo and analytical calculation of proton pencil beams for computerized treatment plan optimization. *Phys Med Biol* 1997;42:1033-53.

111. B Schaffner, E Pedroni and A Lomax. Dose calculation models for proton treatment planning using a dynamic beam delivery system: an attempt to include density heterogeneity effects in the analytical dose calculation. *Phys Med Biol* 1999;44:27-41.

112. H Szymanowski and U Oelfke. Two-dimensional pencil beam scaling: an improved proton dose algorithm for heterogeneous media. *Phys Med Biol* 2002;47:3313-30.

113. M Fippel and M Soukup. A Monte Carlo dose calculation algorithm for proton therapy. *Med Phys* 2004;31:2263-73.

114. S Agostinelli, J Allison, K Amako *et al*. GEANT4 – a simulation toolkit. *Nucl Instr Meth Phys Res A* 2003;506:250-303.

115. A Fasso, A Ferrari, J Ranft and PR Sala. FLUKA: a multi-particle transport code. CERN-2005-10, INFN/TC_05/11, SLAC-R-773. 2005.

116. A Fasso, A Ferrari, S Roesler, PR Sala, G Battistoni, F Cerutti, E Gadioli, M.V. Garzelli F. Ballarini A Ottolenghi, A Empl and J Ranft. The physics models of FLUKA: status and recent developments. 2003; arXiv:hep-ph/0306267.

117. JF Briesmeister. MCNP™ – A general Monte Carlo N-Particle transport code, version 4C. Technical report no. LA-13709-M, Los Alamos National Laboratory, 2000.

118. H Jiang, J Seco and H Paganetti. Effects of Hounsfield number conversion on CT based proton Monte Carlo dose calculations. *Med Phys* 2007;34:1439-49.

119. AJ Lomax. Intensity modulation methods for proton radiotherapy. *Phys Med Biol* 1999;44:185-205.

120. M Goitien and GTY Chen. Beam scanning for heavy charged particle radiotherapy. *Med Phys* 1983;10:831-40.

121. E Pedroni, R Bacher, H Blattman, T Böhringer, A Coray, A Lomax, S Lin, G Munkel, S Scheib, U Schneider and A Tourovsky. The 200-MeV proton therapy project at the Paul Scherrer Institute: Conceptual design and practical realization. *Med Phys* 1995;22:37-53.

122. M Soukup and M Alber. Monte Carlo in the optimization of intensity modulated proton therapy. *Med Phys* 2007;34:2471 (Abstract).

123. H Paganetti, A Niemierko, M Ancukiewicz, LE Gerweck, M Goitien, JS Loeffler and HD Suit. Relative biological effectiveness (RBE) values for proton beam therapy. *Int J Radiat Oncol Biol Phys* 2002;53:407-21.

124. JJ Wilkens and U Oelfke. Optimization of radiobiological effects in intensity modulated proton therapy. *Med Phys* 2005;32:455-65.

125. C Burman, CS Chui, G Kutcher, S Leibel, M Zelefsky, T LoSasso, S Spirou, QW Wu, J Yang, J Stein, R Mohan, Z Fuks and CC Ling. Planning, delivery, and quality assurance of intensity-modulated radiotherapy using dynamic multileaf collimator: A strategy for large-scale implementation for the treatment of carcinoma of the prostate. *Int J Radiat Oncol Biol Phys* 1997;39:863-73.

126. CX Yu. Intensity-modulated arc therapy with dynamic multileaf collimation: an alternative to tomotherapy. *Phys Med Biol* 1995;40:1435-49.

127. PJ Keall, JV Siebers, M Arnfield, JO Kim and R Mohan. Monte Carlo dose calculations for dynamic IMRT treatments. *Phys Med Biol* 2001;46:929-41.

128. HH Liu, F Verhaegen and L Dong. A method of simulating dynamic multileaf collimators using Monte Carlo techniques for intensity-modulated radiation therapy. *Phys Med Biol* 2001;46:2283-9.

129. F Verhaegen and HH Liu. Incorporating dynamic collimator motion in Monte Carlo simulations: an application in modelling a dynamic wedge. *Phys Med Biol* 2001;46:287-96.

130. AML Olteanu, N Reynaert, W De Gersem, B De Smedt, C De Wagter, W De Neve and H Thierens. Monte Carlo simulation of intensity-modulated arc therapy plans. In: Abstract Book of the First European Workshop on Monte Carlo Treatment Planning. 2006;75.

131. M Ding, J Li, J Deng, E Fourkai and CM Ma. Dose correlation for thoracic motion in radiation therapy of breast cancer. *Med Phys* 2003;30:2520-9.

132. PJ Keall, JV Siebers, S Joshi and R Mohan. Monte Carlo as a four-dimensional radiotherapy treatment-planning tool to account for respiratory motion. *Phys Med Biol* 2004;49:3639-48.

133. H Paganetti, H Jiang and A Trofimov. 4D Monte Carlo simulation of proton beam scanning: modelling of variations in time and space to study the interplay between scanning pattern and time-dependent patient geometry. *Phys Med Biol* 2005;50:983-90.

134. E Heath and J Seuntjens. 4D Monte Carlo dose calculations in deforming anatomy using direct voxel tracking. *Radiother Oncol* 2005;76:S45 (Abstract).

135. JS Li, T Pawlicki, J Deng, SB Jiang, E Mok and CM Ma. Validation of a Monte Carlo dose calculation tool for radiotherapy treatment planning. *Phys Med Biol* 2000 ;45 :2969-85.

136. CL Hartmann-Siantar, RS Walling, TP Daly, B Faddegon, N Albright, P Bergstrom, AF Bielajew, C Chuang, D Garrett, RK House, D Knapp, DJ Wieczorek and LJ Verhey. Description and dosimetric verification of the PEREGRINE Monte Carlo dose calculation system for photon beams on a water phantom. *Med Phys* 2001;28:1322-37.

137. E Heath, J Seuntjens and D Sheikh-Bagheri. Dosimetric evaluation of the clinical implementation of the first commercial IMRT Monte Carlo treatment planning system at 6 MV. *Med Phys* 2004;31:2771-9.

138. JE Cygler, GM Dalaskov, GH Chan and GX Ding. Evaluation of the first commercial Monte Carlo dose calculation engine for electron beam treatment planning. *Med Phys* 2004;31:142-53.

Chapter 11

Conclusions

In this thesis, BCRT was implemented into the IMRT treatment planning process at GUH. The developed software allows the incorporation of one or more biological image sets, the specification of a bound-constrained linear relationship between the image signal and the desired radiation dose, the creation of initial beam segments based on the provided biological imaging data, the optimization of the segment shapes and weights, and the evaluation of the final treatment plan.

The feasibility of FDG-PET guided BCRT for head and neck cancer was demonstrated in a planning study. BCRT did not compromise the planning constraints for the OARs. The obtained biological conformity was the best for the lowest level of dose escalation. Compared to uniform dose escalation within a contoured FDG-PET lesion, improved target dose coverage was achieved using BCRT.

Progress in biological imaging has opened a new range of possibilities to individualize RT. Optimal use of the new tools for treatment planning and delivery will require an improved understanding of the radiobiology of tumors.

MC can be used to calculate RT dose distributions with great accuracy. The use of MC is especially advantageous in case of small, irregular treatment fields delivering dose to regions of great tissue inhomogenity, for example in IMRT treatment of head and neck or lung tumors. In this thesis, the added value of MC compared to pencil beam and convolution/superposition algorithms was demonstrated for IMRT lung cancer patients.

MCDE was developed at Ghent University as a highly accurate MC dose engine for IMRT patient dose calculations. In this thesis, the conversion of CT numbers into material composition data for MC dose calculations was studied in detail. Stoichiometric CT scanner calibration and the creation of dosimetrically equivalent tissue subsets resulted in a 14 bin CT conversion scheme, suitable for RT using photons and electrons. MCDE was further improved by the introduction of uncertainty-based stopping criteria, enabling accurate clinical treatment plan evaluation in the shortest possible time.

Finally, the feasibility of integrating MCDE into the IMRT optimization process at GUH was demonstrated for an ethmoid sinus cancer patient case. Patients may benefit from the improvements in dose calculation accuracy using full MC. MC dose engines are currently being implemented into commercial treatment planning systems. Highly accurate dose engines like MCDE are not suitable for routine clinical use, but they represent excellent benchmarking tools, as they can be used in situations where measurements are very difficult or even impossible.

Curriculum Vitae

Personal

Barbara VANDERSTRAETEN
Born on 3 August 1981 in Asse
Belgian
Married

Private address:

Driesstraat 58/101
B-9050 Gent

Working address:

Ghent University
Department of Medical Physics
Proeftuinstraat 86
B-9000 Gent
Tel.: +32 9 264 66 47
Fax: +32 9 264 66 96
E-mail: Barbara.Vanderstraeten@UGent.be

Education

- Ghent University, Faculty of Engineering:
  Master of engineering physics (2003) with highest honors
  Thesis: *Dosis versus beeldkwaliteit bij CT-beeldvorming* (in Dutch)
  Promoter: Prof.dr. H. Thierens

- Ghent University, University Language Centre:
  - "Advanced academic English: conference skills for the biomedical sciences" (2006)
  - "Advanced academic English: writing skills for the biomedical sciences" (2005)

- Ghent University, Institute for Continuing Education:
    - "Praktijkgerichte statistiek" (2005)

- ESTRO (European Society for Therapeutic Radiology and Oncology):
    - Teaching course "IMRT and other conformal techniques in practice", Amsterdam, The Netherlands (2004)
    - Teaching course "Dose determination in radiotherapy: beam characterisation, dose calculation and dose verification", Nice, France (2004)

- BEST (Board of European Students of Technology):
    - International symposium "The use of new learning techniques. Contribution to the ETNET21 thematic network", Vienna University of Technology, Austria (2003)
    - Summer course "Heart and vessels: from engineering to clinical therapy", Ghent University (2002)
    - Summer course "International engineering: preparation for a global career", KTH – Royal Institute of Technology Stockholm, Sweden (2001)

Awards

- Varian Poster Award (First European Workshop on Monte Carlo Treatment Planning, 22-25 October 2006, Gent, Belgium)

Membership

- Belgian Hospital Physicists Association (BHPA)

- European Society of Therapeutic Radiology and Oncology (ESTRO)

- European Work Group on Monte Carlo Treatment Planning (EWG-MCTP)

- Alumni Board of European Students of Technology (BEST) Gent

- LinkedIn.com

Publications

A$_1$ Publications

[1] **B Vanderstraeten**, AML Olteanu, N Reynaert, A Leal, W De Neve and H Thierens. Evaluation of uncertainty-based stopping criteria for Monte Carlo calculations of intensity-modulated radiotherapy and arc therapy patient dose distributions. *Int J Radiat Oncol Biol Phys* 2007;69:628-37.

[2] I Madani, W Duthoy, C Derie, W De Gersem, T Boterberg, M Saerens, F Jacobs, V Grégoire, M Lonneux, L Vakaet, **B Vanderstraeten**, W Bauters, K Bonte, H Thierens and W De Neve. Positron emission tomography-guided, focal-dose escalation using intensity-modulated radiotherapy for head and neck cancer. *Int J Radiat Oncol Biol Phys* 2007;58:126-35.

[3] **B Vanderstraeten**, PW Chin, M Fix, A Leal, G Mora, N Reynaert, J Seco, M Soukup, E Spezi, W De Neve and H Thierens. Conversion of CT numbers into tissue parameters for Monte Carlo dose calculations: a multi-centre study. *Phys Med Biol* 2007;52:539-62.

[4] I Madani, **B Vanderstraeten**, S Bral, M Coghe, W De Gersem, C De Wagter, H Thierens and W De Neve. Comparison of 6 MV and 18 MV photons for IMRT treatment of lung cancer. *Radiother Oncol* 2007;82:63-9.

[5] L Paelinck, B De Smedt, N Reynaert, M Coghe, W De Gersem, C De Wagter, **B Vanderstraeten**, H Thierens and W De Neve. Comparison of dose-volume histograms of IMRT treatment plans for ethmoid sinus cancer computed by advanced treatment planning systems including Monte Carlo. *Radiother Oncol* 2006;81:250-6.

[6] **B Vanderstraeten**, N Reynaert, I Madani, L Paelinck, C De Wagter, W De Gersem, W De Neve and H Thierens. Accuracy of patient dose calculation for lung IMRT: A comparison of Monte Carlo, convolution/superposition, and pencil beam computations. *Med Phys* 2006;33:3149-58.

[7] **B Vanderstraeten**, W Duthoy, W De Gersem, W De Neve and H Thierens. [^{18}F]fluoro-deoxy-glucose positron emission tomography ([^{18}F]FDG-PET) voxel intensity-based intensity-modulated radiation therapy (IMRT) for head and neck cancer. *Radiother Oncol* 2006;79:249-58.

[8] **B Vanderstraeten**, W De Gersem, W Duthoy, W De Neve and H Thierens. Implementation of biologically conformal radiation therapy (BCRT) in an algorithmic segmentation-based inverse planning approach. *Phys Med Biol* 2006;51:N277-86.

[9] B De Smedt, **B Vanderstraeten**, N Reynaert, W De Neve and H Thierens. Investigation of geometrical and scoring grid resolution for Monte Carlo dose calculations for IMRT. *Phys Med Biol* 2005;50:4005-4019.

[10] N Reynaert, M Coghe, B De Smedt, L Paelinck, **B Vanderstraeten**, W De Gersem, B Van Duyse, C De Wagter, W De Neve and H Thierens. Importance of accurate linear accelerator head modelling for IMRT Monte Carlo calculations. *Phys Med Biol* 2005;50:831-846.

A_2 Publications

[1] B De Smedt, **B Vanderstraeten**, N Reynaert, W De Gersem, W De Neve and H Thierens. The influence of air cavities within the PTV on Monte Carlo-based IMRT optimization. *Journal of Physics: Conference Series* 2007;73:012003.

International communications

[1] First European Workshop on Monte Carlo Treatment Planning, 22-25 October 2006, Gent
B Vanderstraeten, B De Smedt, W De Gersem, N Reynaert, W De Neve and H Thierens. Monte Carlo-based IMRT optimization. (Talk)

[2] First European Workshop on Monte Carlo Treatment Planning, 22-25 October 2006, Gent
B Vanderstraeten, N Reynaert, W De Neve, H Thierens. Validation of a stopping criterion for Monte Carlo calculations of IMRT patient dose distributions. (Poster, winner of the Best Poster Award)

[3] 25th Annual ESTRO Meeting, 8-12 October 2006, Leipzig, Germany
I Madani, W Duthoy, M Lonneux, M Saerens, **B Vanderstraeten**, V Grégoire and W De Neve. ^{18}F-FDG-PET guided IMRT of head and neck cancer – Focal dose escalation phase I study. *Radiother Oncol* 2006;81:S333. (Poster, winner of the Best Poster Award)

[4] 25th Annual ESTRO Meeting, 8-12 October 2006, Leipzig, Germany
B Vanderstraeten, N Reynaert, L Paelinck, I Madani, W De Gersem, C De Wagter, W De Neve and H Thierens. Accuracy of patient dose calculations for IMRT treatment of lung cancer. *Radiother Oncol* 2006;81:S365. (Poster)

[5] World Congress on Medical Physics and Biomedical Engineering, 27 August – 1 September 2006, Seoul, Korea
B Vanderstraeten, N Reynaert, W De Neve, H Thierens. Validation of a stopping criterion for Monte Carlo calculations of IMRT patient dose distributions. (Poster)

[6] World Congress on Medical Physics and Biomedical Engineering, 27 August – 1 September 2006, Seoul, Korea
B Vanderstraeten, N Reynaert, I Madani, L Paelinck, W De Gersem, C De Wagter, W De Neve and H Thierens. Accuracy of patient dose calculation for lung-IMRT: a comparison of Monte Carlo, convolution/superposition, and pencil beam computations. (Talk)

[7] 9th Biennial ESTRO Meeting on Physics and Radiation Technology for Clinical Radiotherapy, 24-29 September 2005, Lisbon, Portugal
B Vanderstraeten, E Born, M Fippel, A Leal, G Mora, N Reynaert, J Seco, M Soukup, E Spezi, B De Smedt, F De Bisschop, W De Neve and H Thierens. Conversion of CT numbers into tissue parameters for Monte Carlo dose calculations. *Radiother Oncol* 2005;76:S46-S47. (Talk)

[8] 9th Biennial ESTRO Meeting on Physics and Radiation Technology for Clinical Radiotherapy, 24-29 September 2005, Lisbon, Portugal
L Paelinck, B De Smedt, N Reynaert, M Coghe, W De Gersem, C De Wagter, **B Vanderstraeten**, H Thierens an W De Neve. IMRT dose distributions for ethmoid sinus cancer calculated by five different treatment planning systems. *Radiother Oncol* 2005;76:S108-S109. (Talk)

[9] 9th Biennial ESTRO Meeting on Physics and Radiation Technology for Clinical Radiotherapy, 24-29 September 2005, Lisbon, Portugal
B De Smedt, **B Vanderstraeten**, N Reynaert, W De Neve and H Thierens. The effect of geometrical and scoring voxel dimensions on accuracy and efficacy of Monte Carlo dose calculations for IMRT. *Radiother Oncol* 2005;76:S149. (Poster)

[10] 46th Annual AAPM Meeting, 25-29 July 2004, Pittsburgh, USA
B Vanderstraeten, W De Gersem, W Duthoy, W De Neve and H Thierens. Incorporation of biological imaging voxel intensity information into the IMRT optimization algorithm. *Med Phys* 2004;31:1777. (Talk)

National communications

[1] 21st Annual BHPA Symposium, 20-21 January 2006, Gent
B Vanderstraeten, N Reynaert, L Paelinck, I Madani, W De Gersem, C De Wagter, W De Neve and H Thierens. Accuracy of patient dose calculation for lung-IMRT: a comparison of Monte Carlo, convolution/superposition, and pencil beam computations. (Talk)

Invited lectures

[1] 9th Biennial ESTRO Meeting on Physics and Radiation Technology for Clinical Radiotherapy, Barcelona, 9-13 September 2007
B Vanderstraeten, W De Gersem, I Madani, W De Neve and H Thierens. Implementation of biologically conformal radiation therapy in the clinic. *Radiother Oncol* 2007;84:S90.

[2] AZ-VUB Seminars in Oncology, Brussel, 5 March 2004
Incorporation of [^{18}F]FDG-PET imaging in the IMRT optimization algorithm for head and neck cancer

Other activities

- Co-organiser of the 21st Annual Symposium of the Belgian Hospital Physicists Association "Physics in medicine in the 21st century: new techniques, challenges, problems and solutions", 20-21 January 2006, Gent

- Co-organiser of the 1st European Workshop on Monte Carlo treatment planning "Introduction of Monte Carlo treatment planning into the clinic", 22-25 October 2006, Gent

- Member of the editorial board of *Recent patents in biomedical engineering*

- Referee for *Radiotherapy and Oncology* and *Medical Physics*